THE UNIVERSITY OF HULL

Morphological Quantitation Software in Breast MRI: Application to Neoadjuvant Chemotherapy Patients

Being a Thesis submitted for the Degree of

Doctor of Philosophy

In the University of Hull

By

Arfan Ahmed
MSc in .NET & Distributed Systems Development
BSc (Hons) Computer Science

September 2012

Summary

The work in this thesis examines the use of texture analysis techniques and shape descriptors to analyse MR images of the breast and their application as a potential quantitative tool for prognostic indication.

Textural information is undoubtedly very heavily used in a radiologist's decision making process. However, subtle variations in texture are often missed, thus by quantitatively analysing MR images the textural properties that would otherwise be impossible to discern by simply visually inspecting the image can be obtained. Texture analysis is commonly used in image classification of aerial and satellite photography, studies have also focussed on utilising texture in MRI especially in the brain. Recent research has focussed on other organs such as the breast wherein lesion morphology is known to be an important diagnostic and prognostic indicator. Recent work suggests benefits in assessing lesion texture in dynamic contrast-enhanced (DCE) images, especially with regards to changes during the initial enhancement and subsequent washout phases. The commonest form of analysis is the spatial grey-level dependence matrix method, but there is no direct evidence concerning the most appropriate pixel separation and number of grey levels to utilise in the required co-occurrence matrix calculations. The aim of this work is to systematically assess the efficacy of DCE-MRI based textural analysis in predicting response to chemotherapy in a cohort of breast cancer patients. In addition an attempt was made to use shape parameters in order to assess tumour surface irregularity, and as a predictor of response to chemotherapy.

In further work this study aimed to texture map DCE MR images of breast patients utilising the co-occurrence method but on a pixel by pixel basis in order to determine threshold values for normal, benign and malignant tissue and ultimately creating functionality within the in house developed software to highlight hotspots outlining areas of interest (possible lesions). Benign and normal data was taken from MRI screening data and malignant data from patients referred with known malignancies.

This work has highlighted that textural differences between groups (based on response, nodal status, triple negative and biopsy grade groupings) are apparent and appear to be most evident 1-3 minutes post-contrast administration. Whilst the large number of statistical tests undertaken necessitates a degree of caution in interpreting the results, the fact that significant differences for certain texture parameters and groupings are consistently observed is encouraging.

With regards to shape analysis this thesis has highlighted that some differences between groups were seen in shape descriptors but that shape may be limited as a prognostic indicator. Using textural analysis gave a higher proportion of significant differences whilst shape analysis results showed inconsistency across time points.

With regards to the mapping this work successfully analysed the texture maps for each case and established lesion detection is possible. The study successfully highlighted hotspots in the breast patients data post texture mapping, and has demonstrated the relationship between sensitivity and false positive rate via hotspot thresholding.

Acknowledgements

In the name of Allah, the Beneficent, the Merciful (Quran)

All credit is due to Allah; only the mistakes are my own

It is difficult to overstate my gratitude to my Ph.D. supervisor, Dr. Peter Gibbs. With his enthusiasm, his inspiration, and his great efforts to explain things clearly and simply, he helped to make this research enjoyable for me. Throughout my three years up to and including the thesis-writing period, he provided encouragement, sound advice, good teaching, good company, and lots of good ideas. I would have been lost without him.

I would also like to thank Dr Martin D Pickles for his support, contribution and expertise as my secondary supervisor, Professor Lindsay Turnbull (Scientific Director of Centre for Magnetic Resonance Investigations (CMRI)) for allowing me this great opportunity of studying at CMRI. Moreover, Yorkshire Cancer Research (YCR) for funding my Ph.D.

I am indebted to my colleagues Lawrence Kenning, Dr Martin Lowry, Dr Metab Al-Kubeyyer and all the staff at (CMRI) The University of Hull for providing a stimulating and fun environment in which to learn and grow.

I wish to thank my wife Assiea for her support and supplications, my sons Eesa and Abdullah, my brothers and my sister and my entire extended family for providing a loving environment for me.

Lastly, and most importantly, I wish to thank my parents, Nazir Ahmed and Saleem Ahmed. They bore me, raised me, supported me, taught me and loved me. May Allah grant them the highest place in Paradise.

Contents

1 Introduction (Physics)

Nuclear Magnetic Resonance (NMR) deals with specific isotopes in a magnetic field with respect to the distribution and behaviour of their magnetic moments (NMR is still used today as NMR spectroscopy). First proven experimentally in the 1940's [1, 2], NMR development was primarily focused on chemical and biochemical studies until the 1970s. Since then the NMR method has also been applied to the biomedical field and nowadays it is widely used in the form of magnetic resonance imaging (MRI). It has in modern day medicine become one of the most important radiological techniques due to it being a non invasive method providing information about biochemical processes in living tissue. Over the last quarter of a century, in addition to standard MR imaging, many new MR techniques have been developed for biomedical applications, some examples include measurements of diffusion, perfusion, relaxometry, and in vivo spectrometry. MRI allows the determination of different tissue characteristics; the contrast and signal intensity values can be evaluated using various different mathematical-statistical methods, texture analysis being one of them.

Unlike X-ray imaging MRI utilises relatively low frequencies and thus does not induce ionising radiation damage. The principle of the MR method can be best described as the absorption of radiofrequencies by nuclei that are placed in a strong magnetic field B_0. In general it's possible to produce an MR image for many elements due to the multiple energy levels present within all isotopes with a non-zero magnetic moment. In practical application the NMR sensitivity of hydrogen nuclei (protons) is greater than that of any other nuclei; therefore in biomedicine hydrogen nuclei (protons) are used in nearly all applications. Hydrogen as an element is present in all organic compounds as well as in water. Water is a basic material in the makeup of biological tissues and exists in very high concentrations. The structural composition of a tissue is influenced by the distribution of its water molecules and this is why MR imaging is particularly suited to medical applications.

1.1 Nuclear Spin

Hydrogen nuclei (protons) behave like tiny rotating magnets. This is due to them having magnetic properties as a result of being charged and possessing nuclear spin. This behaviour can be represented using vector notation (fig 1.1). The vector quantities are in parallel, the relation is shown by the equation:

$$\mu = \gamma J \qquad \text{(Equation 1)}$$

where μ is the magnetic moment, J is the angular momentum and γ is the gyromagnetic ratio (constant for a given nucleus).

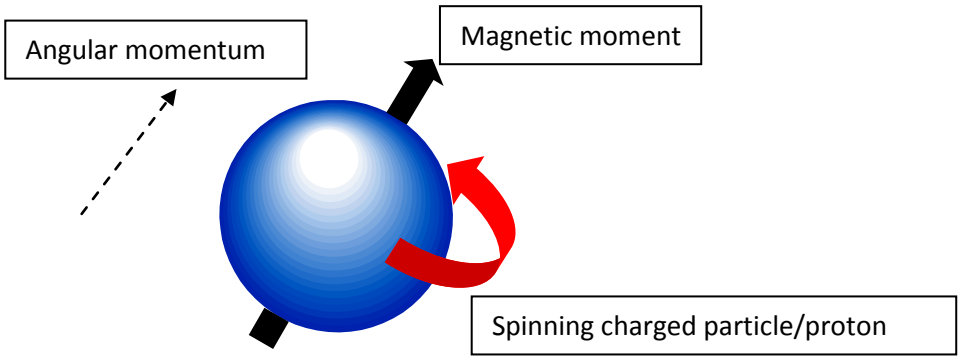

Figure 1.1: A Hydrogen nuclei (proton) rotating, black arrow represents vector (magnetic moment)

1.1.1 Nuclear Spins in an External Field

When nuclei are inserted into a strong external magnetic field (B_0) they will attempt to align themselves with B_0 and spin around an axis parallel with B_0 (fig 1.2). The concept of nuclear spin can be represented by being similar to that of a spinning top, a spinning top rotates on its own axis and rotates around the gravitational field as it does this. Therefore, nuclear spins rotate on their own axis whilst rotating around B_0 as they try to align with B_0. When nuclei are placed in a magnetic field discrete energy levels are created, the magnetic moment has an energy given by the equation:

$$U = -\gamma m_z \hbar B_0 \qquad \text{(Equation 2)}$$

where m is the magnetic spin quantum, m_z is the measurable component of m, B_0 is the magnetic field strength, $\hbar$ is defined as $\frac{h}{2\pi}$ where h is Planck's constant . The energy levels experience a splitting effect, and the energy becomes directly proportional to the strength of the externally applied magnetic field. The following selection rule allows transitions to be induced between these energy levels

$$\Delta m_z = \pm 1 \qquad \text{(Equation 3)}$$

provided the Bohr frequency condition is met:

$$\Delta U = \hbar\omega_0 \qquad \text{(Equation 4)}$$

Equation 4 combines with equation 2 and reduces to:

$$\omega_0 = \gamma B_0 \qquad \text{(Equation 5)}$$

where ω_0 is the frequency of applied radiation, thus the required frequency of the applied radiation is proportional to the applied magnetic field strength.

1.1.2 Larmor Frequency (Precession)

In the external field the magnetic moment tries to align itself with this field whilst it spins on its own axis. A torque is produced as a result of which it precesses about the B_0 axis. The frequency of precession ω_0 (known as the Larmor frequency, see fig 1.2) is dependent on the external magnetic field strength B_0 and on the type of nucleus, (each spin species has a unique gyromagnetic ratio γ). The Larmor frequency is thus given by:

$$\omega_0 = \gamma B_0$$

This frequency is the same as in the previous section (equation 5) which is required to induce transitions i.e. resonance.

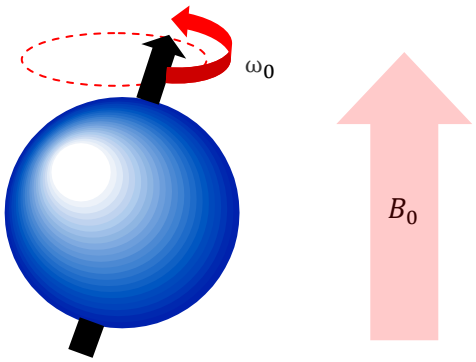

Figure 1.2: Torque is exerted on moment which attempts to align it with the magnetic field, this leads to Larmor precession where angular frequency is given by $\omega_0 = \gamma B_0$.

1.1.3 Net magnetisation

In the absence of an external magnetic field, the sum of all magnetic moments is zero (fig 1.3). In a magnetic field at room temperature there is a small excess of spins parallel to B_0 (low energy state) compared to anti parallel spins (fig 1.4). The spins with lower energy states are naturally more in number due to this state having higher stability than that of the higher energy state (anti-parallel). As a result of this small difference there exists a macroscopic magnetisation M of the system.

Because of the slightly more parallel spins the net magnetisation has a longitudinal component (along the Z axis) aligned with B_0. Due to the spins not rotating in phase, the sum of all the net magnetisation (macroscopic magnetisation) in the transverse component is null. According to the Boltzmann distribution the spins are spread amongst the Zeeman energy levels, the difference in population between the two levels can be shown by the following population distribution equation:

$$N_\uparrow - N_\downarrow \approx \frac{\gamma \hbar N B_0}{2kT} \qquad \text{(Equation 6)}$$

where N is the total number of spins, k is boltzmann's constant, T is absolute temperature and $N_\uparrow (N_\downarrow)$ represent the number of spins in the low (high) energy states. B_0 (Magnetic field

strength) is the only thing that can be easily controlled in order to attempt to increase the magnetisation.

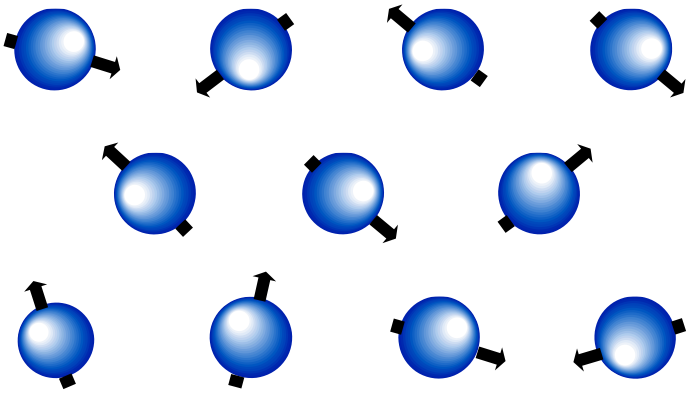

Figure 1.3: The magnetic moments of protons in the absence of an external magnetic field. The sum of all magnetic moments is zero because they are oriented in a random fashion.

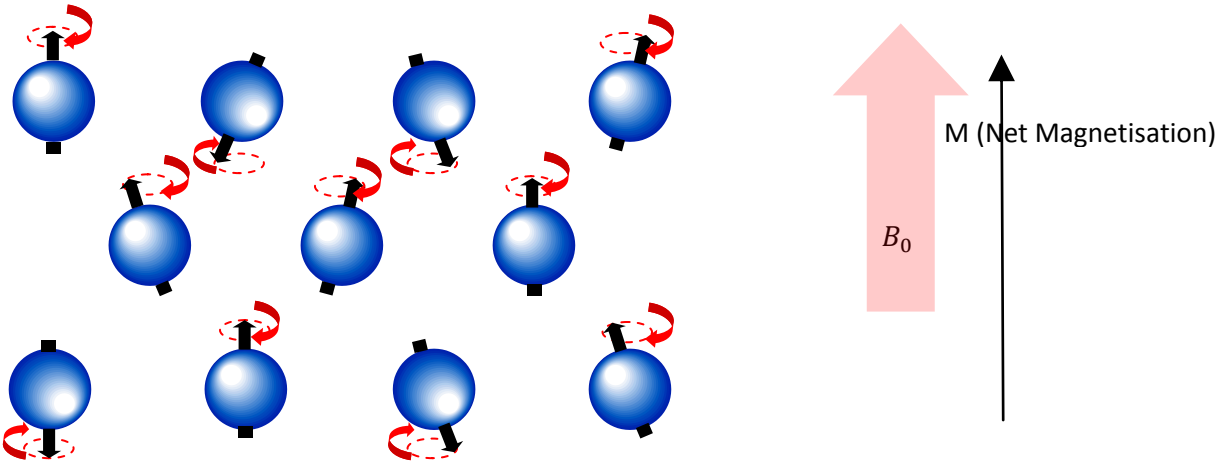

Figure 1.4: The magnetic moments of protons in a non-zero magnetic field B_0. M known as the macroscopic magnetization vector is observed as the sum of all magnetic moments parallel with B_0. This is due to the moments having a (anti) parallel alignment with B_0 and all the transverse components are cancelled since the spins are equally distributed about the cone of precession.

1.1.4 Rf Pulse

A time dependent magnetic field can induce transitions as the macroscopic magnetisation precesses around the total applied field, i.e. the sum of the static magnetic field B_0 and the time dependent magnetic field B_1. An rf pulse is when a B_1 field is applied on resonance for a finite amount of time, hence resonance occurs when the frequency of the stimulus (RF pulse) is the same as the natural frequency (Larmor) of the system. The precessional frequency around B_1 is given by the equation:

$$\omega_1 = \gamma B_1 \qquad \text{(Equation 7)}$$

The only protons that will respond to the RF pulse are the ones that spin with the same frequency as the electromagnetic RF pulse. The magnetisation can be rotated through any desired angle by applying the B_1 field for a certain length of time. The flip angle can be easily manipulated by adjusting either the duration or strength of the applied field. By applying a 180° pulse excess spins will exist in the higher energy state caused by an inversion of the equilibrium population difference, whilst a 90° pulse will equalise the spin populations and individual spins will bunch together in the cone of precession. The angle of rotation can be shown by the formula:

$$\theta = \gamma B_1 \tau \qquad \text{(Equation 8)}$$

where τ is the duration of the rf pulse.

1.1.5 Bloch Equations

Once perturbation has occurred the spin system returns to equilibrium via the dissipation of energy to the surrounding lattice and neighbouring spins over time. The lost energy converts into heat thus raising the temperature of the system. Bloch in 1946 incorporated these relaxation processes into the equation of motion (Bloch equations are phenomenological):

Equation (9)

$$\frac{dM_x}{dt} = \gamma[\underline{M} \Lambda \underline{B}]_x - \frac{M_x}{T_2}$$

$$\frac{dM_y}{dt} = \gamma[\underline{M} \Lambda \underline{B}]_y - \frac{M_y}{T_2}$$

$$\frac{dM_z}{dt} = \gamma[\underline{M} \Lambda \underline{B}]_z - \frac{(M_z - M_0)}{T_1}$$

Where T_1 is the spin-lattice relaxation time and T_2 is the spin-spin relaxation time. The evolution of the transverse (M_x, M_y) and longitudinal (M_z) magnetisation components are independent processes. $\underline{M} \Lambda \underline{B}$ are equal to the vector cross product of M and B.

1.1.6 Relaxation

The process whereby the net magnetisation returns to equilibrium is known as relaxation. During relaxation electromagnetic energy is retransmitted, and this is often referred to as the NMR signal. There are two distinct mechanisms involved in relaxation;

- Longitudinal relaxation: longitudinal magnetisation recovery. Also known as spin lattice relaxation, this occurs when energy exchange between the spins and surrounding lattice re-establishes thermal equilibrium. RF energy is released back into the surrounding lattice as the spins enter back into a low energy state from a high energy state. Figure 1.5 shows the longitudinal recovery. Recovery of the z-component after a 90° excitation is given by the equation:

$$M_z = M_0(1 - e^{-t/T_1}) \qquad \text{Equation (10)}$$

recovery of the z-component after a 180° excitation is given by the equation:

$$M_z = M_0(1 - 2e^{-t/T_1}) \qquad \text{Equation (11)}$$

- Transverse relaxation: transverse magnetisation decay. Also known as spin-spin relaxation, this occurs when spins get out of phase. Referred to as spin-spin interaction; the local magnetic fields interact as the spins move together in turn slightly modifying their precession rate, interaction is random and temporary. Spin-spin relaxation therefore causes a cumulative loss in phase which results in a transverse magnetisation decay. Figure 1.6 shows the transverse relaxation decay. The evolution of a transverse magnetisation after a 90° pulse is given by the equation

$$M_{xy} = M_0 e^{-t/T_2} \qquad \text{Equation (12)}$$

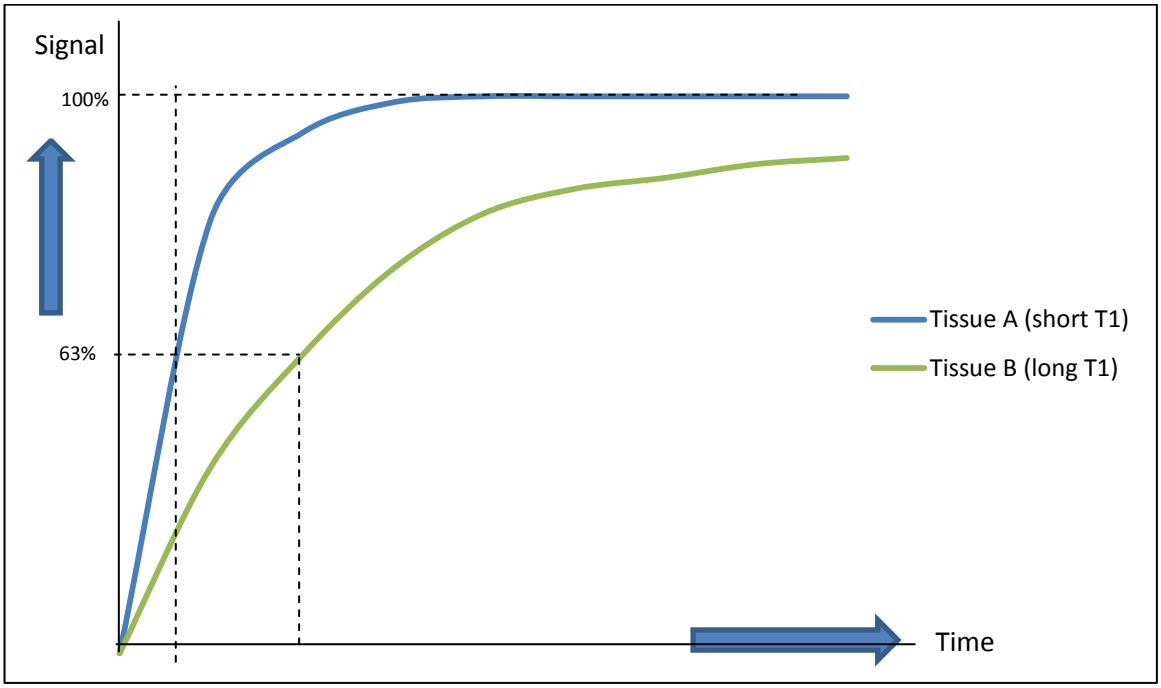

Figure 1.5: Spin-lattice relaxation after a 90 degree RF pulse. The recovery of longitudinal magnetisation follows an exponential curve. T1 is the tissue specific time constant which the recovery rate is characterised by. Longitudinal magnetisation has returned to 63% of its final value after time T1. T1 values are longer at higher field strengths. Tissue A has a shorter longitudinal relaxation time than tissue B and therefore recovers quicker.

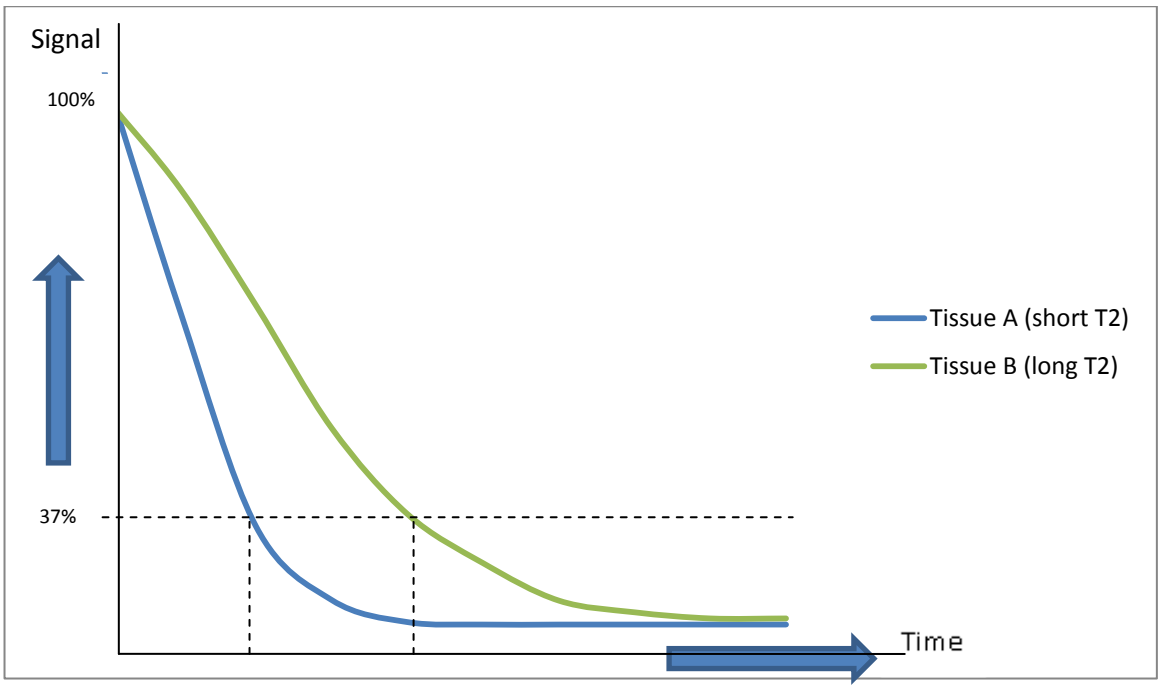

Figure 1.6: Spin-spin relaxation, Tissue B has a longer T2 than Tissue A. The graph shows transverse magnetisation decay characterised by the time constant T2. After time T2, transverse magnetisation has lost 63% of its original value. This type of relaxation (transverse) is a lot faster than longitudinal relaxation. Different tissues have different T2 due to the amount of free water present.

A few additional points to note about T1 and T2 are as follows;

- When motions are slow relaxation is inefficient and T_1 is long.
- When the frequency of the motions match the transition frequency relaxation is efficient and T_1 is short.
- When motions are too fast, relaxation is once again inefficient.For systems high in liquid T1 ranges from 0.1-10 seconds.
- The amount of free water present in a substance has direct relation to T1, the more water there is present then the higher the T1.
- On a T1 weighted image substances with long T1 values will appear dark.

Similarly for T2;

- For a liquid system the T2 value is typically in the range of 10-200 milliseconds.
- The amount of water present in a substance has direct relation to the length of T2, the more water there is present then the longer the T2.
- On a T2 weighted image the long T2 values will appear bright.

Water molecules are in fast exchange between three states, over the time scale of an MRI scan a water proton will either be in a bound, structured or free tissue and wander between these states. The proportion of water in each state determines the amount of time spent in each state. T1 and T2 relaxation times are long when in free water state. When in bound state T2 is very short and T1 is long.

1.1.7 Free Induction Decay and Signal Detection

The signal detected in the transverse plane is determined by the relaxation processes, and the signal oscillates at the Larmor frequency. The envelope height is determined by T2* (see section 1.2) the signal here is what is known as the Free induction decay (FID), figure 1.7 illustrates FID.

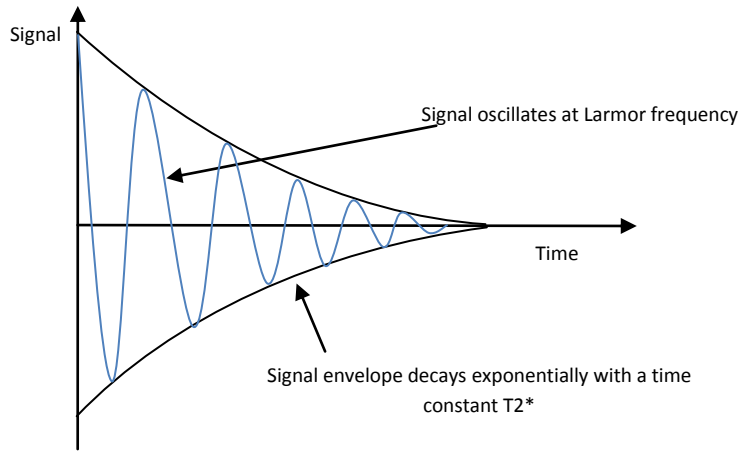

Figure 1.7: Illustrates Free induction decay (FID)

In signal detection often the same coil is used for transmission and reception, since the spin system is not observable during the rf pulse as this would cause saturation of any receiver. Instead at the end of the pulse the receiver is gated open, and the EMF induced in the receiver coil detects the component of magnetisation in the transverse plane as illustrated in figure 1.8.

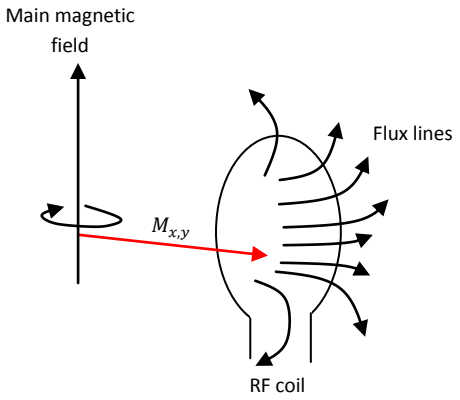

Figure 1.8: Illustrates how signal is induced and detected, often the same coil is used for both

1.1.8 Electronic Shielding and Chemical Shift

The sample or patient present within the MRI scanner has an effect on the externally applied field B_0. The orbital electrons around the nucleus produce small magnetic fields which in turn shield the nucleus from the full influence of B_0 causing the effective field at the nucleus to become:

$$B_{eff} = (1 - \sigma)B_0 \qquad \text{Equation (13)}$$

where σ is the shielding constant, and since the local electronic environment causes the shielding effect σ therefore varies with nuclear position within the molecule. The resonance condition thus can be described by the equation:

$$\omega_0 = \gamma(1 - \sigma)B_0 \qquad \text{Equation (14)}$$

and variations in resonant frequency will be caused by variations in σ. Chemical shifts will be present and are field dependent, it's these chemical shifts that allow an NMR spectroscopist to determine molecular structure. Figure 1.9 shows an example of a chemical shift spectrum from ethanol, the peaks amplitudes are proportional to the number of hydrogen atoms present.

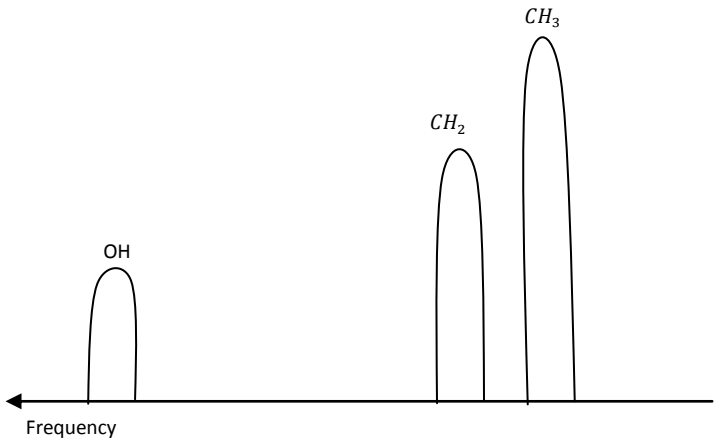

Figure 1.9: Spectrum from ethanol, the Hydrogen atoms are in slightly different chemical environments for each sub-group, and the amplitude of each peak is proportional to the number of hydrogen atoms.

1.2 Magnetic Field Inhomogeneities and T2*

The spin-spin relaxation time (T2) describes how fast the transverse magnetisation decays and is a fundamental property of the tissue. Even if the magnetic field was perfectly homogenous spin-spin relaxation would still occur, however if due to susceptibility effects or inhomogeneities in the main magnetic field there are different magnetic field strengths in different regions of the body then transverse relaxation is speeded up without affecting spin-lattice relaxation. The combined effect of T2 and magnetic field inhomogeneities in a sequence such as that of GE (gradient echo) is referred to as the 'apparent' relaxation time and given the shorthand notation T2* [3]. Nuclei in differing locations within the main field will resonate at

varying frequencies since the static magnetic field is never perfectly homogenous which leads to a reduction in apparent T2.

1.2.1 Spin-Echoes

When looking at the historical aspect spin echo was the first sequence to be used and created a benchmark for all following sequences, this was mainly to do with its contrast. Its 180 degree rephase pulse gives a true T2 signal as opposed to a T2* signal, spin-echo can be used to quantify T2 in NMR (by varying TE).

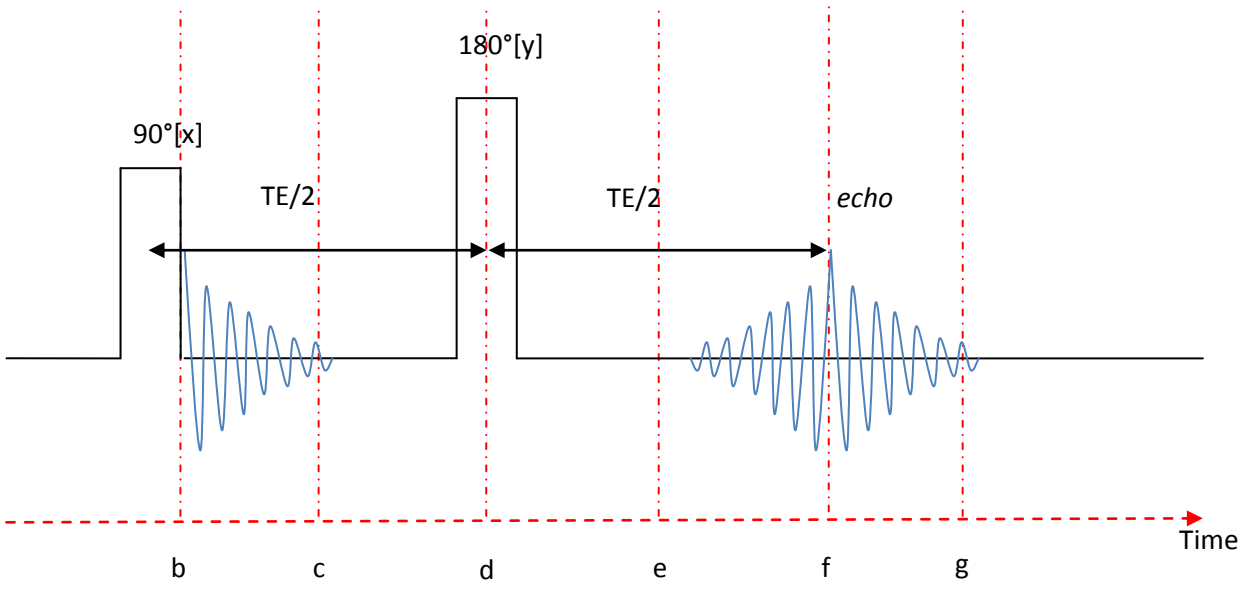

Figure 1.10a: Spin echo pulse sequence, figures 1.10b-1.10g illustrate each phase point b-g in order

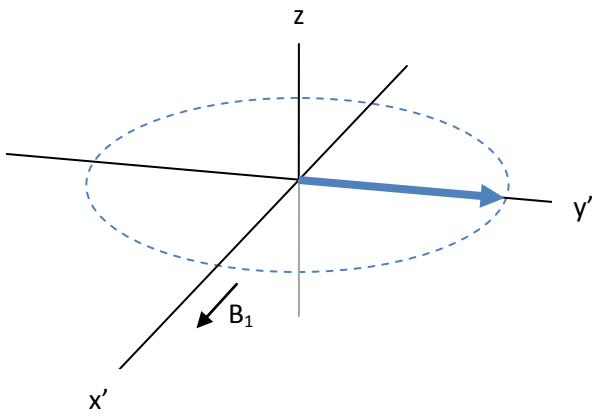

Figure 1.10b: Illustrates point b in figure 1.10a; Spins are initially in phase immediately after the 90° pulse.

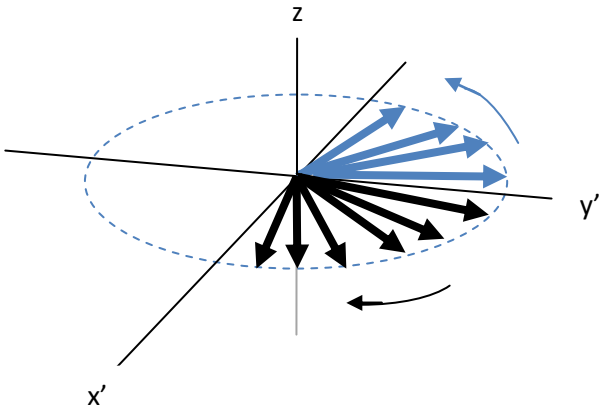

Figure 1.10c: Illustrates point c in figure 1.10a; De-phasing naturally and due to inhomogeneity until the 180° pulse is applied

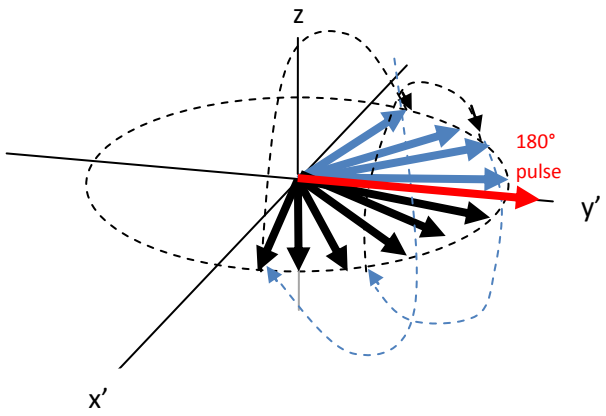

Figure 1.10d. Illustrates point d in figure 1.10a; 180° pulse is applied, 180° pulse can reverse static field inhomogeneities by rephasing spins. After a 180° RF pulse, spins rephase and transverse magnetization reappears.

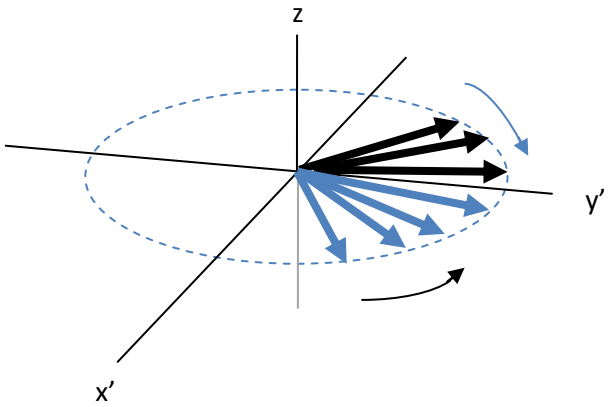

Figure 1.10e: Illustrates point e in figure 1.10a; Phases are reversed immediately after the pulse but de-phasing continues in the same direction

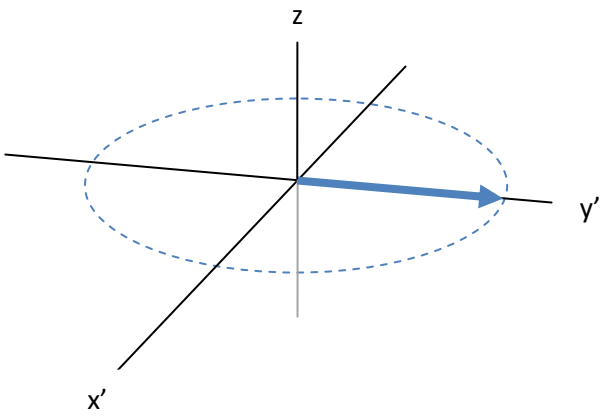

Figure 1.10f: Illustrates point f in figure 1.10a; an echo is formed

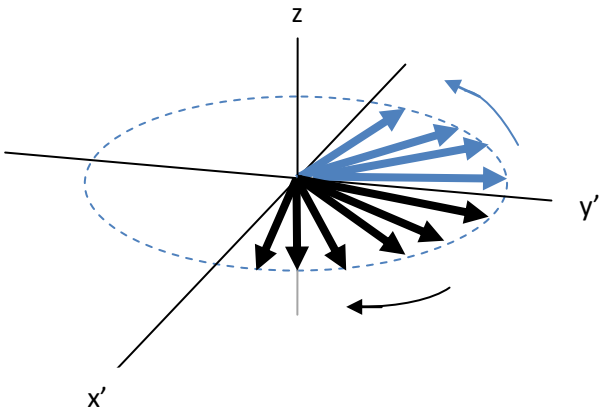

Figure 1.10g: Illustrates point g in figure 1.10a; De-phasing re-occurs

The spin echo sequence is illustrated by figure 1.10a where b-g represent each point and illustrated further by figures 1.10b to 1.10g**.**

- After the 90 degree pulse the spins are left to de-phase naturally for some time
- A 180 degree pulse is applied on the +y' axis, as a result all the spins are flipped through 180° about the y' axis. This reverses the phase angles but will not change the precessional frequencies of the spins.
- Lower magnetic field strength spins de-phase anticlockwise, higher field spins de-phase clockwise and appear to have been in a higher magnetic field as the 180° pulse flips them over.
- The spins will continue to de-phase in the same direction and experience the same magnetic field inhomogeneities.
- All the spins will eventually come back into phase along the +y' axis after a time equal to the delay between the 90° and the 180° pulse thus forming the spin echo.
- Because of the phase reversal T2 is the only process that will affect the echo height.

1.2.2 Magnetic Field Gradients

The signal in MRI needs to be spatially encoded to enable reconstruction of the original sample post data acquisition. The precessional frequency can be made to reflect spatial dependence by varying the static magnetic field with position in a predictable fashion. A range of precessional frequencies across the sample is created giving

$$\omega_0 = \gamma(B_0 + zG_z) \qquad \text{Equation (15)}$$

Where G_z is the strength of the linear field gradient, and z is the position of the molecule along the z axis.

1.2.3 Slice Selection

The Larmor equation states that resonant frequency is proportional to field strength. It is possible to artificially change the resonant frequency of the spins so they are spatially

dependent by applying linear changes in the magnetic field (gradients). Slice selection is illustrated in figure 1.11; by adjusting the gradient or RF waveform properties features of the slice can be manipulated without having to move the patient as in X-ray and CT. A gradient in combination with a limited bandwidth rf pulse excites a strip (slice) of spins. The following slice features can be manipulated electronically via the MRI scanner software:

- Position: varied by changing the carrier/basic frequency of the RF pulse but keeping the gradient strength the same
- Orientation: varied by changing the physical gradient axis, the selected slice is always perpendicular/orthogonal to the gradient applied, sagittal, coronal and transverse views can be obtained (fig 1.12) in addition by combining these physical gradients, oblique and double oblique views are possible
- Thickness: varied by changing the bandwidth (shape) of the RF pulse or the strength of the gradient. By applying a stronger gradient a thinner slice is achieved, also by using a narrower RF pulse bandwidth the same can be achieved (fig 1.13).

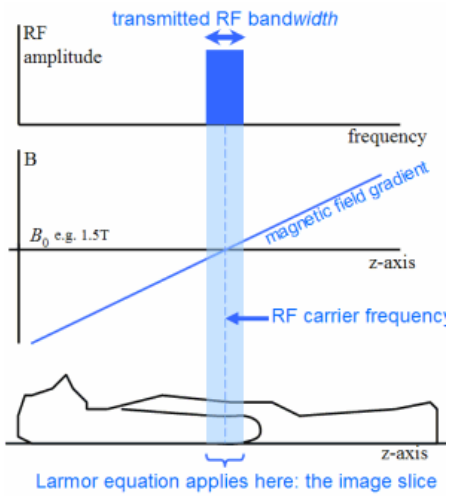

Figure 1.11 [4]: illustration shows how selective excitation is achieved of an image slice by applying a shaped RF pulse and a field gradient simultaneously

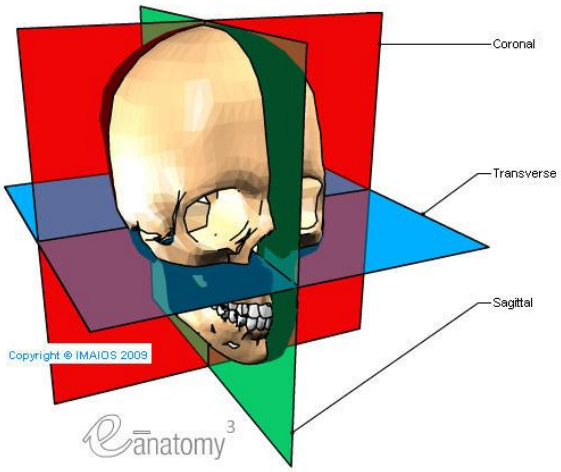

Figure 1.12 [5]: The principle slice orientations using physical gradients axis, by combining the physical gradients, oblique and double oblique views can be obtained.

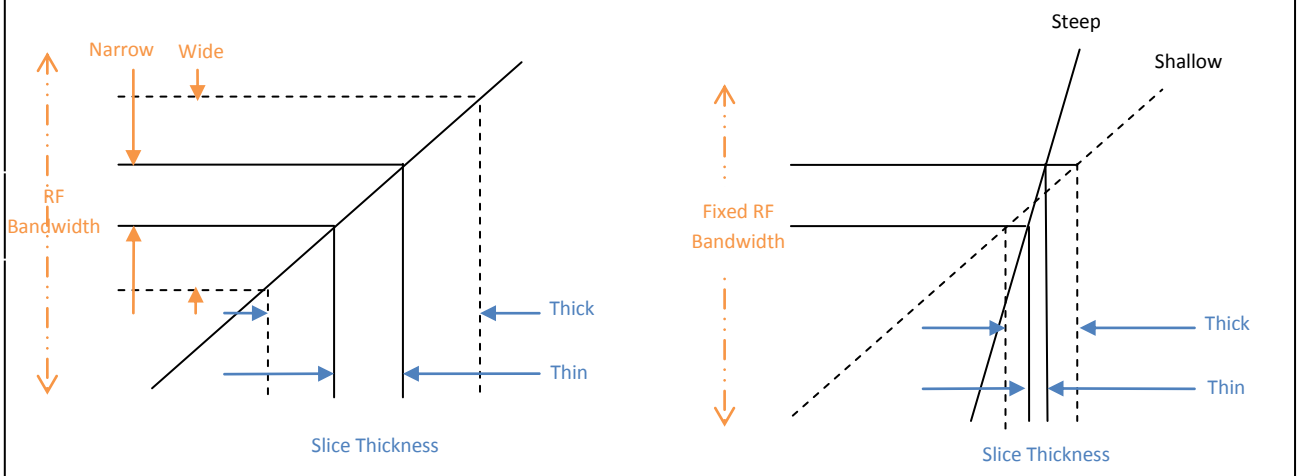

Figure 1.13: illustration shows slice thickness dependence on rf pulse bandwidth and applied field gradient strength, slice thickness can be reduced by either an increase in gradient strength or reducing rf pulse bandwidth

1.2.4 Frequency Encoding Gradient

A frequency encoding gradient, in a manner similar to the slice selection gradient, is a static gradient field which causes a range of Larmor frequencies to exist in the direction in which it is applied according to the Larmor equation. A Fourier transform (see next section) can then be used to separate the frequencies out once an MRI signal is measured. The signal is recorded under a frequency encoding gradient which allows the ability to provide projection reconstruction imaging if the direction of gradient is varied, frequency encoding gives a projection in that direction.

1.2.5 Fourier Transforms

According to Fourier's theorem any continuous periodic function S(t) can be expressed as the sum of a series of sine and cosine terms with appropriate frequencies and amplitudes. The Fourier transform is the mathematical tool used to relate these two functions giving the

equation:

$$S(t) \overset{FT}{\Leftrightarrow} S(f) \text{ where } S(t) \text{ and } S(f) \qquad \text{Equation (16)}$$

forming a Fourier transform pair.

The signal measured from MRI consist of signals from all over the object/patient being imaged, all signals can be treated as a series of sine waves, each having an individual frequency and amplitude. The Fourier transform has the ability to analyse these frequencies and amplitudes and in short since frequency is made dependent on position the Fourier transform can turn a signal against time graph into a signal against frequency (and ultimately position) graph.

1.2.6 Phase Encoding

Phase encoding is when a gradient is applied in order to spatially discriminate signal along a particular direction, this process is repeated many times unlike that of frequency encoding. The effect a gradient has on a spin's phase is that the spins precess slightly faster when a positive gradient is applied and when the gradient removal occurs the spins revert to their original Larmor frequency. It's this difference with/without the gradient that produces what's known as the phase shift in the signal (fig 1.14 illustrates this).

The amount of phase shift produced can be increased by increasing the gradient strength (or duration), the rate of change of phase (frequency) can be measured by repeating the experiment with an increasing gradient strength. When the signal is recorded at any one instant each individual spin does not possess a unique phase and frequency. Multiple measures are taken to establish each individual spin's combination of rate of change of phase (phase encoding) and baseline frequency (frequency encoding) which will be unique for each. A Fourier transform is then applied to determine each spin's position within the main magnetic field.

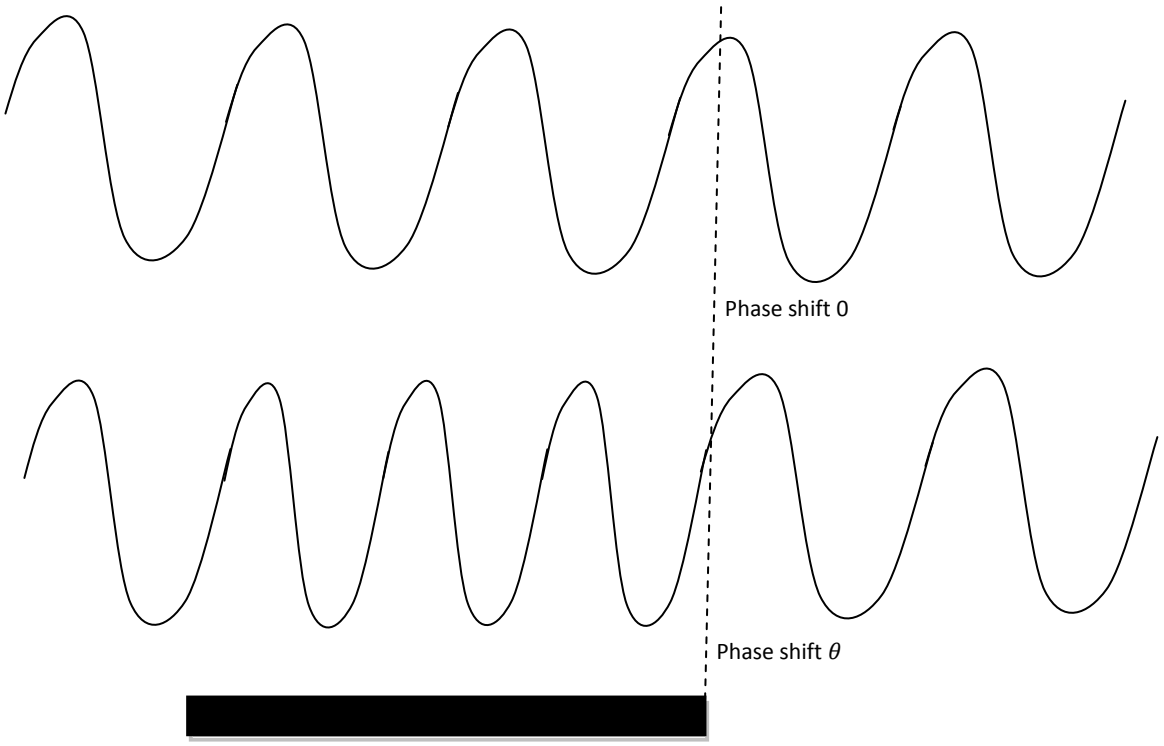

Figure 1.14: spins precess slightly faster when a positive gradient applied, when gradient is removed the spins revert to their original Larmor frequency, the difference with/without gradient produces a phase shift in the signal

1.3 Imaging Sequences

Imaging sequences are concerned with improving acquisition speed and image quality and trying to get a trade off between the two when obtaining MRI images. A sequence will consist of a combination of radio frequency pulses and gradients, the aims are to favour the signal of a particular tissue without degrading the signal to noise ratio and trying to limit the number of artefacts. There are literally hundreds of different sequences with different manufacturers having their own names for each. There are however 2 main families of sequence, spin echo sequences and gradient echo sequences; numerous variations of these two families have been developed.

The two main building blocks for any given sequence are radiofrequency pulses and gradients.

There are some essential components of any given imaging sequence which are outlined below;

- For the purpose of magnetic resonance an RF excitation pulse must exist
- For the purpose of spatial encoding be it 2D or 3D there need to be gradients
- A combined signal reading of one or more echo types

These are not exhaustive lists and there are various techniques for achieving each of the three options above. There are also sequence parameters that need to be set in order to find the best compromise between contrast, spatial resolution and speed, the parameters include repetition time(TR), echo time (TE), flip angle, field of view and matrix size.

- TR: The time interval between two excitation pulses which is normally a 90 degree pulse, this controls the T1 weighting
- TE: The time from pulse excitation to the signal induced in the receiver coils maximum value; known as time to spin echo formation, T2 weighting level is determined by TE.

1.3.1 Spin echo Imaging Sequence

Spin echos have already been discussed in section 1.2.1. This section will look at how these are used in imaging sequences, figure 1.15 illustrates the steps that occur in spin-echo imaging:

1. A 90° pulse is applied in conjunction with the slice select gradient
2. Phase differences are created along the phase encoding axis by the phase encoding gradient
3. After an initial time delay (TE/2) the refocusing 180° pulse is applied
4. The spin echo is then formed at the TE
5. During echo formation the frequency encoding gradient is applied, the frequency is dependent on the position along the gradient
6. An analogue to digital convertor samples the signal during the readout gradient

7. The process is repeated with a different phase encoding gradient amplitude after a time TR (Time to Repetition)
8. Image data is produced the size of which is dependent on the number of phase encoding steps and the number of points that were sampled per spin-echo

Long T2 weighted spin echo images have the major trade off of having long TR which results in long acquisition times. Spin echos are excellent in clinical environments as they produce T2 weighted images of good quality, for T1 weighted images a faster type of sequence is normally desired.

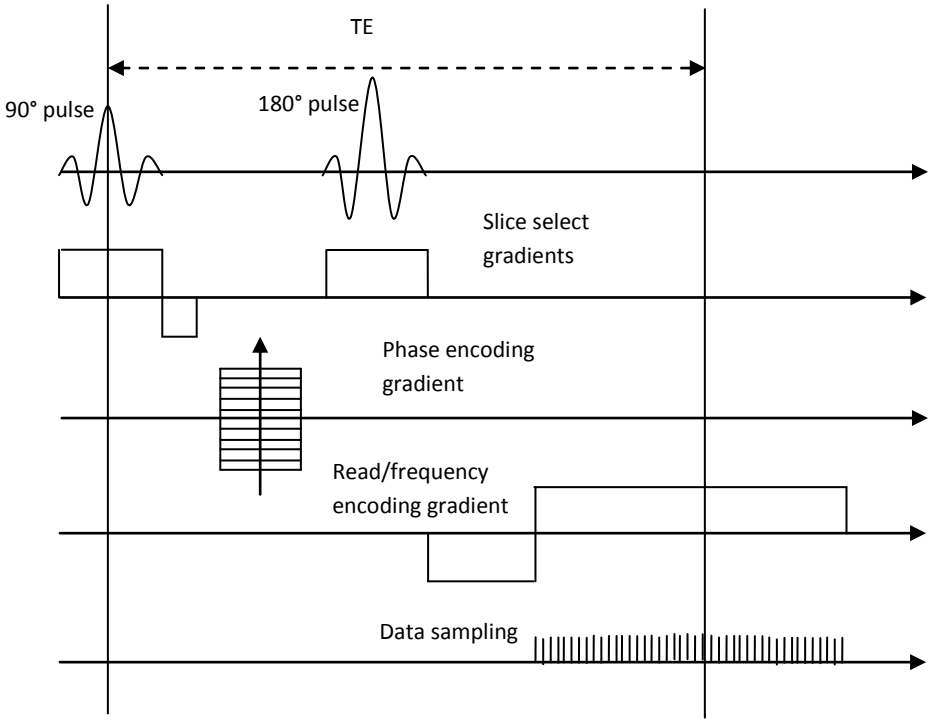

Figure 1.15: Spin echo imaging sequence showing applied rf pulse, slice select gradients, phase encoding gradient, frequency encoding gradient and data sampling

1.3.2 Gradient echo Imaging Sequence

The major differences between a gradient echo sequence and a spin echo sequence are that with a gradient echo;

- The flip angle is normally below 90°.
- There is no 180° RF re-phasing pulse

The partial flip angle (lower than 90°) causes the amount of magnetisation in the transverse plane to be decreased. Advantages of gradient echo and low flip angle excitations include;

- Faster acquisitions
- Different contrast between tissues
- A short TR normally leads to a weaker MR signal due to T1 saturation

The fraction of magnetisation tipped into the transverse plane and the quantity of magnetisation left on the longitudinal axis is determined by the flip angle. A lower tipped magnetisation will occur if there is a lower flip angle excitation.

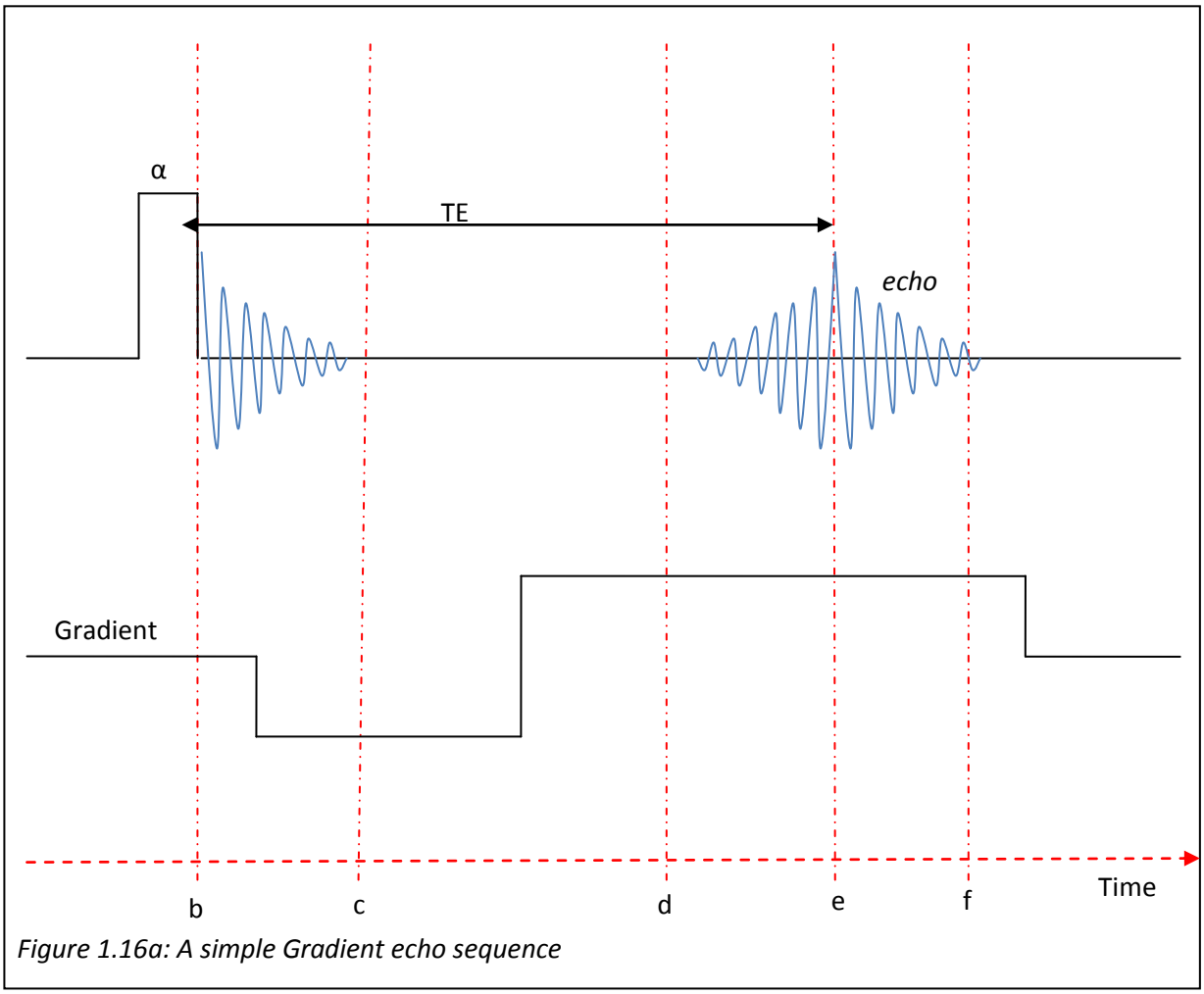

Figure 1.16a: A simple Gradient echo sequence

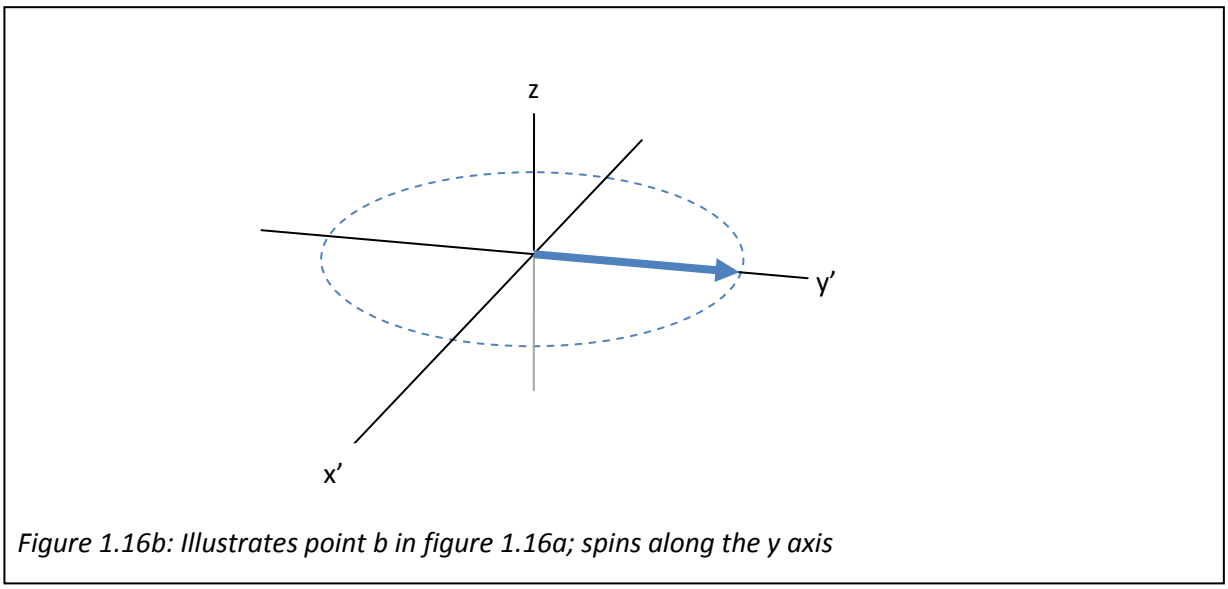

Figure 1.16b: Illustrates point b in figure 1.16a; spins along the y axis

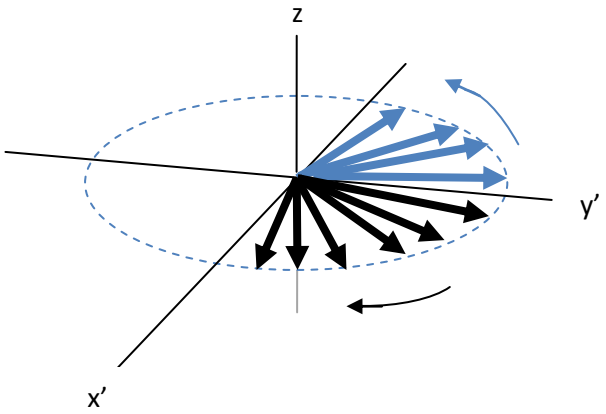

Figure 1.16c: Illustrates point c in figure 1.16a; Spins de-phased by the negative lobes

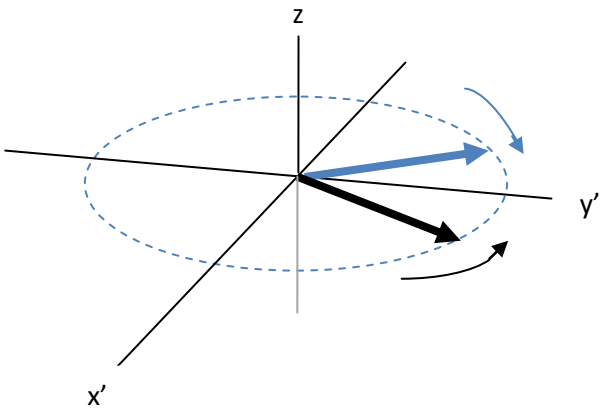

Figure 1.16d: Illustrates point d in figure 1.16a; Gradient switched to positive

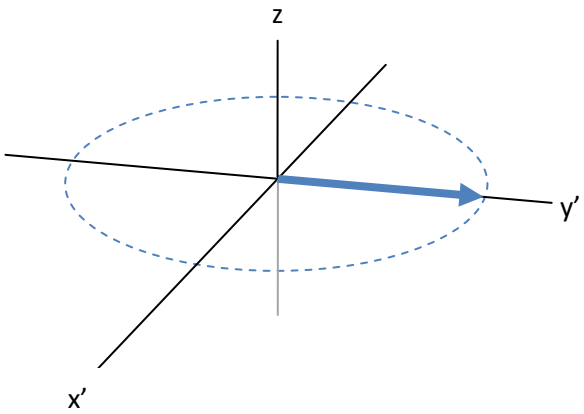

Figure 1.16e: Illustrates point e in figure 1.16a; the spins begin to rephase, forming an echo

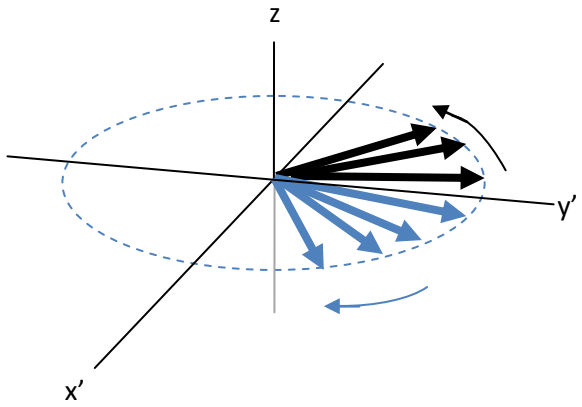

Figure 1.16f: Illustrates point f in figure 1.16a; if the gradient is left on de-phasing reoccurs

Figure 1.16a-1.16f illustrates a gradient echo sequence;

- A negative gradient lobe is applied immediately after the excitation pulse.
- A rapid de-phasing of the transverse magnetisation is caused
- A positive gradient is applied after the negative lobe, which reverses the magnetic field gradient
- Spins previously precessing at a low frequency due to their position in the gradient will now precess at a higher frequency and vice versa.
- Previously de-phasing spins begin to re-phase, after a set time period when gradient areas are equal they all come back into phase along the +y' axis, thus forming a gradient echo
- T2 and T2* effects are not reversed with a gradient echo

1.3.3 Paramagnetic Contrast Agents

Contrast agents allow the production of an extra set of images with different contrast with only a short increase in the total scan time of the patient, this increases specificity and clarifies tissue discrimination. The most commonly used contrast agents are based on gadolinium (Gd). Gd contains seven unpaired electrons. Gd is a highly toxic substance therefore it is encapsulated within another chemical structure such as diethylenetriaminepentaacetic acid (DTPA). Once injected into the body Gd is rapidly distributed throughout the vascular supply, it then gradually excretes through a patients kidneys taking around 24 hours to do so. Having the

presence of Gd during MRI scans has the effect of shortening T1 in tissues where it accumulates, therefore on post contrast T1 –weighted images these tissues will experience enhanced signals. As a result highly vascular tumours will become brighter as the area of disruption will cause the Gd to leak into the lesion thus enhancing that area. Figure 1.17 shows post contrast and pre contrast images of a breast MRI scan.

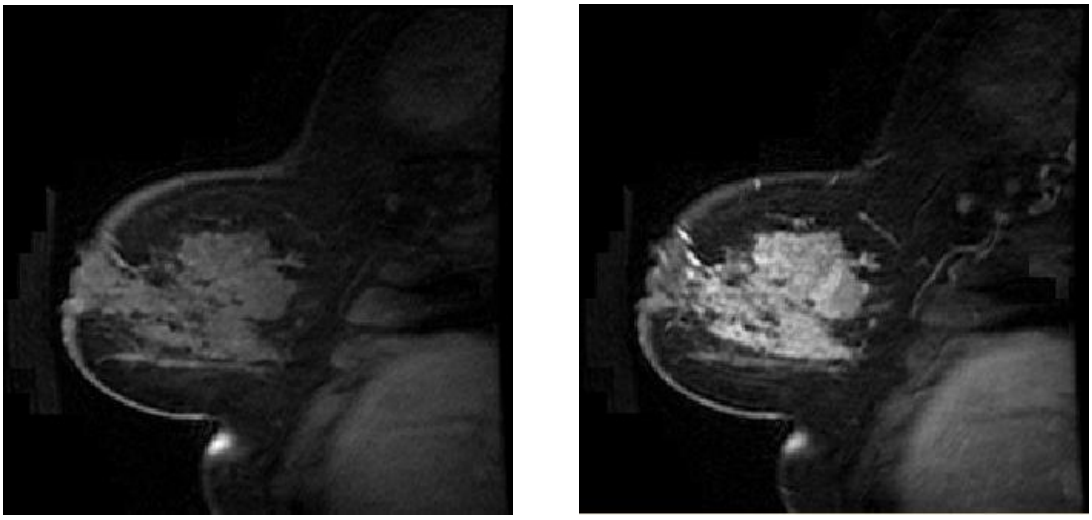

Figure 1.17: pre-contrast (left) and post contrast (right) at 2min post Gd injected MR images of breast, image on right shows enhanced lesion area. Images taken from data acquired by The University of Hull of patients undergoing neoadjuvent chemotherapy.

1.4 Instrumentation

For the purpose of this study the dataset consisting of patients undergoing neoadjuvant chemotherapy was acquired using a superconducting GE magnet running at 3 tesla (3.0T HDx, GE Healthcare, Milwaukee, WI) in combination with an 8-channel dedicated breast coil. Superconducting magnets have generally low running costs and excellent homogeneity and are available at field strengths of up to 8T. Superconducting magnets are normally wound from niobium-titanium filaments having a transition temperature of 7.7K, they contain a chamber of liquid Helium (He) known as the cryostat and are further surrounded by vacuum chambers.

There are three types of orthogonal linear magnetic field gradient coils to produce gradients in the x, y and z directions. These are mounted on a cylindrical former just inside the bore of the magnet. Various radiofrequency coils exist for different parts of the body and often the transmitting and receiving is done via the same coil, for this study a standard breast coil has been used to acquire the breast data (receive only).

2 Literature Review

This chapter will look at previously conducted studies that lead to the study in this PhD thesis of morphology (texture) and shape. The chapter begins by outlining the diagnostic techniques available which are used both in screening and in clinical studies for prediction and monitoring of tumour response in breast including the Bi-RADS lexicon. This is followed by examining the need for automatic analysis of DCE-MRI data and post-contrast images including pharmacokinetic modelling. Existing work on morphology and discussion of the different methods of texture and shape analysis concludes the chapter.

2.1 Diagnostic techniques

This section will examine the different techniques currently in use for diagnosing or detecting breast cancer. Many of these are commonly used for screening purposes as well as monitoring of known lesions.

2.1.1 Clinical Breast Examination

Sensitivity measures the proportion of actual positives which are correctly identified as such, specificity measures the proportion of negatives which are correctly identified. A perfect predictor would be described as 100% sensitivity and 100% specificity. Examinations by clinicians usually involve a physical examination; these can vary in accuracy based on time spent per session and level of expertise of the clinician [6]. Community practice reported results showed sensitivity ranging from 28-36%. A study highlighted 42.5% of physicians who performed a screening breast examination on manufactured breast models used no discernible systematic search pattern at all. Sensitivity improved when using a systematic approach, and spending more time, however the number of false positive examinations may increase with training [6].

2.1.2 Breast Self-examination

Breast self examination appeals to women as it allows them to become comfortable with their own bodies and is non-invasive. However the extent of its current practice is believed to be low and it seems to create an increase in false positive findings and therefore a diminished specificity [6].

2.1.3 Mammography

Mammography uses low dose amplitude x-rays to look for tumours in breasts with the aim of detecting cancer early which increases the subsequent chances of a cure. Mammography is commonly used as a screening and diagnostic tool for early detection of breast cancer, this is usually done through the detection of characteristic masses (for example a cancerous area, see fig 2.1) and/or micro calcifications (see figures 2.2 and 2.3) which are tiny calcium deposits that show up as fine white specs on a mammogram. Various randomised trials have studied mammography's effectiveness. A Swedish study [7] concluded that breast screening reduces breast cancer mortality and this persists after long term follow up. The effect was found to be age dependent: highest effect in women aged 55-69 years at randomisation and lowest in women aged 50-54 years at randomisation. A UK study [8] concluded that mammographic screening does reduce mortality from breast cancer. A review paper on screening for breast cancer [6] outlines that there are flaws with the randomised studies but further in depth reviews of the criticisms of the trials have concluded that especially in women aged 50-69 mammography is still efficient in reducing breast cancer mortality. Women in their 40s generally have denser breast tissue which can lower the sensitivity of mammography [6].

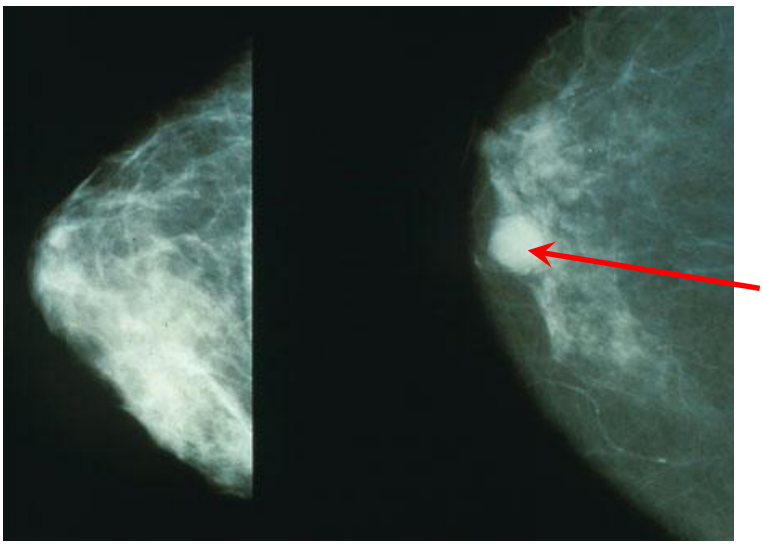

Figure 2.1 [9]: Mammography image showing normal breast tissue (left) versus the whitish area in the tissue on the right (arrow), which is cancerous.

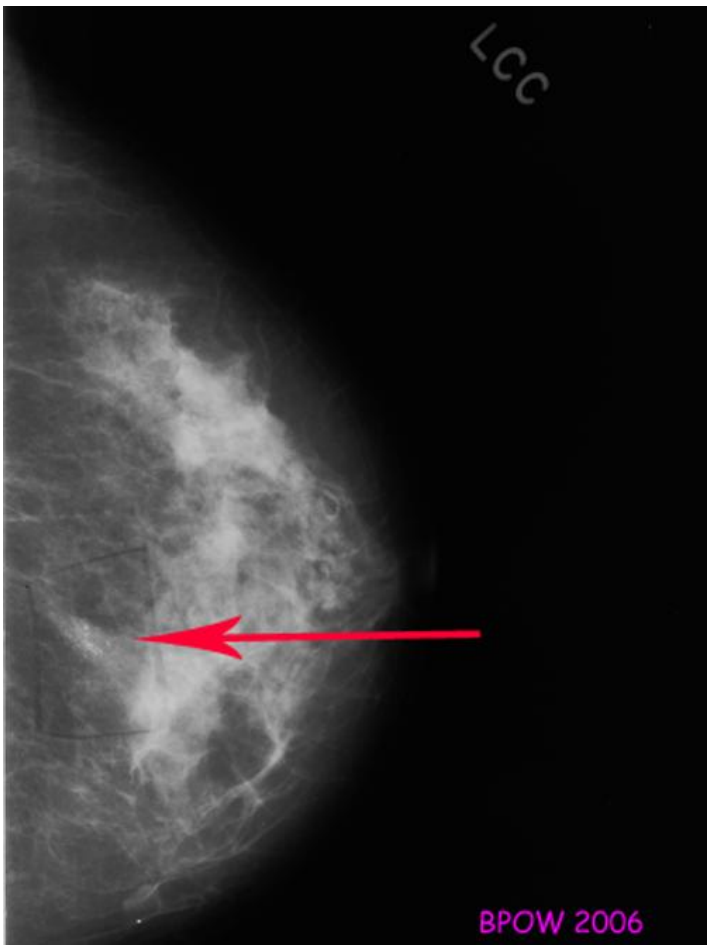

Figure 2.2 [10]: mammogram showing cluster of micro calcifications (red arrow)

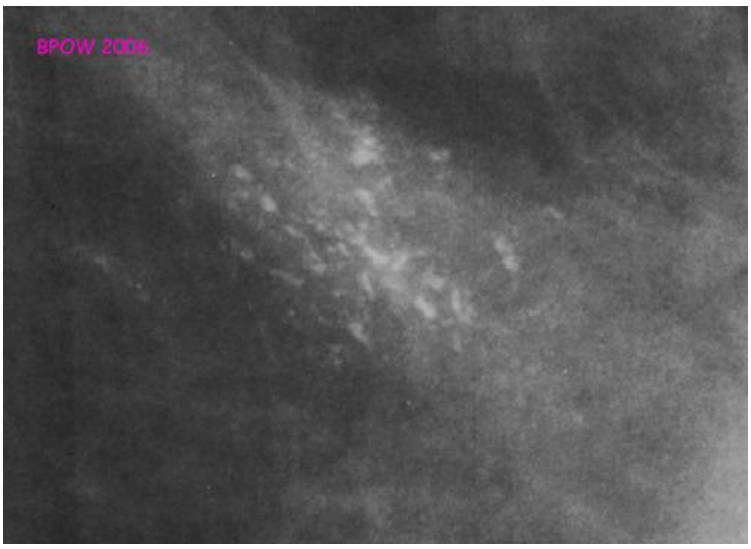

Figure 2.3 [10]: a closer look at the micro calcifications from figure 2.2

2.1.4 Full-Field Digital Mammography and Computer Aided Detection programs

As the name suggests the major difference between screen-film mammography and digital mammography is that with the latter the image is captured digitally as opposed to on a film. Digital images have the additional benefits of being interpreted directly from a computer monitor in addition to being printed on film for viewing as with conventional mammographs. The advantages are immediately obvious as digital images can be stored electronically and various adjustments made like altering the contrast and brightness of the image as well as magnifying areas of interest all of which aid the radiologist's decision making process without having to perform extra x-rays on the patient. In addition computer aided detection programs can potentially aid in the assessment of diagnostic accuracy to give radiologists a computerised second opinion (figure 2.4). A study by Freer et al [11] of 12860 women showed that when a computer program was used that was able to mark calcifications, masses, or other potential lesions on the mammogram this increased the number of cancers detected from 41 to 49. However, the overall recall screening rate increased from 6.5% to 7.7%. A further much larger clinical study by Gur et al [12] included 59139 mammograms interpreted with computer-aided detection and 56432 without and showed that cancer detection rates and recall rates did not

significantly differ. Depending on the expertise level of the radiologist computer-aided detection may be a helpful aid.

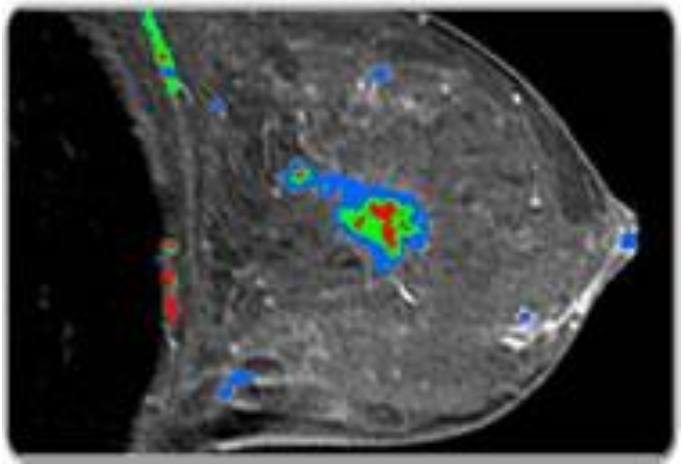

Figure 2.4 [13]: digital mammogram with computer aided detection outlining suspicious areas

2.1.5 Ultrasound

Ultrasound is beneficial in a targeted diagnostic examination, for example when the focus is on a specific area of concern. Ultrasound may help in distinguishing between cysts and solid masses as well as between benign and malignant masses [14]. Figures 2.5 and 2.6 show an ultrasound scan after a 44 year old woman found a lump on self-examination. Ultrasound has a higher rate of false positive results than mammography, and in a study reviewing the accuracy of technology in screening for breast cancer the false positive rate based on a solid lesion for ultrasound was 2.4% to 12.9% compared with 0.7% to 6% for mammography [15].

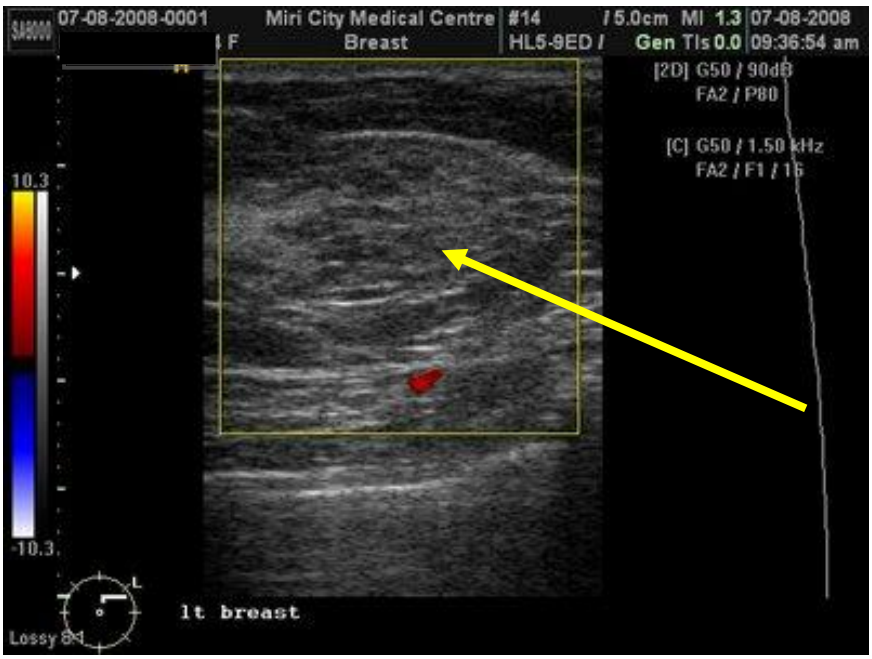

Figure 2.5 [13]: Ultrasound showed a 3cm solid mass in the upper outer quadrant of the left breast (yellow arrow). As she is over 40 years of age and the mass is more than 2cm, a biopsy is recommended.

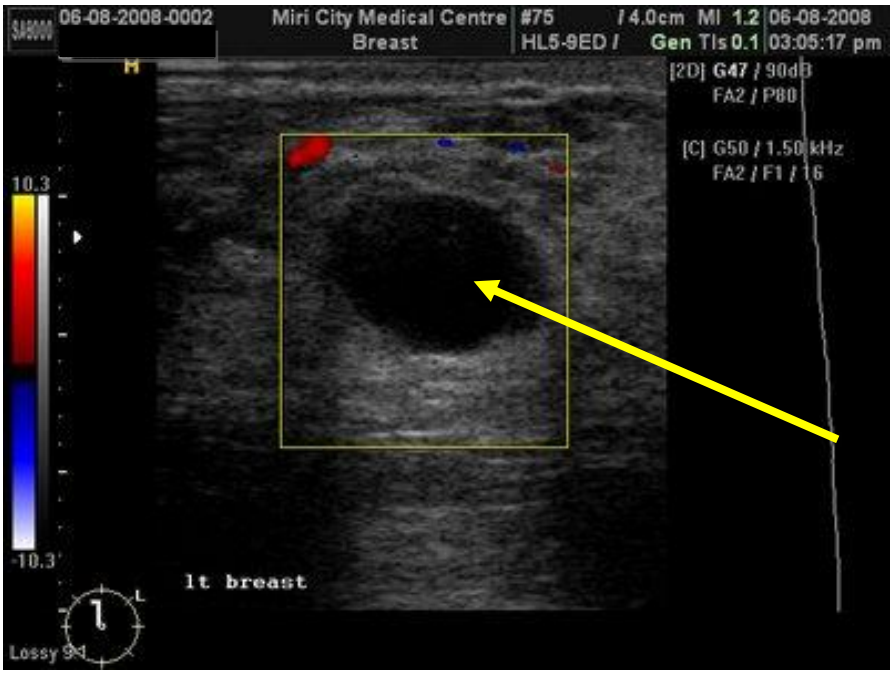

Figure 2.6 [13]: In contrast, this 34 year old lady with similar presentation was found to have a benign breast cyst in the upper quadrant of the left breast (yellow arrow). After some assurance, no further investigation was necessary.

2.1.6 Magnetic Resonance Imaging (MRI)

MRI as discussed in detail in chapter one produces images from radio waves using a strong magnetic field combined with computer processing. MRI can be especially helpful in cases where mammography is not optimal. Sensitivity in MRI is normally higher than that of mammography, as per a study by Kuhl et al [16]. In 105 asymptomatic women with validation of the 1st-year screening results, the sensitivities of mammography, US, and MR imaging were 33%, 33% (mammography and US combined, 44%), and 100% respectively. Specificity is normally lower in MRI than in mammography but in this same study this was not the case as specificities of mammography, US, and MR imaging of 93%, 80%, and 95% were reported respectively. A study by M Kriege et al [17] agrees with the norm wherein the specificity of clinical breast examination, mammography, and MRI for detecting invasive breast cancer was 98.1%, 95.0%, and 89.8%, respectively.

According to a later study in 2007 which looked at the effectiveness of MRI as an addition to mammography and ultrasound in screening young women at high risk of breast cancer [18] there is strong evidence that MRI in addition to conventional screening tests increases early detection of breast cancer in young high risk women, but does pose a higher risk of unnecessary false positive findings [18].

2.2 MRI and breast tumours

The previous few sections have aimed to give a comparative overview of the different techniques which are mainly used for screening of breast tumours. This section will look at more detail regarding MRI and its use for diagnostic purposes in breast tumours, including the use of contrast agents and discussion of MRI as an extremely sensitive technique that seems to have limited specificity and high sensitivity [19].

2.2.1 Pathophysiologic basis

MR contrast agents are more often than not used as an intravenous injection in order to enhance lesions which would otherwise be difficult if not impossible to identify. In order to generate contrast a gadolinium based agent is used. The different lesion and diagnosis detection techniques shall be discussed here in further detail.

Angiogenesis is the physiological process where new blood vessels are formed from pre-existing vessels, malignant lesions release angiogenic factors, the effect of this angiogenic activity is that firstly there is an increased vessel density (vascularity), this leads to a focally increased inflow of contrast material as well as an increase in vessel permeability which ultimately results in accelerated leakage into the surrounding tissue known as extravasation of contrast material at the site of the tumour[19]. Invasive breast cancers are detectable due to their strong enhancement i.e. due to the increase in signal intensity on T1 weighted images in dynamic breast MR images, the signal intensity peaks early after contrast injection. The diversion of blood from an artery directly to a vein known as an arteriovenous shunt along with increase in vascular permeability seem to contribute to a wash out in breast cancers i.e. the signal intensity decreases in the early or intermediate post-contrast period. Tumour vascularity seems to correlate with tumour aggressiveness and the potential for it to be metastatic / malignant. It's clear then that the presence of contrast agents such as gadolinium in the veins helps create a high contrast image in MRI, but lesion enhancement is far from being a simple process as it is determined by a variety of different factors, including but not limited to; vessel permeability, vessel density, contrast material diffusion rates, composition of the interstitial (interstitial fluid is a solution that surrounds and bathes the cells) tumour matrix and baseline and post contrast tissue relaxation times.

An important point to note is that contrast enhancement merely enhances some types of malignant lesions in breast, a lack of or only shallow contrast enhancement is also found in some malignant changes. Fibroids (benign tumours) enhance in a similar way to malignant

breast tumours. Simply having contrast enhancement present does not determine the presence or absence of malignancy in breast MRI. Before a final diagnosis is established various additional diagnostic criteria and all clinical, mammographic and sonographic information that is available has to be considered. Detection and differentiation of breast lesions and the criteria used will be the topic of discussion in the following sections.

2.2.2 Diagnosing techniques

The decision to take a biopsy is needed when an enhancing area is detected on post contrast subtracted images or a suspicious mass is seen on pre contrast images in order to establish whether it is benign or malignant, as none of the diagnostic criteria discussed provide definitive diagnosis of an area being benign or malignant, therefore a core biopsy is always the most cost effective and safest way to clarify suspicion lesions. In addition each case will have its own individual factors for deciding if a biopsy is recommended or not, these include but are not limited to patient history, present clinical or radiological findings, and personal concerns of the patient.

2.2.2.1 Morphologic features of lesion

Looking at the morphological features (structure, and shape) of a breast image is one way of diagnosing breast cancer. Lesion configuration is determined and classified as either mass, non-mass-related focal enhancement, segmental, linear/linear-branching or regional/patchy enhancement. A mass like lesion is treated as suspicious and can be seen on a pre-contrast image. If present its shape and borders should be evaluated, if an irregular (fig 2.7) or spiculated (fig 2.8) shape exists this strongly suggests that it is a malignant lesion and roundish or ovoid shapes suggest a benign mass (fig 2.9). Non-mass-related focal enhancement are lesions that only shows up after contrast injection, unlike a mass no space occupying properties can be observed in pre-contrast images. Some small breast cancers as well as many unidentified bright breast objects (UBOs) are categorised as non-mass. As with mass lesions if small cancers are present their shape and borders should be evaluated, if an irregular (fig 2.7)

or spiculated (fig 2.8) shape exists this strongly suggests that it is a malignant lesion and roundish or ovoid shapes suggest a benign mass. Spatial resolution plays vital importance in seeing well circumscribed focal mass or tiny spiculae. For the most subtle variations in morphological details of enhancing lesions a maximum spatial resolution is required. Adjacent parenchyma (bulk or functional part of tissue) will enhance progressively, in the very early pre-contrast period the parenchyma/lesion-contrast is best, and hence for morphological analysis a good temporal resolution is required. Finally the lesion should be looked at in terms of its internal architecture and determine whether it is homogenous or not and if it shows low-signal-intensity internal septations (fig 2.10), if either is true this suggests the lesion is benign, on the other hand if it is heterogeneous with areas showing strong and others with only shallow enhancement or if the enhancement is confined to the lesion periphery then the lesion is probably malignant. This was found to be true in a 93 patient study which concluded that to help distinguish between benign and malignant disease the architectural features revealed by high-spatial resolution MR imaging of the breast need to be analysed [20]. Segmental lesions are confined to the area of a duct or the ductal system and are usually triangular in shape with the tip pointing towards the nipple (fig 2.11).

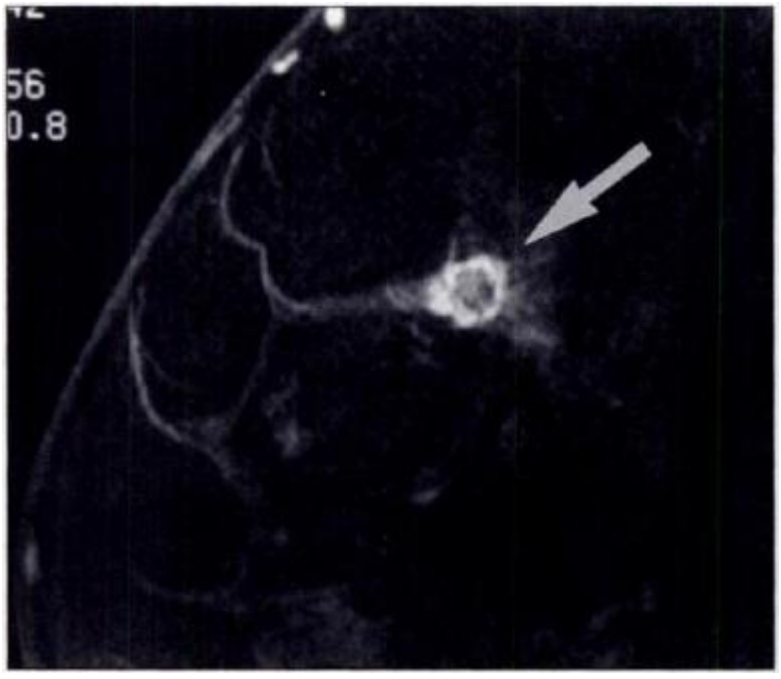

Figure 2.7 [20]: image of 67 year old woman with invasive ductal carcinoma, the gadolinium

enhanced image shows the lesion represented by the arrow with irregular borders and rim enhancement.

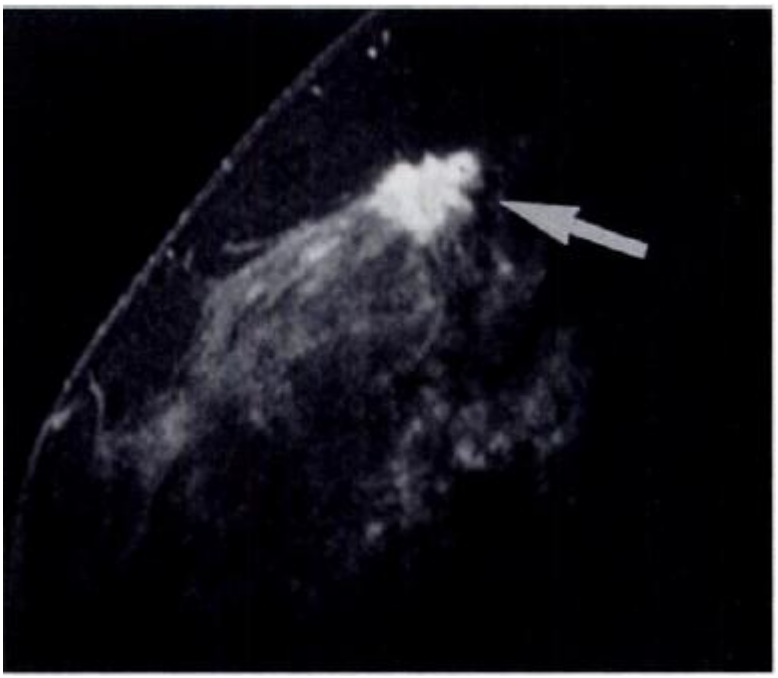

Figure 2.8 [20]: image of 51 year old woman with invasive ductal and intraductal carcinoma, the gadolinium enhanced image shows the lesion represented by the arrow with spiculated borders.

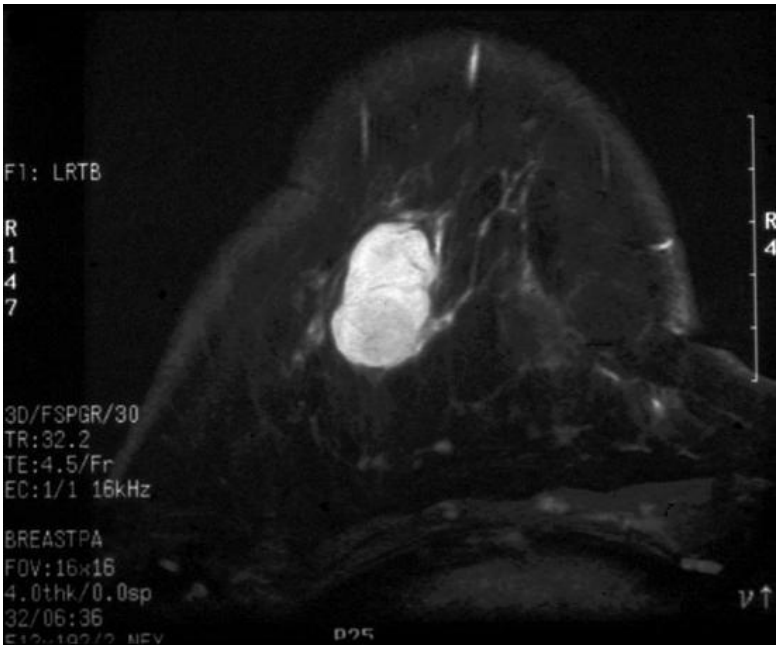

Figure 2.9 [21]: scan showing typical findings in a fibroadenoma, with ovoid shape, smooth margins and homogenous internal architecture

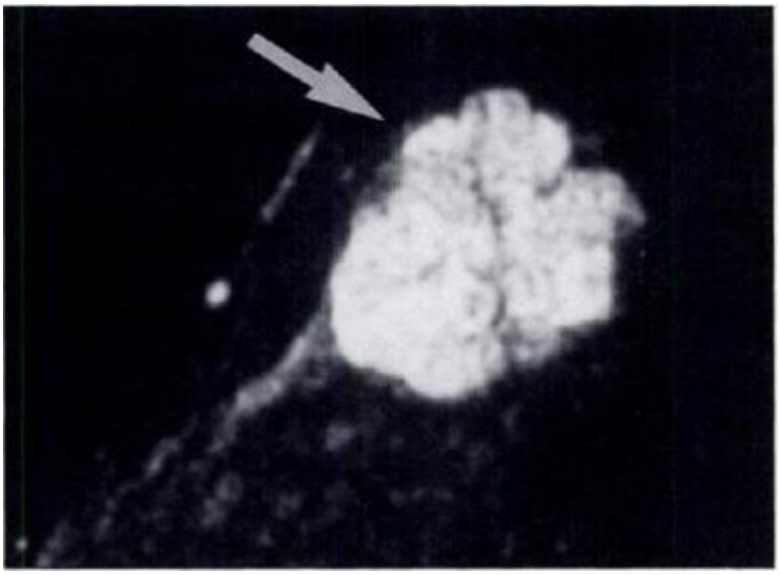

Figure 2.10 [20]: image of 37 year old woman with fibroadenoma, lesion represented by arrow with lobulated borders and non enhancing internal septations

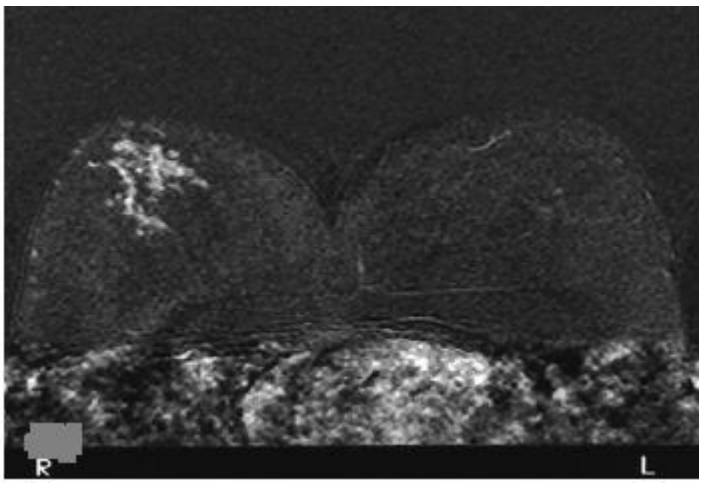

Figure 2.11 [19]: intermediate post contrast image, segmental enhancement as hallmark of ductal in situ cancer (DCIS), with the almost triangular shape, tip pointing towards the nipple and the heterogeneous internal architecture.

2.2.2.2 Enhancement kinetics

The evaluation of lesion enhancement kinetics should be done on subtracted and non-subtracted images over all the dynamic series and time/signal intensity curves plotted on lesions that look to be benign (normally distinguished by continuous enhancement by a type 1 curve) or malignant (normally associated with a type 3 curve) in terms of their morphology. A good temporal resolution is essential in order to evaluate all kinetic criteria, although what the optimal temporal resolution is has been a matter for discussion [19]. Initially experiences with ultra high temporal resolution suggested an improved specificity for differential diagnosis [22]. Eighty-seven lesions were evaluated and gadolinium-enhanced TurboFLASH imaging had a sensitivity of 95%, a specificity of 86%, and an overall accuracy of 93% in differentiating benign from malignant lesions. The study went on to conclude that gadolinium-enhanced TurboFLASH imaging is a valuable method in the examination of breast lesions suspected of being malignant [22]. Most evidence suggests that temporal resolution should be of approximately 1-2 min per dynamic scan and it seems studies show that it is not useful to sacrifice spatial resolution in favour of improving temporal resolution far beyond the 1 min margin [19] for the purpose of diagnosis.

2.3 Breast Imaging Reporting and Data System (BI-RADS Lexicon)

Historically the terminology used for reporting purposes often provided inconsistent recommendations by radiologists, this often led to confusion for clinicians on how to conduct further evaluation. In order to provide a certain level of consistency in interpretation it was necessary to form some sort of standards, the American College of Radiology (ACR) did just this in the form of The Breast Imaging Reporting and Data System (BI-RADS) [23]. The BI-RADS lexicon as it is known today is a tool which includes within it a section containing illustrations of each mammographic feature, a section on mammographic practice and some sample reports.

BI-RADS is a quality assurance tool designed to standardise mammography reporting. It contains a lexicon for standardised terminology (descriptors) originally for mammography, breast Ultrasonography (US) and latterly in a revised version for MRI. The BI-RADS lexicon tool aims to standardise terminology, assessment of findings and recommendations for action based on findings [24]. This assessment coupled with management recommendations has implications for clinical care, teaching, and evaluation of screening by radiologists. This section aims to provide an illustration of the BI-RADS lexicon as well as discussion of its advantages and disadvantages.

2.3.1 BI-RADS Mammography

The BI-RADS lexicon for mammography of the ACR describes four classes of breast parenchymal density and their effect on diagnostic accuracy [24]:

1. Mostly fatty (fig 2.12)– very high diagnostic accuracy
2. Fibroglandular (fig 2.12) – high diagnostic accuracy
3. Heterogeneously dense (fig 2.12) – limited diagnostic accuracy
4. Dense (fig 2.12) – limited diagnostic accuracy

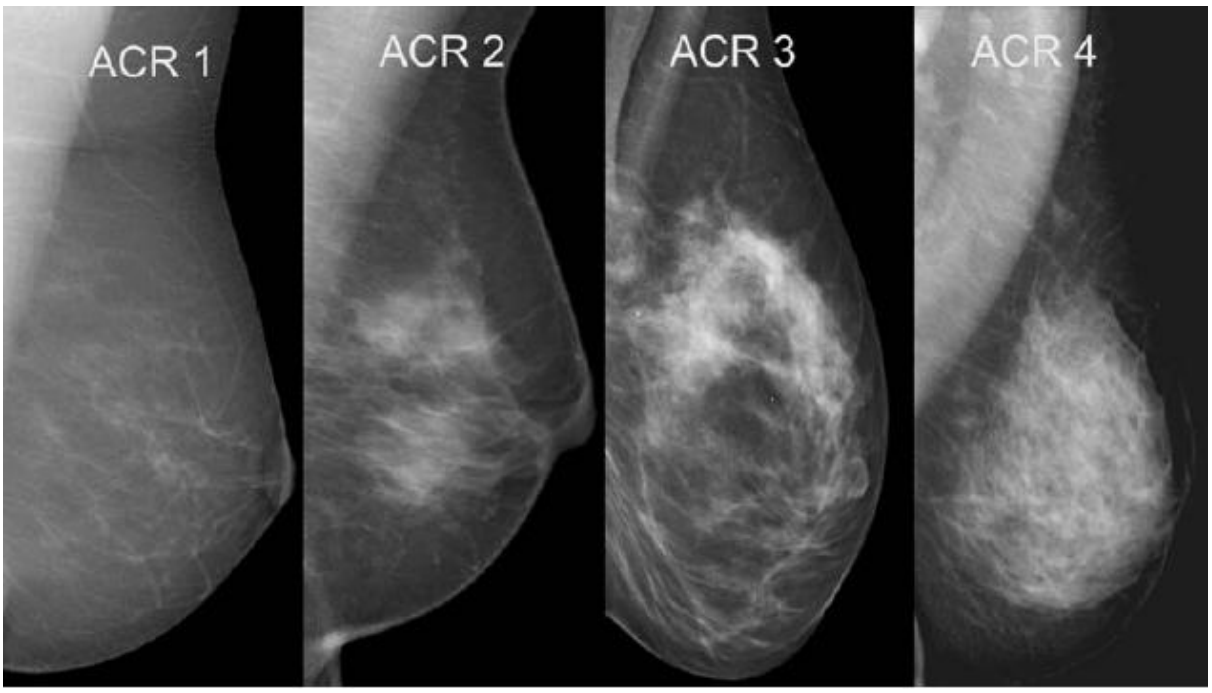

Figure 2.12 [24]: different types of breast tissue density according to the ACR where ACR 1 illustrates fatty breast tissue, ACR 2 fibroglandular breast tissue, ACR 3 heterogeneously dense breast tissue and ACR 4 extremely by dense breast tissue.

Earlier in the chapter morphological features of a lesion were discussed, there are similar categories defined for the types of lesion within the BI-RADS lexicon:

- Masses – if a lesion is seen in 2 different projections it is a mass otherwise if it is only seen in a single projection it is a density, there are three classifications of masses:
    - Shape of mass can be (fig 2.13, top):
        - Round
        - Oval
        - Lobular
        - Irregular
    - Margin of mass can be described in five different ways (fig 2.13, middle):
        - Well or sharply circumscribed
        - Undulation with short cycles (microlobulated)

        - Hidden by superimposing adjacent tissue (obscured)
        - Ill-defined (indistinct)
        - Spiculated
    - Density of mass in relation to the surrounding parenchyma or fat equivalent can be (fig 2.13, bottom):
        - Higher
        - Equivalent (isodense)
        - Lower
- Calcifications (fig 2.14), are classified as follows:
    - Benign calcifications include skin, vascular, coarse or popcorn-like, large rod-like, round, lucent centred, “eggshell” or “rim”, milk or calcium, salure, dystrophic and punctuate calcifications
    - Intermediate concern calcifications include amorphous or indistinct calcifications
    - Malignant (high probability of malignancy) include pleomorphic or heterogeneous (granular) calcifications and fine linear, fine linear branching (casting) calcifications
    - Distribution of microcalcifications (fig 2.15); include diffuse or scattered, regional, linear, segmental and group or clustered.
    - Other features include architectural distortion where the architecture is distorted with no definite mass visible which can be associated with malignancy.

In addition there are also various associated findings which can be used with masses or calcifications or when no other abnormality can be seen, these include nipple retraction, skin lesion and skin retraction.

Location of the lesion is classified by the following parameters:

- Side (left, right or both)
- Location (according to clock face and subareolar, central or axillary)
- Depth (anterior, middle or posterior)

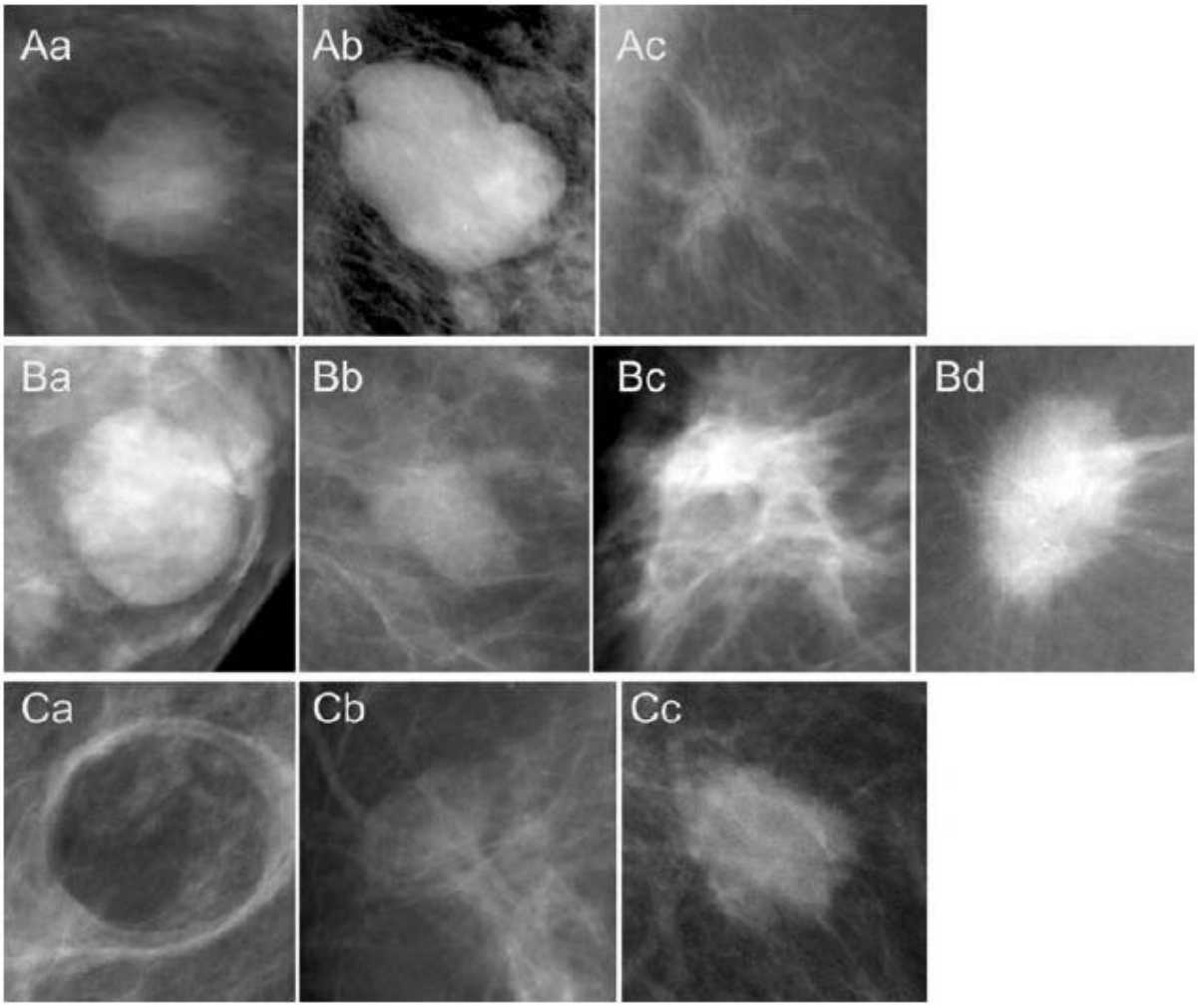

Figure 2.13 [24]: Set of images categorised according to the Bi-Rads lexicon, top row of images show shape: round/oval (Aa), lobular (Ab), irregular (Ac). Middle row of images show margin: well-defined (Ba), ill-defined (Bb), obscured (Bc) and spiculated (Bd). Bottom row of images showing density: fat containing (Ca), isodense (Cb) and high density (Cc)

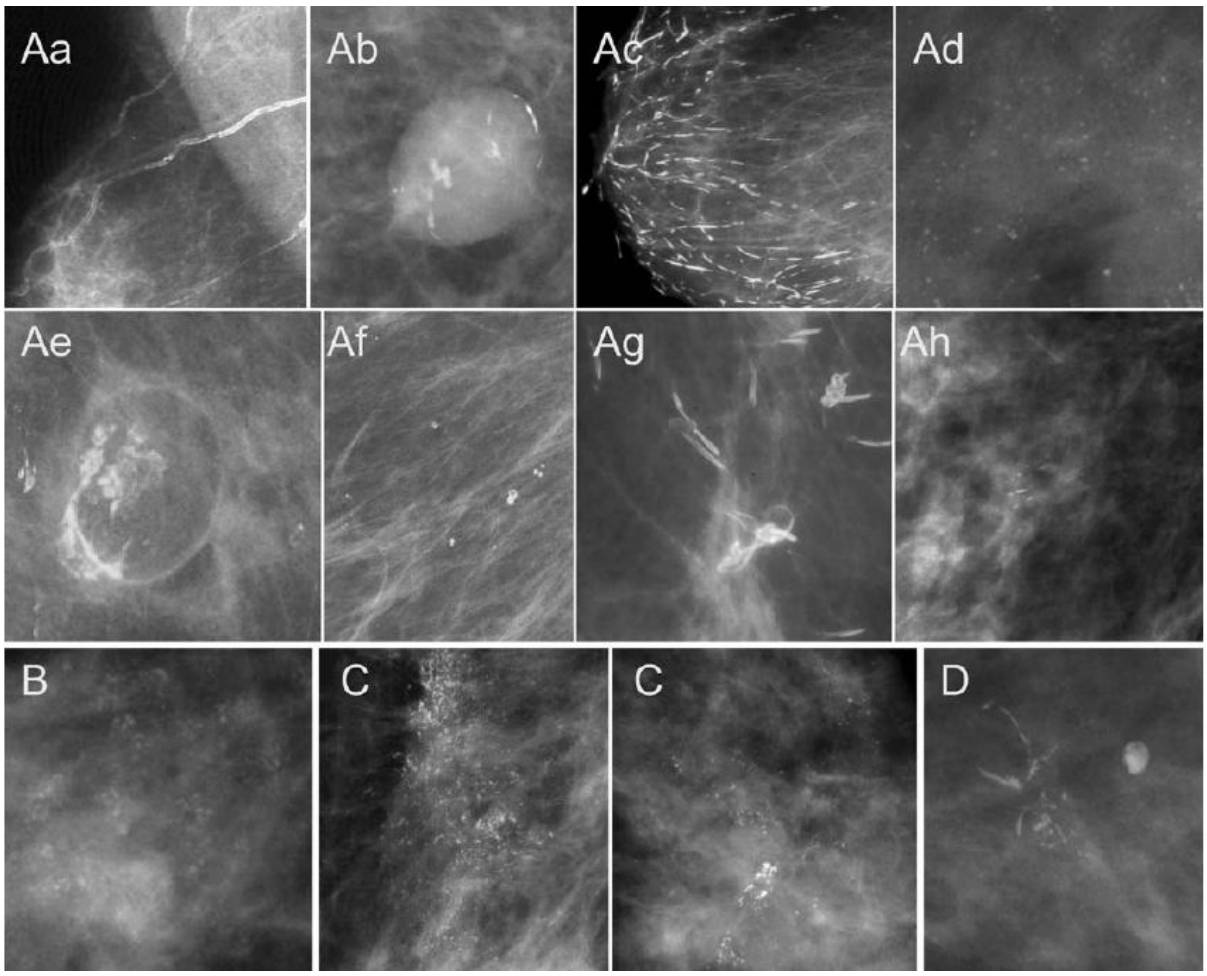

figure 2.14 [24]: images of types of calcifications according to the BI-RADS lexicon. Top and middle rows show benign findings: vascular (Aa), coarse or popcorn-like (Ab), large rod-like (Ac), round (Ad), "eggshell" (Ae), lucent centred (Af), suture (Ag), milk or calcium calcifications (Ah). Bottom row of images show intermediate-concern calcifications: amorphous calcifications (B) and higher probability of malignancy: pleomorphic (C) and fine linear branching calcifications (D)

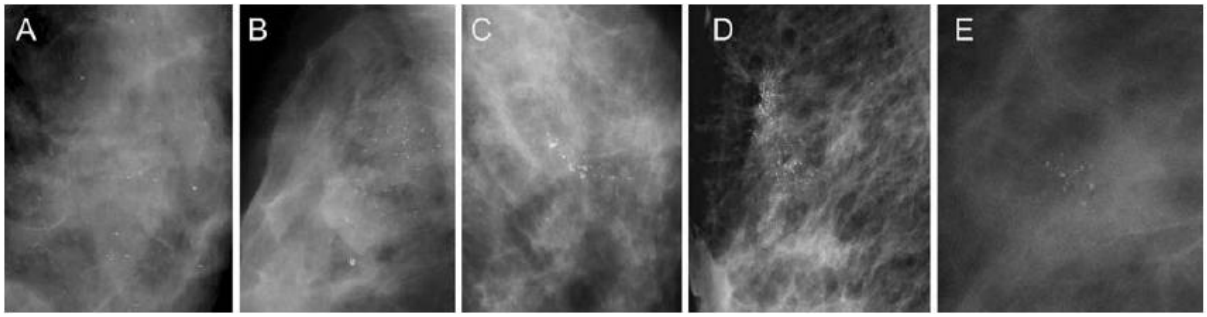

figure 2.15 [24]: images showing the distribution of microcalcifications according to the BI-RADS lexicon: diffuse(A), regional (B), linear (C), segmental (D), and clusters of microcalcifications (E)

2.3.2 Report

Once a clear description of the findings is made a report is compiled indicating the categorisation of the lesion(s) according to the BI-RADS classification with implications on the next course of action (table 2.1).

Category	Finding	Probability of malignancy (%)	Recommendation
0	Needs additional imaging evaluation, incomplete	–	Additional imaging by spot compression, magnification, special mammographic views, ultrasound
1	Negative	0	Normal interval follow-up
2	Benign	0	Normal interval follow-up
3	Probably benign	<2	Short-interval follow-up
4	Suspicious abnormality	>2–3	Biopsy should be considered
5	Highly suggestive of malignancy	≥95	Appropriate action should be taken
6	Histologically proven malignancy	100	Appropriate therapy

Table 2.1 [24]: ACR BI-RADS categories for mammographic lesions according to their probability of being malignant and recommendations.

2.3.2 BI-RADS Ultrasonography (US)

A similar lexicon exists with the six categories for Ultrasonography with additional sub-categories A-C for category 4, some slight differences in description wording exist.[25, 26].

2.3.3 BI-RADS MRI

In the same way the BI-RADS lexicon was formed for mammography, the increasing use of breast MRI in cancer detection, diagnosis and management led to a need for a revised lexicon. This was fulfilled by the American college of Radiology through the development of the BI-RADS MRI lexicon. The lexicon is very similar to the mammography BI-RADS lexicon with a few minor additions with MRI imaging in mind. In addition to the categorisation of masses by

shape, margin and other characteristics similar to mammography BI-RADS there is an additional category Focus and Foci, these are when enhancements measure less than 5mm that cannot be otherwise specified (fig 2.16). Focus or foci are frequently stable on follow-up images and are known to result from hormonal changes [27]. As with the Mammography BI-RADS the MRI BI-RADS has a category for associated findings (fig 2.17), these findings include:

- nipple retraction
- inversion
- skin retraction
- skin thickening
- skin invasion
- pectoralis muscle or chest wall invasion
- high signal intensity in ducts on unenhanced images
- abnormal signal void
- hematoma
- edema
- lymphadenopathy
- cysts

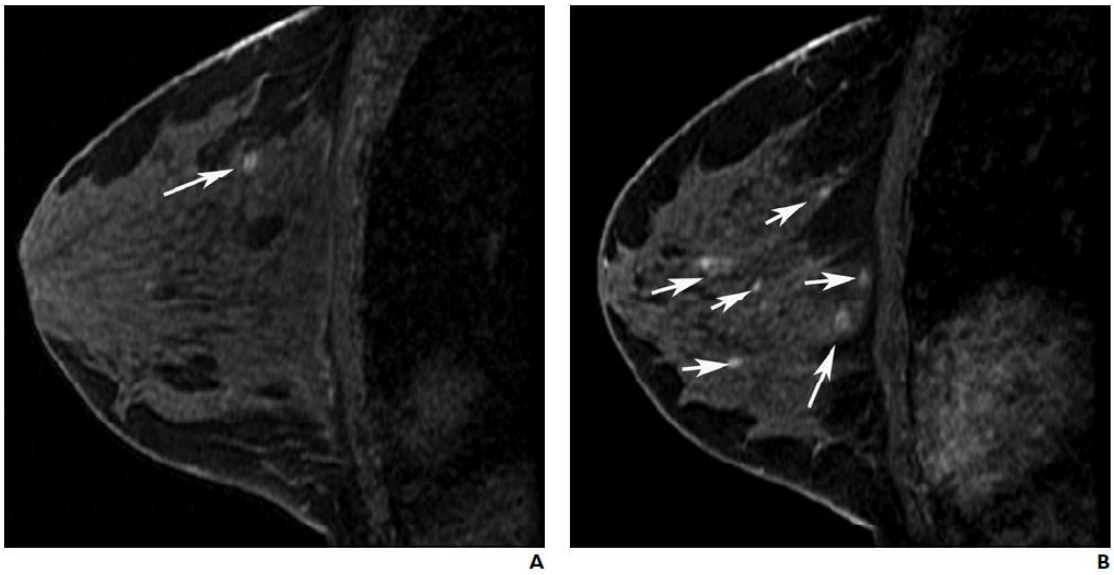

Figure 2.16 [27]: Focus and foci of enhancement. MRI images from 49 year old woman with palpable abnormality in right breast, radiologic findings suggested fibrocystic disease. Image A (left) shows dynamic contrast-enhanced image of left breast with subcentimeter focus (arrow) of delayed enhancement in upper aspect of right breast. Image B (right) shows multiple foci of enhancement (arrows) throughout right breast. All foci were stable for at least 1.5 years and considered benign.

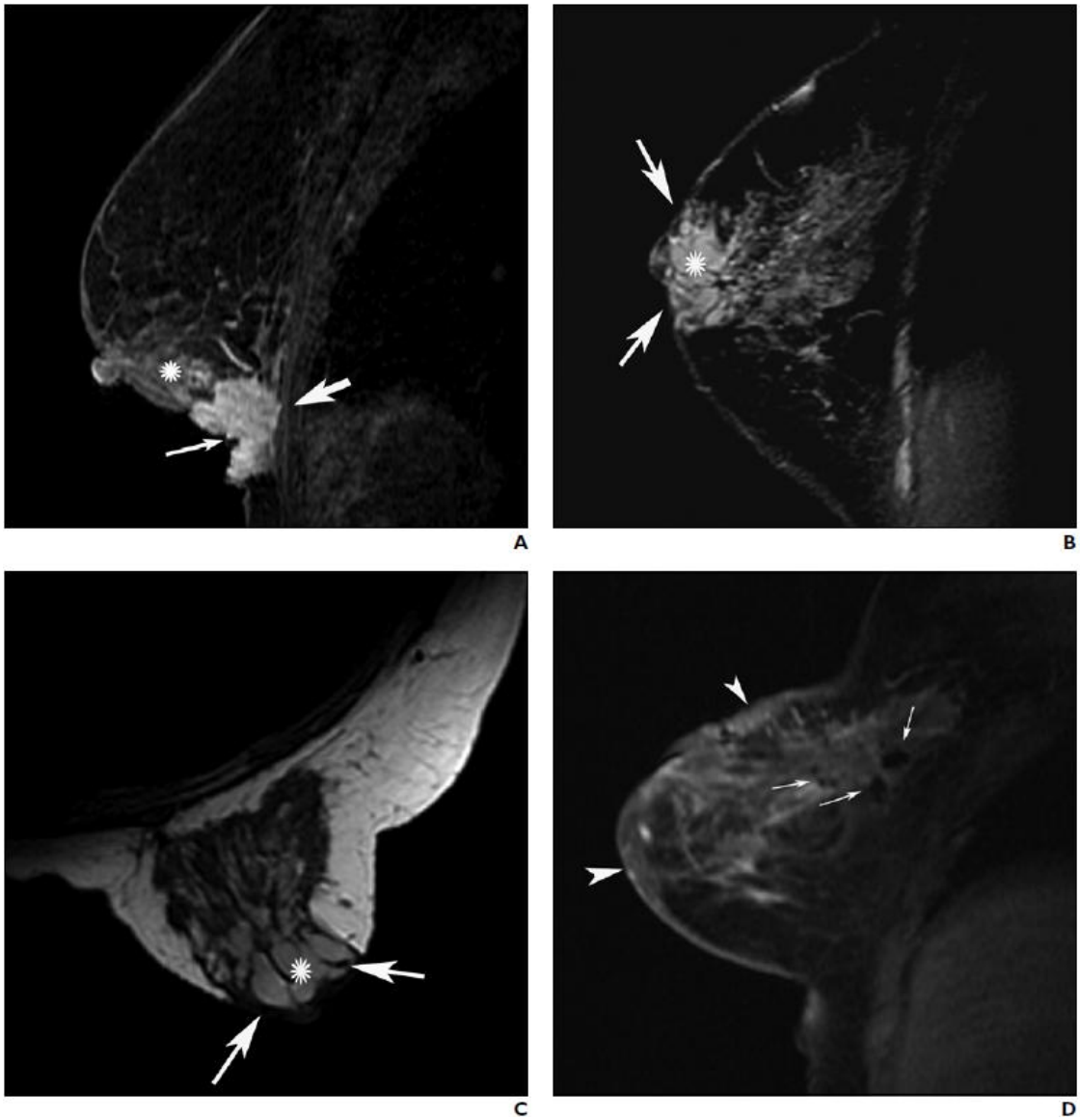

Figure 2.17 [27]: Images of the associated findings category of the BI-RADS MRI lexicon. Image A shows pectoralis muscle or chest wall invasion (thick arrow), skin involvement (thin arrow), and reticular enhancement (asterisk) in a woman with T4 breast cancer. Images B and C show unenhanced high signal intensity in ducts. Sagittal T2 (B) and axial T1 (C) images show subareolar dilated ducts (arrows) with areas of high signal intensity (asterisks). These areas represent benign ectatic ducts containing secretion with increased protein content. Image D of right breast after right segmentectomy for invasive ductal cancer shows abnormal signal voids (arrows) that denotes surgical clips. Deformity and skin thickening (arrowheads) due to surgery and radiation are evident.

2.3.4 Limitations of the BI-RADS lexicon

The BI-RADS lexicon categories are useful as a means of predicting malignancy but as with any tool are not free from limitations. Even before the use of the BI-RADS lexicon variability in the mammographic interpretation had been reported in various studies. Elmore et al [28] published a study in which ten radiologists reviewed 150 mammograms including 27 cancers. Work-up was recommended for 74% to 96% of women with cancer and 11% to 65% without cancer, the study concluded that although mammography is of value in screening women for breast cancer, radiologists can differ, sometimes substantially in their interpretations of mammograms and in their recommendations for management [28]. Since the introduction of the BI-RADS lexicon, observer variability has been re-evaluated by various studies [29, 30]. The studies concluded that even with a standardised lexicon present, variability in mammographic reports persists [24]. In a more recent study [31] four observers evaluated 103 lesions (49 malignant and 54 benign) and looked at variability in the description of morphologic and contrast enhancement characteristics in MRI of breast lesions, the author concluded that there was considerable variability in the use of most generally accepted terms. In addition the preparation of the regions of interest (ROIs) was a major source of variability in the interpretation of enhancement curves. Although BI-RADS is a helpful guide for use in everyday practice; continued development of methods to improve standardisation in mammographic interpretation is needed [30]. In time this will help to achieve its purpose of standardising mammographic reports and improving clarity and enabling better communication.

2.4 Automatic Analysis of Dynamic contrast enhanced (DCE) MR images

DCE-MRI is discussed in more detail in the introduction chapter (1.3.3). This section will look at the need for automated analysis of DCE-MRI data and post contrast images. There are various ways for hospitals performing breast MRI exams to classify tumours (for example BI-RADS as discussed in previous sections). There tends to be a fixed workflow for each patient study from the scan through to the report being generated. Once the data is acquired a technologist manually creates subtraction images at the MRI workstation and sends them to the radiologist workstation for examination, the radiologist then manually has to go through all the slices looking for suspicious regions which is a very time consuming task especially as the regions can be very small. The human factor can be one of the main reasons for missing suspicious regions, once one is detected the region is then analysed by the radiologist, this is normally a manual process where the radiologist specifies a region of interest (ROI) within the suspicious region. For the ROI a corresponding time-signal curve is computed and the region is finally classified, each suspicious region has to be analysed and hence this is a lengthy process which can take around 30-40 minutes per patient. Performing several of these examinations per day can lead to fatigue and inattention for the radiologist. To overcome this various studies have been conducted to optimise this workflow by using breast DCE-MRI data with various computer aided design (CAD) techniques and as a result these are able to automatically analyse DCE-MRI images. There are many CAD packages available; a few will be discussed in this section, which aim to automate some of the radiologists otherwise manual work.

Two factors can enhance tumour regions, firstly the effect of angiogenesis resulting in increased vascularity or vessel density which causes increased contrast uptake. Second increased vessel permeability which leads to increased leakage of the contrast agent into the tumour site. Dynamic imaging of the breast or a ROI makes it possible to functionally analyse the contrast intake or washout, using signal-time curves [32], these factors can assist in improving the sensitivity and specificity of the lesions [33].

Subramanium et al [33] developed a system to identify, process, visualise and quantify lesions

from breast DCE-MRI volumes, based on time signal curves. The application has the following features/benefits [33]: easy manipulation of signal-time intensity curves, 2D and 3D visualisation views, with 3D providing better characterisation of shape and size and 2D views providing lesion information about specific parts of the volume, easy navigation between 2D and 3D views without loss of spatial context, and a function which accurately computes tumour volumes.

In the Subramanium [33] study the system was tested on four breast tumour cases; Invasive ductal cancer, benign fibrodenoma, DCIS and lobular carcinoma. The system was in agreement for the first three cases, in the fourth case (lobular carcinoma) the tools assessment differed from the radiological assessment (false negative).

Pediconi et al [34] took another approach in software which employs time-signal curves of DCE-MRI volumes to automatically display a false colour map, where each type of curve is mapped to a different colour. The regions that correspond to the different type of curve are simultaneously displayed using different colours. The software features a semiautomatic pixel by pixel analysis of the ROI which makes the procedure mainly operator independent which the study claims can help radiologists distinguish different patterns inside a single lesion, possibly allowing to reduce false negative evaluation [34].

Coto Ernesto et al [35] produced 'MammoExplorer' (fig 2.18) a CAD application that requires as input a DCE-MRI sequence containing at least two time steps, first being pre-contrast and the rest post contrast time steps. MammoExplorer automatically computes, for every post contrast time step in the input sequence, its subtraction from the pre-contrast time step. It then displays a control panel which contains the following (fig 2.18):

- An enhancement scatter plot for each subtracted volume;

  this serves as an interface for a sophisticated segmentation algorithm, which allows the radiologist to look at the breast DCE-MRI data in an intuitive way where every

interesting region can be explored using the usual slice through approach and cross-sectional views

- A 3D view;

  this is able to display advanced volume renderings of the data and the ROIs

- A time-signal curve view

  this view is available for radiologists that are familiar with this method, all views are linked for effective correlation of all data

- 3 cross sectional views (sagittal, coronal and axial)

Coto Ernesto et al [35] believe that this application allows radiologists to perform a more in depth exploration of the breast whilst considerably reducing the usual workflow time, and that this will lead to more accurate diagnosis.

As with any software application none of the above are free from limitations, the application in the study by Subramanium et al [33] has the ability for the user to pick a few voxels central to a lesion, and examine their time-signal curves but this requires the radiologist to find the suspicious regions manually, a confidence degree of malignancy is then assigned. The user when using this approach is limited to detect lesions with time-signal behaviour which is approximately similar to the specified mean curve, the radiologist could miss this type [35]. The application developed by the Carotenuto et al [34] study also has its criticisms as outlined by Coto Ernesto et al [35] that when the type of curve is mapped to a different colour it is a discrete mapping as opposed to a smooth transition between the different kinds of curves, it is therefore impossible to tell the difference between certain and uncertain regions which can ultimately lead to incorrect interpretations.

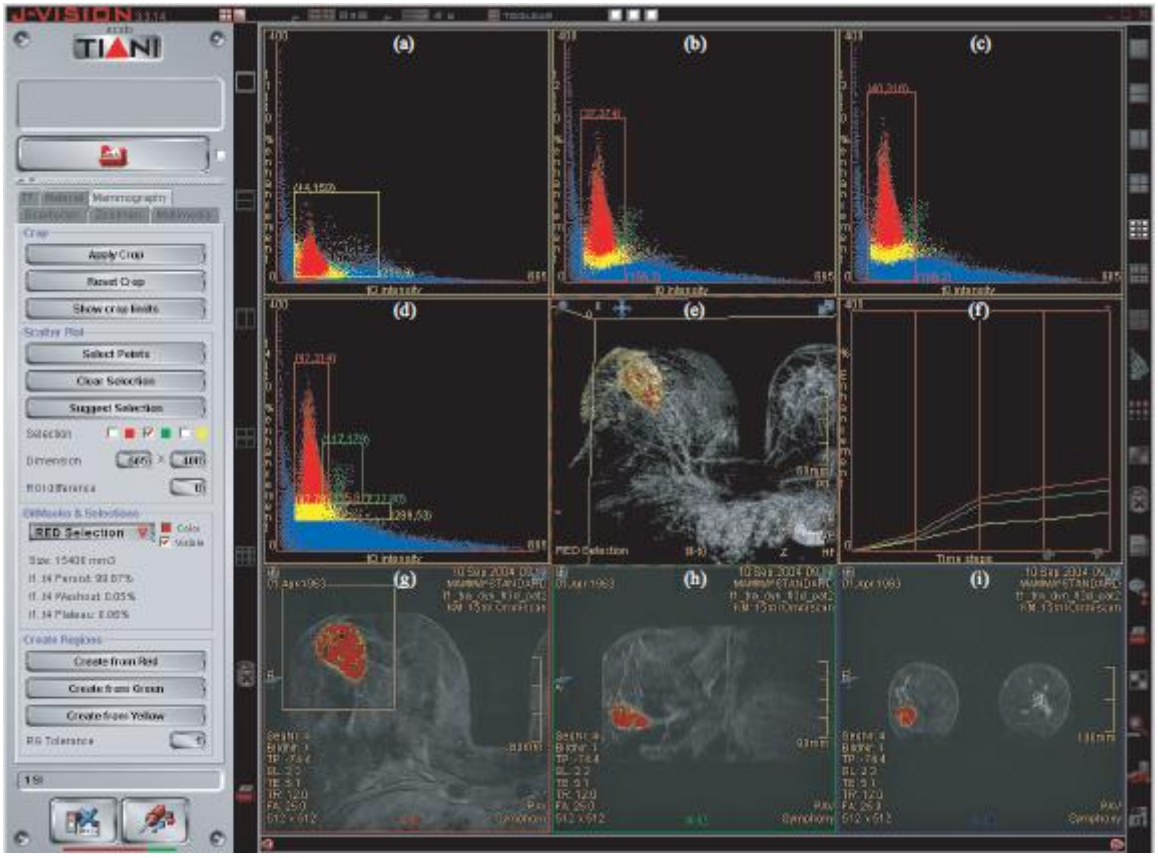

Figure 2.18 [35]: MammoExplorer working with a DCE-MRI sequence of five scans. (a)- (d) Enhancement scatter plots for subtracted volumes t1-t0, t2-t0, t3-t0 and t4-t0. (e) 3D view. (f) time-signal curve view. (g)- (i) axial, sagittal, and coronal views.

A more up to date system CADstream has the following features for MRI of breast [36]; Image registration (using adaptive motion correction as well as artefact detection (fig 2.19)), subtraction images (indicating abnormal tissues by comparing different series (fig 2.20)), multiplanar reformatting (allowing sagittal, axial and coronal views allowing localization of lesions and their relationships to other anatomy (fig 2.21)), maximum intensity projections (provide interactive 3D viewing), volume summaries (3D rendering, grow and shrink segmented lesions, isolate vascular areas, lesion diameter measurements, location information with distance to nipple, skin and chest wall, automatic detection of most suspicious washout, plateau and persistent curves, morphology characterizations, BI-RADS atlas lexicon for lesion classification (fig 2.22)), angiogenesis maps and curves (in accordance to the ACR BI-RADS Atlas), Interventional guidance (calculate more efficiently coordinates for MR-guided

interventions at the point of procedure, provides real time reports for needle position), portfolio for reporting (including BI-RADS classification (fig 2.23)).

The CADstream package claims continuous validation by a growing body of published research [36]. A study by Lehman et al published in 2006 highlighted that the use of CADstream interpreted breast MR examinations accurately showing significant enhancement in all the malignant lesions while depicting 12 of 24 benign lesions as showing insignificant enhancement [37]. The study states such CAD programs improve specificity, may decrease heterogeneity of interpretations across radiologists of varying levels of breast MR interpretation experience, as well as reducing time required for image processing and interpretation.

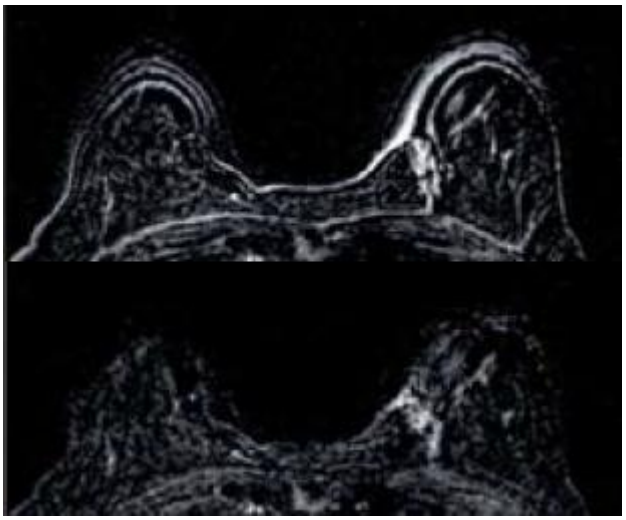

Figure 2.19 [37]: CADstream image registration uses 2D/3D adaptive motion correction and is efficient in demonstrating the ability to reduce artefact in subtraction images

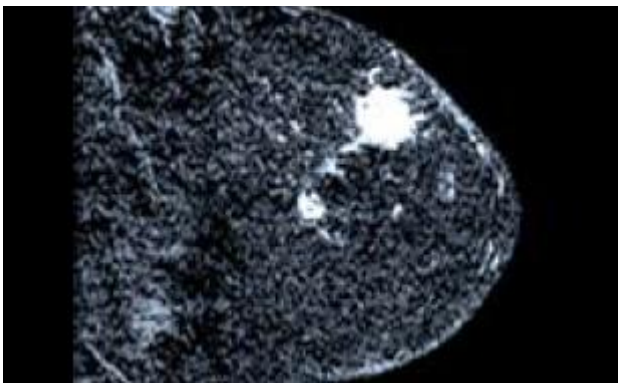

Figure 2.20 [37]: CADstream subtraction compares different series and highlights bright areas that may indicate abnormal tissue

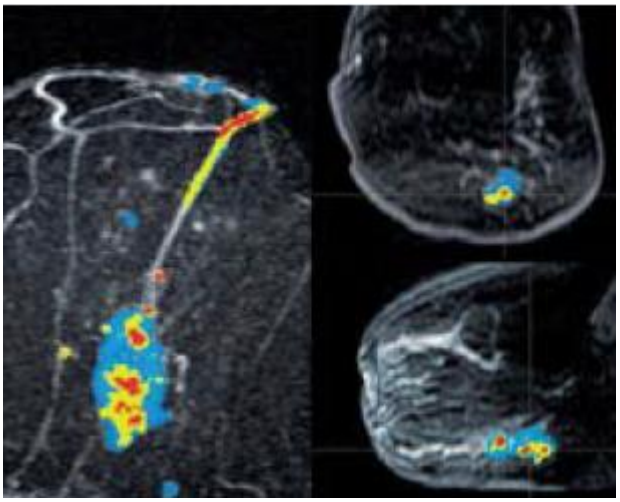

Figure 2.21 [37]: Multiplanar Reformatting (MPR) allows user to view studies in multiple planes (sagittal, axial and coronal)

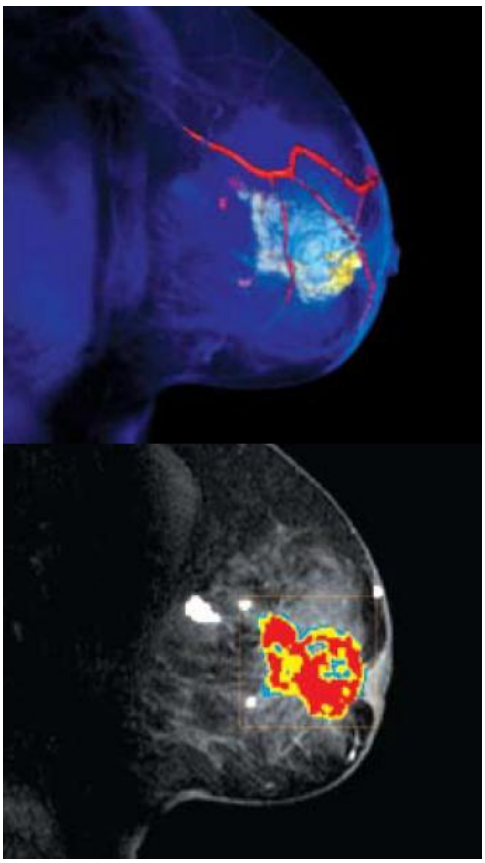

Figure 2.22 [37]: CADstream Volume Summaries creates lesion (volume) characterizations automatically with 3D renderings and data calculations for each volume

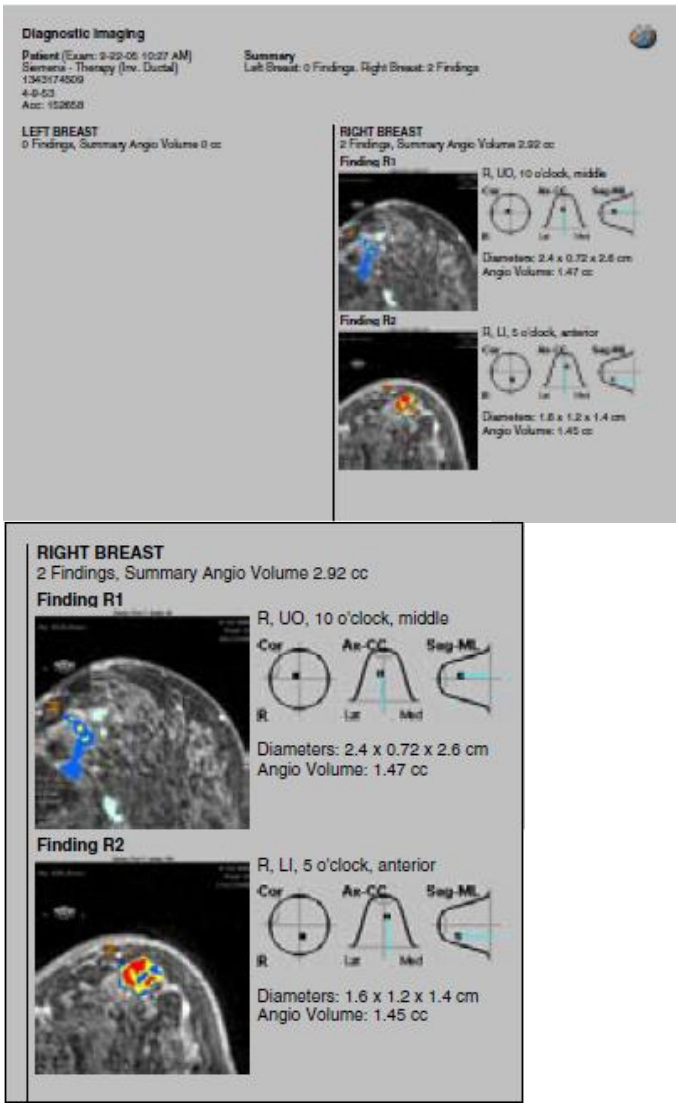

Figure 2.23 [37]: CADstream Portfolio for Reporting automatically generated with reference images, size and location information and radiologist assigned BR-RADS Atlas classification for each lesion.

2.5 Pharmacokinetic modelling

Pharmacokinetics (PK) is a branch of pharmacology that involves administering drugs externally to a living organism, and determines where these substances/drugs end up. Simple mathematical schemes representing complex physiological spaces or processes are known as pharmacokinetic models. Signal enhancement that is prevalent on dynamic acquisition of T1-weighted images can be assessed in two ways, either by the analysis of the signal intensity changes (semi-quantitative) or by the quantification of contrast agent concentration change using pharmacokinetic modelling techniques. Generally quantitative techniques involve the

modelling of tissue contrast agent concentration, in reality some model intensity changes, which assume that signal intensity changes are proportional to contrast agent concentration changes. During a dynamic enhancement acquisition the signal intensity changes measured can be used to estimate contrast agent concentration, concentration-time curves are then mathematically derived using one of the pharmacokinetic modelling techniques, some of the parameters used in this type of modelling include [38]:

- K^{trans} (permeability) - the volume transfer constant of the contrast agent, also known as permeability (surface area product per unit volume of tissue)
- v_e - leakage space as a percentage of unit volume tissue
- k_{ep} - the rate constant
- The above have the mathematical relationship of $k_{ep} = K^{trans}/v_e$
- [C](t) – concentration vs. time [39]

In order to determine precise elimination rate it is important to have accurate PK modelling, the most widely used types of PK models include:

- one-compartment model (fig 2.24); used for drugs which equilibrate rapidly with the tissue compartment, for example a drug which takes 15-30 minutes
- two-compartment model (fig 2.25); used for drugs which equilibrate slowly with the tissue compartment, for example drugs which take 1 to 2 hours

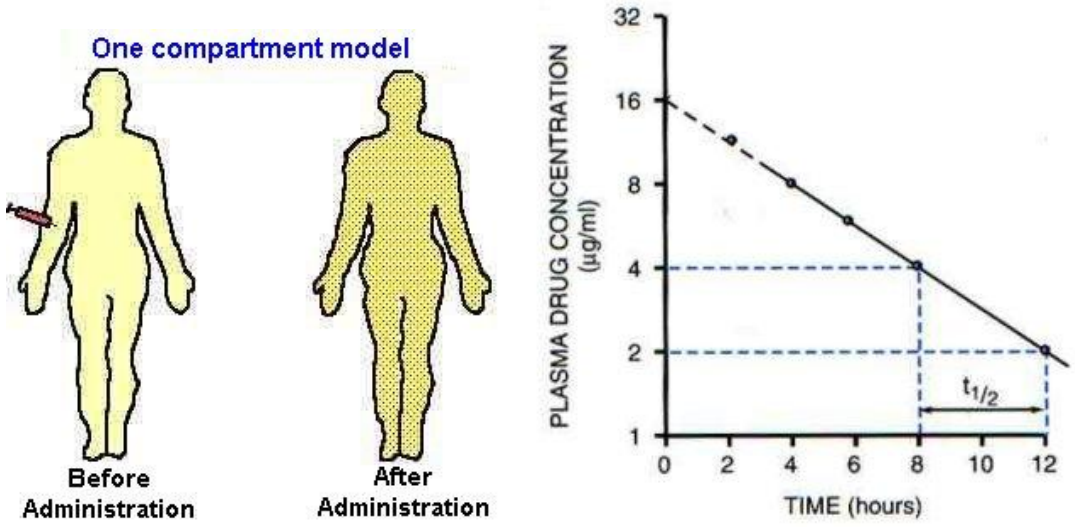

Figure 2.24 [40]: the one-compartment model (left) with a serum level plot on the right showing how this model yields a straight line when using a log scale on the y axis

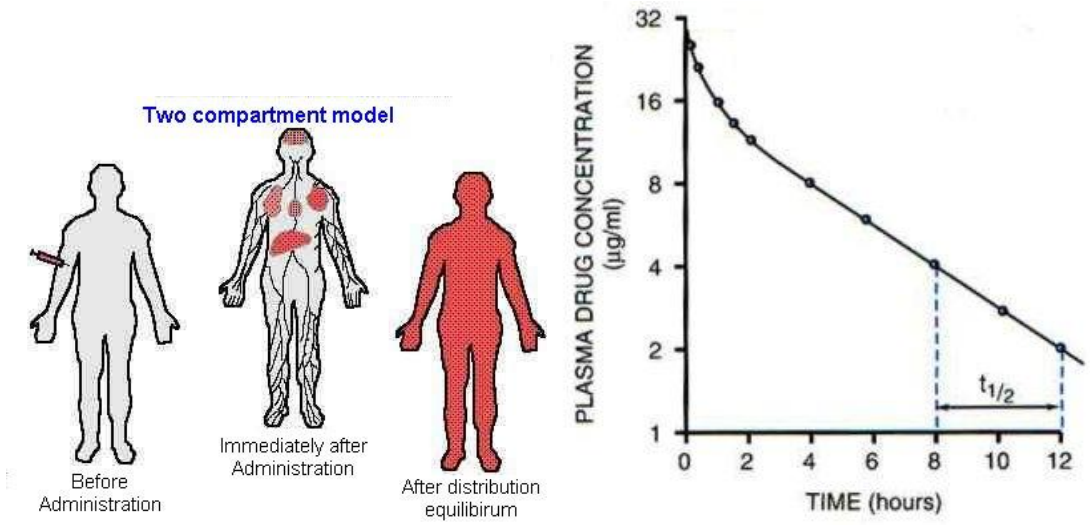

Figure 2.25 [40]: the two-compartment model (left) with a serum plot on the right showing how this model yields a biphasic line when using a log scale on the y axis

For the purpose of detecting and evaluating breast disease researchers [38] often use quantitative T1-weighted dynamic contrast MRI (T_1-w DCE-MRI). Within this technique gadolinium (Gd) contrast agent is intravenously injected during rapid (~sec), repeated T1-weighted imaging, the Gd concentration vs. time ([C] (t)) of a lesion of interest can be estimated from these images. By then applying pharmacokinetic modelling to [C] (t)

parameters such as extraction-flow product (EF, which is equivalent to $\mathrm{K}^{\mathrm{trans}}$) can be extracted which in turn are used for lesion diagnosis and tracking of treatment progress [39].

Slice selective (two dimensional) spoiled gradient-recalled echo (2D SPGR) imaging is the pulse sequence frequently used for T1-w DCE-MRI as it produces relatively artefact free images when performed with high temporal resolution (<~15 sec), this is useful in distinguishing benign and malignant breast lesions [39]. The 2D SPGR images allow the measurement of the signal vs. time (S (t)) of a pixel or an ROI in a lesion. The S (t) can then be converted to $\mathrm{T}_1(\mathrm{t})$ and this can then be used to compute [C](t) for PK modelling [38]. In order to get the relationship between S and $\mathrm{T}_1$the $\mathrm{T}_1(\mathrm{t})$ is estimated from S(t) by utilising a 2D SPGR signal strength equation, $\mathrm{T}_1$is measured before the injection of Gd contrast agent ($\mathrm{T}_{1\mathrm{pre}}$) or by measuring one or more values of S in order to determine the signal strength equations overall scaling factor. Significant errors can occur, in fact greater than 50% [39] in the estimated [C](t), due to the signal strength in the 2D SPGR being very sensitive to even the slightest of variations in the transmit magnetic field (B_1) which can cause inaccuracies in the signal strength equation as the T_1shortens and [C] increases post-injection. In turn this leads to errors in the PK parameters that have been estimated, thus reducing sensitivity and specificity and making this method less consistent for tracking treatment progress [39].

Greg O. Cron et al [39] showed that a single pre-injection T_1measurement was not sufficient for estimating [C](t) reliably from rapid 2D SPGR imaging for PK modelling, the study concluded that this was due to discrepancy between the measured 2D SPGR signal strength and its theoretical value is not consistent from lesion to lesion. the study put the inconsistencies down to unexpected variations in the B_1 or slice-select profile, which it deemed to be caused by factors such as variations from patient to patient in breast geometry or inconsistently set transmit gains.

Another study by Giovanni et al [41] on the accuracy of PK parameter measurement in DCE-MRI of the breast at 3T states that accurate and robust PK parameters are needed if it is to be used in routine clinical practice, the study found sources of error in three areas in parameter

estimation. It concluded that improving the native T_1 calculation, B_1 inhomogeneity and ensuring that the dynamic temporal resolution is not lower than 20 s would aid in minimising errors.

2.6 Morphology

The BI-RADS lexicon describes calcification morphology (shape) and distribution. This helps radiologists to score breast lesions and determine whether they are benign or malignant, but the BI-RADS is highly subjective (clinician decides if they think lesion is spiculated, smooth etc). Pharmacokinetics looks at dynamic information objectively. Clinically there is no means of quantitatively analysing lesions in terms of their morphological features (shape or texture).

Texture analysis is already an established method in image classification of aerial and satellite photography. More recently, attempts have been made to utilise texture in MRI, particularly in the brain [42-44], but also in other organs such as the breast [45-50] wherein lesion morphology is known to be an important diagnostic and prognostic indicator. The following sections will begin by looking at the various morphological techniques including shape and texture and eventually discuss their applications in both medical and non-medical fields.

2.6.1 Textural Analysis methods

Texture features are mathematical parameters computed from the distribution of pixels, the mathematical parameters characterise the texture type and the underlying structure of the objects in the image [51]. This section will aim to compare the different techniques of texture analysis currently known. The methods of textural analysis used to evaluate the inter-relationships of the pixels in an image can be discussed by four categories; structural (represent texture by the use of well defined primitives), model-based (represent texture using sophisticated mathematical models), statistical (represent texture by looking at properties controlling the distribution and relationships of grey level values in an image) and transform methods (analysing texture properties of an image in a different space such as frequency or scale space) [52]. Structural methods provide a good symbolic description of an image whilst

model-based methods are computationally complex. Statistical methods in medical images have the advantage of achieving higher discrimination indexes than structural or transform methods [51]. A later section will discuss successful texture analysis studies using MRI that would normally be impossible to discern by simply visually inspecting the MR image, various examples will be discussed including studies involving texture analysis in the brain [42-44] and breast [48]. Of the four categories of texture analysis mentioned the most commonly used for medical applications is the statistical approach [51], this section will discuss this class in more detail along with the model-based and transform class, there are no known examples of the structural class method of texture analysis being applied to medical images [51] therefore this class will be omitted in the discussion. Texture parameters are commonly derived from six main categories which the remainder of this section will discuss, these categories are histogram, absolute gradient, run-length matrix and co-occurrence matrix all of which are utilised in the statistical form of texture analysis. The final 2 categories are auto-regressive model (model class) and wavelets (transform class).

2.6.1.1 Image Histograms

The histogram of an image counts the number of pixels in a given image with respect to its grey level value. 8 bit images values range from 0 to 255 and most digital images are of this nature. Medical MR images on the other hand give more definition of the object of the image which can only be achieved using higher bit images, for example a 12 bit image will have grey values ranging from 0 to 4095, lower values are attributed to darker grey levels and higher to lighter colour grey levels. A value of 0 represents a black pixel and white will have value of 4095 (or 255 if it's an 8 bit image). In this thesis the images from the GE scanner are acquired at 12 bit and stored at 16 bit. Figure 2.26 shows an example of a digital image and its corresponding histogram can be seen in figure 2.27. The numbers of pixels are then counted of each given grey level value; figure 2.27 shows an example of how the results from the digital image (fig 2.26) can be represented as a histogram chart. Parameters that can then be derived

from the histogram include its mean, variance and percentiles. Histograms are useful but they do not contain any localised information, figure 2.28 shows another digital image, the images in figures 2.26 and 2.28 will have the same histogram (fig 2.27) as although visually they look different the number of pixels with respect to their grey levels remain the same.

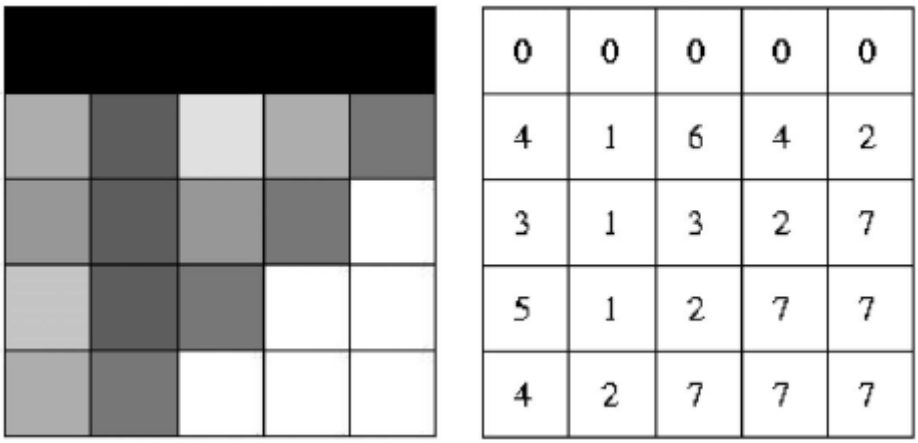

0	0	0	0	0
4	1	6	4	2
3	1	3	2	7
5	1	2	7	7
4	2	7	7	7

Figure 2.26 [51]: a 5x5 digital image (left) with grey level values where 0 is black and 7 is white. The matrix (right) illustrates the numerical representation of the image

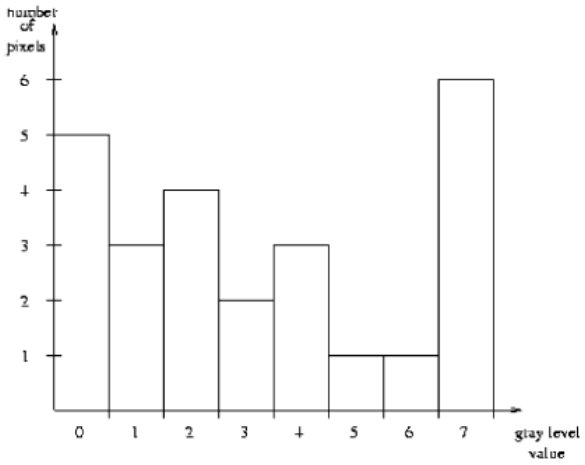

Figure 2.27 [51]: histogram chart of the image shown in figures 2.26 and 2.28

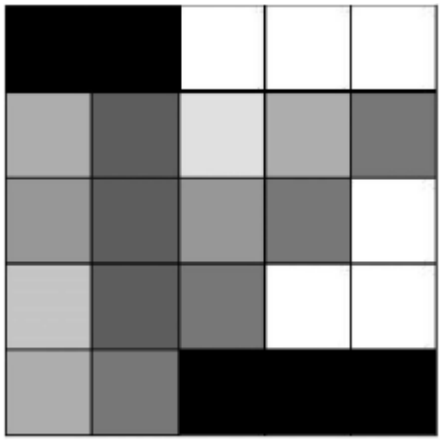

0	0	7	7	7
4	1	6	4	2
3	1	3	2	7
5	1	2	7	7
4	2	0	0	0

Figure 2.28: a 5x5 digital image (left) with grey level values where 0 is black and 7 is white. The matrix (right) illustrates the numerical representation of the image

2.6.1.2 Absolute gradient

The absolute gradient is a measure of the spatial variation of grey levels across an image. It aims to see if the image varies from grey to white at a given point (high gradient value) or if it varies smoothly from a dark grey to a slightly lighter grey (low gradient value). The gradient can be either negative (light to dark) or positive (dark to light), generally when applying this measure the interest is in whether the grey level variation is smooth or abrupt therefore the absolute gradient is used (ignoring the negative/positive sign). Figure 2.29 shows a coronal slice of a T1 weighted cerebral MRI and the corresponding absolute gradient, the image gradient emphasises the contours of the original image with the strongest (whitest) where the changes in grey level in the original image is the greatest [51]. Texture parameters that can be derived from the absolute gradient include the mean and variance.

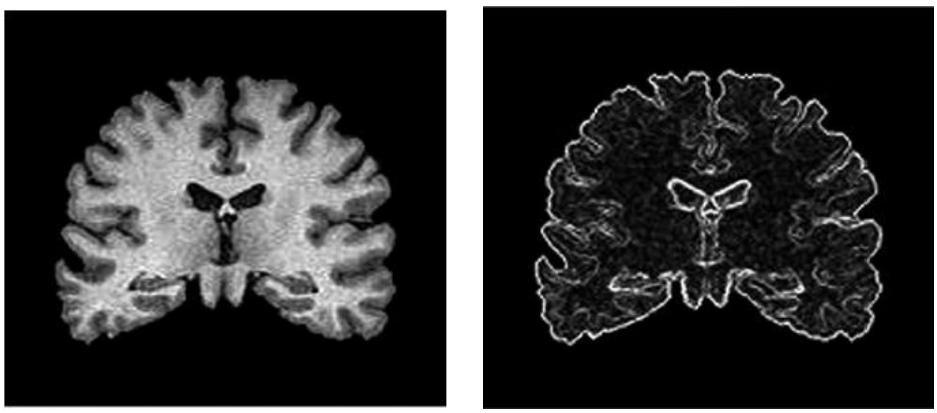

Figure 2.29 [51]: coronal slice of a T1 weighted cerebral MRI (left) and its corresponding absolute gradient image

2.6.1.3 Run-length matrix

A run-length matrix searches an image across a given direction, looking for pixels that have (run) the same grey level value. For example if looking in the vertical direction the run length matrix would measure for each grey level value how many times there are runs of 2 consecutive pixels with the same value, then for 3 consecutive pixels with the same value, then 4, 5, 6 and so on and this can be repeated for many directions but is normally done for 4 (horizontal, vertical and 2 diagonals) [51]. Figure 2.30 illustrates a horizontal and a diagonal run-length matrix of the image in figure 2.26. From the run-length matrix parameters that can be computed include fraction of image in runs which measures the percentage of image pixels that are part of any of the runs considered for the matrix computed and short-run emphasis which is a measure of the proportion that occur in an image with a short length [51].

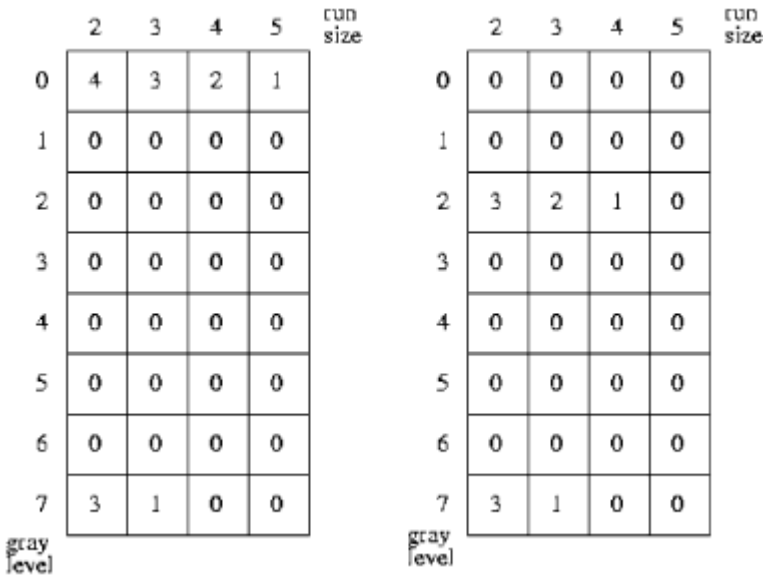

Figure 2.30 [51]: corresponding run length matrices for the image in figure 2.26 with an example of horizontal (left) and a 45° (right) run-length matrices

2.6.1.4 Co-occurrence method

Textural analysis within aerial and satellite photography has long been an established method of image classification. Some attempts have been made to utilise texture in MRI, particularly in the brain [42-44]. Freeborough et al [42] focused a study on assessing the value of MR based texture as a measure of change in Alzheimer's disease. Texture features were calculated over a large range of offset distances. Texture was calculated using the co-occurrence matrix and the Haralick texture formulas f1-f13 [53], this statistical technique known as the spatial gray-level dependence matrix method has the ability to study the 2nd order statistics of pixels at difference spacing's and angles. Graycommatrix function in programming environments such as Matlab generates the GLCM by calculating how often a pixel with gray-level (greyscale intensity) value i occurs horizontally adjacent to a pixel with the value j. (You can specify other pixel spatial relationships using the 'Offsets' parameter). Each element (i,j) in GLCM specifies the number of times that the pixel with value i occurred horizontally adjacent to a pixel with value j (fig 2.31). The Freeborough study [42] demonstrated that a texture descriminant function derived from MRI brain scans, yields significantly different values for Alzheimer's

disease patients compared to normal controls [42]. In addition this measure reflects the progression of the disease over time, and these measures could be useful as aids in the diagnosis and tracking of Alzheimer's disease.

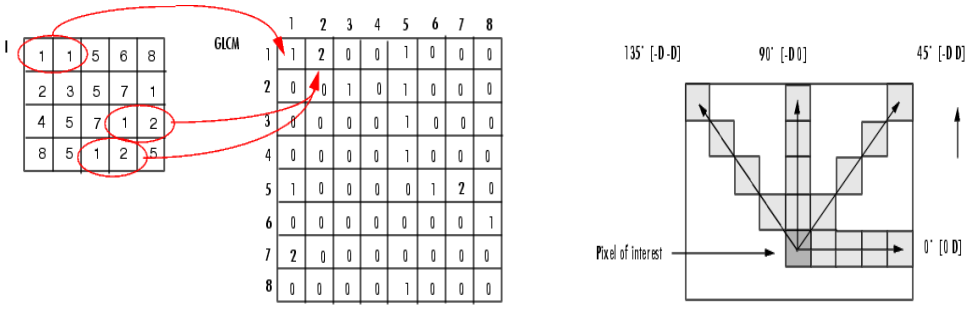

Figure 2.31 [54]: matrix on top left is an example of an original matrix, matrix next to it is the generated GLCM matrix, generation of Gray level co-occurrence matrix (GLCM) by calculating how often a pixel with gray-level (greyscale intensity) value i occurs horizontally adjacent to a pixel with the value j . You can specify other pixel spatial relationships using the 'Offsets' parameter, each element (i,j) in GLCM specifies the number of times that the pixel with value i occurred horizontally adjacent to a pixel with value j. Top right shows the different directions the GLCM can be calculated in and the distance that can be varied from the pixel of interest.

As the co-occurrence matrix looks at the grey level distribution of pixel pairs it is sometimes referred to as the second-order histogram. Calculations that can be derived from the co-occurrence method include over 14 texture parameters such as contrast, entropy and angular second moment. These are discussed further in section 2.6.3 with example uses in studies by Haralick [53] and Conners [55].

2.6.1.5 Auto-regressive model

The auto-regressive model finds relationships between groups of neighbouring pixels and uses these as a way of describing shapes within the image. The parameters from the auto-regressive technique are the set of weights used to establish the relations between groups of neighbouring pixels, the relations are said to be unique for any given type of object or shape in an image therefore this can aid in characterising the object [51]. Figure 2.32 illustrates an

example of a pixel neighbourhood that can be used to compute parameters of the auto regressive model (example parameters include curvature and radius), in this example the white pixels (neighbourhood) are shown that could be used to characterise the centre black pixel using this model. The figure shown would suggest that every pixel in the images grey level value would be characterised according to its neighbouring pixel values as per the pattern shown.

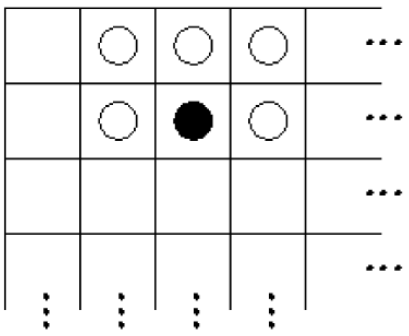

Figure 2.32 [51]: pixel neighbourhood example that could be used to compute parameters of the auto-regressive model.

2.6.1.6 Wavelet transforms

Wavelets are best explained by first looking at fast and slow variations of grey level values and their spatial frequencies. Given a 2-D image if its grey level value varies fast it is said to have many variations within a small piece of the image, it is said this image has a high spatial frequency in this part of the image. Similarly if the grey level value varies slowly, to the point where it is almost the same throughout the region of the image then it is said the region has a low spatial frequency. The scale of the image region is what the concept of fast or slow grey level value variations depends upon [51]. This can be further elaborated if looking at certain satellite images and comparing with close up images of scenery, for example a very large scale image taken by satellite of a terrain or forest like scenery would appear almost like a constant green stain, if this same image was taken by a low flying aircraft it would be much smaller scale and the image would show more variations and details. Thus the satellite image would have lower frequency content and the one taken from the low altitude aircraft of the same forest

land would have higher frequency content. In addition it is also necessary to take into account the direction of the variations in 2-D. Wavelets themselves then can be described as a technique that involves the analysis of the frequency content of an image for different scales of that image [51]. The analysis will yield a set of wavelet coefficients which correspond to different scales and different frequency directions. A set of numbers is associated with each pixel when computing the wavelet transform of an image, these are known as the wavelet coefficients and characterise the frequency content of the image at that point over a set of scales. It is from these coefficients that a set of texture parameters can then be computed. Figure 2.33 shows an example of a wavelet transform of the original image in figure 2.29, where the top left shows a small-scale low frequency version of the original image and all other parts of the image show versions of the original image in high frequency and on different scales.

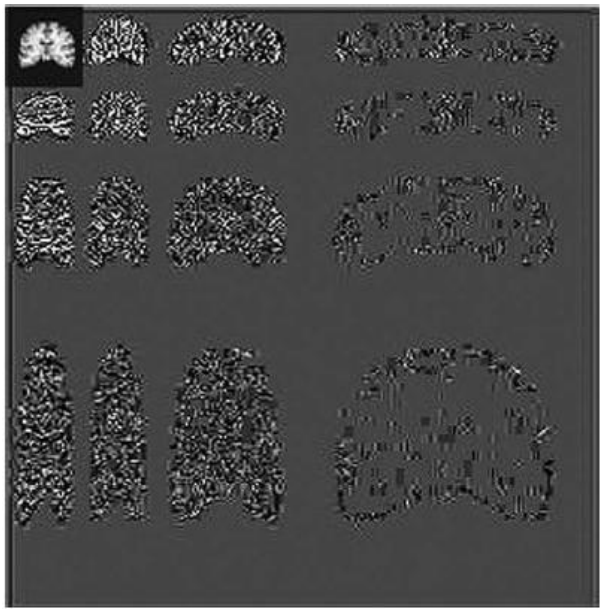

Figure 2.33 [51]: wavelet transform of the image in figure 2.29. Top left is low frequency, small scale version of the original image whereas all other parts of the image are showing high frequency versions of the original image on different scales.

The statistical approaches to texture analysis described (histogram, absolute gradient, run-length matrix and co-occurrence matrix) do not explicitly attempt to understand the

hierarchical structure of the texture. Second order statistical methods that look at statistics given by pairs of pixels have shown to give higher discrimination rates than that of transform based methods such as wavelets [52]. Model based approaches to texture analysis such as the auto regressive model described earlier tend to be computationally complex and lack orientation selectivity and are considered not suitable for describing local image structures [52]. Models based on transform methods such as Fourier, Gabor and wavelet transforms (discussed earlier) look at coordinates in space of an image and how this coordinate system can be interpreted with its relations to the characteristics of a texture (such as frequency or size). This is an area where co-occurrence or run length features may lack the sensitivity to identify large scale or more coarse changes in spatial frequency [56]. In practice Fourier transforms perform poorly due to their lack of spatial localisation, Gabor filters in contrast have better spatial localisation but in practice are not very useful due to lack of single filter resolution at which one can localise a spatial structure in natural textures [52]. Wavelet transforms offer several advantages over Gabor transforms in that varying the spatial resolution results in textures being able to be represented at the most suitable scale. Wavelets are also useful due to having a wide range of choices so that a specific application can choose wavelets that are best suited for texture analysis. Wavelet transforms are therefore a good choice for texture segmentation, a disadvantage of wavelet transforms is that they are not translation invariant [52]. More recently in 2010 Kassner and Thornhill said that run length features performed comparably well with those derived from GLCM and were considered to be superior to wavelet features [56]. Wavelet transforms are computationally complex and therefore implementation in a clinical setting is considered a substantial disincentive. In conclusion then texture analysis has potential to be a valuable and versatile tool especially in MR imaging but can contain many pitfalls such as statistical over fitting. Statistical or spectral textural features have outperformed visual assessment in discerning subtle anatomical changes in the medical field, and the robustness of texture analysis makes it particularly attractive for monitoring disease progression or treatment response with time [56].

2.6.2 Shape Analysis techniques

Visually shape is an important feature and one of the basic features used to describe content of an image. Representing shapes and describing them can be a difficult task, one dimension of image informarion is lost when a 3-D real world object is projected onto a 2-D image plane. A partially represented objects shape is seen as a result as well as seeing the corruption in terms of noise, defects, distortion and occlusion. Also as with texture analysis general points to consider include computational complexity of any calculation. Shape representation and descriptors are generally of two classifications: contour based methods (features extracted from the contour) and region based methods (features extracted from the whole region). These two are further divided into structural approaches (shape represented as a whole) and global approaches (shape represented by segments/sections (primitives)), these approaches are further split into space domain (features derived from spatial domain) and transform domain (features derived from transformed domain) [57]. Figure 2.34 illustrates this hierarchy.

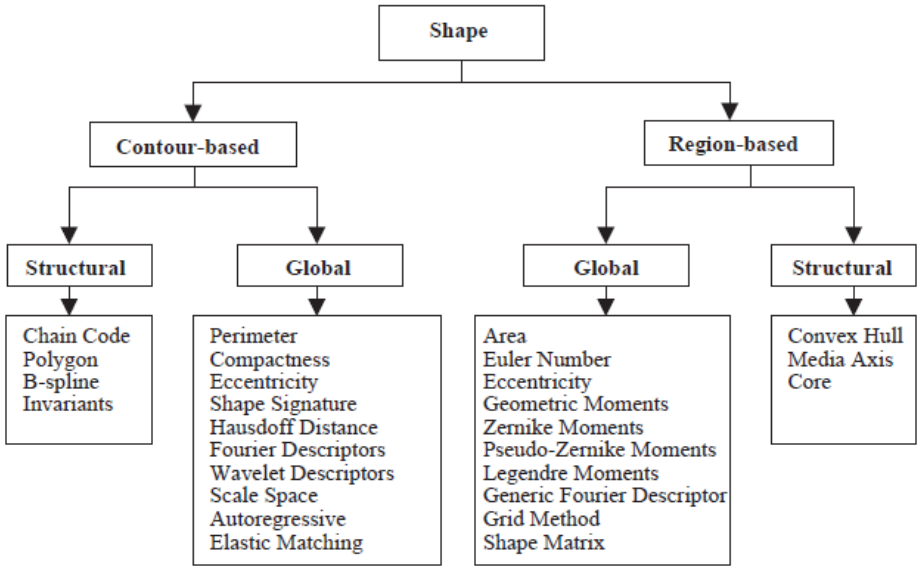

Figure 2.34 [57]: classification of shape representation and description techniques

Humans are thought to discriminate shapes mainly by their contour features and for this reason in literature this approach seems to be more popular than region based approaches. In addition shape contour is the only interest in many cases and shape interior content may not

normally be important [57]. Contour based methods have several limitations, firstly as they only use a small part of shape information (contour information) the shape descriptors are generally sensitive to noise and variations, sometimes the shape contour is simply not available and finally shape contour information sometimes isn't enough and the shape content is more important. Region based methods are used to overcome these limitations. Region based methods are said to be more robust as information is used from all of the shape. Although region based look at the whole shape information they are not strictly speaking any more complex than contour based as some of the region based methods are simple to implement [57].

Structural approaches are complex to implement in comparison to global approaches as there are lots of complex calculations that aid the matching of shapes and thresholding in order to determine similarities between primitives of two shapes in the matching process as well as majority of structural approaches using angle as a feature which adds another parameter into the system to accommodate the rotation invariant. These parameters in turn need to be finely tuned for different applications [57]. In favour of structural approaches is that they do allow partial matching which is useful when a large part of the shape is missing (boundary of shape is not closed) or occluded.

Methods working in the spatial domain suffer from two major drawbacks of having high dimension and noise sensitivity. The problems are solvable via histogram, moments, scale space and spectral transforms with spectral transforms among the four solutions being the best solution especially Fourier transform [57]. Using histogram and scale space will increase robustness to noise and compactness but matching using histogram and scale space can be computationally expensive. Moments are also robust and compact, however moments of higher order are difficult to assign to any physical meaning. For generic shape representations the generic Fourier Descriptor (GFD) is a desirable solution due to its retrieval performance whether they are used for contour based shapes (without interior content) or region based shapes (with interior content) makes no difference. GFD cannot do partial matching although

does work well where part of a shape is missing or occluded.

In conclusion then structural approaches are useful when partial matching of a shape is needed. For general purpose shape applications the complex moments and spectral transforms are the best choices such as GFD as they have good retrieval accuracy, compact features are good for general application with low computational complexity and robust retrieval performance [57].

2.6.3 Shape and Texture in non-medical fields

Gabor filters are linear functions used for edge detection, and are similar to those of the human visual system, in particular they have been found to be appropriate for texture representation and discrimination. A set of Gabor filters with different frequencies and orientations may be helpful for extracting useful features from an image [58]. Various studies exist within the MRI field [59] where the use of Gabor filters has been demonstrated. More commonly Gabor filters have been used outside the medical field in remote sensing and content-based image retrieval studies. Remote sensing is when an object is measured from far away in terms of its properties such as cloud and terrain classification, content based image retrieval uses image content as a search key for example in water, sky, forest etc all of which have texture as an important characteristic. Xiaojing Yuan et al [60] used evolution strategies to derive a feature identification system, the study states that the most critical component of the feature extraction system is the filter bank, the filter banks are chosen to extract features in the image by differentiating them from the background or other features.

Richard Conners et al [55] segmented high resolution urban scenes using various texture parameters, the parameters were calculated using Haralick's co-occurrence method [53], some of the features proposed by Haralick were calculated along with additional features such as cluster shade and cluster prominence. The study concluded with an overall 90% correct classification confirming the ability of texture algorithms to characterise land use classes. Haralick's study [53] originally performed texture analysis on photographic quality images

mainly aerial and satellite images, an important point to note from the study is that Haralick outlines that although features extracted contain textural characteristics in an image, it is difficult to identify which of the textural characteristics are specifically represented by these features. Haralick's studies have been the most influential in terms of the co-occurrence matrix and the texture features that can be calculated from the model. The study discusses in detail the Grey Level Co-occurrence Matrix (GLCM) and attempts to define some of the features and what they mean [53]. For example f_1 (angular second moment (ASM)) is defined as a measure of homogeneity of an image. Homogenous images (figure 2.35b) contain very few dominant grey-tone transitions, hence the P matrix for this image will have fewer entries of large magnitude, whereas a more inhomogeneous image (fig 2.35a) will have a large number of small entries within the P matrix and hence its ASM feature (calculated by the sum of squares of the entries) will be smaller. Figure 2.35 shows the digital printout of two 64 x 64 image blocks taken from a satellite picture over the Californian coastline. Figure 2.35a shows grassland and 24b represents a sample of water bodies in the area, the corresponding values of features f_1, f_2 and f_3 obtained from GLCM matrices for distance d=1 are shown below figure 2.35.

The overall results of the Haralick [53] study indicated that an identification accuracy of 89% was achieved when textural features were computed with the sandstone image set and 83% accuracy for satellite imagery of land use images. The study outlines possible pitfalls, it states that in the same way two people examining photographs of the same texture may actually be seeing two different but related kinds of tones in the texture, one photograph may have been developed so its tones are light and thin whereas the other may have been developed with dark and heavy tones. The majority of people would make the observation that both images have the same texture. For a machine to find that the textures are the same the images need to be probability quantised. Haralick is possibly trying to point out the importance of normalising the images and applying the correct number of grey levels as well as applying techniques such as histogram equalisation in order to achieve invariance under monotonic

grey-tone transformations. More specifically the texture features which contain this invariance property are angular second moment, entropy, sum entropy, difference entropy, information measure of correlation and maximal correlation coefficient. The study also recognised the need for further work in order to establish the size of the sub-image region and distance that would be optimum when computing the grey level matrices.

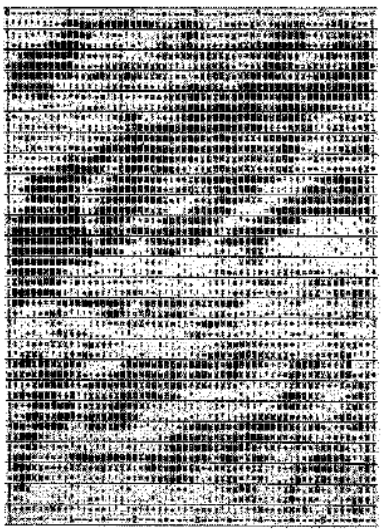

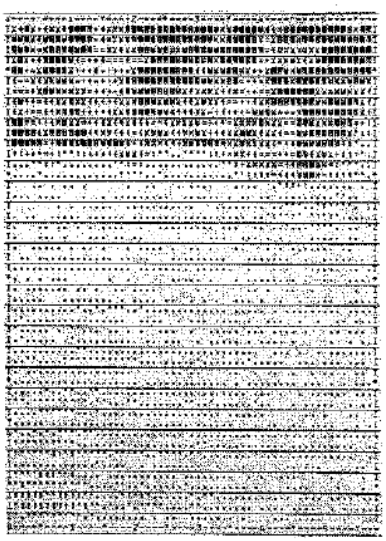

Grassland

Angle	ASM	Contrast	Correlation
0°	.0128	3.048	.8075
45°	.0080	4.011	.6366
90°	.0077	4.014	.5987
135°	.0064	4.709	.4610
Avg.	.0087	3.945	.6259

(a)

Water Body

ASM	Contrast	Correlation
.1016	2.153	.7254
.0771	3.057	.4768
.0762	3.113	.4646
.0741	3.129	.4650
.0822	2.863	.5327

(b)

Figure 2.35 [53]: textural features for two different land-use categories

2.6.4 Texture in MRI

R.A Lerski et al performed texture analysis in an attempt to investigate its use in tissue characterisation [61], the results of this study suggests that statistical image texture analysis of MR images of the human brain is clinically important when aiming to discriminate between brain tumour and oedema, the study acknowledged that further verification would be needed by carrying out a further clinical study.

A study by L Kjaer et al [62] looked at texture analysis in tissue characterisation of normal brain and intracranial tumours, the study found that much texture information was present in MR images that was useful for tissue characterisation of the normal brain, in addition the study

found that texture information showed promising potential in the differentiation of intracranial tumours.

Kovalev et al [43] suggested a new method for 3-D texture analysis of MRI brain datasets. The methods used for the study were based on extended, multi-sort co-occurrence matrices which use the combination of intensity, gradient and anisotropy image features in a systematic and consistent way. Reduced versions of the general 6-D co-occurrence matrices can be employed for texture analysis depending on the problem in question. The co-occurrence descriptors used are natively 3D, reflection and translation invariant and can also be rotation-insensitive [43]. Comparisons of brain regions with different sizes and inter-subject analysis are provided by the normalisation of the co-occurrence descriptors. The comparative section of the study revealed the following:

- the most sensitive texture descriptors are general 6-D matrices
- changes that appear to be subtle in appearance do not seem to show any changes in textural features

The study demonstrated that the extended co-occurrence descriptors are an efficient tool when used in various MRI brain image analysis tasks such as for classification of brain datasets and segmentation of diffuse brain lesions. Haralicks co-occurrence matrix was further used in a glioma study [44] with 3D as opposed to a 2D co-occurrence matrix. The results of the study demonstrated that various tumour parts that are usually difficult to distinguish were able to be enhanced using 3D-co-occurrence texture analysis without the need of contrast or additional acquisition sequences [44]. The study found that 3D co-occurrence either validated the 2D co-occurrence results but more importantly in some cases an improvement in tumour characterisation was seen with 3D co-occurrence. 3D co-occurrence gives better interclass separation values than the 2D co-occurrence method, which in turn means identifying suspect tumour areas that could otherwise appear normal.

Recent research has focused on other organs such as the breast, a 79 patient study by Gibbs et al [48] demonstrated significant differences in textural features between benign and malignant breast tumours. The study showed variance, entropy and sum entropy as important factors in lesion discrimination when combined with a logistic regression model, the findings were consistent with the perception that benign lesions have a more homogenous appearance.

A study of various features of contrast enhanced MR images of the breast by Sinha S et al [50] included extracting 8 of the Haralick [53] features, for 23 benign and 20 malignant breast lesions. This study showed significant differences in only three of the eight texture features calculated. An attempt was made to find the best combination of features yielding the highest classification accuracy. The specificity and sensitivity of combined texture features were 70% and 75% respectively.

In an extension to the study by Gibbs et al [48] a further study was carried out by Chen et al [47] but focussing on 3D GLCM as opposed to a 2D version, the study presented a volumetric texture analysis approach for computerised analysis of breast lesions on DCE-MRI. The study showed that texture features calculated based on 3D analysis yielded significantly better classification results than those based on 2D analysis [47]. Although this study generated 3D co-occurrence matrices and yielded significant differences from using 2-D the MRI images themselves were not true 3-D. In order to obtain 3-D MRI images they would need to be isotropic so in a sense the images obtained where similar to that of Gibbs et al, Chen et al used multiple slices with ROIs and used 3D interpolation to yield isotropic voxels.

A more recent study by Neha Bhooshan et al, 2010 [46] used texture analysis along with other computerised methods such as shape and kinetic features on DCE-MRI breast lesions in an attempt to make use of them as prognostic markers. The study found that lesion heterogeneity was a common indicator of malignancy, which in terms of texture can be described by using different mathematical algorithms namely the Haralick features [53] but extending his model to a 3-D volumetric grey-level co-occurrence matrix method. Unlike most MRI related studies that look at morphological features and for the purpose of the study are

only interested in quantifying the Haralick features, this study describes the 14 Haralick features with a brief definition of each as follows [46]:

1. Contrast: measure of local image variation
2. Correlation: measure of image linearity
3. Energy: measure of image homogeneity
4. Homogeneity: measure of local homogeneity
5. Entropy: measure of randomness of grey levels
6. Variance: measure of how spread out the grey level distribution is
7. Sum average: measure of overall image brightness
8. Sum variance: measure of how spread out the sum of the grey levels of voxel pairs is
9. Sum entropy: measure of randomness of the sum of the grey of neighbouring pixels
10. Difference in variance: measure of variation in the difference in grey levels between voxel pairs
11. Difference in entropy: measure of randomness of the difference in neighbouring grey levels
12. Information measure of correlation 1: measure of nonlinear grey-level dependence
13. Information measure of correlation 2: measure of nonlinear grey-level dependence
14. Maximal correlation coefficient: measure of nonlinear grey-level dependence

In addition according to the authors of a study by Conners et al [55] the texture parameters cluster shade and cluster prominence are believed to gauge the perceptual concepts of uniformity and proximity.

Whilst previous research has generally concentrated on quantifying morphology in high resolution data there appears to be some value in assessing lesion texture in dynamic contrast-enhanced (DCE) images [45], especially with regards to changes during the initial enhancement and subsequent washout phases.

Studies have also experimented using test objects for the study of texture measurement in MR imaging. Lerski [63] used reticulated foam as texture test objects, foams were inserted in test tubes embedded in agarose gel. A further study by the same group [64] involved multicentre analysis of the same test objects created in a similar manner of that of their earlier study [63]. In this study [64] the group scanned the same test objects across multiple centres and found some MRI equipment out performed others in terms of texture analysis. In addition the study concluded that texture measures were not easily comparable between centres, although the test object itself was deemed a successful standard object for the measurement of texture. Both studies [63, 64] considered first order parameters such as mean and skewness as well as texture parameters from the co-occurrence, gradient and run length methods.

In a more recent study Waugh [65] used a custom-made phantom containing different grades of reticulated foam embedded in agarose gel. They looked at assessing the ability of texture analysis to distinguish between different texture objects, an objective that the work in this thesis decided to adopt. The Waugh study also looked at outcome of texture analysis when imaging sequences were changed and concludes that changes to sequence parameters were less critical for the outcome of texture analysis. The study however did reliably differentiate, using texture analysis, between four grades of foam. By simply visually inspecting the MR images of foam different porosities of foam were deemed indistinguishable.

A study on texture analysis of the human liver by Daniel Jirak et al [66] recognised that many features can be applied for texture analysis, programs such as MaZda [67] used in this study produces 256 features, but not all carry information necessary for successful texture classification [66]. The subjects examined consisted of 43 patients with liver cirrhosis of various etiology. Within the study methods were used to distinguish the features that would be useful for the study, in conclusion the results showed successful use of texture analysis for the separation of cirrhotic patients and healthy volunteers, the study also found that a combination of features significantly improves texture analysis' ability in confirming the

classification of the subjects. The authors hypothesise training a higher number of patient and control sets will improve the classification power of texture analysis which can be useful for detecting early and mild cirrhosis.

Mathias et al applied texture analysis to the spinal cord in an attempt to quantify pathological changes that occur in multiple sclerosis (MS) [68]. The results using the co-occurrence method with MR images of the spinal cord for 10 control subjects (healthy volunteers) and 40 patients with clinically definite MS demonstrated that significant differences existed in texture between normal controls and MS patients. The texture differences seen indicated that texture features can detect changes in pathology early in the disease, before the occurrence of spinal cord atrophy. The results also revealed significant correlation between texture and disability. The results showed an increase in variance grey level, mean gradient, and mean entropy, as well as a decrease in mean angular second moment, in MS patients. This suggests that spinal cords in MS are less homogeneous and more complex than in normal healthy volunteers [68].

Marius Mayerhoefer et al performed texture analysis on knee joints in a multicenter study of 63 patients [69]. Texture analysis was performed with the software package MaZda [67], the results showed that despite texture information differences among MR images from different centres, feature sets were able to be used from one centre for successful tissue discrimination in data from other centres, which is important within future clinical applications. It was found at one of its 3 centres the best discriminative texture analysis feature was based on wavelet transform, in addition the feature selection method the study used identified a single feature that was present in the top 10 features of all 3 centres , which was derived from wavelet transform.

Yao J [70] looked at breast tumour analysis in DCE MRI using texture features and wavelet transform and concluded that both are useful tools in breast tissue classification using DCE-MRI.

The spatial grey-level dependence matrix method, as proposed by Haralick [53], appears to be the commonest form of analysis for texture, but there is no direct evidence concerning the most appropriate pixel separation and number of grey levels to utilise in the required co-occurrence matrix calculations. One of the aims of this PhD study is to systematically assess the efficacy of DCE-MRI based textural analysis in predicting response to chemotherapy in a cohort of breast cancer patients.

2.6.5 Shape in MRI

Unlike in texture analysis where the most commonly used statistical technique due to its ability to study the 2nd order statistics of pixels at different spacings and angles is the Haralick model [53], the most appropriate shape/geometry features are not as clear cut and there exist various ways of calculating mathematically the geometry of a given shape or lesion, from traditional means like circularity to features such as moment analysis. Neha Bhooshan et al [46] used shape (geometric) analysis along with other computerised methods such as texture and kinetic features on DCE-MRI breast lesions in an attempt to make use of them as prognostic markers. The shape features included; size (lesion volume, in cubic millimetres), circularity (conformity of lesion to circular shape), irregularity (deviation of 3D lesion surface from sphere surface), margin sharpness (mean image gradient at lesion margin), variance in margin sharpness (variance in image gradient at lesion margin) and variance in radial gradient histogram (how well enhancing structures in a lesion extend in a radial pattern originating from centre of lesion).

The study found that in terms of shape features ductal carcinoma in situ (DCIS) lesions are generally non-mass like with enhancement being in a linear fashion as opposed to invasive ductal carcinoma (IDC) and benign lesions being mass-like. The circularity feature proved to be an effective way of classifying IDC versus DCIS lesion. The study also recognised that DCIS can appear to be mass-like enhancement; thus in their analysis both morphological and kinetic features were used for classification purposes.

Agner et al [45] has also looked at shape features and concluded that, due to the increases in specificity, sensitivity and AUC when combining texture features with shape/morphological features, the pairing of morphology and signal intensity kinetic features with lesion attributes such as texture kinetics could result in improved diagnostic of breast cancer on breast DCE-MRI [45]. According to BIRADS lexicon descriptors [23] for mass-like lesions there are two important lesion descriptors; lesion shape (for example round, oval, lobular, and irregular) and

lesion margin (for example smooth, irregular, and spiculated). This study [45] looks at six different quantitative descriptors modelled on the BI-RADS attributes- the area overlap ratio (measure of lesion roundness), normalised average radial distance ratio, standard deviation of normalised distance ratio, variance of distance ratio, compactness and smoothness. All of the descriptors with the exception of area overlap ratio being descriptors for quantifying irregularity of the lesion boundary.

SInha et al [50] looked at a multi-feature study of Gd-enhanced MR images of the breast, utilising some shape features reporting some significant differences between benign and malignant lesions in the breast. The features used within this study included compactness, entropy, bending energy, and ratio of minimum to maximum radial length.

2.6.6 Shape in non-MRI Breast

Wei Yang et al [71] looked at shape symmetry of breast tumours on ultrasound images. Five shape reflective symmetry measures were investigated with the aim of distinguishing benign and malignant lesions. Results showed that reflective symmetry (RMSL) was significantly different between benign and malignant tumours, RMSL was computed directly from the binary mask image, this paper also refers to various other symmetry calculation methods such as that by Zabrodsky et al which defines symmetry distance (SD) as “a quantifier of the minimum ‘effort’ required to transform a given shape into a symmetric shape. This ‘effort’ is measured by the mean of the square distances each point is moved from its location in the original shape to its location in the symmetric shape” [72].

A study by Toshiro Yokoyama et al [73], looked at irregularity of cluster shape in cytological diagnosis of breast tumours, although the study is beyond the capabilities of this thesis as it involves the extraction of cell cluster specimens of breast tumours by fine-needle aspiration (FNA), nevertheless the shape analysis features maybe something worth considering by applying the shape analysis techniques to the ROI within MR images of breast lesions. The study looked at the following shape parameters (some of which have been applied in previous

MR studies) cluster area, circumference, maximal length, maximal breadth, cluster roundness, cluster size, edge and distribution image fractal dimensions for cluster analysis (which the study used to evaluate the irregularity in the cell cluster shape and determine the correlation to cluster size).

The results of the study demonstrated differences in the irregularity of the cluster shape between fibroadenoma (FA) and invasive ductal carcinoma (IDC) with weak cellular atypia, the study also revealed important factors indicative of malignancy such as cell overlap, cell adhesion, and irregular nucleus shape [73].

Mohamed Eisa et al [74] studied the classification of breast masses by applying moments to mammograms combined with texture features to improve retrieval performance. The main aim of the work was to present a Content Based image retrieval (CBIR) approach, which is a method of managing databases and effectively retrieving images using descriptions of the image content, the study investigated and applied a content based image retrieval system to a domain of medical images. Images were characterised by a set of geometric moment invariants which are independent to translation, scale, rotation and contrast and some texture features, retrieval was then based on similar images existing within the database [74]. Table 2.2 outlines the evaluation results of the study, showing that overall performance of all methods was very similar.

The Algorithms	Precision %	Recall %
textures	61.32	59.01
moments	63.84	62.75
Textures & moments	66.03	64.23

Table 2.2 [74]: evaluation results, the overall performance of all methods is very similar with the texture and moments algorithm performing best.

The geometric moments features extracted in the study [74] were central moments, mass and area, centre of mass (the point where all the mass of the image could be concentrated without the changing of the image about any axis), orientations, projections and moment invariants.

In addition mammogram texture features were extracted from the masses, shape and texture features being the basis of mass detection [74], these were mass area (concerned with the pixels inside the region of mass), mass perimeter length (the total length of the mass edge), compactness (a measure of contour complexity versus enclosed area, high compactness values represent a mass with a rough contour, lower values represent mass with a smooth contour), normalised radial length (the normalised sum of the Euclidean distances from the mass centre to each of the boundary coordinates), minimum and maximum axis (minimum axis of a mass is a measure of the smallest distance connecting one point on a border to another through the centre of mass, the maximum axis of a mass is a measure of the largest distance connecting one point on a border to another through the centre of mass), average boundary roughness, mean and standard deviation of the normalised radial length, eccentricity (the length of a ROI, if the value is close to 1 the ROI is almost circular, values close to zero represent more stretched ROIs), roughness, average mass boundary.

2.7 Image Analysis Applications

This section aims to outline some of the various image analysis applications available that allow users to perform morphology, including texture and shape analysis. There are various systems that are available such as MaZda and Fiji [67, 75] and studies in the past have made use of these [66, 69]. In other studies authors have chosen to program their own applications using various programming environments [48].

Whichever route is taken all image processing applications that aim to provide texture information be it on medical images or satellite and aerial images of sceneries and objects, the parameters used for analysis tend to be the same. Most studies looking at texture analysis for example utilise some of the 14 texture parameters originating from Haralicks original study from 1973 [53], for shape analysis there are various descriptors some more common than others. Although the various systems share some of the same analysis output, often the method of deriving the texture properties can differ, i.e. some systems may use different

algorithms or image transformation techniques therefore the end results can differ from system to system which can be vital especially when looking for subtle changes in texture. This is the reason why some researchers prefer to write their own applications from scratch so they can apply formulas and image formatting/enhancement techniques such as histogram equalisation in different ways or using alternative methods which may suit their research area more appropriately rather than using an off the shelf software package such as MaZda [67]. Another option available to authors is making use of open source applications such as Fiji that allow a user full access to code giving the option to amend the underlying code/formulas used to derive calculations. The options available as discussed are packages such as MaZda [67] and Fiji [75] but Fiji's not really well known for texture analysis and none of the studies discussed in this chapter mention any use of it. MaZda is more widely adopted but does not compute all Haralick's parameters and although it has some options for changing the number of grey levels it's not unlimited as can be done if the decision is made to write your own texture analysis code in environments such as Matlab, which have built in functions and toolboxes to aid texture analysis [76]. The plug-in modules available in Fiji do not allow you to have accurate ROI representation as, although you use a pencil like pointer to draw the ROI, the Fiji application only interprets this as a rectangle [77]. Matlab is a matrices based programming language and computationally its performance is incomparable when dealing with complex image datasets such as Dicom. Fiji is a java based environment, and is also known for high performance applications especially in the mobile games industry, the large open community in Fiji means lots of free code has already been written for anyone to use and customise as has indeed been done for the purpose of texture analysis. Trying to understand and modify complex code can be a daunting task even for the most experienced software developer. From a research point of view you would want to apply the algorithms you believe are known best methods, sometimes the only option would be writing your own code from scratch. Aside from the mathematical differences in algorithms there are other differences for example Fiji will only allow 8 bit images, while in Matlab you can apply texture analysis to 16 bit images. Mazda

only runs on windows, while Matlab code can be recompiled into Mac, Windows or Unix. The argument for advantages and disadvantages can go on, ultimately it can boil down to simple personal preference to determine which method is used.

3 Software

3.1 Introduction

Before embarking on the development of the software required for this thesis it was decided that proper planning and documentation according to normal software development practices should be adhered to in an attempt to make the final software robust and easy to modify in the future. With the author being from a Computer Science background it was felt the most appropriate way to relay this information to the reader was by adhering to the software lifecycle as followed by industry standards. This document therefore contains information and planning that was required before the development of the final product including a detailed user manual which was written once the package was complete. The chapter aims to provide information on the software lifecycle stages applied in the development of the DicomReader software, in short this document will summarise the different stages of the software development from requirements through to testing.

3.1.1 Requirements Analysis

Development of a software package capable of analysing both single slice 2D data and multiple slice 2D data. Textural analysis will be implemented using Haralick parameters calculated from co-occurrence matrices. The software will be capable of varying the degree of grey level decimation. The software will also be required to have the ability to run wavelet transform analysis as well as shape analysis. Conventional first order histogram features (e.g. mean, and standard deviation) will also be calculated for comparison.

The application will be displayed to the user in the form of a simple to use Graphical User Interface (GUI) and will read in images in DICOM format. The application will read in large datasets often containing over 1800 images therefore the design should allow the application to process large amounts of data efficiently. The application will also read in binary files containing regions of interest (ROIs) pre drawn and calculate texture analysis on the corresponding image slice.

In addition the application will allow the user to step through each slice and phase and adjust contrast and brightness levels. As well as loading pre-drawn files containing ROIs the user will also be able to draw, using a pen like tool, new ROIs and calculate texture properties of the region drawn, all of which will be output to a spreadsheet.

The application will allow the user to employ histogram equalisation on the pre-drawn and hand drawn ROIs. There will then be an option to choose whether the texture analysis is to be performed on the histogram equalised version of the ROI or the non histogram equalised ROI.

Texture mapping will also be available in the application. This will take each pixel at a time and texture analysis of the 16 parameters will be performed in each pixel value of any given image. As with the texture analysis the option will be there to histogram equalise (the full image) before performing texture analysis, and the number of grey levels will also be adjustable. In addition each pixel's surrounding pixel area matrix will be user defined. The results will be saved in an image file showing 1 map per texture parameter (f_1, f_2 ... f_{16}). In addition the histogram of a texture mapped image can be viewed as this can aid in the threshold values used when using a hotspot search facility which will highlight suspected lesions or areas of interest.

Shape analysis facility of the software will allow the user to analyse a set of shape parameters on a given ROI, most of the calculations will not require pixel values to be taken into account as the shape of the region is the only input required but some of the calculations may require image intensity values as part of the shape calculation formulas.

Wavelet transform analysis function will be contained in the software, the wavelet transform will allow the frequency of the signals and the time associated with those frequencies in an image to be analysed, the software will output energy levels that will be calculated from the wavelet coefficients using the Haar method of wavelets calculation. As the Matlab environment along with the wavelets toolbox already contains a package for calculating

wavelet coefficients for Haar the only remaining section that will need to be coded is extracting energy levels from the generated wavelet coefficients.

As there will be a large number of mathematical calculations the application will be continuously unit tested against the design specification to verify the implementation of the formulae.

3.1.2 Design Specification

This section outlines the class and use case diagrams for the proposed software system.

3.1.2.1 Class Diagram

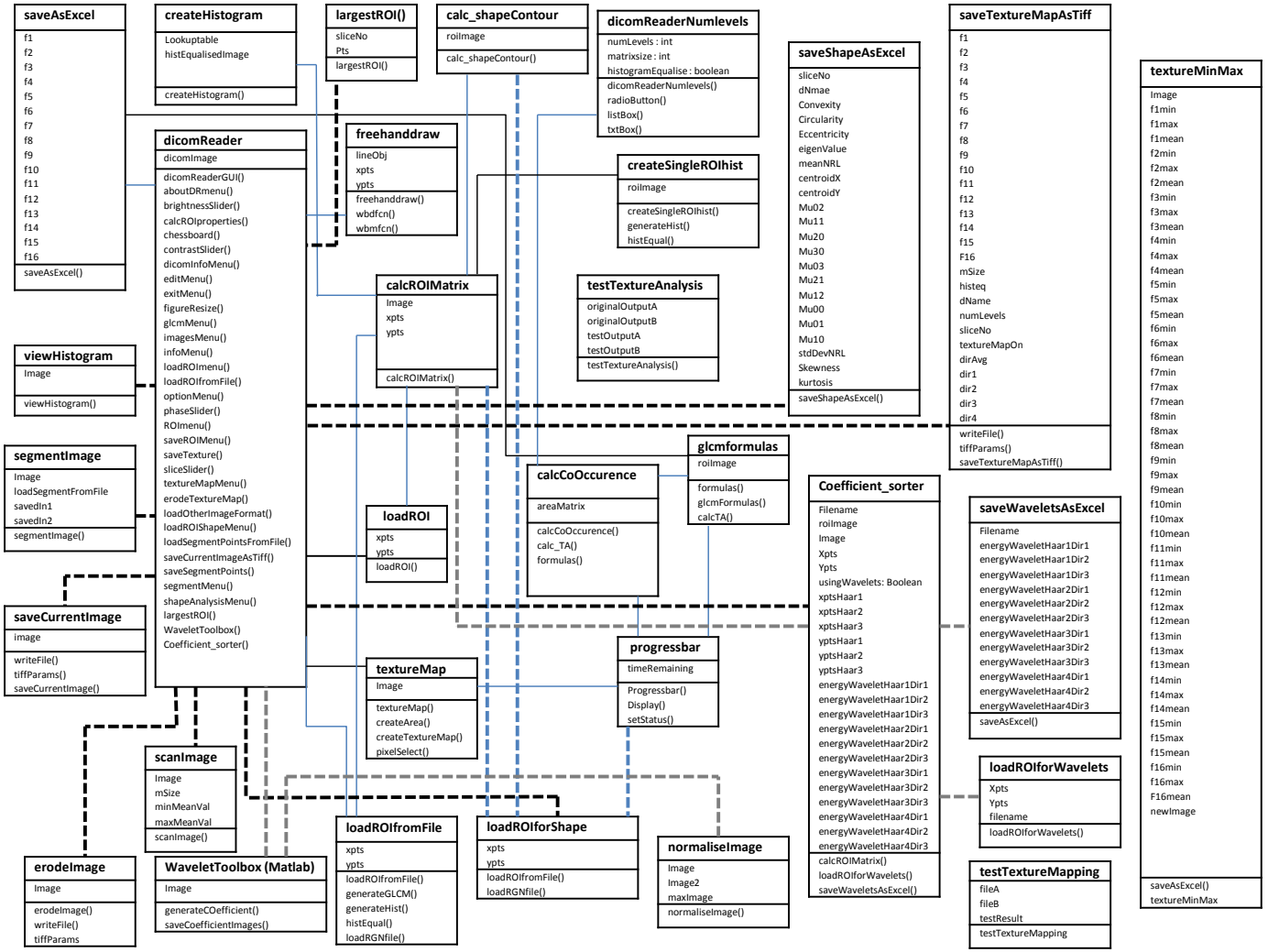

3.1.2.2 Use case Diagram

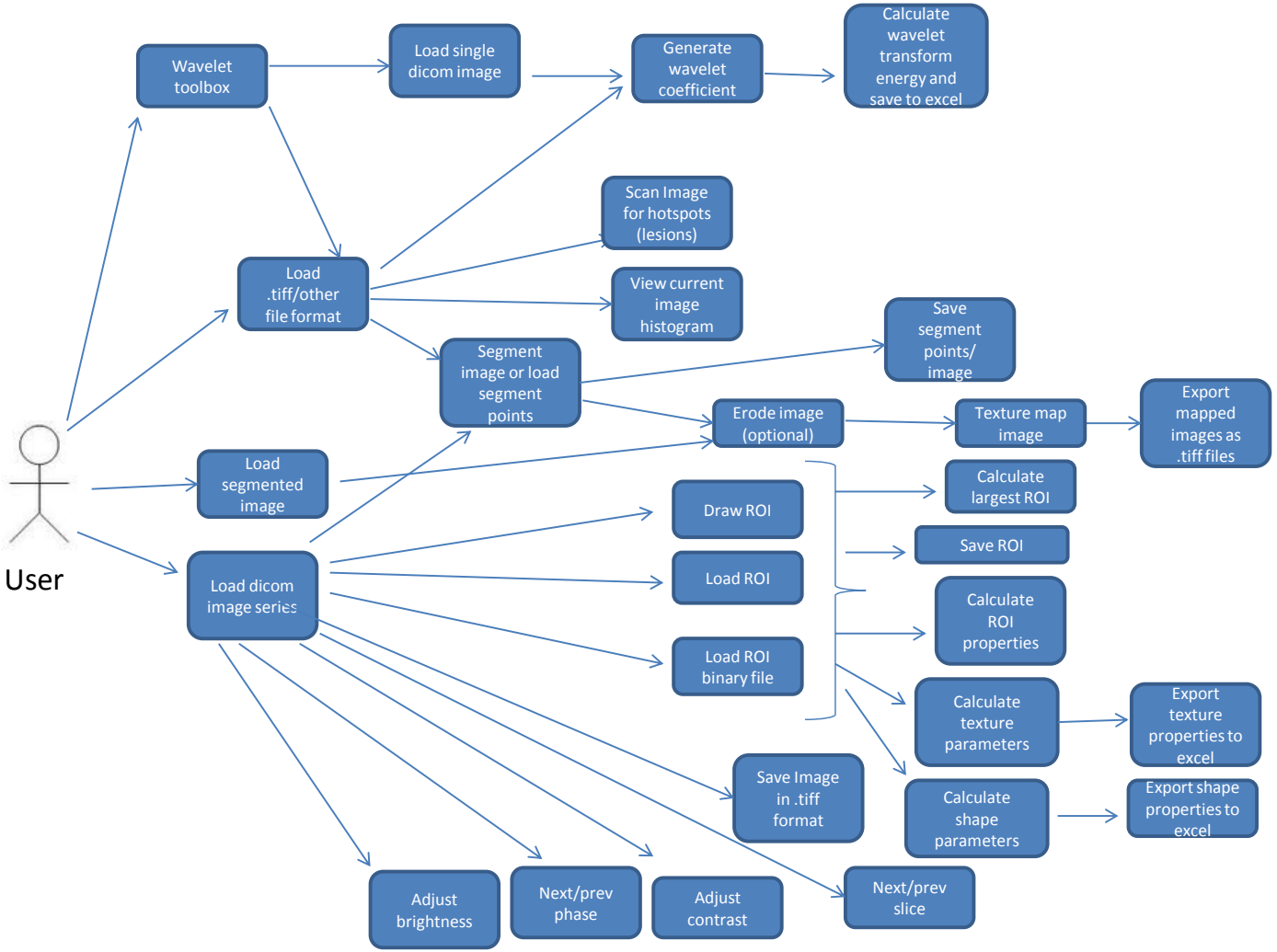

3.2 Texture Analysis

The application will be coded using Matlab as the language of choice as Matlab is a matrices based language and is already widely used in the medical research industry for analysing image data.

3.2.1 Load Dicom Image dataset

The application shall allow the user via a GUI to select a dataset containing a large number of images in DICOM format; these images are then displayed to the user. By pointing to the directory containing all the images the application will load only one image at a time as loading the whole dataset which can contain over 1800 images would be a real issue for performance.

Sample code: `k=1;`

```
for j=1:k
        str_j=num2str(j);
        file=strcat(str_j);
        file_path=strcat(dname,'\IM',file);
         info = dicominfo(file_path);
         I = dicomread(info);
end
imshow(I,'DisplayRange',[]);
```

3.2.2 Slice slider control

A slider control will be available once an image has been displayed which will allow the user to scroll through the various slices in the loaded dataset. When the slice slider is adjusted the corresponding slice is displayed to the user and the phase slider synchronises accordingly. To the top of the slider numerical values are to be displayed indicating the current slice number. To be implemented using Matlab's slider GUI.

3.2.3 Phase slider control

A phase slider control will be available once an image is displayed. The user is able to scroll through the different phases in the loaded dataset. When the phase slider is adjusted the corresponding slice is displayed to the user and the slice slider synchronises accordingly. To the

top of the slider numerical values are to be displayed indicating the current phase number. To be implemented using Matlab's slider GUI.

3.2.4 Contrast slider control

A contrast slider control will be added to allow the user to adjust the contrast of the image. It is important to note that any analysis done on the image will work on the original image and not the one that is displayed to the user with the adjusted contrast via the slider, therefore it is vital that the contrast of the original image is maintained in memory.

```
for i=contrast_setting:contrast_setting

      contrast_setting = contrast_setting + 0.01;
      if contrast_setting > 1
         contrast_setting = 1.0;
      end
       J = imadjust(I,stretchlim(I),[0 contrast_setting]);

  end
imshow(J); %show image J as we need to retain image I in its original
form for purpose of analysing ROI etc
```

3.2.5 Brightness slider control

A brightness slider control will be added to allow the user to adjust the brightness of the image. It is important to note that any analysis done on the image will work on the original image and not the one that is displayed to the user with the adjusted brightness via the slider, therefore it is vital that the brightness of the original image is maintained in memory.

```
  if brightness_setting > 1.0
         brightness_setting = 1.0;
      end
      if brightness_setting < -1.0
         brightness_setting = -1.0;
      end
      %maintain contrast -
  J = imadjust(I,stretchlim(I),[0 contrast_setting]);
imshow(J);
```

3.2.6 Dicom Information

When selected the Dicom header information/data about the current file shall be displayed to the user.

3.2.7 Draw Region of Interest (ROI)

A freehand draw tool will be available to draw onto any loaded image, this will be similar to the freehand pen like function in such applications as paint. The x and y points will need to be stored in memory so that ROI based calculations can be performed.

3.2.8 Save ROI

A save function will allow the user to save the current ROI drawn on screen as a Matlab file.

3.2.9 Load ROI

A load function will allow the user to load a previously saved ROI on any given image.

3.2.10 Calculate ROI properties

Once the ROI is drawn the program will output the mean and standard deviation values to the user and these values will be stored in Matlab's memory to be used for further calculations

```
[J,temp] = roifill(I, xpts, ypts);
 pts = sum(temp(:)); %no of entries ie 1's in ROI
roi = uint16(temp).*uint16(I); %creates roi as part of I, roi is all
entries ????
%roiImage is the image showing null values as NaNs
roiImage = double(roi).*(0./double(temp) + 1); %divide using 0 get the
NaN(null)values and add 1 shows non null from null values
sumRoiImage = sum(roiImage(~isnan(roiImage))); %sum of non null values
npts = sum(temp(:)); %number of(qty)of values
mean = sumRoiImage/npts; %calculates mean

% calc standard deviation
a = (roiImage - mean);

a2 = a.*a;
b = sum(a2(~isnan(a2)));% sum all values that are not nan
c = b/(pts-1);
sd = sqrt(c);
```

3.2.11 Calculate TA

When selected this will calculate 16 texture analysis parameters on the current ROI using the formulas below (detailed formulas can be found in chapter 5).

$$\sum_{i}\sum_{j} p(i,j)^2$$

(f_1 Angular Second Moment)

$$\sum_{n=0}^{N-1} n^2\, p_{x-y}(n)$$

(f_2 Contrast)

$$\frac{\sum_i \sum_j (ij)p(i,j) - \mu_x^2}{\alpha_x^2}$$

(f_3 Correlation)

$$\sum_{i} p(i-\mu_x)^2\, p_x(i)$$

(f_4 Variance)

$$\sum_{i}\sum_{j} \frac{1}{1+(i-j)^2} p(i,j)$$

(f_5 Inverse Difference Moment)

$$\sum_{n=2}^{2N} n\, p_{x+y}(n)$$

(f_6 Sum Average)

$$\sum_{n=2}^{2N} (n-f_6)^2\, p_{x+y}(n)$$

(f_7 Sum Variance)

$$-\sum_{n=2}^{2N} p_{x+y}(n) \log\left(p_{x+y}(n)\right)$$

(f_8 Sum Entropy)

$$-\sum_{i}\sum_{j} p(i,j) \log\left(p(i,j)\right)$$

(f_9 Entropy)

$$\sum_{n=0}^{N-1} (n-\mu_{x-y})^2 p_{x-y}(n)$$

(f_{10} Difference Variance)

$$-\sum_{n=0}^{N-1} p_{x-y}(n) \log\left(p_{x-y}(n)\right)$$

(f_{11} Difference Entropy)

$$\frac{f_9 + \sum_i \sum_j p(i,j) \log\left(p_x(i) p_x(j)\right)}{-\sum_i p_x(i) \log\left(p_x(i)\right)}$$

(f_{12} Information Measure of Correlation 1)

$$\sqrt{1 - e^{-2(H_{xy} - f_9)}}$$

(f_{13} Information Measure of Correlation 2)

$$\sqrt{\text{Second largest eigenvalue of } Q}$$

(f_{14} Maximal Correlation Coefficient)

$$\sum_{i}\sum_{j} (i + j - \mu_x - \mu_y)^3 p(i,j)$$

(f_{15} Cluster Shade)

$$\sum_{i}\sum_{j} (i + j - \mu_x - \mu_y)^4 p(i,j)$$

(f_{16} Cluster Prominence)

3.2.12 Load ROI data from binary file and calculate Texture Analysis(TA)

Given a dataset of Dicom images a file in binary format containing many pre drawn ROI coordinates and Image slice number that each set of coordinates corresponds to. This file will be read into the application and loaded onto the corresponding image/slice, the ROI in turn will be displayed to the user when the slice slider is moved to the appropriate slice.

```
dimWidth = double(info.Width);
dimHeight = double(info.Height);
dim = [dimWidth,dimHeight];
DIM = dim;
if (greyLevelCalc == true)
     fid = fopen(ROIFILEPATH, 'r');

else
[filename,pathname] = uigetfile('E:\Patient Data\*.rgn','Select ROI
File');
handles.Numlevels = dicomReaderNumlevels;
file1 = [pathname,filename];
ROIFILEPATH = file1;
fid = fopen(file1, 'r');
end
num_rois = fread(fid, 1, 'int16', 'b');

roi_slice = zeros(num_rois,1);
roi_pts = zeros(num_rois,1);
global num_rois I

glcmX = zeros(Numlevels, Numlevels, 4);
progress=0;
p=progressbar();
roiGreyLevels = 0;

for i = 1:num_rois

progress = progress + 1 / num_rois;

  roi_slice(i) = fread(fid, 1, 'int16', 'b');
    roi_pts(i) = fread(fid, 1, 'int16', 'b');
    data_pts = fread(fid, 2*roi_pts(i), 'float32', 'b');
    sliceNumber = roi_slice(i) +1;


    xpts = data_pts(1:2:end);
   ypts= dim(2) - data_pts(2:2:end);
    str_slice=num2str(int32(sliceNumber));
        file1=strcat(str_slice);
    file_path1=strcat(dname,'\IM',file1); %C:\....
         info = dicominfo(file_path1);
         I = dicomread(info);
        imshow(I,'DisplayRange',[]);
   line(xpts,ypts,'tag','tmpregsel');
```

3.2.13 Adjust Number of Grey levels

A pop up box will appear allowing the user to adjust the number of grey levels the concurrence matrix should be working to, this will have a default value with the ability for the user to change to the desired integer value.

3.2.14 Calculate Texture Properties

Once the ROI binary file is loaded the application will automatically calculate all the texture properties as in 'Calculate ROI properties' function, in this case texture analysis will be calculated on summed co-occurrence matrices of all ROIs.

3.2.15 Export TA properties to Excel

A pop up box will prompt the user to export the calculated TA properties to an excel spreadsheet and save the file to a location and name of choice. The spreadsheet will also contain additional information such as date/time of creation, mean and standard deviation of last image in dataset with a loaded ROI, as well as slice/phase numbers of the final image. In addition the same function will be available to the user to export to excel in the event that the user originally decided not to export and decides to export at a later time or decides to export TA properties to excel on a self drawn ROI.

```
[filename,pathname] = uiputfile('E:\Patient Data\TA\*.*','Save As:');
file = [pathname,filename];
  xlswrite(file, d, 'Texture Properties of ROI', 'A1')
```

3.2.16 Progress bar

Progress bar in command window to show remaining execution time and elapsed time.

3.2.17 Maximise Window

User can maximise the image by clicking the maximise windows icon in top right corner of display window, this will magnify the image and will aid the user to draw a ROI more accurately.

3.2.18 Exception handling

As the main user of the application will be the programmer himself the need for exception handling and error checking on the scale that would be required in a commercial project is not necessary. Therefore limited exception handling will be required such as warning the user when a correct file type is not selected. In addition all function menus that are not available to the user shall be greyed out to avoid the user clicking on these and the system subsequently throwing error.

3.2.19 Chessboard

A chessboard image will be loaded on activation of this function which will mainly be used to aid the user in testing purposes as the output values are easier to verify for a black and white image. This function shall remain in the application as it will aid in testing future enhancements to the software application.

3.2.20 Histogram Equalisation of ROI

The option will appear in the popup menu when a user selects to perform texture analysis either on pre-drawn ROIs or on an individual ROI. The user can select the ROI to be histogram equalised before the Haralick texture parameters are calculated. The inbuilt function of Matlab cannot be used as this will apply histogram equalisation to the whole image, therefore the following 2 functions will need to be created to do this appropriately:

```
function createHistogram

hgramSum = sum(hgramTotal);
% NORMALISES HISTOGRAM (EFFECTIVELY TURNS HISTOGRAM INTO PROBABILITY)
hgramNormalise = hgramTotal/hgramSum;
% CALCULATES CUMULATIVE NORMALISED HISTOGRAM (LAST VALUE SHOULD ALWAYS
BE
% 1)
hgramCum = cumsum(hgramNormalise);

% CREATES A LOOKUP TABLE
look_up = zeros(1,overallRoiMax+1);


% THE CLEVER BIT!
gry_lvl = 0;
```

```
% GOES THROUGH EACH IMAGE INTENSITY (O TO MAX - OFFSET BY 1) AND
CALUCLATES WHAT FINAL GREY LEVEL FOR THIS
% INTENSITY SHOULD BE
for i=1:overallRoiMax+1
% IF CUMULATIVE HISTOGRAM IS LESS THAN EG (0+1)/16 THEN ALL VALUES OF
I ARE GOING TO BE ASSIGNED GRY LEVEL O
    elseif hgramCum(i) <= (gry_lvl+1)/Numlevels
        look_up(i) = gry_lvl;
% WHEN CUMULATIVE HISTOGRAM IS LARGER THAN 1/16 THEN INCREASE FINAL
GREY LEVEL BY 1 AND ASSIGN FOR I
    else
        gry_lvl = gry_lvl+1;
        look_up(i) = gry_lvl;
    end
end


function generateHist()
hgram = zeros(1,overallRoiMax+1); %max value for all roi's

% CREATES HISTOGRAM OF ROI DATA

h=1;
 temp = double(temp);
 for x=1:DIM(1)
     for y=1:DIM(2)

        if (temp(x, y) ~= 0)
            hgram(roiImage(x,y)+1) = hgram(roiImage(x,y)+1)+1;
            h = h+1;
         end
     end
 end
hgramTotal = hgram + hgramTotal;

  createHistogram()% reuse the createHistogram function
end
function histEqual

% AFTER LOOK UP FILE CREATED NOW JUST GO THROUGH ROI IMAGE AND ASSIGN
APPROPRIATELY

for x=1:DIM(1)
    for y=1:DIM(2)
        if (temp(x,y) ~= 0)
            roiImage(x,y) = look_up(roiImage(x,y)+1)+1;
        else roiImage(x,y) = NaN;
        end
    end
end
```

3.2.21 Exit

When pressed the application will exit and clear all variables stored in memory.

3.3 Shape Analysis

3.3.1 load RGN and perform shape analysis

This feature will allow the user to perform shape analysis on the current set of images and the software will automatically pick the largest ROI in order to do the calculations. Results will be saved in a spreadsheet. In cases where the ROI appears multifocal on any slice the coding needs to take into account and eliminate any minor ROI clusters and only take the main region area ie the one with the most pixels.

The following shape parameters need to be calculated when this function is run (more details on these parameters can be found in chapter 6)

Mean Normalised Radial Length, StdevNRL, skewnessNRL, kurtosisNRL, Convexity and Circularity, also for Moments: μ_{02}, μ_{11}, μ_{20}, μ_{30}, μ_{03}, μ_{21}, μ_{12}, μ_{00}, μ_{01}, μ_{10}, Eigenvalue and Eccentricity.

It is important that the correct ROI is mapped onto the corresponding slice as some of the above moments calculations also take into account the pixel intensity values and not just the shape of the ROI.

3.4 Texture Mapping

For this a function will be created that will loop through any given dicom image and perform the co-occurrence calculations on each pixel. The co-occurrence matrices are calculated using surrounding pixels and it will be up to the user as to how many surrounding pixels the calculations will allow, this will be customisable to the user via the same popup menu that allows input of number of grey levels and if the calculation is to be histogram equalised or not. The user can input any number (odd number) ie 3x3, 5x5 and so on. For example selecting matrix size 5 will create a 5x5 matrix with the pixel in question being the centre pixel, once this is calculated for each pixel in the image and for each of the 16 parameters the application will

output 16 image files one for each parameter. The outer most pixels will need to be padded according to the matrix size otherwise there will be null entries.

```
%loop through the matrix selecting each pixel at a time
    function pixelSelect(paddedI)
        sizeRow = size(paddedI,1);
        sizeColumn = size(paddedI,2);
for i=mSizeValue+1:sizeRow -mSizeValue
    progress = progress + 1 / sizeRow;
    for j = mSizeValue+1:sizeColumn - mSizeValue
       paddedI(i,j) ;
       createArea(i,j)%run createArea function with i and j as input
    end
```

3.4.1 segment Image

This function will be used to segment the image for example from nipple to chest wall prior to performing texture mapping, the user should be able to select the start and end points of where the image is to be segmented

3.4.2 save segment points

The segment points should be saved in a Matlab file.

3.4.3 load segment points from file

This function will allow the saved segment points to be loaded onto any given image

3.4.4 save segmented image

The segmented image should be saved as a tiff file using this function

3.4.5 erode and save texture map

This function will allow erosion techniques to be applied to the segmented image in order to further eliminate chest wall border pixels

3.4.6 view histogram for current image

This function will display the histogram of the current image to the user. The user can then employ the Matlab built in tools to obtain pixel values from the histogram

3.4.7 scan Image for hotspots

This function will allow the user to enter min and max (range) pixel values with a specified matrix size that will take the average of each pixel area (of matrix size) and check if it is within the range specified and if it is the display will highlight these areas on the current image.

3.5 Wavelet Analysis

This function will allow the user to perform wavelet analysis based on a previously saved ROI file. A file menu option will be available in the tools section which the user can select and thus open up the Wavelet Matlab toolbox. This function for calculating coefficient values uses a built in Matlab toolbox so no coding is needed for this part. In order to process the energy efficient values a coefficient sorter class will be required which will extract the wavelet energy values once the user has selected the relevant ROI and previously saved coefficient file. These values will then be saved into an excel spreadsheet. The coefficient sorter class will only need to deal with wavelet coefficient files generated using wavelet type Haar down to level 4 (see wavelet section, chapter 5.4) as for the purpose of this research this is the only setting that will be used.

3.5.1 Wavelet toolbox

User will have the ability to open the wavelet toolbox using the sub menu in the tools section of the dicomreader software main GUI.

3.5.2 Coefficient sorter

This class will require a GUI menu in the main dicomreader interface and will run when the user selects 'load coefficient file and calculate wavelet energy' function from the tools menu under the wavelets sub menu. The user will be prompted to select a coefficient file (this will be generated using Matlabs wavelet toolbox) and the corresponding ROI file. The calculated values will be saved in an excel spreadsheet and the user will be prompted when file is saved and its location displayed in the Matlab command window.

In order to correctly read the coefficient files code similar to the following may be executed:

```
% Import the file
%newData1 = load('-mat', fileToRead1);
newData1 = load(fileToRead1);

% Create new variables in the base workspace from those fields.
vars = fieldnames(newData1);
for i = 1:length(vars)
    assignin('base', vars{i}, newData1.(vars{i}));
end

% Extract coefficent and size data from current workspace
coefs1D = evalin('base', 'coefs');
coef_size = evalin('base', 'sizes');
wave_type = evalin('base', 'wname');

% Number of levels calculated
b = size(coef_size);
num_levels = b(1) - 2;

% Create dummy output array for numbering purposes
v = genvarname(wave_type, who);
T = evalc([v ' = num_levels']);

% Turn coefficient file into appropriate 2D array
for k=num_levels:-1:1
    clear temp_array;
    temp_array = zeros(coef_size(k+1,1),coef_size(k+1,2),3);
    for w_dirn=1:3
        for y=1:coef_size(k+1)
            for x=1:coef_size(k+1)
                temp_array(x,y,w_dirn) =
coefs1D(w_dirn*coef_size(k+1,1)*coef_size(k+1,2) + x + (y-
1)*coef_size(k+1,1));
            end
        end
    end
    v = genvarname(wave_type, who);
    T = evalc([v ' = temp_array']);
end
```

As each image for each Haar level is smaller in size the calcROIMatrix() function will be utilised and code will be needed to shrink the ROI loaded to the correct scale for the appropriate Haar level. The following code is an example of how this may be done, for Haar level 1:

```
%for haar 1
for j = 1:3 % ie all 3 directions
  I = (haar1(:,:,j));%put this in here so can use for ROI into
calcROIMatrix
 xpts = xptsHaar1;%change xpts and ypts values so can be used in
calcROIMatrix to generate new ROI
ypts = yptsHaar1;
calcROIMatrix(); % run this before each Haar level to get the new roi
(ie shrunk for each wavlelet haar level)
```

```
%this section of code is merely to visualise the changes not needed
for actual calc but good for testing purposes
 imshow(I,'DisplayRange',[])%display the current image, probably dont
need to but goo dway to check if ROI is correct
line(xpts,ypts,'tag','tmpregsel','Color',[1 0 0],
'LineWidth',1.2);%line color red

 %haar1_dir = (haar1(:,:,j)); %direction 1 - 3
haar1_dir = roiImage; %name it haar1_dir as it helps rename further
down this code??
 squared_haar1 = haar1_dir.*haar1_dir; %takes each pixel in matrix and
multiplied by iteself ie squared saves doing all the code below
%      sumhaar1 = (dir(i).*dir(i)) + sumhaar1; %sum of each pixel
squared as per formula from mazda user manual for  wavelet energy

 %energyWavelet =
(sum(sum(squared_haar1)))/(size(haar1,1)*size(haar1,1)); %divide by
total no. of pixels ie size of column * size of column
pixels = ~isnan(haar1_dir);
 pixelsSum = sum(pixels(:));

  squared_haar1(isnan(squared_haar1)) = 0; %replace all NaN in matrix
values with a 0
 energyWavelet = (sum(sum(squared_haar1)))/(pixelsSum); %divide by
total no. of pixels
 %this bit of code will create variable names according to direction
ie take j as part of var name
 varname = strcat('energyWaveletHaar1Dir' ,num2str(j));
 eval( [ sprintf(varname) '=energyWavelet'] )

end
```

3.5.3 Normalise Image

A function allowing the image to be normalised will be available in the form of normaliseImage class, this will be similar to the following:

```
I = dicomread('C:\PhD Data\neoadjuvantData\PC_2min\E08429\IM28');%
example image
maxI = max(I(:));
I2 = double(I)./double(maxI).*255;
```

3.6 Testing

Testing as with any piece of software played a crucial part in the development of this software. Testing and retesting was done at every stage, largely due to the fact that complex formulas were being applied and matrix models being created right from the start which all had to be verified for correctness as any error would mean the next stage of calculation would be incorrect.

As a means of testing for correct mean and standard deviation values of a drawn ROI the chessboard example was used. An ROI was drawn on a chessboard and the expected output was tested against the actual, expected output which was calculated manually without the use of any software and this was used as 'expected output' once it was determined that it was mathematically correct. For the main application itself again a set of data was used that had already had its texture properties calculated manually. A unit test table below shows the testing procedure.

Some of the tests were automated in the sense that certain matrices were coded to display in the command window of Matlab so that the output could be compared to the expected output. Once testing had passed these features where disabled. In actual fact all unit testing was done manually as this was seen as a sufficient method of testing for this project. The results of the final unit test can be seen below:-

Unit Test No.	Test Description	Procedure/Input	Expected Output	Actual Output	Pass/Fail
1	Test for correctness of mean and standard deviation values.	1)Load software application 2)from file menu navigate to the 'load chessboard' menu option 3)from 'Tools' menu select 'Draw ROI' option 4)using the mouse draw a ROI that covers approximately 2 full black squares, 2 white squares and part of(1 pixel) of each black and white square above and 1 pixel of each box to the right 5)from the 'Tools' menu select the 'calculate ROI properties' option	Mean value: 128.117 Standard Deviation Value: 127.058	Mean value: 128.117 Standard Deviation Value: 127.058 See screenshot 1a	Pass
2	Load image dataset	1)From file menu select 'load image dataset' 2)point to directory where dataset is saved	Image 1 of whole series is loaded	Image 1 of whole series is loaded	Pass
3	Load .rgn file	1)From file menu select 'load image dataset' and load set of images with rgn file E04506_roi.rgn 2)from file menu select 'load .RGN file and perform TA' option 3)point to corresponding RGN file 'E04506_roi.rgn' 4)when prompted enter Numlevels as default of 16 in pop up box	1)final ROI is shown on slice 72, phase 1 2)results as per spreadsheet 1b	1)final ROI is shown on slice 72, phase 1 2)results as per spreadsheet 1b	Pass
4	Check for correctness of glcm and normalise matrices	1)In debug mode put break points so that all outputs of each ROI GLCM matrix is output, as well final GLCM values and matrix for each normalisation 2)follow steps as per unit test 3)	1)for purpose of this document only ROI number 1 is shown, see screen shots 1c), 1d) and 1e)	Screenshots 1c), 1d) and 1e)	Pass
5	Validate final output	1)follow steps as per unit test 3)	1)Values as per screenshot 1b)	1)values as per screenshot 1b)	Pass
6	Save ROI as .met file	1)from file menu select 'save ROI as .mat file' 2)select directory and file name	1).mat file saved	1).mat file saved	Pass
7	Load ROI from .mat file	1)from file menu select 'load ROI from .mat file' 2)select directory and file name	1).mat file saved and ROI displayed on current image	1).mat file saved and ROI displayed on current image	Pass
8	Slice slider	1)follow steps as per unit test 2) 2)move the slice slider	1)moves to previous/next image in dataset	1)moves to previous/next image in dataset	Pass
9	Phase slider	1)follow steps as per unit test 2) 2)move the phase slider	1)moves to previous/next phase in dataset	1)moves to previous/next phase in dataset	Pass
10	Contrast slider	1)follow steps as per unit test 2) 2)adjust contrast slider	Contrast adjusts up/down	brightness adjusts up/down	Pass
11	Brightness slider	1)follow steps as per unit test 2) 2)adjust brightness slider	Brightness adjusts up/down	brightness adjusts up/down	Pass
12	System exit	Go to File menu and select 'exit'	Application closes	Application closes	Pass
13	Dicom information	Go to Info menu and select 'Dicom Information' option	Dicom info displayed in command window	Dicom info displayed in command window	Pass
14	Progress bar	1)follow steps as per unit test 3)	Progress bar displayed in command to show time remaining for current execution	Progress bar displayed in command to show time remaining for current execution	Pass
15	Greyed out menus	1)load application	All menus greyed out except 'Load image dataset' and 'load chessboard'	All menus greyed out except 'Load image dataset' and 'load chessboard'	Pass

16	Enable menus	1)draw ROI as per unit test 1)	'Calc ROI properties' menu now enable	'Calc ROI properties' menu now enable	Pass
17	Texture analysis	Using the DicomReader software GUI 1)Run texture analysis on the test data located in folder \TEST FILES\TextureAnalysis using 16 grey levels and histogram equalisation 2) Run texture analysis on the test data located in folder \TEST FILES\TextureAnalysis using 16 grey levels and NON histogram equalisation 3) open the file testTextureAnalysis.m in MATLAB and amend so it points to the appropriate files where the original files are pointing to TESTEDhisteq16g.xls and TESTEDnonHisteq16g and the files to be tested are the excel files just saved as output	Both histogram equalised and non histogram equalised tests show 'pass' markers in Matlab command window	Both tests show 'pass' output	Pass
18	Shape analysis	Run shape analysis on the square and circle ROIs by loading onto the images used in test files (see user manual if help needed on how to perform shape analysis) contained in the folder TA_Application\TEST FILES\shape Compare the output of all shape parameters with the output files contained in TA_Application\TEST FILES\shape folder Visually examine to see if parameters in test file match the newly generated files	Shape analysis output files match the output files in TA_Application\TEST FILES\shape folder for square and circle ROIs	Files match	Pass
19	Texture mapping	Using the DicomReader software GUI Run texture mapping on the brick image from brodatz and test for each direction coocurrence matrix using 16 grey levels and histogram equalisation. Then open the testTextureMapping.m in MATLAB and point the files for testing ie A = mapped files just created and B= test files located in TA_Application\TEST FILES\TextureMapping\histeq16GreyTESTED	Output = 1 showing test has passed and both files match	Output = 1	Pass
20	Load single image (non dicom format) example .tiff files	1)Using the DicomReader GUI software: 2)Go to File menu > load single image 3)Point to any non dicom image for example an image with the .tiff format	Image is displayed on the screen	Image is displayed on the screen	Pass
21	Save current image as .tiff	1)load any slice from any of the dicom series 1)Using the DicomReader GUI software: 2)Go to File menu > save current image as .tiff 3)select a location and give the file a name (different to the original) 4)using test 20 reload the saved file	Same image is displayed on screen and is saved now as .tiff file	Same image is displayed on screen and is saved now as .tiff file	Pass
22	Segment image	Follow user manual on how to segment breast image using the 'segment image' sub menu in the tools menu	Image is blanked before the selected area (nipple area) and past the chest wall	New image now displays segmented (ie all points before and after segmented areas no longer displayed	Pass
23	Save segment points	Follow test 22 and the click on file menu and 'save segment points' sub menu Give the file an appropriate name and location Reload saved segment file as per test 24 on the original non segmented image or any other image will segment at the same points	Saved file present and Segmented image displayed	Saved file present and Segmented image displayed	Pass
24	Load segment points	load saved segment file on the original non segmented image or any other image will segment at the same points	Segmented image displayed	Segmented image displayed	Pass

25	Erode image	1)Follow instructions on erosion in user manual by eroding a texture mapped image that was segmented before being texture mapped 2)use the erosion function an any texture mapped breast image 3)can be viewed using the load single image function	Mapped image now gets eroded and saved can be viewed using load single image function	Mapped image now gets eroded and saved	Pass
26`	Calculate min/max values	Run Textureminmaxcode.m file changing the file names to point to the series of texture mapped images you want to obtain min max values for	Min, max and median values saved in excel spreadsheet	Min, max and median values saved in excel spreadsheet	Pass
27	Scan image for hotspots	1)Run the scan Image for hotspots function of the software as per user manual 2)open imtool Matlabs in built image viewer by typing in imtool in command window 3) in debug mode run this feature again and compare if the range selected are the actual values that are highlighted on the image using the pixel region feature in imtool	1)Lesion hotspots highlighted 2)correct pixel values highlighted when compared within imtool	1)Lesion hotspots highlighted 2)correct pixel values highlighted when compared within imtool	Pass
28	View histogram	1)Load any image on DicomReaderGUI application 2)go to tools and 'view histogram'	Histogram displayed	Histogram displayed	Pass
29	Open wavelet toolbox	1)follow instructions on wavelet section of user manual	1)Wavelet menu opened and correctly load image 2)spreadsheet containing wavelet energy levels is produced	Wavelet menu opened and spreadsheet containing wavelet energy values saved	Pass
30	Code level test for wavelet analysis	Using debug mode in Matlab coding environment, place debug break points in code so that matrices and the corresponding images with original matrix and roi matrix can be viewed for Haar4 dir1, haar4 dir 2 and haar4 dir 3. Test should be done using the relevant files in test files>wavelets folder. Note this test is performed as per user manual instructions but ignoring the normalisation of image section. For reference purposes the image file used for testing is id E04246 slice 22	Screenshots 2a to 2m produced	Screenshots 2a to 2g produced	Pass
31	Normalise Image	As this is not part of a GUI feature of the software type in the Matlab command window a Matrix as follows: I = [1, 4, 5 ; 3, 5,3 ; 3, 7, 76] Then run the normaliseImage function: maxI = max(I(:)) I2 = double(I)./double(maxI).*255	maxI = 76 I2 =[3.3553,13.4211, 16.7763;10.0658, 16.7763,10.0658;10.0658,23.4868, 255.0000]	maxI = 76 I2 =[3.3553,13.4211, 16.7763;10.0658, 16.7763,10.0658;10.0658,23.4868,255.0000]	Pass

3.7 Screenshots

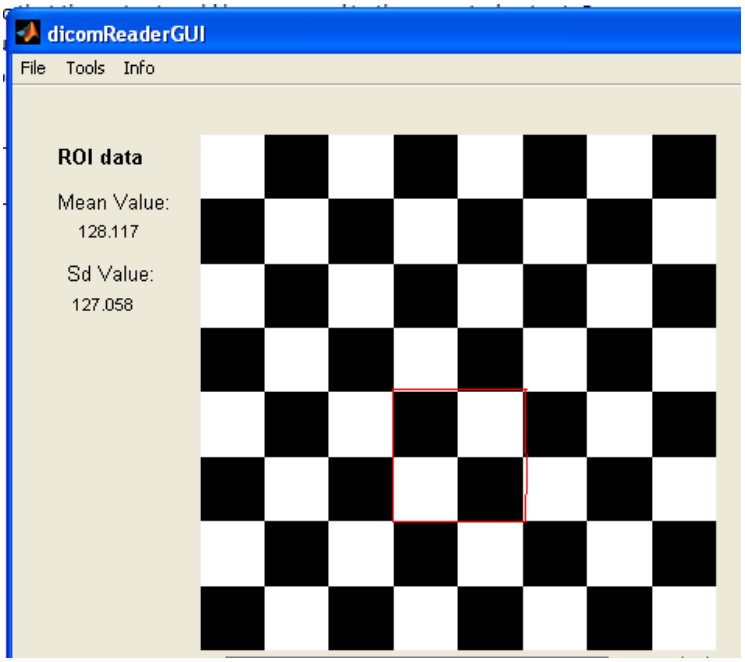

Figure 3.1a: The chessboard feature used for testing purposes.

correctOUTPUT2.xls

	A	B	C	D	E	F
1		0° [0 1]	45° [-1 1]	90° [-1 0]	135° [-1 -1]	Average
2	f1_angularSecondMoment	0.042410713	0.033087	0.038609638	0.032495554	0.036650652
3	f2 contrast	1.048607814	2.099202	1.299681931	1.809605792	1.564274404
4	f3 correlation	0.918651449	0.801613	0.88164103	0.792395493	0.848575294
5	f4 variance	3.812313604	3.141659	3.690639725	3.465118801	3.527432832
6	f5 inverse diff moment	0.677471213	0.581777	0.645956262	0.586934633	0.623034806
7	f6 sum Average	17.98303475	18.1114	17.99516361	18.03173973	18.03033328
8	f7 sum Variance	16.33172168	14.78538	16.09901369	15.67095657	15.72176716
9	f8 sum Entropy	4.035734707	3.968948	4.026152242	4.006898028	4.009433274
10	f9 entropy	5.073539546	5.472204	5.221095503	5.452477889	5.304829347
11	f10 difference Variance	0.543044763	1.032221	0.652116679	0.840963329	0.767086412
12	f11 difference Entropy	1.494454311	1.874514	1.613270847	1.78929891	1.692884498
13	f12 info Measure Of Correlation 1	-0.3603441	-0.22107	-0.311339533	-0.234562131	-0.281829144
14	f13 infoMeasure Of Correlation 2	0.93545985	0.819832	0.91369736	0.874406799	0.885848944
15	f15 cluster Shade	-21.18436378	-17.933	-20.97242063	-21.77883625	-20.46714906
16	f16 cluster Prominence	756.5553138	618.3808	738.5437406	712.2000248	706.4199634
17						
18	Mean of ROI	778.7692308				
19	Standard Deviation of ROI	299.4017111				
20	Slice No	72				
21	Phase No	1				
22						
23	generated by matlab@	22/12/2009 14:19				

Figure 3.1b: Example output of texture parameters.

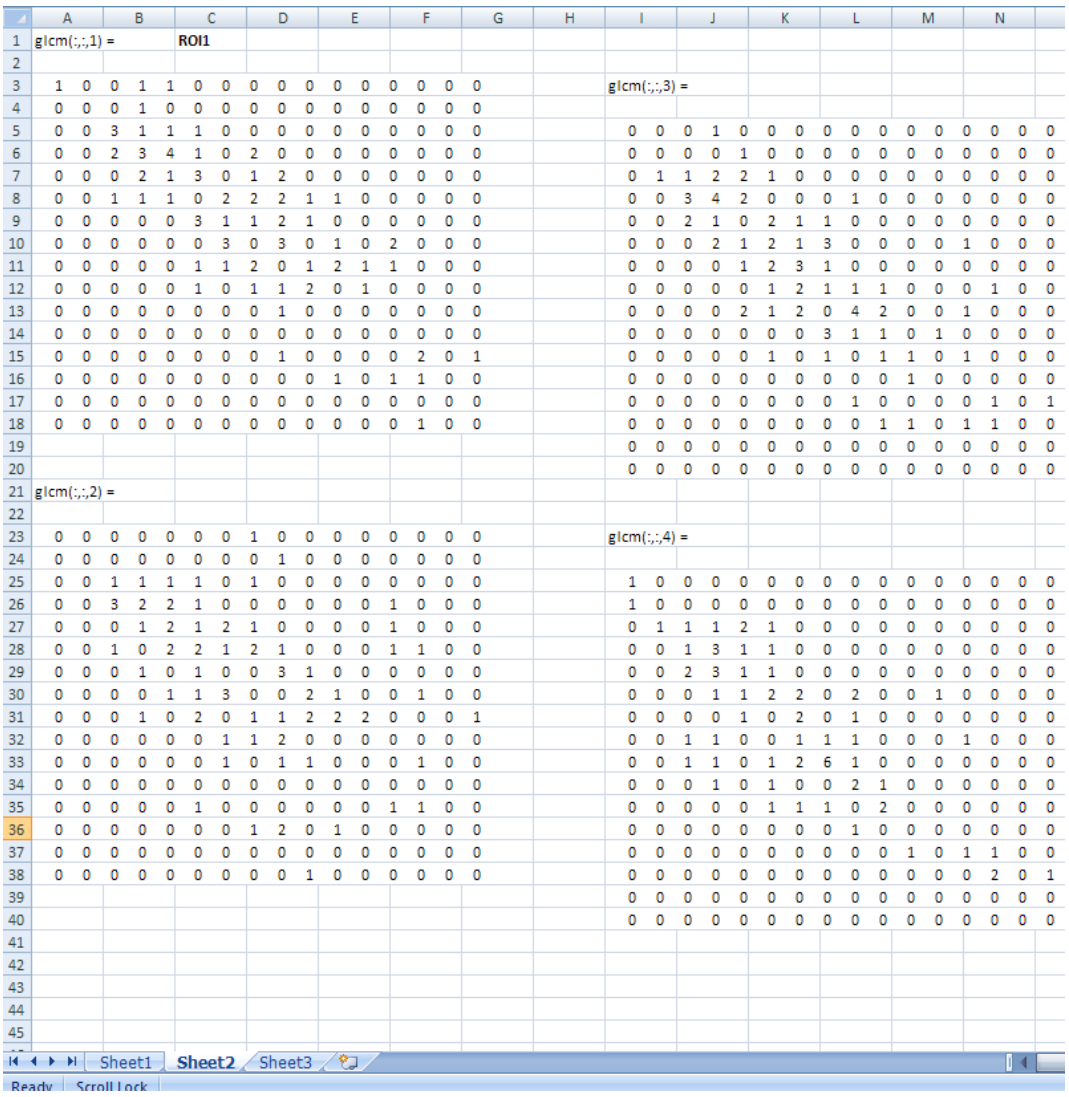

glcm(:,:,1) =

ROI1

1	0	0	1	1	0	0	0	0	0	0	0	0	0	0	0
0	0	0	1	0	0	0	0	0	0	0	0	0	0	0	0
0	0	3	1	1	1	0	0	0	0	0	0	0	0	0	0
0	0	2	3	4	1	0	2	0	0	0	0	0	0	0	0
0	0	0	2	1	3	0	1	2	0	0	0	0	0	0	0
0	0	1	1	1	0	2	2	2	1	1	0	0	0	0	0
0	0	0	0	0	3	1	1	2	1	0	0	0	0	0	0
0	0	0	0	0	0	3	0	3	0	1	0	2	0	0	0
0	0	0	0	0	1	1	2	0	1	2	1	1	0	0	0
0	0	0	0	0	1	0	1	1	2	0	1	0	0	0	0
0	0	0	0	0	0	0	0	0	1	0	0	0	0	0	0
0	0	0	0	0	0	0	0	0	0	0	0	0	0	0	0
0	0	0	0	0	0	0	0	1	0	0	0	0	2	0	1
0	0	0	0	0	0	0	0	0	0	1	0	1	1	0	0
0	0	0	0	0	0	0	0	0	0	0	0	0	0	0	0
0	0	0	0	0	0	0	0	0	0	0	0	0	1	0	0

glcm(:,:,2) =

0	0	0	0	0	0	0	1	0	0	0	0	0	0	0	0
0	0	0	0	0	0	0	0	1	0	0	0	0	0	0	0
0	0	1	1	1	1	0	1	0	0	0	0	0	0	0	0
0	0	3	2	2	1	0	0	0	0	0	0	1	0	0	0
0	0	0	1	2	1	2	1	0	0	0	0	1	0	0	0
0	0	1	0	2	2	1	2	1	0	0	0	1	1	0	0
0	0	0	1	0	1	0	0	3	1	0	0	0	0	0	0
0	0	0	0	1	1	3	0	0	2	1	0	0	1	0	0
0	0	0	1	0	2	0	1	1	2	2	2	0	0	0	1
0	0	0	0	0	0	1	1	2	0	0	0	0	0	0	0
0	0	0	0	0	0	1	0	1	1	0	0	0	1	0	0
0	0	0	0	0	0	0	0	0	0	0	0	0	0	0	0
0	0	0	0	0	1	0	0	0	0	0	0	1	1	0	0
0	0	0	0	0	0	0	1	2	0	1	0	0	0	0	0
0	0	0	0	0	0	0	0	0	0	0	0	0	0	0	0
0	0	0	0	0	0	0	0	0	1	0	0	0	0	0	0

glcm(:,:,3) =

0	0	0	1	0	0	0	0	0	0	0	0	0	0	0	0
0	0	0	0	1	0	0	0	0	0	0	0	0	0	0	0
0	1	1	2	2	1	0	0	0	0	0	0	0	0	0	0
0	0	3	4	2	0	0	0	1	0	0	0	0	0	0	0
0	0	2	1	0	2	1	1	0	0	0	0	0	0	0	0
0	0	0	2	1	2	1	3	0	0	0	0	1	0	0	0
0	0	0	0	1	2	3	1	0	0	0	0	0	0	0	0
0	0	0	0	0	1	2	1	1	1	0	0	0	1	0	0
0	0	0	0	0	2	1	2	0	4	2	0	0	1	0	0
0	0	0	0	0	0	0	3	1	1	0	1	0	0	0	0
0	0	0	0	0	1	0	1	0	1	1	0	1	0	0	0
0	0	0	0	0	0	0	0	0	0	1	0	0	0	0	0
0	0	0	0	0	0	0	0	0	1	0	0	0	0	1	0
0	0	0	0	0	0	0	0	0	0	1	1	0	1	1	0
0	0	0	0	0	0	0	0	0	0	0	0	0	0	0	0
0	0	0	0	0	0	0	0	0	0	0	0	0	0	0	0

glcm(:,:,4) =

1	0	0	0	0	0	0	0	0	0	0	0	0	0	0	0
1	0	0	0	0	0	0	0	0	0	0	0	0	0	0	0
0	1	1	1	2	1	0	0	0	0	0	0	0	0	0	0
0	0	1	3	1	1	0	0	0	0	0	0	0	0	0	0
0	0	2	3	1	1	0	0	0	0	0	0	0	0	0	0
0	0	0	1	1	2	2	0	2	0	0	1	0	0	0	0
0	0	0	0	1	0	2	0	1	0	0	0	0	0	0	0
0	0	1	1	0	0	1	1	1	0	0	0	1	0	0	0
0	0	1	1	0	1	2	6	1	0	0	0	0	0	0	0
0	0	0	1	0	1	0	0	2	1	0	0	0	0	0	0
0	0	0	0	0	1	1	1	0	2	0	0	0	0	0	0
0	0	0	0	0	0	0	0	0	1	0	0	0	0	0	0
0	0	0	0	0	0	0	0	0	0	0	1	0	1	1	0
0	0	0	0	0	0	0	0	0	0	0	0	0	0	2	0
0	0	0	0	0	0	0	0	0	0	0	0	0	0	0	0
0	0	0	0	0	0	0	0	0	0	0	0	0	0	0	0

Sheet1 Sheet2 Sheet3

Ready Scroll Lock

Figure 3.1c: Four co-occurrence matrices corresponding to 0°, 45°, 90° and 135° directions for the first ROI in a series of images.

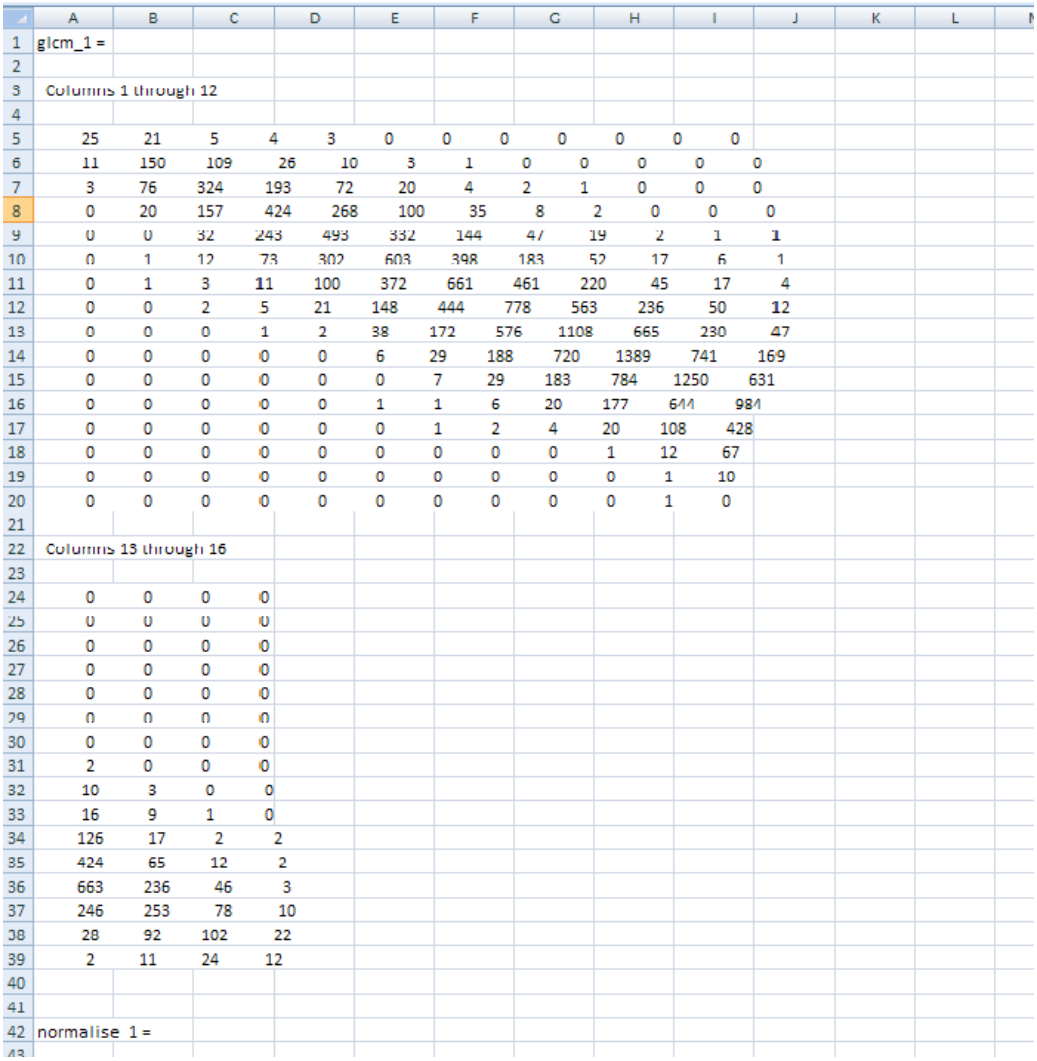

glcm_1 =

Columns 1 through 12

25	21	5	4	3	0	0	0	0	0	0	0
11	150	109	26	10	3	1	0	0	0	0	0
3	76	324	193	72	20	4	2	1	0	0	0
0	20	157	424	268	100	35	8	2	0	0	0
0	0	32	243	493	332	144	47	19	2	1	1
0	1	12	73	302	603	398	183	52	17	6	1
0	1	3	11	100	372	661	461	220	45	17	4
0	0	2	5	21	148	444	778	563	236	50	12
0	0	0	1	2	38	172	576	1108	665	230	47
0	0	0	0	0	6	29	188	720	1389	741	169
0	0	0	0	0	0	7	29	183	784	1250	631
0	0	0	0	0	1	1	6	20	177	644	984
0	0	0	0	0	0	1	2	4	20	108	428
0	0	0	0	0	0	0	0	0	1	12	67
0	0	0	0	0	0	0	0	0	0	1	10
0	0	0	0	0	0	0	0	0	0	1	0

Columns 13 through 16

0	0	0	0
0	0	0	0
0	0	0	0
0	0	0	0
0	0	0	0
0	0	0	0
0	0	0	0
2	0	0	0
10	3	0	0
16	9	1	0
126	17	2	2
424	65	12	2
663	236	46	3
246	253	78	10
28	92	102	22
2	11	24	12

normalise_1 =

Figure 3.1d: Summation of the co-occurrence matrices for all ROIs in image series.

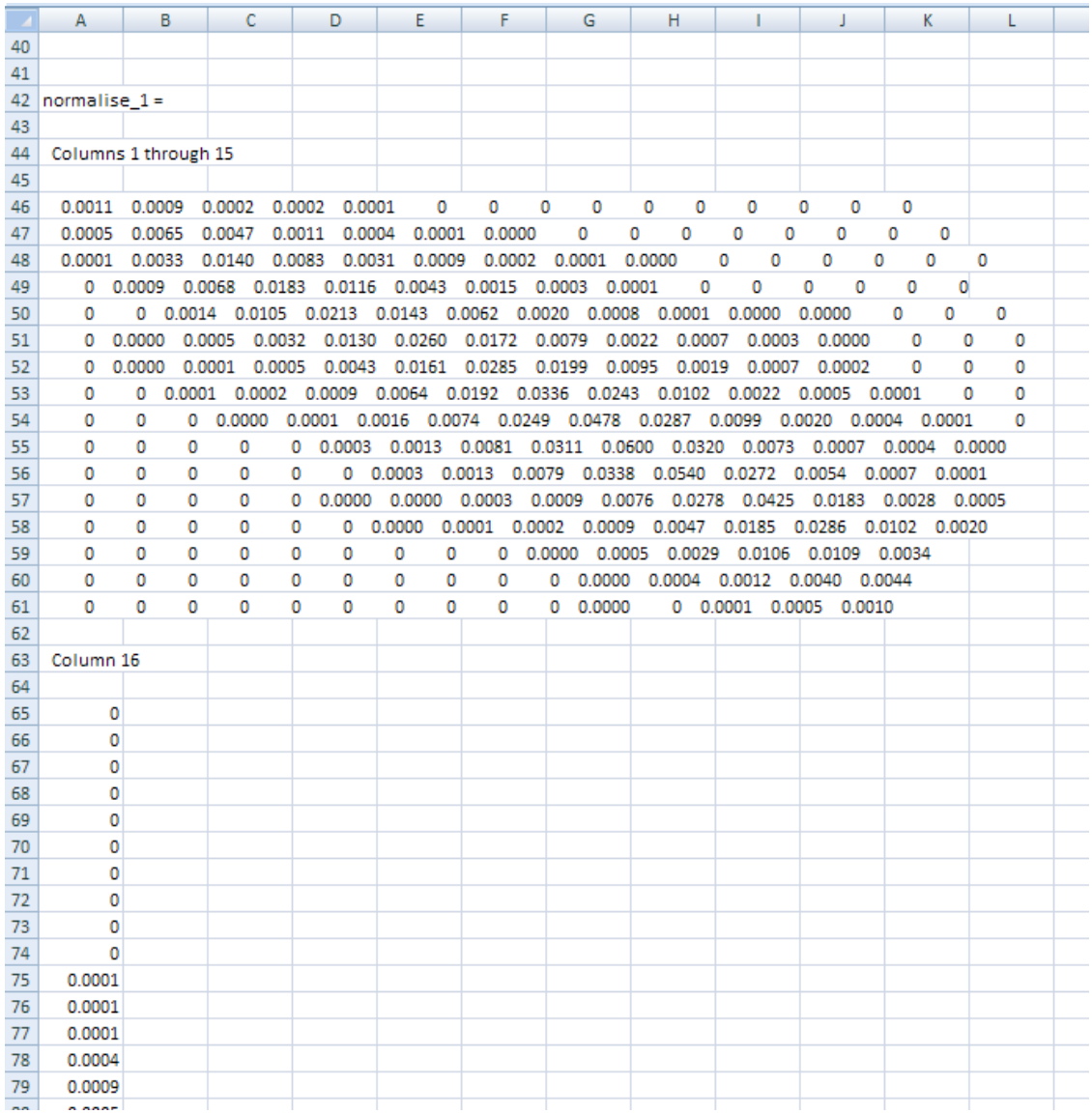

normalise_1 =

Columns 1 through 15

0.0011	0.0009	0.0002	0.0002	0.0001	0	0	0	0	0	0	0	0	0	0
0.0005	0.0065	0.0047	0.0011	0.0004	0.0001	0.0000	0	0	0	0	0	0	0	0
0.0001	0.0033	0.0140	0.0083	0.0031	0.0009	0.0002	0.0001	0.0000	0	0	0	0	0	0
0	0.0009	0.0068	0.0183	0.0116	0.0043	0.0015	0.0003	0.0001	0	0	0	0	0	0
0	0	0.0014	0.0105	0.0213	0.0143	0.0062	0.0020	0.0008	0.0001	0.0000	0.0000	0	0	0
0	0.0000	0.0005	0.0032	0.0130	0.0260	0.0172	0.0079	0.0022	0.0007	0.0003	0.0000	0	0	0
0	0.0000	0.0001	0.0005	0.0043	0.0161	0.0285	0.0199	0.0095	0.0019	0.0007	0.0002	0	0	0
0	0	0.0001	0.0002	0.0009	0.0064	0.0192	0.0336	0.0243	0.0102	0.0022	0.0005	0.0001	0	0
0	0	0	0.0000	0.0001	0.0016	0.0074	0.0249	0.0478	0.0287	0.0099	0.0020	0.0004	0.0001	0
0	0	0	0	0	0.0003	0.0013	0.0081	0.0311	0.0600	0.0320	0.0073	0.0007	0.0004	0.0000
0	0	0	0	0	0	0.0003	0.0013	0.0079	0.0338	0.0540	0.0272	0.0054	0.0007	0.0001
0	0	0	0	0	0.0000	0.0000	0.0003	0.0009	0.0076	0.0278	0.0425	0.0183	0.0028	0.0005
0	0	0	0	0	0	0.0000	0.0001	0.0002	0.0009	0.0047	0.0185	0.0286	0.0102	0.0020
0	0	0	0	0	0	0	0	0	0.0000	0.0005	0.0029	0.0106	0.0109	0.0034
0	0	0	0	0	0	0	0	0	0	0.0000	0.0004	0.0012	0.0040	0.0044
0	0	0	0	0	0	0	0	0	0	0.0000	0	0.0001	0.0005	0.0010

Column 16

0
0
0
0
0
0
0
0
0
0
0.0001
0.0001
0.0001
0.0004
0.0009

Figure 3.1e: Co-occurrence matrix of figure 3.1d after normalisation.

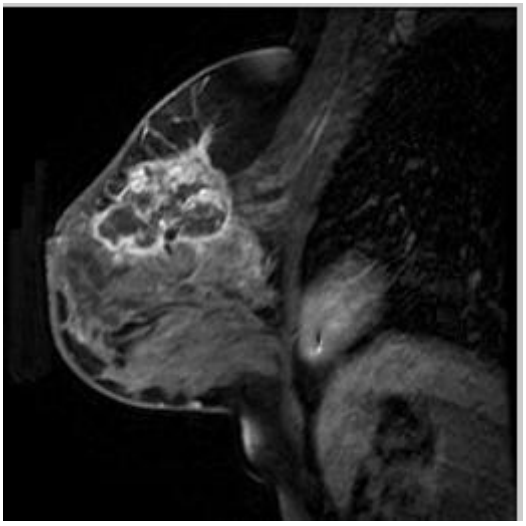

Figure 3.2a: Original image used for the purpose of testing the Wavelet function of the software

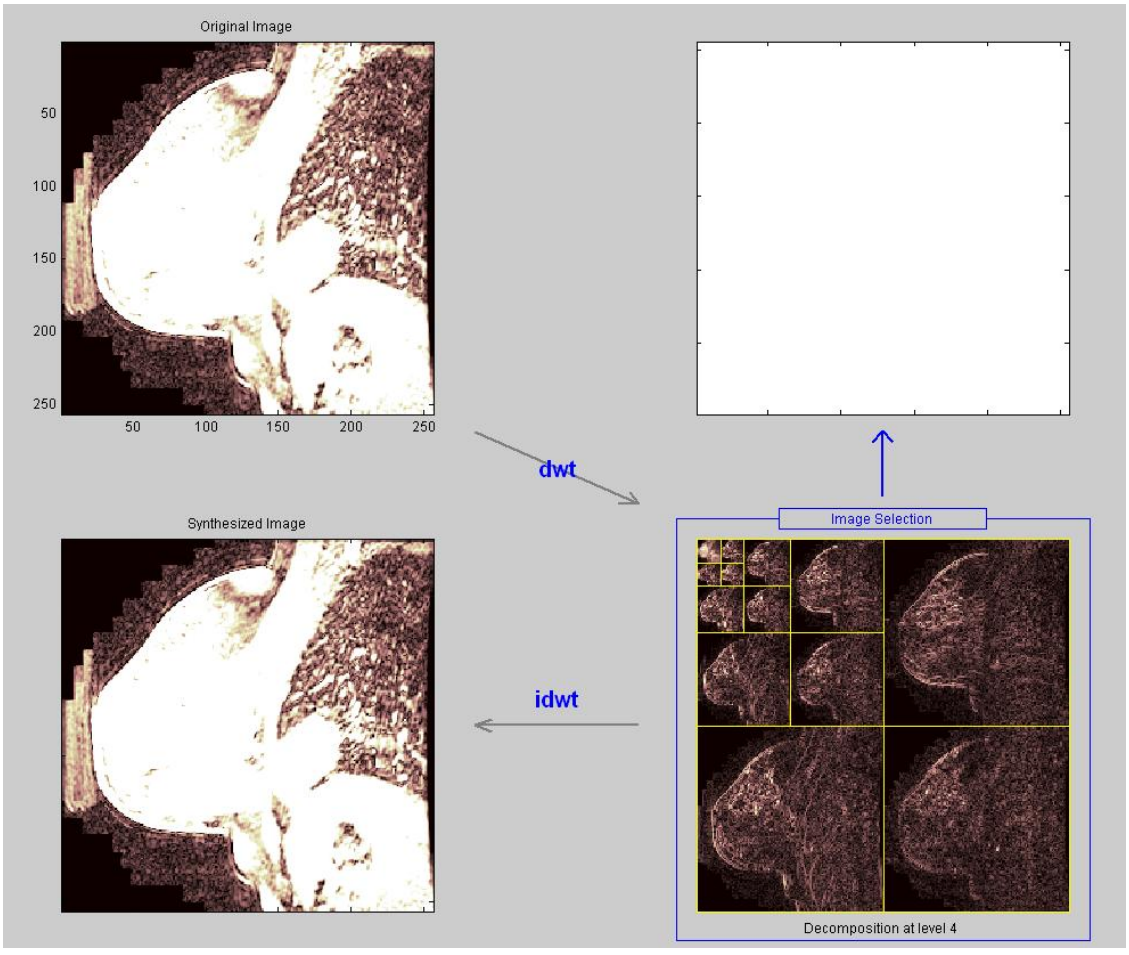

Figure 3.2b: Wavelet coefficient images using haar level4 generated from the image in 2a

1		Wavelet Energy Results
2	energyWaveletHaar1Dir1	40258.47067
3	energyWaveletHaar1Dir2	34393.60772
4	energyWaveletHaar1Dir3	4162.045587
5	energyWaveletHaar2Dir1	333171.2445
6	energyWaveletHaar2Dir2	306366.4262
7	energyWaveletHaar2Dir3	85386.96557
8	energyWaveletHaar3Dir1	2133374.332
9	energyWaveletHaar3Dir2	822564.7543
10	energyWaveletHaar3Dir3	627045.1467
11	energyWaveletHaar4Dir1	7933332.571
12	energyWaveletHaar4Dir2	3373224.374
13	energyWaveletHaar4Dir3	2563552.938
14	results for wavelet file	E04246_sl22COEFF.mat
15	generated by matlab@	01/02/2012 14:23
16		
17		

Figure 3.2c: Wavelet energy parameters calculated using the wavelet coefficient images generated in 3.2b

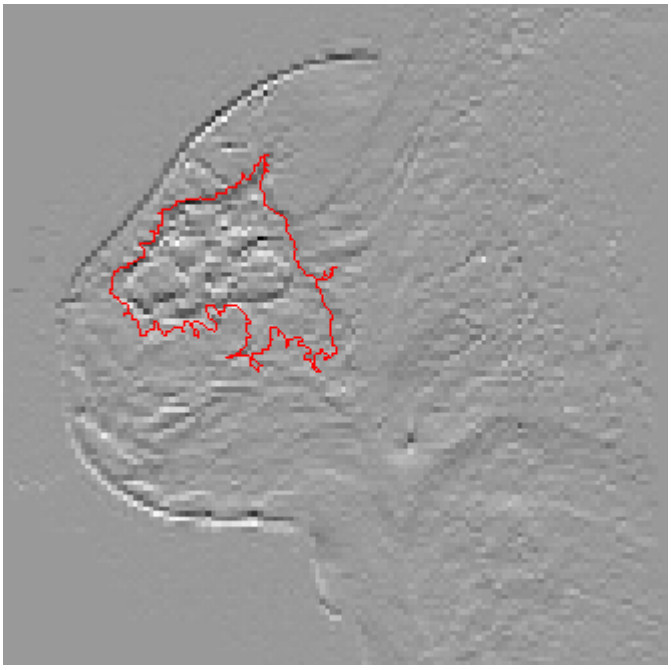

Figure 3.2d: ROI displayed on Haar 1 dir 1 coefficient image generated by the wavelet section of the software

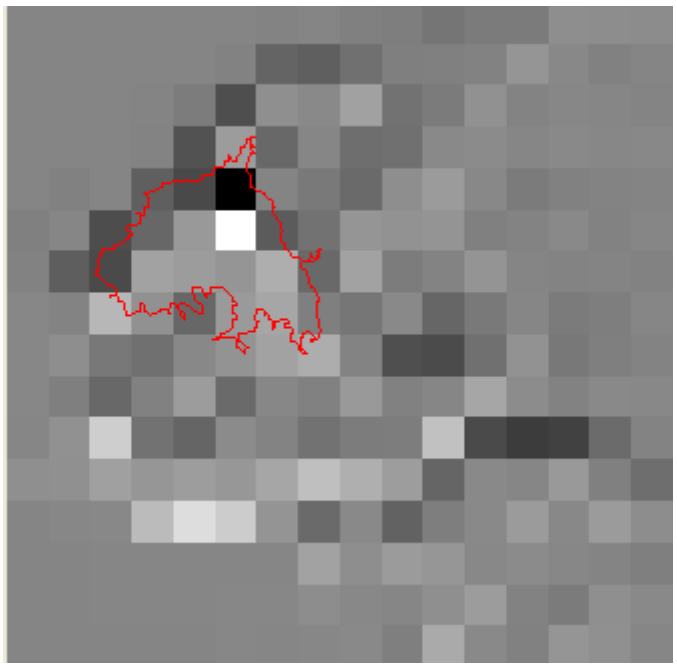

Figure 3.2e: ROI displayed on haar 4 dir 1 coefficient image generated by the wavelet section of the software

I: 16x16 double =

1.0e+003 *

Columns 1 through 11

0	0	0	0	0	-0.0378	-0.0942	-0.0310	-0.2404	-0.3708	-0.7700
0	0	0	-0.0260	-0.0263	-0.1399	-1.6078	-1.8618	-0.9708	-0.3284	-0.2671
0	0	-0.0336	-0.0655	-0.4351	-2.6489	0.4588	0.1864	1.3274	-0.9101	-0.5121
0	0	-0.0357	-0.1066	-2.4745	1.0926	-1.4361	0.0381	-1.1276	-1.0046	0.1718
-0.0079	-0.2114	-0.0219	-1.8271	-2.8837	-6.4413	-0.0911	-0.6103	-1.2956	0.4151	1.0410
-0.2819	0.0062	-2.7062	-1.4508	0.9467	5.8732	-2.0311	-0.9567	0.7497	0.5839	0.6953
-0.1680	-1.8950	-2.8748	1.3917	1.0993	0.7701	1.9458	-1.3803	1.3894	-0.4643	-0.1361
0.0869	-0.1285	2.3992	0.5509	-1.4813	1.0141	1.5876	-0.3189	-0.7477	0.2092	-1.5291
0.0547	0.4234	-0.6235	-0.9908	0.1472	0.6581	1.3610	1.8945	-0.1374	-2.6006	-2.8041
0.0784	-0.3055	-1.4142	-0.1945	1.0981	-1.3031	0.0566	-0.2106	0.9510	-0.2172	0.0116
0.0291	0.5415	3.5121	-0.9532	-1.5416	0.2769	-0.1134	-0.9108	-0.4343	-0.3826	2.8802
0.4669	0.4991	1.2918	0.7951	1.1141	0.8651	1.5586	2.7614	1.9909	1.1369	-1.5733
0.0034	0.0733	0.1228	2.6304	4.2319	3.3890	0.6851	-1.3179	0.2170	-1.7249	-0.3587
0	0	0.0388	0.0112	0.0481	0.0494	0.0228	1.3684	0.4002	1.0463	0.8120
0	0	0.0121	0.0395	0.0423	0.0694	0.0536	0.3861	0.1343	0.0514	0.4483
0	0	0	0	0	0.0923	0.0273	0.0822	0.1861	-0.3214	1.7424

Columns 12 through 16

-0.5165	-0.5201	0.4009	0.3714	0.3331
-0.1515	0.7399	0.1085	-0.1934	-0.0327
0.5754	-0.1306	0.0570	0.0187	-0.0666
0.2689	0.0493	0.1566	0.0814	0.1328
0.1256	-0.5089	-0.2287	-0.1335	-0.0880
-0.2458	-0.0982	0.1597	-0.1511	0.0329
0.7248	-0.0294	-0.1176	-0.0616	-0.1597
-0.6121	0.0374	-0.4777	-0.3756	0.0393
-0.9755	0.5838	-0.6291	-0.3283	-0.1294
1.5696	0.2948	-0.1796	0.1644	0.1239
-2.8789	-3.5259	-3.2988	-1.2586	-0.1206
0.1997	0.0431	0.9470	-0.2377	-1.1241
0.1735	1.0163	0.1374	1.0197	0.3467
0.1106	0.2901	0.0979	-0.0797	-0.3195
1.0761	-0.1581	-0.5037	0.4453	0.1755
0.1894	-0.2080	0.7429	0.5094	0.0121

Figure 3.2f: Haar 4 dir 1 raw image matrix generated by the wavelet section of the software

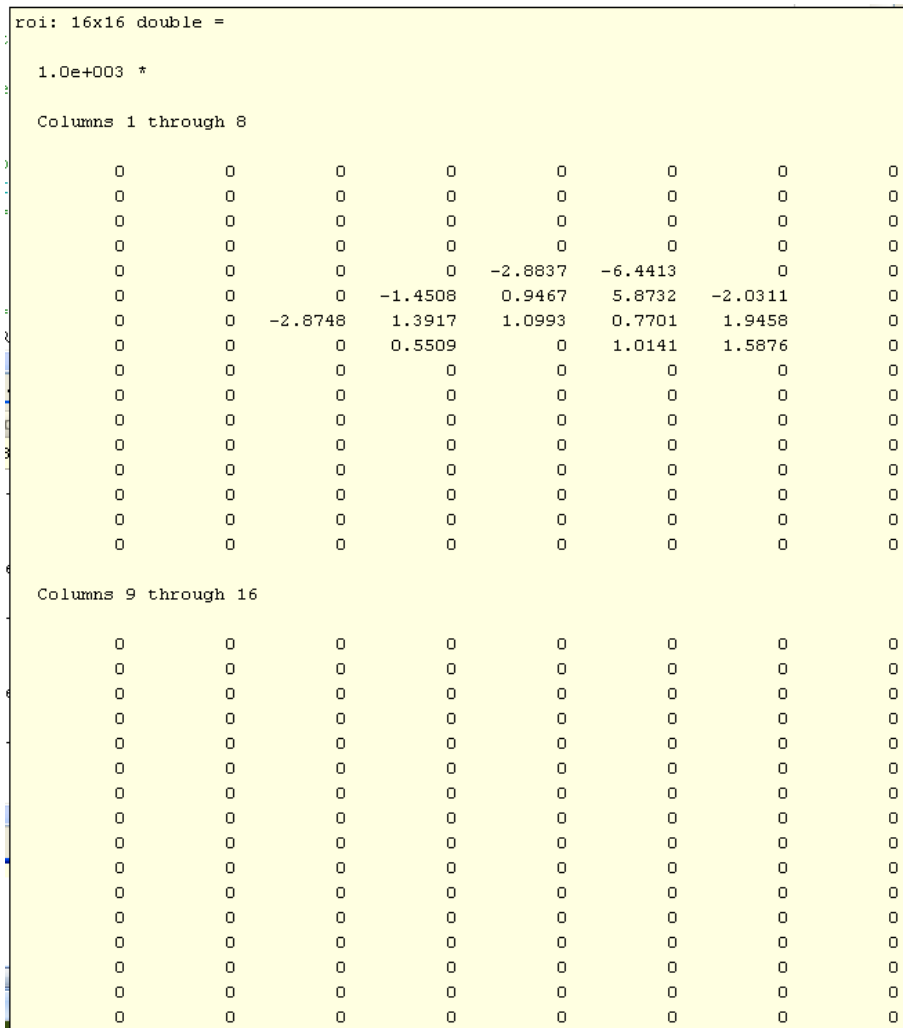

```
roi: 16x16 double =

  1.0e+003 *

  Columns 1 through 8

         0         0         0         0         0         0         0         0
         0         0         0         0         0         0         0         0
         0         0         0         0         0         0         0         0
         0         0         0         0         0         0         0         0
         0         0         0         0   -2.8837   -6.4413         0         0
         0         0         0   -1.4508    0.9467    5.8732   -2.0311         0
         0         0   -2.8748    1.3917    1.0993    0.7701    1.9458         0
         0         0         0    0.5509         0    1.0141    1.5876         0
         0         0         0         0         0         0         0         0
         0         0         0         0         0         0         0         0
         0         0         0         0         0         0         0         0
         0         0         0         0         0         0         0         0
         0         0         0         0         0         0         0         0
         0         0         0         0         0         0         0         0
         0         0         0         0         0         0         0         0
         0         0         0         0         0         0         0         0

  Columns 9 through 16

         0         0         0         0         0         0         0         0
         0         0         0         0         0         0         0         0
         0         0         0         0         0         0         0         0
         0         0         0         0         0         0         0         0
         0         0         0         0         0         0         0         0
         0         0         0         0         0         0         0         0
         0         0         0         0         0         0         0         0
         0         0         0         0         0         0         0         0
         0         0         0         0         0         0         0         0
         0         0         0         0         0         0         0         0
         0         0         0         0         0         0         0         0
         0         0         0         0         0         0         0         0
         0         0         0         0         0         0         0         0
         0         0         0         0         0         0         0         0
         0         0         0         0         0         0         0         0
         0         0         0         0         0         0         0         0
```

Figure 3.2g: Corresponding ROI raw matrix for haar 4 dir 1 generated by the wavelet section of the software

4 Texture Analysis Repeatability using Agar Phantom

4.1 Introduction

The importance of texture analysis in MRI has been discussed at length in chapter 2 (literature review) which looked at texture analysis in the context of MRI, as well as in non MRI based images such as satellite images of terrain. In the medical context textural information is undoubtedly very heavily used in a radiologist's decision making process. However, subtle variations in texture are often missed, thus by quantitatively analysing MR images the textural properties that would otherwise be impossible to discern by simply visually inspecting the image can be obtained. This information can then potentially be used to aid diagnosis, monitor treatment response and as a screening tool.

In this study reticulated foams of varying porosities embedded in agarose gel are used as phantoms and texture analysis is performed using the in house developed software in order to test the repeatability of texture analysis. In addition an attempt was made to establish whether texture analysis could be used reliably with clinical protocols to distinguish between different objects.

In a 1998 study Lerski [63] used reticulated foam as texture test objects, foams were inserted in test tubes embedded in agarose gel. The study found the test object useful for the study of texture measurement in MR imaging.

Another study by the same group the following year [64] involved multicentre analysis of the same test objects created in a similar manner of that of their earlier study [63]. In this study [64] the group scanned the same test objects across multiple centres and found some MRI equipment out performed others in terms of texture analysis. In addition the study concluded that texture measures were not easily comparable between centres, although the test object itself was deemed a successful standard object for the measurement of texture. Both studies [63, 64] considered first order parameters such as mean and skewness as well as texture parameters from the co-occurrence, gradient and run length methods.

In a more recent study Waugh [65] used a custom-made phantom containing different grades of reticulated foam embedded in agarose gel. They looked at assessing the ability of texture analysis to distinguish between different texture objects, an objective that the work in this thesis has adopted. The Waugh study also looked at outcome of texture analysis when imaging sequences were changed and concludes that changes to sequence parameters were less critical for the outcome of texture analysis. The study however did reliably differentiate, using texture analysis, between four grades of foam. By simply visually inspecting the MR images of foam different porosities of foam were deemed indistinguishable. In this thesis assessment of repeatability and correlations are performed using 7 grades of foam as opposed to the 4 used in the Waugh study.

4.1.1 Aims

To assess the repeatability of texture analysis by applying in house developed software to MR images of reticulated foam phantoms.

To assess texture analysis in differentiating foams of varying porosity that look visually indistinguishable on MR images.

4.2 Methods

Reticulated foams of specific porosities were ordered as samples from Foam Engineers Limited, Dashwood Avenue, High Wycombe, Buckinghamshire, HP12 3EA. Seven different breast-mimicking phantoms were created using foams with pore sizes of 10, 20, 30 , 45, 60, 75 and 90 pores per inch (PPI) as shown in figure 4.1, each piece of foam was cylindrical in shape with an approximate diameter of 7cm and depth of 4cm.

Figure 4.1: The seven different foam samples with a range of pore sizes from left to right of 10, 20, 30, 45, 60, 75 and 90 PPI

4.2.1 Phantom Chemistry

The method used closely replicated that in the Waugh [65] study. The foam samples were added to individual beakers containing a 2% agarose solution (ca. 400 ml) with a 1.75 millimolar concentration of the DOTAREM contrast agent at 70 deg C. The foam samples were repeatedly compressed (ca. 20-30 compression cycles) while being held at 70 deg C in a water bath to remove all air bubbles. They were then removed from the water bath and allowed to cool to room temperature prior to sealing with parafilm (figure 4.2). A series of test phantoms were created and scanned before making the actual phantoms from the sample foam in order to optimise the procedure.

Figure 4.2: Phantoms suspended in agarose having undergone compression during preparation

4.2.2 MRI Protocol

All phantoms were scanned on a 3.0T HDx (GE Healthcare, Milwaukee, WI) scanner in combination with an 8-channel dedicated breast coil. Two sequences were utilised. A sagittal vibrant sequence [10° flip, TR 4ms, TE 1.6ms/Fr, bandwidth 41.7kHz, 20x20cm FOV, 220x160 matrix, 4mm slice thickness] was equivalent to DCE images detailed elsewhere.

A fast spin-echo sequence employing echo-times of 28ms and 113ms was used for T_2 mapping in the coronal plane [90° flip, TR 4000ms, bandwidth 32.2kHz, 20x20cm FOV, 320x320 matrix, 4mm slice thickness]. All scans for T_2 mapping and vibrant were performed twice in order to assess repeatability.

4.2.3 Quantitative Analysis

After data acquisition ROIs were generated using the in house developed software draw ROI feature. Both a larger and a smaller ROI were drawn on the Vibrant data. The smaller ROI approximately covered a third of the foam in the MR image (1006 pixels) and the larger ROI (2752 pixels) tried to cover as much as possible whilst avoiding edges and noisy sections of the image (fig 4.3). Once drawn each ROI was saved and these two ROIs were used for all future analysis of the Vibrant data. Similarly a small (565 pixels) and a large (13885 pixels) ROI were drawn for the T_2 mapping data (fig 4.4) and saved and all future analysis of T_2 data used these two ROIs. In both Vibrant and T_2 mapping data ROIs were only drawn on one set of data then translated onto others.

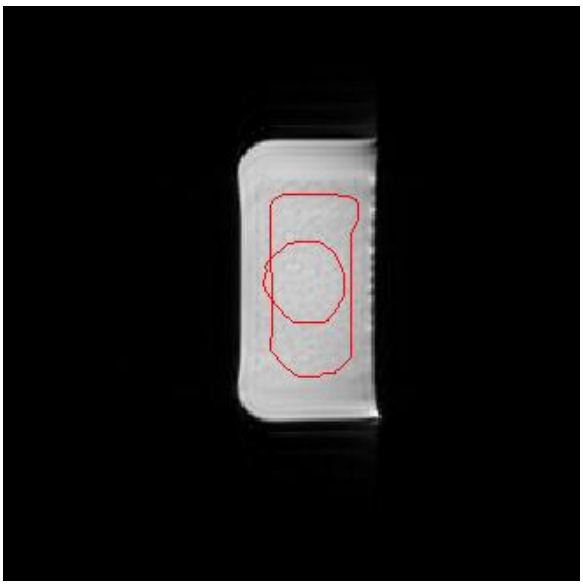

Figure 4.3: Vibrant MR image of one foam phantom (PPI 10) with the larger (2752 pixels) and smaller (1006 pixels) ROIs illustrated

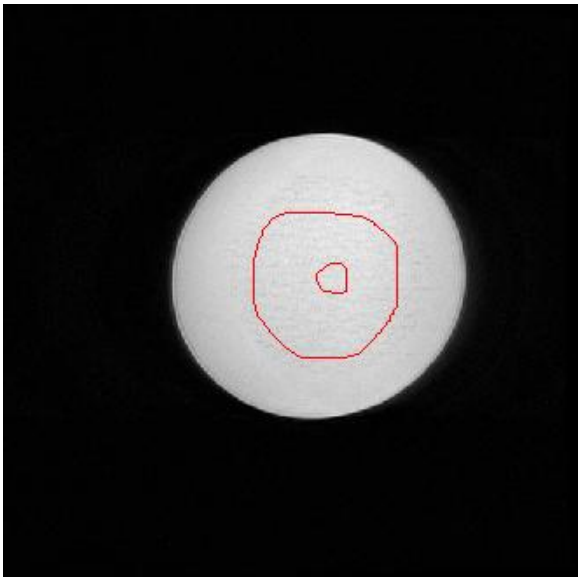

Figure 4.4: FSE image of one foam phantom (PPI 10) with the larger (13885 pixels) and smaller (565 pixels) ROIs illustrated

4.2.4 Texture Analysis

Texture analysis was then performed on a single slice from the Vibrant phantom data and the same slice was utilised from each series. To ensure positioning for each test was the same only one pre-scan was run on the MRI scanner with the first test phantom in position and no pre-scans were run on the remainder of the test phantoms as the same settings were maintained.

In addition each beaker was manually put in to the same position of the breast coil prior to scanning. To prevent sparseness within subsequently calculated co-occurrence matrices the ROI data underwent grey level decimation to 16 grey levels via histogram equalisation.

Co-occurrence matrices, which contain the joint probability of two adjacent pixels along a given direction θ having co-occurring values i and j, were calculated for θ = 0°, 45°, 90° and 135° and subsequently averaged. The 14 textural features as defined by Haralick [53] (denoted f_1 to f_{14} and including entropy, angular second moment and correlation) were then determined alongside two further parameters cluster shade (f_{15}) and cluster prominence (f_{16}) [55] (detailed formulas and explanations on the co-occurrence matrices are included in chapter 5; texture analysis on neoadjuvant data).

4.2.5 T_2 Mapping Analysis

T_2 maps were calculated for each texture phantom, maps were generated via the in house software's T_2 mapping feature and saved as .tiff images. Maps were calculated using the formula:

$$T_2 = \frac{TE_2 - TE_1}{\ln {S_1}/{S_2}}$$

Where TE is echo time(s) and S is signal for image(s) 1 and 2.

4.2.6 Statistical Analysis

Pearsons correlation tests were performed between texture parameters and porosity and between T_2 values and porosity. Correlations were performed for both ROI sizes using SPSS version 18. Repeatability tests were performed for both T_2 mapping and Vibrant data, wherein independent test results on identical items obtained with the same method in the same laboratory are compared [78]. A repeatability assessment would enable the magnitude of treatment-induced change required for reliable detection to be established. Repeatability was

estimated using the methodology previously described by Bland and Altman [79] wherein it is calculated as 2.77 times the common standard deviation of repeated measures. The common standard deviation of repeated measures is often referred to as within-subject standard deviation.

4.3 Results

4.3.1 Correlation of texture analysis with porosity

Visually inspecting the images acquired using the vibrant data series, looking at the same slice for each different pore sized foam phantom (figure 4.5) it can clearly be seen that with the exception of a) PPI 10 it is near impossible to distinguish the different pore sizes. The results of the texture analysis however show differences in texture between pore sizes as highlighted in the correlation graphs.

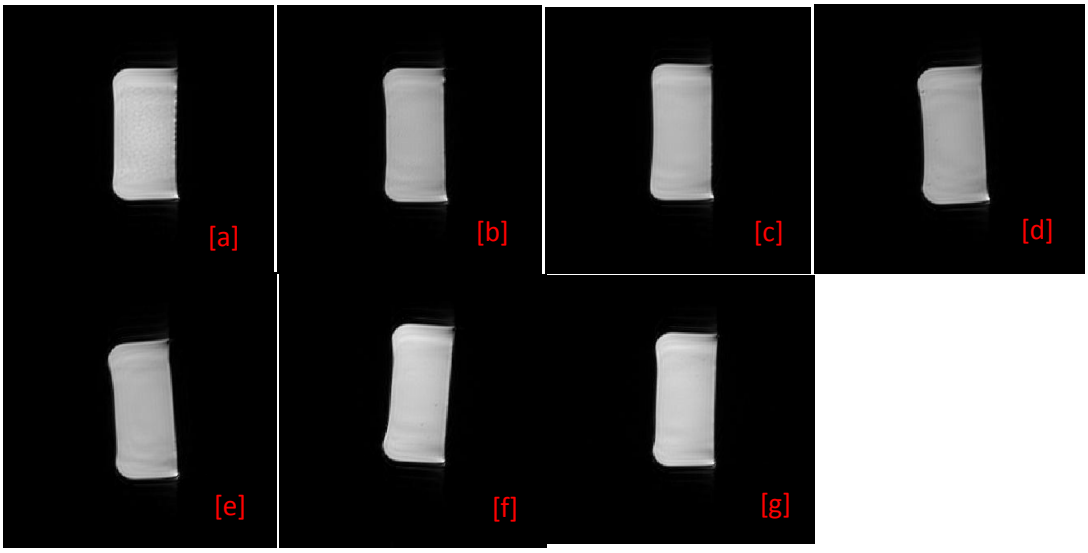

Figure 4.5: MR images from Vibrant sagittal data with a) 10, b) 20, c) 30, d) 45, e) 60, f) 75 and g) 90 pores per inch (PPI) foam

Table 4.1 highlights the results for the large and small ROIs after texture analysis was performed and the results of each texture parameter were correlated against each foam (according to PPI). In addition table 4.2 shows the actual texture values for three of the parameters (f_1, f_{15} and f_{16}) against PPI size for the small ROIs. For the larger ROI table 4.1 highlights reasonable correlation between PPI and texture parameters although p-values were not significant in most cases. The two texture parameters that had p-values < 0.05 (f_{15} and f_{16}) and reasonable R^2 values are highlighted in figures 4.6 and 4.7. In figure 4.6 for the parameter f_{15} the R^2 value of 0.611 highlights that the PPI contributes to 61% of the variation in f_{15} and the remainder 39% of variation in the texture parameter has nothing to do with change in PPI, having a p-value of < 0.05 shows that the confidence level of 61% variation is good. The p-value of <0.05 indicates there is only a 5% chance (ie confidence level is 95%) that the R^2 value of 0.611 is by chance, the closer the R^2 value is to 100% the better correlated the data is. In addition texture parameter f_1 had a p-value of 0.052 (close to significant) and the correlation graph can be seen in figure 4.8. In all three examples (f_1, f_{15} and f_{16}) the graphs show the smaller the pore size the higher the texture parameters value showing that PPI sizes clearly affect the value of texture analysis parameters in these cases although visually the MR images look indistinguishable.

It is clear when comparing larger ROI results with smaller ROI results (both shown in table 4.1) that the results for smaller ROI show no p-values of < 0.05 and therefore no texture parameters are significantly correlated with PPI.

Texture parameters	R^2		P value	
	Large	small	large	small
$\mathbf{f_1}$ (angular 2nd moment)	0.563	0.295	0.052	0.208
$\mathbf{f_2}$ (contrast)	0.398	0.477	0.129	0.086
$\mathbf{f_3}$ (correlation)	0.421	0.480	0.115	0.085
$\mathbf{f_4}$ (variance)	0.433	0.444	0.108	0.102
$\mathbf{f_5}$ (inv diff moment)	0.510	0.386	0.072	0.136
$\mathbf{f_6}$ (sum average)	0.152	0.170	0.386	0.357
$\mathbf{f_7}$ (sum variance)	0.458	0.412	0.095	0.120
$\mathbf{f_8}$ (sum entropy)	0.433	0.310	0.108	0.194
$\mathbf{f_9}$ (entropy)	0.477	0.336	0.086	0.173
$\mathbf{f_{10}}$ (difference variance)	0.401	0.456	0.127	0.096
$\mathbf{f_{11}}$ (difference entropy)	0.472	0.377	0.088	0.142
$\mathbf{f_{12}}$ (info m' of corr' 1)	0.477	0.335	0.086	0.173
$\mathbf{f_{13}}$ (info m' of corr' 2)	0.327	0.438	0.180	0.105
$\mathbf{f_{14}}$ (max corr' coeff')	0.256	0.410	0.247	0.121
$\mathbf{f_{15}}$ (cluster shade)	0.611	0.109	0.038	0.470
$\mathbf{f_{16}}$ (cluster prominence)	0.589	0.482	0.044	0.083

Table 4.1: correlation results for texture parameters against foam PPI size for the large and small ROIs

	$\mathbf{f_1}$	$\mathbf{f_{15}}$	$\mathbf{f_{16}}$
PPI 10	.006934	-45.62	8942
PPI 20	.009775	-115.17	9825
PPI 30	.017214	-31.98	11533
PPI 45	.017257	-62.11	11463
PPI 60	.012289	-54.25	11011
PPI 75	.014444	-43.27	11345
PPI 90	.015614	-46.89	11346

Table 4.2: texture analysis results for texture parameters f_1, f_{15} and f_{16} against foam PPI size for the small ROIs, results show fairly large change in values according to PPI of each phantom (for parameter f_1 77.26% variation around the mean)

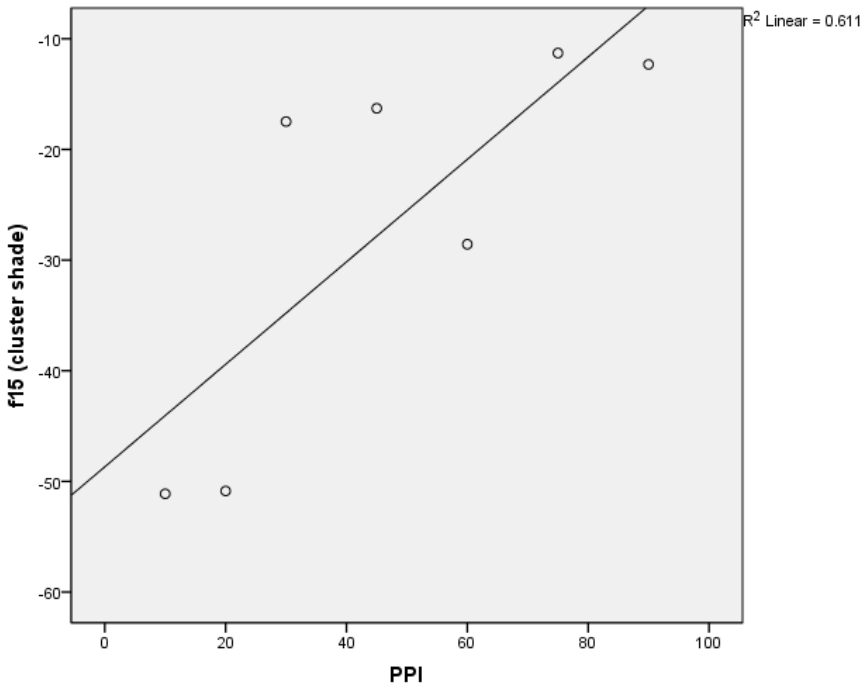

Figure 4.6: Pearson correlation graph for texture parameter f_{15} (cluster shade) against PPI for the larger ROI

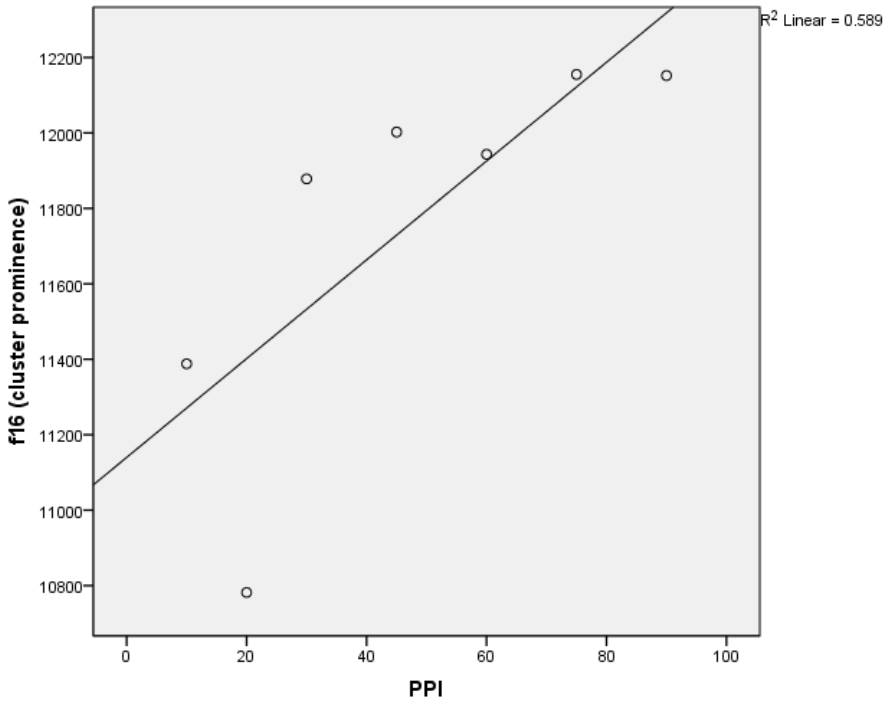

Figure 4.7: Pearson correlation graph for texture parameter f_{16} (cluster prominence) against PPI for the larger ROI

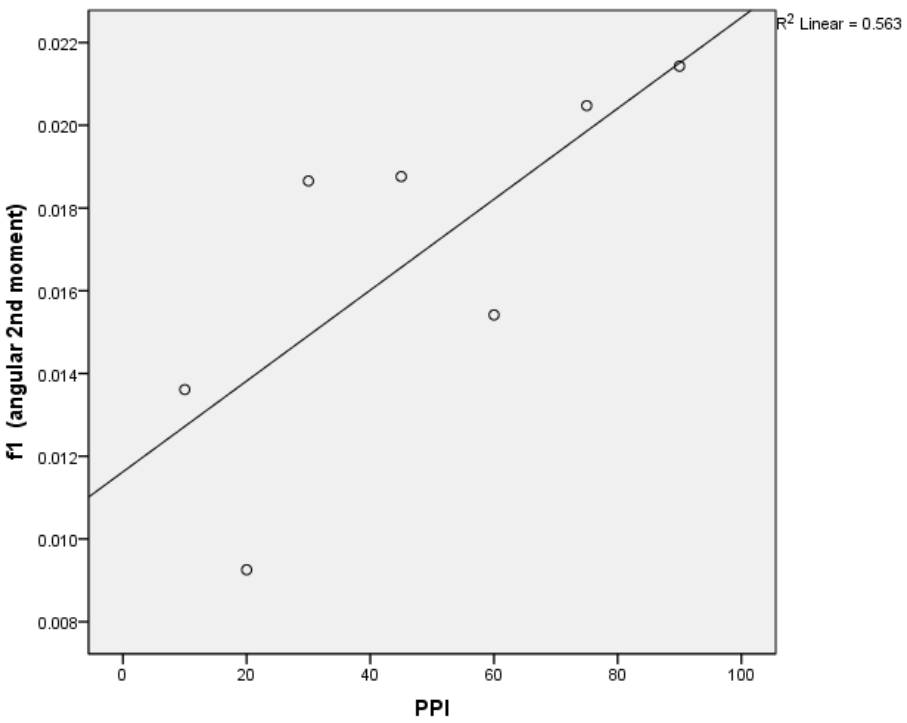

Figure 4.8: Pearson correlation graph for texture parameter f_1 (angular 2nd moment) against PPI for the larger ROI

4.3.2 Correlation of T_2 values with porosity

Once the T_2 maps were obtained for each foam sample Pearson correlation coefficients were calculated, the graphs revealed reasonable R^2 values (fig 4.9) of 0.479 indicating that 48% of the variation in the larger ROI mean data can be explained by the change in pore size. The p-values were not significant with 0.085 (large ROI) and 0.162 (small ROI) indicating a poor confidence level (table 4.3). In addition variations in mean T_2 values between pore sizes of foam were very small, for the large ROI (Table 4.4) the variation around the mean was only 4.4% and even less at 3.9% for the small ROI. These very small variations around the mean indicate virtually no way of distinguishing different pore sizes using T_2 Mapping alone.

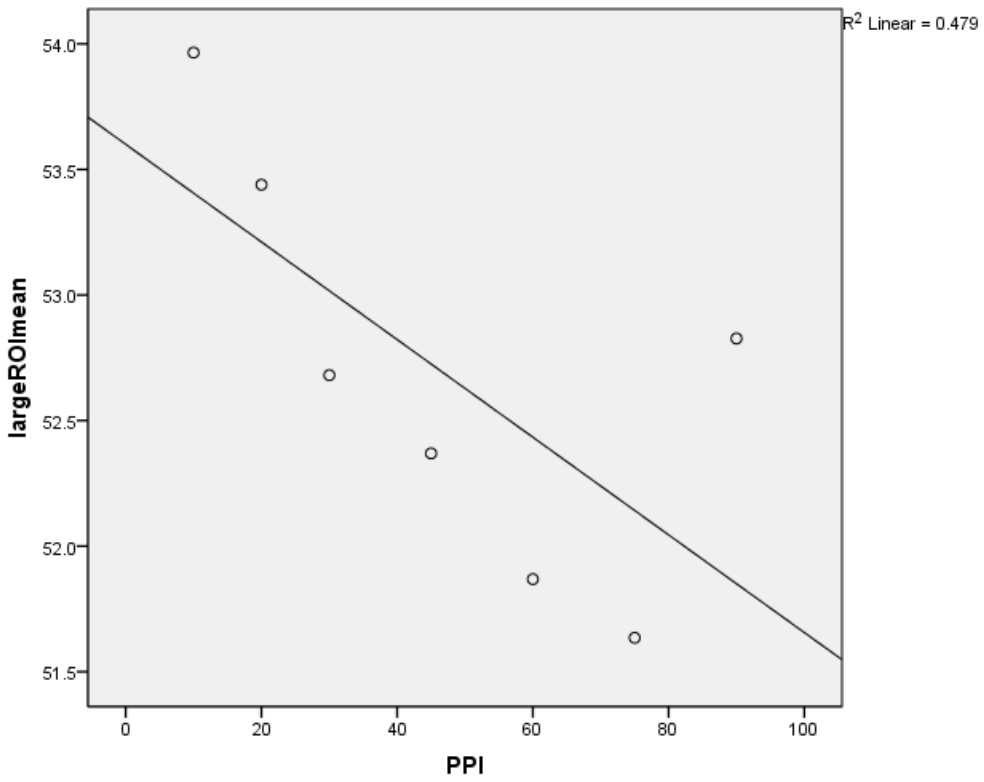

Figure 4.9: Pearson correlation graph for large ROI mean T_2 value against PPI

ROI size	R^2	P value
large	0.479	0.085
small	0.35	0.162

Table 4.3: correlation results for mean T_2 values against varying foams according to PPI size for small and large ROIs

	mean large ROI	mean small ROI
PPI10	53.9651	53.7752
PPI20	53.4393	53.2053
PPI30	52.6806	52.5009
PPI45	52.3691	52.2673
PPI60	51.8683	51.8991
PPI75	51.6349	51.7469
PPI90	52.8267	52.9327

Table 4.4: mean values taken from the T_2 maps of each pore size. The results clearly show very small change in values according to PPI of each foam phantom (4.4% variation around the mean for the large ROI and 3.9% for the smaller ROI)

4.3.3 Repeatability of texture analysis

Repeatability was also tested between the two sets of vibrant scans that were obtained for both the small and large ROI. The results as per Tables 4.5 and 4.6 clearly indicate that texture analysis is repeatable as it shows similar results on analysis of scans taken at different times using the same MRI protocols. The tables show mean, repeatability and percentage change of each texture parameter calculated using two separate scans for each of the seven PPI sizes of the foam phantom. Figures 4.10 and 4.11 highlight the most and least repeatable texture parameters f_8 and f_{15} respectively in the form of Bland Altman scatter plots.

Texture parameters	Mean	Repeatability	% change
f_1 (angular 2nd moment)	0.017	0.001	**4.66%**
f_2 (contrast)	2.876	0.533	**18.55%**
f_3 (correlation)	0.923	0.013	**1.42%**
f_4 (variance)	19.414	0.266	**1.37%**
f_5 (inv diff moment)	0.581	0.015	**2.59%**
f_6 (sum average)	17.138	0.027	**0.16%**
f_7 (sum variance)	80.768	0.569	**0.70%**
f_8 (sum entropy)	4.934	0.006	**0.12%**
f_9 (entropy)	6.276	0.079	**1.26%**
f_{10} (difference variance)	1.362	0.302	**22.19%**
f_{11} (difference entropy)	1.924	0.106	**5.51%**
f_{12} (info m' of corr' 1)	-0.431	0.020	**4.61%**
f_{13} (info m' of corr' 2)	0.974	0.004	**0.45%**
f_{14} (max corr' coeff')	0.960	0.004	**0.38%**
f_{15} (cluster shade)	-26.848	7.158	**26.66%**
f_{16} (cluster prominence)	11757.247	131.088	**1.11%**

Table 4.5: Repeatability test values for all PPI sizes of foam showing values for each texture parameter using two separate MRI scans and running texture analysis using the larger ROI

Texture parameters	Mean	repeatability	% change
f_1 (angular 2nd moment)	0.013	0.001	**7.93%**
f_2 (contrast)	6.767	1.211	**17.89%**
f_3 (correlation)	0.825	0.028	**3.44%**
f_4 (variance)	17.411	0.568	**3.26%**
f_5 (inv diff moment)	0.468	0.031	**6.61%**
f_6 (sum average)	17.165	0.049	**0.29%**
f_7 (sum variance)	76.721	1.139	**1.48%**
f_8 (sum entropy)	4.909	0.011	**0.23%**
f_9 (entropy)	6.642	0.104	**1.56%**
f_{10} (difference variance)	2.968	0.473	**15.95%**
f_{11} (difference entropy)	2.429	0.131	**5.40%**
f_{12} (info m' of corr' 1)	-0.340	0.026	**7.56%**
f_{13} (info m' of corr' 2)	0.942	0.008	**0.83%**
f_{14} (max corr' coeff')	0.914	0.019	**2.09%**
f_{15} (cluster shade)	-57.041	14.008	**24.56%**
f_{16} (cluster prominence)	10780.491	319.303	**2.96%**

Table 4.6: Repeatability test values for all PPI sizes of foam showing values for each texture parameter using two separate MRI scans and running texture analysis using the smaller ROI

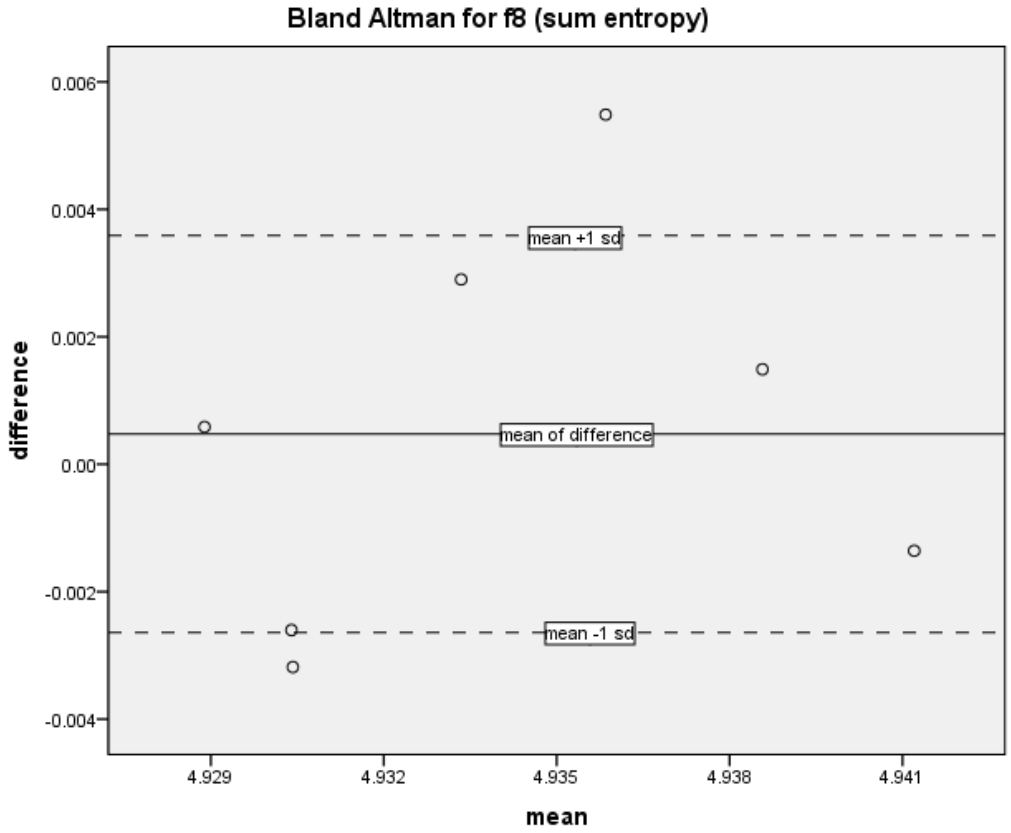

figure 4.10: Bland Altman plot showing mean and difference values for texture parameter f_8 (sum entropy) for the larger ROI

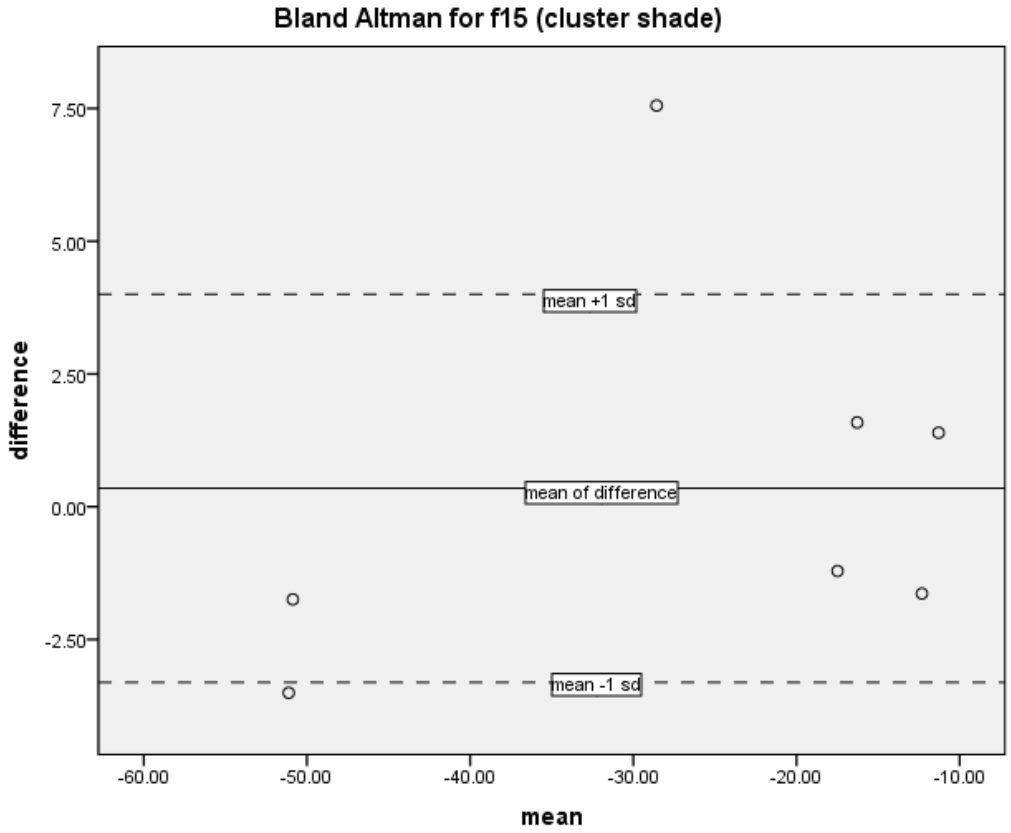

Figure 4.11: Bland Altman plot showing mean and difference values for texture parameter f_{15} (cluster shade) for the larger ROI

4.3.4 Repeatability of T_2 Mapping

Repeatability was also tested between the two sets of FSE scans that were obtained for both the small and large ROI. The results as per table 4.7 clearly show excellent repeatability percentage values indicating that T_2 Mapping is highly repeatable. The tables show mean of differences, standard deviation of differences and repeatability of each ROIs mean T_2 Mapped value calculated using two separate scans for each of the seven PPI sizes of the foam phantom.

ROI size	Mean of differences	Std dev of differences	repeatability (%)
large	0.040	0.156	**0.58%**
small	-0.053	0.081	**0.30%**

Table 4.7: Repeatability test values for all PPI sizes of foam showing values for each ROI using two separate MRI scans and calculating the mean of T_2 Mapped images using the small and large ROIs

4.4 Discussion

Pearson correlation graphs for T_2 maps indicated that 48% of the variation in the larger ROI mean data can be explained by the change in pore size (fig 4.9). The p-values 0.085 and 0.162 for large and small ROI's respectively indicate a poor confidence level. Variations in mean T_2 values between pore sizes of foam were very small (3.9% variation around the mean for the small ROI) (table 4.4). These very small variations in mean indicate virtually no way of distinguishing different pore sizes using T_2 Mapping alone.

For texture analysis the PPI contributes to 61% of the variation in f_{15} (fig 4.6), having a p-value of < 0.05 shows that the confidence level of the 61% variation is good. In the 3 texture parameters (f_1, f_{15} and f_{16}) the graphs show general trend of the smaller the pore size the higher the texture parameters value, this demonstrates that PPI sizes clearly affect the value of texture analysis parameters in these cases despite the MR images looking visually indistinguishable. Unlike the mean T_2 values the texture parameters have much larger variation (Table 4.2), for example a variation around the mean of 77.26% was noted for parameter f_1 between different pore sizes for the smaller ROI. These larger variations in texture parameters indicate pore sizes are clearly distinguishable when using texture analysis. Having this bigger percentage change in texture shows promise for use in a clinical environment. Clinical images will also suffer from lower SNR therefore having very small variations using T_2 mapping alone may not be useful as this small change could be attributed to SNR and therefore unreliable. However this was not a phantom of breast tissue therefore requires caution in extrapolating results.

The texture parameters proved to have good repeatability with 12 of the 16 (Tables 4.5 and 4.6) parameters being more repeatable with the larger ROI than the smaller ROI, this shows that the co-occurrence method of texture analysis relies heavily upon having good counting statistics. This indicates that in clinical images distinguishing smaller lesions using texture analysis may be problematic. The 3 parameters (f_2, f_{10} and f_{15}) that showed poorer

repeatability values for both large and smaller ROIs need to be investigated further and establish whether mathematically there is an underlying cause. With the exception of texture parameter f_{10} for which repeatability value decreases from 22.19% for the large ROI to 15.95% for the smaller ROI (tables 4.5 and 4.6), the results show that the larger ROI is more repeatable when texture analysis is performed on the MRI scan. Any variation would need to be higher than the values in the repeatability column of the two tables for each texture parameter in order for it to be perceived as an actual valid treatment induced change. In vivo repeatability will probably be worse due to lower SNR from clinical images.

4.5 Conclusion

Texture analysis reliably demonstrated its ability to differentiate between varying grades of foam in an agar embedded phantom despite them appearing visually indistinguishable on an MR image. This study proved that texture analysis demonstrates good repeatability in MR.

5 Texture Analysis on Breast Cancer Patients

5.1 Texture Analysis as a Predictor of Chemotherapeutic Response

5.1.1 Introduction

Predicting response to chemotherapy is important, both from the economic perspective as treatment is expensive and due to the incidence of side effects including bone marrow depression, gastrointestinal upset and alopecia. Knowing whether a patient will respond to chemotherapy is difficult to predict, but if accurate assessment was possible would allow prompt change in chemotherapy regime or early resort to surgery.

The identification of specific types of breast cancer is important in a clinical setting as these influence prognosis and response to treatment. The traditional triple receptor negative phenotype (TNBC) [negative staining for estrogen receptor(ER), progesterone receptor (PR), human epidermal growth factor receptor2 (HER2)], can be subdivided into “basal-like” and “normal-like” subgroups on further assessment. Profiling gene expression in breast cancer provides five sub-groups based on transcriptomic similarity: luminal A, luminal B, normal-like, Her2/neu positive and basal-like (BBC) [80, 81]. The BBC is a particularly aggressive subtype, although not all TNBC are basal-like in subtype and not all BBC are triple receptor negative. TNBC are associated with a particularly poor outlook, in part due to the lack of treatment options other than chemotherapy. Consequently novel targeted chemotherapeutic strategies are being developed for this group, prompting the need for close monitoring to predict response to therapy. Approximately 30% of all patients respond sub-optimally to treatment and this is known to vary between immuno-receptor subtypes. It is becoming increasingly important to assess response to treatment, both early so that recourse to alternative therapy can be considered, and at the end of treatment prior to definitive surgery.

Response Evaluation Criteria in Solid Tumours (RECIST) is a simplified, conservative, means of extracting measurements of solid tumour from imaging data and is widely applied in clinical trials. RECIST presumes that linear measures are an adequate substitute for area and/or volume and registers four response categories: CR (complete response) = disappearance of all

target lesions; PR (partial response) = 30% or greater decrease in the sum of the longest diameters of target lesions; PD (progressive disease) = 20% or greater increase in the sum of the longest diameters of target lesions; SD (stable disease) = small changes that do not meet above criteria [82]. Other studies have not always followed this criteria strictly. Manton et al [83] used a volume measurement of 65% as the cut off between PR and SD, this being equivalent to a decrease in cross-sectional area of 50%, itself broadly equivalent to a 50% decrease in the product of maximum orthogonal diameters (a RECIST criterion).

For the purpose of detecting and evaluating breast disease researchers [38] often use quantitative T1-weighted dynamic contrast-enhanced MRI (T_1-w DCE-MRI). This technique involves the intravenous administration of a gadolinium (Gd) based contrast agent during repeated T1-weighted imaging. The Gd concentration vs. time curve ([C](t)) of a lesion of interest can be estimated from these images. By applying pharmacokinetic modelling, parameters such as extraction-flow product can be extracted to aid lesion diagnosis and tracking of treatment progress [39]. However these parameters are prone to error. For example, minor variations in the transmit magnetic field (B_1) can result in up to 50% error on the estimated [C](t) in 2D spoiled gradient echo sequences (SPGR) [39]. In turn this leads to errors in the estimated PK parameters, thus potentially reducing the sensitivity and specificity of this technique and limiting its applicability for tracking treatment progress [39].

Analysis of images for functional information is not the only way of determining the presence of disease; as outlined in the Bi-RADS lexicon [23] morphology is also an important factor used in assessing MR images. Textural analysis is one such method of assessing morphology, and sSome attempts have been made to utilise texture in MR image analysis [42-50, 53, 59, 61, 62, 68, 69], particularly in the brain [42-44, 61, 62].

Freeborough et al [42] assessed the value of MR derived textural parameters as a measure of evaluating change in Alzheimer's disease. Texture was calculated using a co-occurrence matrix

and the Haralick texture formulae f_1-f_{13} [53]. This statistical technique, known as the spatial gray-level dependence matrix method, has the ability to study 2nd order statistics of pixels at different spacings and angles of adjacent or nearest-neighbour pixels. The Freeborough [42] study demonstrated that a texture discriminant function derived from MRI brain scans using a spoiled gradient-echo technique on a 1.5T system yielded significantly different values for Alzheimer's sufferers compared to normal controls [42]. In addition, this measure reflected the progression of the disease over time, and could potentially be useful as an aid in the diagnosis and in tracking of disease progression.

A study by Kjaer et al [62] found that considerable texture information was contained in MR images that was useful for characterisation of normal brain tissue. In addition the authors found that texture information showed potential for differentiation between sub-types of intracranial tumours. Lerski et al also performed texture analysis on images for tissue characterisation [61] in the human brain, and demonstrated clinical utility for discriminating between brain tumour and oedema.

Recent research has focussed on other organs including the breast. A 79 patient study by Gibbs et al [48], using data taken from the largest cross-sectional area of individual lesions acquired using contrast-enhanced MRI, demonstrated significant differences in textural features between benign and malignant breast tumours. Variance, entropy and sum entropy, all measures of image heterogeneity, were found to be important factors in lesion discrimination when combined using a logistic regression model. In a smaller study of 23 benign and 20 malignant breast lesions, Sinha et al [50] examined the utility of textural features derived from DCE-MRI using 8 of the 13 Haralick features [53]. This study showed significant differences in only three of the eight texture features calculated, but using a combination of features obtained a specificity and sensitivity of 70% and 75% respectively.

In an attempt to verify the findings by Gibbs et al [45] a further study was carried out by Chen et al [47] focussing on the use of a 3D grey level co-occurrence matrix (GLCM), as opposed to a 2D version. The work described a volumetric texture analysis approach for computerised analysis of breast lesions on DCE-MRI. The study showed that texture features from a 3D analysis yielded significantly better classification results than from a 2D analysis.

A more recent study by Bhooshan et al, (2010) of DCE-MRI breast images used texture analysis along with other computerised methods such as shape and kinetic features, in an attempt to determine their utility as prognostic markers. The authors found that in terms of textural features, a common indicator of malignancy was lesion heterogeneity, which could be described by using different mathematic algorithms for texture analysis such as contrast and maximal correlation coefficient [46].

Whilst previous research has generally concentrated on quantifying morphology from high resolution data, there appears to be some value in assessing lesion texture in DCE-MRI [45], especially with regards to changes in signal intensity following contrast administration during the initial enhancement and subsequent washout phases. A study by Agner et al of 41 cases (17 benign and 24 malignant) demonstrated that when DCE-MRI was analysed using textural parameters combined with morphological descriptors, utilising a probabilistic boosting tree framework as its learning model, the resulting classifier yielded 89% accuracy, 99% sensitivity, 76% specificity and an AUC of 0.91 [45].

The spatial grey-level dependence matrix method, as proposed by Haralick [53], is the commonest form of analysis for texture, but there is no direct evidence concerning the most appropriate pixel separation and number of grey levels required to utilise the optimum co-occurrence matrix calculations. The aim of this study is to systematically assess the efficacy of DCE-MRI based textural analysis, throughout the contrast enhanced time course, in predicting

and assessing response to neoadjuvant chemotherapy in a cohort of breast cancer patients. The impact of varying the number of grey levels employed is further examined.

5.1.1.1 Aims

The aims of this research include:

- Develop a robust software package for texture analysis of MRI data
- Apply developed software to cohort of 100 patients undergoing neoadjuvant chemotherapy of breast cancer, to help predict tumour response

5.1.2 Methods: The Data

5.1.2.1 Patient Population

The data acquired from 100 patients, age range of 31-77 years, median age of 48 years, all undergoing neoadjuvant chemotherapy for treatment of locally advanced breast cancer at this Institute between April 2006 and September 2008 was retrospectively reviewed. This study was approved by the Local Ethics Committee and NHS Trust. Post treatment biopsy grade was known in 97 patients (4 not specified, 6 grade 1, 32 grade 2, 55 grade 3). Details of treatment regime were available in 95 patients, the majority of whom (57) had a combination of EC (Epirubicin and Cyclophosphamide) and Docetaxel. MR data was acquired prior to treatment and information on tumour response was obtained on completion of all cycles of NAC. The number of days between initial baseline MR scan and chemotherapy starting ranged from 1-45 days with a median of 11.5 days.

After treatment the patients were categorized according to their response to chemotherapy from MR data: partial responders (PR) corresponding to a decrease in longest diameter of tumour of greater than 50% (40 patients) and non-responders (NR) corresponding to a decrease of less than 50% (49 patients). Data for the remaining 11 patients was not available.

Data was also split based on factors that are known to influence response: TNBC (22 patients) vs. all other combinations of the three appropriate markers (49 patients) with 29 patients data

unavailable; subdivided into nodal status by examining node negative (45 patients) vs. node positive (46 patients) with data in 9 patients not available; and tumour grade derived from pre-treatment biopsy, biopsy grade 1 or 2 (38 patients) vs. biopsy grade 3 (55 patients) and 7 patients data was not available.

5.1.2.2 MRI Protocol

All patients were scanned on a 3.0T HDx (GE Healthcare, Milwaukee, WI) scanner in combination with an 8-channel dedicated breast coil. This study used data from a dynamically acquired contrast-enhanced sequence employing the following parameters: sagittal 3D T1W fat nulled Volume Imaging for Breast Assessment (VIBRANT) sequence [10° flip, TR 4.1ms, TE 1.6ms/Fr, 41.7kHz, 22x22cm FOV, 220x160 matrix, 4/-2mm slice/gap (4/0 in first 21 exams), parallel imaging x 2]. This dynamic sequence included 2 phases pre-contrast and 10 phases post-contrast administration, with an average temporal resolution of 33.6 seconds (range 23.5 to 44.6 seconds). Minor alterations in temporal resolution were noted due to the variable number of slices required to image both breasts in their entirety. Contrast medium was delivered by a Spectris Solaris power injector (Medrad, Warrendale, PA). At the start of the 3rd phase a bolus injection of gadolinium (Schering, Magnevist) contrast agent (0.05 mmol/kg body weight) was immediately followed by a 20ml saline flush, with a total injection time of 10 seconds for all patients.

5.1.2.3 Quantitative Analysis

Regions-of-interest (ROIs) were generated semi-automatically on all slices utilising early arterial phase data, whereby a seed point was selected on each slice and an ROI was automatically generated based on the Otsu thresholding method. Following a strict software lifecycle, a robust software package was created in house allowing texture analysis to be performed on pre-contrast and 1, 2, 3, 4 and 5 minutes post-contrast data. To prevent sparseness within subsequently calculated co-occurrence matrices, the ROI data underwent grey level decimation via histogram equalisation. ROI data was reduced to 8, 16, 32 and 64

grey levels since the optimal number of grey levels required for textural analysis is unknown (reducing the number of grey levels improves SNR at the expense of discriminatory power). The ROIs were selected on images across multiple slices all containing tumour, thus giving a complete representation of the tumour.

Co-occurrence matrices, which contain the joint probability of two adjacent pixels along a given direction θ having co-occurring values i and j, were calculated for θ = 0°, 45°, 90° and 135° and subsequently averaged. The 14 textural features as defined by Haralick [53] (denoted f_1 to f_{14} and including entropy, angular second moment and correlation) were then determined alongside two further parameters namely cluster shade (f_{15}) and cluster prominence (f_{16}) [55]:

$$\sum_i \sum_j (i + j - \mu_x - \mu_y)^3 \, p(i,j)$$

(f_{15} Cluster Shade)

$$\sum_i \sum_j (i + j - \mu_x - \mu_y)^4 \, p(i,j)$$

(f_{16} Cluster Prominence)

where $p(i,j)$ is the probability of i, j in the co-occurrence matrix,

$$\mu_x = \sum_i i \, P_x$$

$$\mu_y = \sum_i i \, P_y$$

$$P_x = \sum_j p(i,j)$$

$$P_y = \sum_i p(i,j)$$

The 14 Haralick parameters f_1 to f_{14} applied in the software application have been previously described by this group (Gibbs et al [48]):

Notation: N is the number of distinct gray levels in the histogram equalized image; $p(i,j)$ is the (i,j)th entry in a normalized spatial gray-level dependence matrix; and $p_x(i)$ is the i-th entry in the marginal-probability matrix obtained by summing the rows of $p(i,j) = \sum_j p(i,j)$

$$P_{x+y}(n) = \sum_i \sum_{\substack{j \\ i+j=n}} p(i,j)$$

with n = 2, 3, ..., 2N

$$P_{x-y}(n) = \sum_i \sum_{\substack{j \\ [i-j]=n}} p(i,j)$$

with n = 0, 1, ..., N - 1

Textural Feature:

$$\sum_i \sum_j p(i,j)^2$$

(f_1 Angular Second Moment)

$$\sum_{n=0}^{N-1} n^2 \, p_{x-y}(n)$$

(f_2 Contrast)

$$\frac{\sum_i \sum_j (ij)p(i,j) - \mu_x^2}{\alpha_x^2}$$

(f_3 Correlation)

Where μ_x and α_x are the mean and standard deviations of p_x, respectively

$$\sum_{i} p(i - \mu_x)^2 \, p_x(i)$$

(f_4 Variance)

$$\sum_{i} \sum_{j} \frac{1}{1 + (i - j)^2} p(i, j)$$

(f_5 Inverse Difference Moment)

$$\sum_{n=2}^{2N} n \, p_{x+y}(n)$$

(f_6 Sum Average)

$$\sum_{n=2}^{2N} (n - f_6)^2 \, p_{x+y}(n)$$

(f_7 Sum Variance)

$$-\sum_{n=2}^{2N} p_{x+y}(n) \log \left(p_{x+y}(n)\right)$$

(f_8 Sum Entropy)

$$-\sum_{i} \sum_{j} p(i, j) \log \left(p(i, j)\right)$$

(f_9 Entropy)

$$\sum_{n=0}^{N-1} (n - \mu_{x-y})^2 p_{x-y}(n)$$

(f_{10} Difference Variance)

Where μ_{x-y} is the mean of p_{x-y}

$$-\sum_{n=0}^{N-1} p_{x-y}(n) \log (p_{x-y}(n))$$

(f_{11} Difference Entropy)

$$\frac{f_9 + \sum_i \sum_j p(i,j) \log (p_x(i) p_x(j))}{-\sum_i p_x(i) \log (p_x(i))}$$

(f_{12} Information Measure of Correlation 1)

$$\sqrt{1 - e^{-2(H_{xy} - f_9)}}$$

(f_{13} Information Measure of Correlation 2)

where $H_{xy} = -\sum_i \sum_j p_x(i) p_x(j) \log (p_x(i) p_x(j))$

$$\sqrt{\text{Second largest eigenvalue of } Q}$$

(f_{14} Maximal Correlation Coefficient)

where $Q(i,j) = \sum_k (p(i,k) p(j,k)) / (p_x(i) p_x(k))$

5.1.2.4 Statistical Analysis

Statistical analysis of the individual texture parameters was performed to establish whether the results were normally or non-normally distributed. The texture data was combined with all relevant clinical data. Mann Whitney and t-tests were executed using SPSS version 15.0 on the combined data, as appropriate, with a p-value of <0.05 regarded as indicating significant difference between groups. Since this study can be regarded as hypothesis generating no corrections for performing multiple statistical tests were made.

5.1.3 Methods: The software application

5.1.3.1 GLCM

The software application was created using the matrix based programming language MATLAB, the grey-level dependence matrix (GLCM) method was used and is illustrated in detail in section 2.6.1.4.

5.1.3.2 Region of Interest (ROI)

A vital part of the software application is its ability to obtain pixel values from a pre-drawn ROI as well as accurately draw an ROI using the computers mouse, the accuracy of this is paramount as the pixel values obtained are the backbone of any future calculations. Regions-of-interest (ROIs) were generated semi-automatically on all slices utilising early arterial phase data whereby a seed point was selected on each slice and an ROI was automatically generated based on the Otsu thresholding method. ROIs were subsequently saved in binary file format, the application created for this study reads in these binary files and maps the correct ROI to the correct slice of the dataset. Each ROI file could contain anything from one to any number (no limit) ROI's and a given slice may also contain more than one ROI. The software application then allows the user to scroll through slice by slice with the correct ROI loaded onto each slice, the user may then perform texture analysis for the current slice in the application viewer or perform a full texture analysis on multiple slices (fig 5.1).

For the texture analysis calculations the software application utilises ROIs on the breast images across multiple slices, this gives a complete representation of the tumour as opposed to just a single slice.

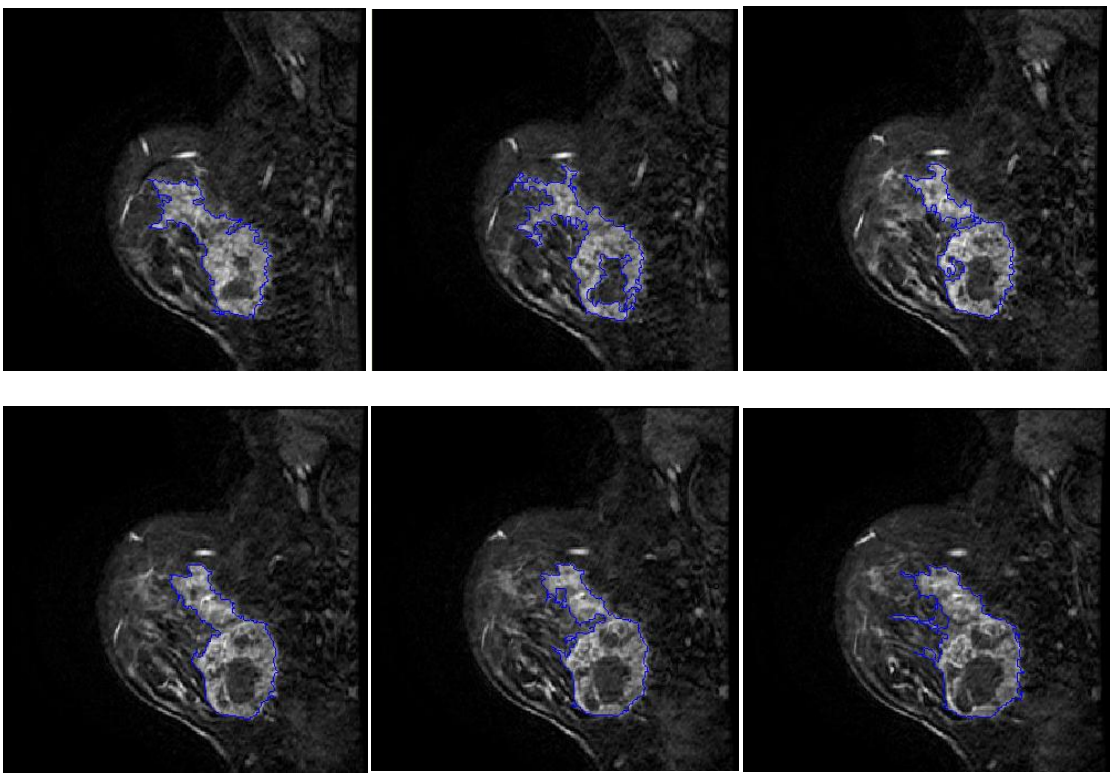

Figure 5.1: : Images obtained at 2 minutes post contrast, in breast cancer patient (age 48, grade on biopsy 3, Node –ve, HER2 –ve, PR-, ER-) prior to undergoing neoadjuvant chemotherapy. Patient subsequently defined as partial responder with a >50% reduction in tumour size. The total lesion pixel count for all slices was 57745 pixels. The images show the variable appearance through each slice of the tumour and the absence of contrast uptake centrally due to tumour necrosis. Treatment 4 cycles EC, 4 cycles Docetaxel.

5.1.3.3 Histogram Equalisation

Histogram equalisation removes the overall brightness information in an image. In a given digital image the graphical representation of the tonal distribution of that image in the form of a histogram is referred to as the image histogram, it plots the number of pixels for each tonal value. The entire tonal distribution can be judged at a glance by looking at the histogram for a specific image. Histogram equalisation is a method in image processing of adjusting contrast using the histogram of that image [84]. Histogram equalisation normally increases the global contrast of lots of images, especially when the image has close contrast values, this adjustment allows the intensities to be better distributed on the histogram. In turn this allows areas of

lower local contrast to gain higher contrast. Histogram equalisation achieves this by effectively spreading out the most frequent intensity values [84]. It is a useful method in images where the foregrounds and backgrounds are either both dark or both bright.

Although MATLAB has its own function for histogram equalising an image for the purpose of this study a new class had to be written, this was because Matlab's function applies histogram equalisation to the whole image and does not allow the user to apply it to the ROI only, which is important for the purpose of this study. Figure 5.2 shows a normal image MRI image of the breast, figure 5.3 shows the same image after applying histogram equalisation. Histogram equalisation improves counting statistics at the expense of discriminatory power.

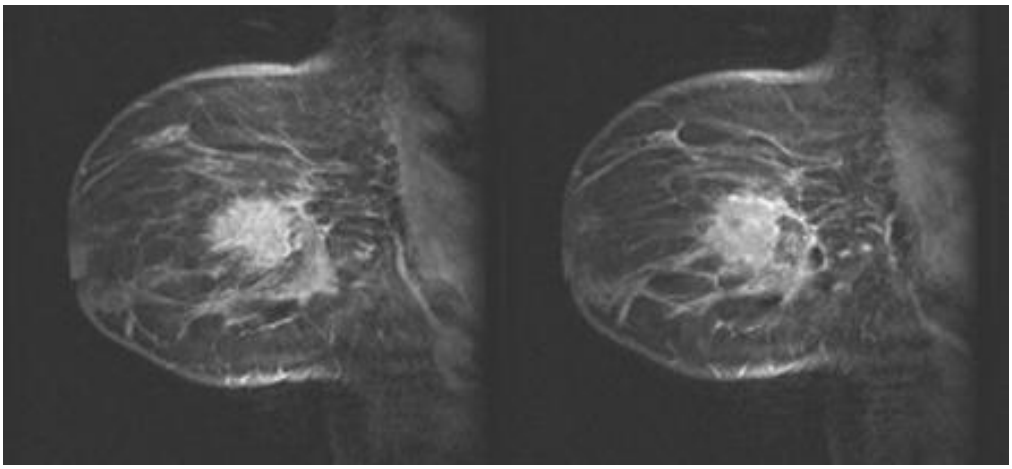

Figure 5.2: MRI breast image prior to histogram equalisation

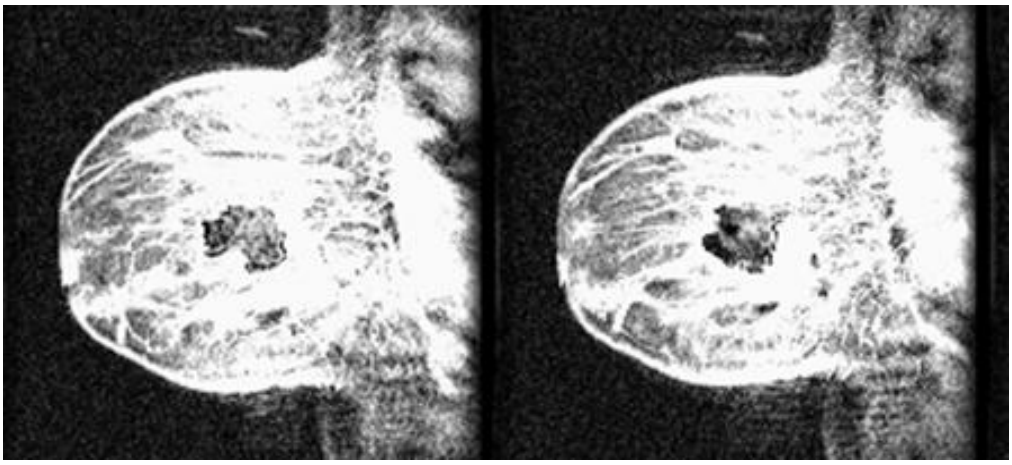

Figure 5.3: MRI breast image post histogram equalisation of lesion only

5.1.3.4 Grey levels

The number of grey levels determines the size of the GLCM matrix, it is difficult to know the optimum as having too large a GLCM and the matrix becomes noisy. Within the application created in this study the grey levels are user selectable to 8, 16, 32, 64..., the application then averages (normalises) the GLCM matrix to remove directional bias (figures 5.4, 5.5 and 5.6), the figures also outline the issue of having higher number of grey levels results in a noisier matrix albeit with more information. The histograms in figures 5.7 and 5.8 show pre and post gray level decimation.

```
glcm(:,:,1) =

          54          53           0           0           0           0           0           0
          52        1696         402          13           0           0           0           0
           1         385        2479         979          36           1           0           0
           0          28         913        7099        1502          18           0           0
           0           0          28        1411        4761         455          11           0
           0           0           2          34         447         726          55           1
           0           0           0           1           2          63          75          10
           0           0           0           0           0           1          10          12


glcm(:,:,2) =

          27          75           5           0           0           0           0           0
          73        1516         498          73           3           0           0           0
           6         498        2008        1230         119           2           0           0
           1          63        1082        6030        2005          73           1           0
           0           8          93        1684        4034         572          27           0
           0           2           9          77         530         542          65           3
           0           0           0           8           9          71          50          12
           0           0           0           0           2           5           8           8


glcm(:,:,3) =

          45          59           3           0           0           0           0           0
          58        1645         418          41           1           0           0           0
           4         435        2315        1112          59           1           0           0
           0          23         987        6741        1719          37           1           0
           0           0          43        1474        4522         499          11           0
           0           0           0          37         468         668          64           1
           0           0           0           0           6          67          64          13
           0           0           0           0           0           3          11           9


glcm(:,:,4) =

          32          71           2           2           0           0           0           0
          67        1472         527          84          10           3           0           0
           6         530        1922        1259         157           7           1           0
           2          80        1141        6016        1917          98           7           1
           0           9         154        1730        3957         539          17           0
           0           0          10          87         501         550          58           3
           0           0           0           1          25          54          57          13
           0           0           0           0           1           5          11           6
```

Figure 5.4: an example of GLCM matrix using 8 gray levels in four directions, averaged to remove directional bias. Adjacent pixel entries are similar as one would expect

```
glcm(:,:,1) =

  Columns 1 through 12

         0         2         0         0         0         0         0         0         0         0         0         0
         2        50        45         8         0         0         0         0         0         0         0         0
         0        48       558       230        38         4         3         0         0         0         0         0
         0         4       242       666       290        70         8         2         0         0         0         0
         0         0        27       295       642       393       102        12         2         0         0         0
         0         1         6        57       379      1065       701       164        28         6         1         0
         0         0         1        19        89       667      2304      1170       180        29         2         1
         0         0         2         6        21       136      1107      2518      1121       172        15         0
         0         0         0         0         9        15       151      1100      2144       734        81        12
         0         0         0         0         0         4        14       146       741      1142       313        49
         0         0         0         0         0         2         6        16        82       317       403        98
         0         0         0         0         0         0         8         4         8        40       115       110
         0         0         0         0         0         0         0         1         1         1        12        38
         0         0         0         0         0         0         0         0         0         0         2        11
         0         0         0         0         0         0         0         0         0         0         1         0
         0         0         0         0         0         0         0         0         0         0         0         0

  Columns 13 through 16

         0         0         0         0
         0         0         0         0
         0         0         0         0
         0         0         0         0
         0         0         0         0
         0         0         0         0
         0         0         0         0
         0         0         0         0
         1         0         0         0
        10         0         0         0
        18         2         0         0
        28         7         1         0
        27        20         3         0
        15        13         7         0
         4         6         6         2
         0         0         2         2
```

Figure 5.5: GLCM matrix using 16 gray levels

```
glcm(:,:,1) =

  Columns 1 through 25

    0     0     0     0     0     0     0     0     0     0     0     0     0     0     0     0     0     0     0     0     0     0     0     0     0
    0     0     1     1     0     0     0     0     0     0     0     0     0     0     0     0     0     0     0     0     0     0     0     0     0
    0     1     4     9     1     0     0     0     0     0     0     0     0     0     0     0     0     0     0     0     0     0     0     0     0
    0     1     5    32    28    16     6     2     0     0     0     0     0     0     0     0     0     0     0     0     0     0     0     0     0
    0     0     5    34   128    95    26    12    10     0     1     0     0     0     0     0     0     0     0     0     0     0     0     0     0
    0     0     0     9    89   246   146    46    19     9     2     1     2     1     0     0     0     0     0     0     0     0     0     0     0
    0     0     0     3    34   148   231   133    66    23    13     7     2     1     0     0     0     0     0     0     0     0     0     0     0
    0     0     0     1    17    43   148   154   123    78    29    21     3     2     1     1     0     0     0     0     0     0     0     0     0
    0     0     0     0     7    12    57   137   167   137    85    49    19    11     1     2     0     1     0     0     0     0     0     0     0
    0     0     0     0     4     4    31    70   158   180   159   100    51    21     4     5     1     0     0     0     0     0     0     0     0
    0     0     0     1     1     3     8    28    79   164   246   226   141    53    29     8     5     1     0     0     0     0     0     0     0
    0     0     0     0     0     2     3    18    38    98   219   374   338   169    88    39    15     7     5     1     1     0     0     0     0
    0     0     0     0     1     0     1     9    13    52   133   313   573   503   243    94    38    15     6     1     0     0     0     0     0
    0     0     0     0     0     0     4     5     4    20    60   161   464   764   573   260    95    32    17     5     1     1     1     0     0
    0     0     0     0     1     0     0     5     1    13    15    75   230   529   705   551   276    92    40    16     2     0     0     0     0
    0     0     0     0     0     1     0     1     2     5    10    36    94   254   544   718   524   229    70    46     7     6     0     0     0
    0     0     0     0     0     0     0     0     3     4     3     6    28    84   252   510   638   472   193    57    21     5     3     1     0
    0     0     0     0     0     0     0     0     1     1     1     5     9    30    92   246   452   582   364   120    41    14     6     2     0
    0     0     0     0     0     0     0     0     0     0     0     2     2     8    27    86   176   368   425   235    79    26    16     3     0
    0     0     0     0     0     0     0     0     0     0     1     1     0     4    11    22    70   127   220   262   148    60    24     6     0
    0     0     0     0     0     0     0     0     0     0     2     0     1     3     3     6    16    43    89   151   151    76    32    13     0
    0     0     0     0     0     0     0     0     0     0     0     0     2     0     2     5     8    15    24    53    90    86    36    17     0
    0     0     0     0     0     0     0     0     0     0     0     0     3     5     0     1     4     2    12    22    34    47    42    23     0
    0     0     0     0     0     0     0     0     0     0     0     0     0     0     1     2     1     1     2     4    11    23    22    23     0
    0     0     0     0     0     0     0     0     0     0     0     0     0     0     0     1     0     1     0     1     3     3    13    13     0
    0     0     0     0     0     0     0     0     0     0     0     0     0     0     0     0     0     0     0     0     3     3     5     7     0
    0     0     0     0     0     0     0     0     0     0     0     0     0     0     0     0     0     0     0     0     0     1     5     3     0
    0     0     0     0     0     0     0     0     0     0     0     0     0     0     0     0     0     0     0     0     1     0     2     1     0
    0     0     0     0     0     0     0     0     0     0     0     0     0     0     0     0     0     0     0     0     1     0     0     0     0
    0     0     0     0     0     0     0     0     0     0     0     0     0     0     0     0     0     0     0     0     0     0     0     0     0
    0     0     0     0     0     0     0     0     0     0     0     0     0     0     0     0     0     0     0     0     0     0     0     0     0

  Columns 26 through 32

    0     0     0     0     0     0     0
    0     0     0     0     0     0     0
    0     0     0     0     0     0     0
    0     0     0     0     0     0     0
    0     0     0     0     0     0     0
    0     0     0     0     0     0     0
    0     0     0     0     0     0     0
    0     0     0     0     0     0     0
    0     0     0     0     0     0     0
    0     0     0     0     0     0     0
    0     0     0     0     0     0     0
    0     0     0     0     0     0     0
    0     0     0     0     0     0     0
    0     0     0     0     0     0     0
    0     0     0     0     0     0     0
    0     0     0     0     0     0     0
    0     0     0     0     0     0     0
    0     0     0     0     0     0     0
    0     0     0     0     0     0     0
    0     0     0     0     0     0     0
    0     0     0     0     0     0     0
    0     0     0     0     0     0     0
    2     0     0     0     0     0     0
    2     1     0     0     0     0     0
    1     1     0     0     0     0     0
    4     3     1     0     0     0     0
    4     1     2     1     0     0     0
    6    10     3     2     1     0     0
    7     4     3     0     0     0     0
    6     2     2     2     0     0     0
    1     5     4     4     1     0     0
    3     2     3     3     1     1     0
    0     0     1     1     1     1     0
    0     0     0     1     0     0     1
    0     0     0     0     1     0     1
```

Figure 5.6: GLCM matrix using 32 gray levels, its clear there is more information.

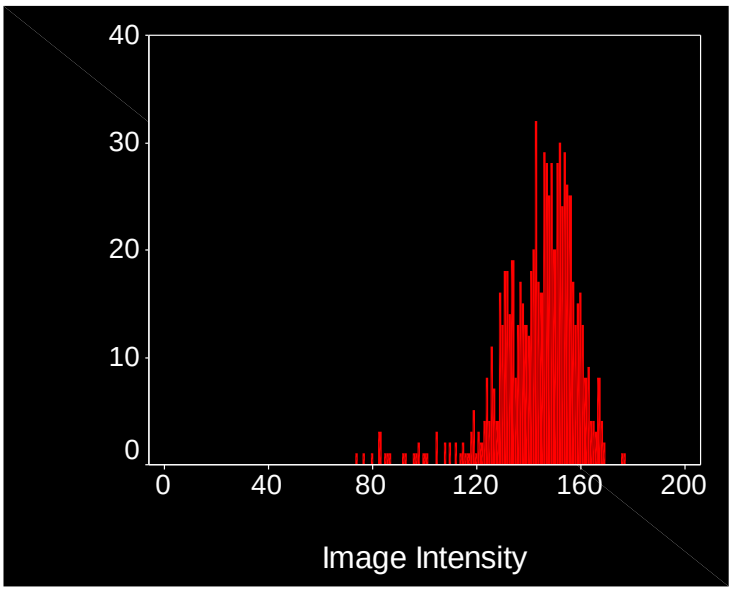

Figure 5.7: prior to gray level decimation

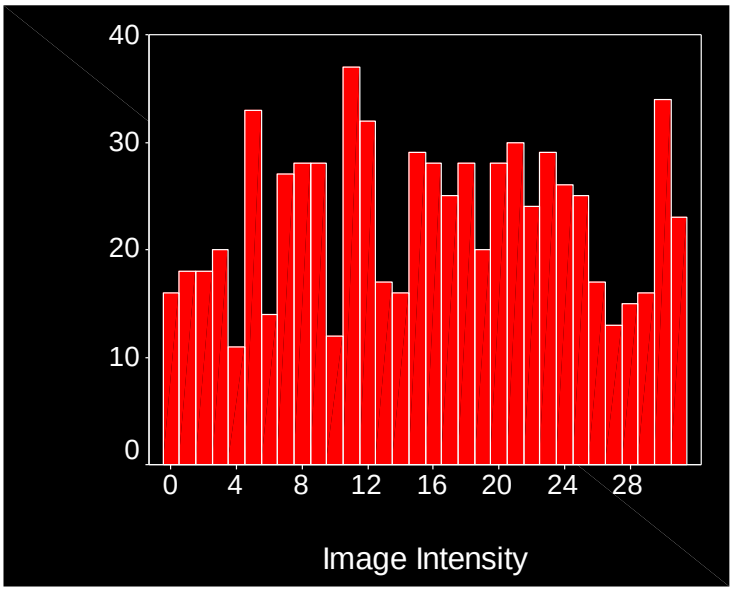

Figure 5.8: post gray level decimation and histogram equalisation

5.1.3.5 Application of formulas

The heart of the results obtained from the application is undoubtedly reliant on the mathematics, this is in the form of the texture formulas that are applied to each ROI once the ROI binary file is loaded onto the set of images (detailed in chapter 3). The texture analysis formulas as shown previously in 5.1.2.3 had to be mathematically simplified and transformed

into MATLAB code so that they could be applied once a co-occurrence matrix had been generated. There are in total 16 texture parameters [48], 14 of which were originally proposed by Haralick [53] which give information about the texture of any given image, primarily for the purpose of this study breast MRI images and the lesions identified within them. In order to ensure a robust software application was developed the software life cycle was followed as outlined in section 3.1.

5.1.4 Results

For the texture analysis calculations the software application utilises ROIs from breast images across multiple slices, to provide a complete assessment of the volume of tumour present. Over the 100 patient datasets examined the pixel count for each patient ranged from 220 to 69725 pixels, with a median count of 6424.5 pixels. Figure 5.1 shows a snapshot of 6 slices from a patient undergoing neoadjuvant chemotherapy; the images show the variable appearance of the tumour through the slices and the presence of central necrosis. All the data used for PR/NR and nodal status determination was found to be normally distributed and hence t-tests were performed. Similarly t-tests were performed on the data found to be normally distributed for the group TNBC vs. all others, some of this data was non-normally distributed and Mann-Whitney tests were performed in those cases. Tumour grade data also contained a mixture of normally distributed and non-normally distributed data and appropriate tests were performed.

5.1.4.1 Response to Neoadjuvant Chemotherapy (% change in longest diameter)

Table 5.1 shows the mean/standard deviation (for normally distributed data) or median/range (for non normally distributed data) and p-values for all 16 texture parameters with highlighted areas demonstrating significant differences between groups for the results obtained with 16 grey levels and at the 2 minute post contrast time point. Table 5.2 summarises the significant differences in texture between PR and NR patients across all time points and grey levels. It is evident that f_2 and f_{10} provide consistent significant differences between partial responders

and non-responders at 1 and 2 minutes post contrast administration, with p-values ranging from 0.039 to 0.048.

Texture parameters	Mean value ± Standard Deviation		P value
	NR	PR	
16 grey levels (2min post contrast)			
f_1 (angular 2nd moment)	0.010±0.001	0.010±0.001	0.640
f_2 (contrast)	8.89 ± 2.05	8.02 ± 1.86	0.042
f_3 (correlation)	0.80±0.05	0.81±0.05	0.083
f_4 (variance)	16.41±1.24	16.70±1.09	0.244
f_5 (inv diff moment)	0.41±0.04	0.42±0.04	0.130
f_6 (sum average)	17.64±0.36	17.65±0.35	0.918
f_7 (sum variance)	74.79±3.10	75.07±2.68	0.654
f_8 (sum entropy)	Median:4.94 Min:4.81 Max:4.95	Median:4.94 Min:4.91 Max:4.95	0.468mw
f_9 (entropy)	7.14±0.19	7.11±0.15	0.348
f_{10} (difference variance)	4.20 ± 0.85	3.83 ± 0.82	0.043
f_{11} (diff entropy)	2.72±0.17	2.66±0.16	0.072
f_{12} (info measure corr 1)	-0.21±0.05	-0.22±0.04	0.397
f_{13} (info measure corr 2)	0.89±0.04	0.90±0.03	0.161
f_{14} (maximal corr coeff)	0.82±0.05	0.83±0.04	0.156
f_{15} (cluster shade)	-56.92±24.48	-55.97±30.32	0.871
f_{16} (cluster prominence)	10579.32±690.51	10620.57±574.32	0.763

Table 5.1: Comparison of PR and NR (determined by greater than or less than 50% change in largest diameter). Mean/SD or median/range and p-values for all texture parameters using 16 grey levels at the 2 minute post-contrast time point are shown. P-values determined using t-test or Mann Whitney test (labelled mw) as appropriate.

Grey levels

It is further evident from Table 5.2 that varying the number of grey levels utilised has little effect on the results at 2 minutes post contrast, possibly due to the fact that at all the varying grey levels counting statistics are high regardless due to using a multi slice approach. Minimal effect was noted at 1 minute post contrast where f_2 and f_{10} were borderline significant (p = 0.053 and p = 0.064 respectively), and thus not shown in table 5.2 at 32 grey levels.

Time points

Significant differences were consistently seen at 1 and 2 minute post contrast time points. No

significant differences were seen on the pre-contrast phase and no significant differences reported at 3 and 4 minutes post contrast. The 5 minute post-contrast data was only significantly different when using 64 grey levels.

Texture parameters	Mean value ± Standard Deviation		P value
	NR	PR	
8 grey levels (1min post contrast)			
$\mathbf{f_2}$ **(contrast)**	2.32 ± 0.50	2.10 ± 0.48	0.041
$\mathbf{f_{10}}$ **(difference variance)**	1.18 ± 0.22	1.09 ± 0.21	0.046
16 grey levels			
$\mathbf{f_2}$ **(contrast)**	8.94 ± 2.05	8.05 ± 1.94	0.040
$\mathbf{f_{10}}$ **(difference variance)**	4.23 ± 0.86	3.86 ± 0.83	0.044
64 grey levels			
$\mathbf{f_2}$ **(contrast)**	141.2 ± 32.92	126.8 ± 31.07	0.039
$\mathbf{f_{10}}$ **(difference variance)**	64.80 ± 13.64	58.94 ± 13.21	0.044
8 grey levels (2min post contrast)			
$\mathbf{f_2}$ **(contrast)**	2.31 ± 0.51	2.09 ± 0.46	0.045
$\mathbf{f_{10}}$ **(difference variance)**	1.17 ± 0.22	1.08 ± 0.21	0.047
16 grey levels			
$\mathbf{f_2}$ **(contrast)**	8.89 ± 2.05	8.02 ± 1.86	0.042
$\mathbf{f_{10}}$ **(difference variance)**	4.20 ± 0.85	3.83 ± 0.82	0.043
32 grey levels			
$\mathbf{f_2}$ **(contrast)**	35.21 ± 8.26	31.70 ± 7.46	0.040
$\mathbf{f_{10}}$ **(difference variance)**	16.26 ± 3.42	14.77 ± 3.28	0.040
64 grey levels			
$\mathbf{f_2}$ **(contrast)**	140.5 ± 33.09	126.4 ± 29.89	0.040
$\mathbf{f_{10}}$ **(difference variance)**	64.46 ± 13.71	58.50 ± 13.10	0.039
64 grey levels (5min post contrast)			
$\mathbf{f_{10}}$ **(difference variance)**	63.38 ± 14.42	56.61 ± 116.41	0.048

Table 5.2: Summary of significant differences in texture parameters between PR and NR patients. The number of grey levels employed is detailed for each texture parameter.

5.1.4.2 TNBC (ER–negative PR–negative HER2–negative) vs. all others

Table 5.3 shows the mean/standard deviation or median/range and p-values for the TNBC vs. all other types for all 16 texture parameters between groups for 16 grey levels at the 2 minute post contrast time point. Highly significant differences were obtained for f_6, f_7, f_{15} and f_{16} (p-values 0.001 to 0.012) with a p-value of 0.023 obtained for f_8. Table 5.4 provides further results for these texture parameters that showed significant differences in texture based on TNBC vs. all other types.

Texture parameters	Mean value ± Standard Deviation		P value
	TNBC	All others	
16 grey levels (2min post contrast)			
f_1 (angular 2nd moment)	0.010±0.001	0.010±0.001	0.467
f_2 (contrast)	8.56±2.22	8.42±1.81	0.775
f_3 (correlation)	0.80±0.05	0.81±0.04	0.569
f_4 (variance)	16.84±1.23	16.10±1.06	0.127
f_5 (inv diff moment)	0.42±0.04	0.41±0.03	0.491
f_6 (sum average)	17.42±0.35	17.76±0.25	<0.001
f_7 (sum variance)	76.12±2.92	74.29±2.60	0.011
f_8 (sum entropy)	Median:4.94 Min:4.91 Max:4.95	Median:4.94 Min:4.81 Max:4.95	0.023mw
f_9 (entropy)	7.13±0.18	7.12±0.16	0.930
f_{10} (difference variance)	4.11±0.95	3.98±0.80	0.555
f_{11} (diff entropy)	2.70±0.19	2.69±0.15	0.961
f_{12} (info measure corr 1)	-0.22±0.05	-0.22±0.04	0.953
f_{13} (info measure corr 2)	0.89±0.04	0.89±0.03	0.900
f_{14} (maximal corr coeff)	0.82±0.05	0.82±0.04	0.594
f_{15} (cluster shade)	-43.00±26.21	-63.65±20.83	0.001
f_{16} (cluster prominence)	10856.51±595.89	10467.12±588.46	0.012

Table 5.3: Comparison of TNBC vs. all other combinations of these three markers. Mean/SD or median/range and p-values for all texture parameters using 16 grey levels at the 2 minute post-contrast time point are shown. P-values determined using t-test or Mann Whitney test (labelled mw) as appropriate.

Time points

From Table 5.4 the results clearly show that the greatest number of significant differences are seen at 1-3 minute post contrast time points. At the 1 minute post contrast time point significant differences were found for texture parameters f_4, f_6 ,f_7, f_8 , f_{15} and f_{16}. At 2 and 3

minute post contrast time points significant differences were found for texture parameters f_6 ,f_7, f_8 , f_{15} and f_{16}. At 4 and 5 minute post contrast time points significant differences were only found for texture parameters f_6 and f_{15}. No significant differences were reported for the pre-contrast phase.

Grey levels

From Table 5.4 it appears that the number of grey levels used had minimal effect as significant differences were reported across all grey levels (8, 16, 32 and 64) for the majority of parameters. The only exception to this was for f_8, sum entropy where results were variable between grey levels.

Texture Parameter	**Grey Levels**	**P value**
(1 min post contrast)		
f_4 (variance)	All	<0.041
f_6 (sum average)	All	<0.001
f_7 (sum variance)	All	<0.002
f_8 (sum entropy)	16, 64	<0.025
f_{15} (cluster shade)	All	<0.005
f_{16} (cluster prominence)	All	<0.003
(2 min post contrast)		
f_6 (sum average)	All	<0.001
f_7 (sum variance)	All	<0.015
f_8 (sum entropy)	16, 32, 64	<0.045
f_{15} (cluster shade)	All	<0.001
f_{16} (cluster prominence)	All	<0.021
(3 min post contrast)		
f_6 (sum average)	All	<0.001
f_7 (sum variance)	All	<0.027
f_8 (sum entropy)	16, 32, 64	<0.049
f_{15} (cluster shade)	All	<0.004
f_{16} (cluster prominence)	All	<0.024
(4 min post contrast)		
f_6 (sum average)	All	<0.001
f_{15} (cluster shade)	All	<0.008
(5 min post contrast)		
f_6 (sum average)	All	<0.001
f_{15} (cluster shade)	All	<0.001

Table 5.4: Summary of significant differences in texture parameters between TNBC vs. all other immuno-receptor sub-types. The number of grey levels employed is detailed for each texture parameter.

5.1.4.3 Nodal status data (Node-negative vs. Node-positive)

Table 5.5 shows the mean/standard deviation and p-values for all 16 texture parameters for 16 grey levels at the 3 minute post contrast time point. Table 5.6 summarises the significant differences in texture found between node -ve and node +ve patients.

Time points

From table 5.6 the results clearly show significant differences at 2-5 minute post contrast time points, but with the most significant seen at 3 minutes with p-values ranging from 0.015 to 0.021.

Grey levels

From Table 5.6 it appears that the number of grey levels used had minimal effect as similar significant differences were found across all grey levels (8, 16, 32 and 64). The only exception to this was for 4 minutes post contrast where results were more variable.

Texture parameters	Mean value ± Standard Deviation		P value
	Node -ve	Node +ve	
16 grey levels (2min post contrast)			
f_1 (angular 2nd moment)	0.010±0.001	0.010±0.001	0.443
f_2 (contrast)	8.43±2.15	8.57±2.00	0.740
f_3 (correlation)	0.80±0.05	0.80±0.05	0.964
f_4 (variance)	16.58±1.39	16.50±1.07	0.779
f_5 (inv diff moment)	0.42±0.04	0.41±0.38	0.521
f_6 (sum average)	17.53 ± 0.38	17.71 ± 0.33	0.016
f_7 (sum variance)	75.01±3.40	74.83±2.56	0.783
f_8 (sum entropy)	Median:4.94 Min:4.82 Max:4.95	Median:4.94 Min:4.91 Max:4.95	0.592 mw
f_9 (entropy)	7.10±0.19	7.15±0.15	0.259
f_{10} (difference variance)	4.00±0.91	4.03±0.82	0.873
f_{11} (diff entropy)	2.69±0.18	2.71±0.16	0.560
f_{12} (info measure corr 1)	-0.22±0.05	-0.21±0.04	0.234
f_{13} (info measure corr 2)	0.90±0.04	0.89±0.03	0.266
f_{14} (maximal corr coeff)	0.82±0.05	0.82±0.05	0.632
f_{15} (cluster shade)	-47.57 ± 36.83	-62.58 ± 21.73	0.021
f_{16} (cluster prominence)	10629.26 ±737.93	10599.89±568.24	0.832

Table 5.5: Comparison of Nodal status of patients. Mean/SD or median/range and p-values for all texture parameters using 16 grey levels at the 3 minute post-contrast time point are shown. P-values determined using t-test or Mann Whitney test (labelled mw) as appropriate.

Texture parameters	Mean value ± Standard Deviation		P value
	Node -ve	Node +ve	
8 grey levels (2min post contrast)			
$\mathbf{f_6}$ **(sum average)**	9.29 ± 0.18	9.36 ± 0.159	0.041
$\mathbf{f_{15}}$ **(cluster shade)**	-6.41 ± 4.01	-7.88 ± 2.44	0.039
16 grey levels			
$\mathbf{f_6}$ **(sum average)**	17.58 ± 0.37	17.73 ± 0.32	0.043
$\mathbf{f_{15}}$ **(cluster shade)**	-51.05 ± 32.13	-63.23 ± 19.37	0.032
32 grey levels			
$\mathbf{f_6}$ **(sum average)**	34.17 ± 0.74	34.47 ± 0.65	0.044
$\mathbf{f_{15}}$ **(cluster shade)**	-409.8 ± 258.1	-505.9 ± 154.5	0.035
64 grey levels			
$\mathbf{f_6}$ **(sum average)**	67.34 ± 1.49	67.92 ± 1.30	0.050
$\mathbf{f_{15}}$ **(cluster shade)**	-3272 ± 2071	-4012 ± 1223	0.042
8 grey levels (3min post contrast)			
$\mathbf{f_6}$ **(sum average)**	9.26 ± 0.19	9.35 ± 0.16	0.015
$\mathbf{f_{15}}$ **(cluster shade)**	-5.93 ± 4.49	-7.79 ± 2.68	0.020
16 grey levels			
$\mathbf{f_6}$ **(sum average)**	17.53 ± 0.38	17.71 ± 0.33	0.016
$\mathbf{f_{15}}$ **(cluster shade)**	-47.57 ± 36.83	-62.58 ± 21.73	0.021
32 grey levels			
$\mathbf{f_6}$ **(sum average)**	34.06 ± 0.77	34.42 ± 0.65	0.016
$\mathbf{f_{15}}$ **(cluster shade)**	-381.2 ± 295.2	-503.6 ± 173.8	0.019
64 grey levels			
$\mathbf{f_6}$ **(sum average)**	67.11 ± 1.54	67.85 ± 1.30	0.016
$\mathbf{f_{15}}$ **(cluster shade)**	-3042 ± 2364	-4027 ± 1380	0.018
8 grey levels (4 min post contrast)			
$\mathbf{f_6}$ **(sum average)**	9.241 ± 0.194	9.327 ± 0.163	0.024
16 grey levels			
$\mathbf{f_6}$ **(sum average)**	17.49 ± 0.394	17.65 ± 0.35	0.043
32 grey levels			
$\mathbf{f_6}$ **(sum average)**	33.98 ± 0.79	34.33 ± 0.67	0.025
$\mathbf{f_{15}}$ **(cluster shade)**	-356.8 ± 318.7	-468.4 ± 193.5	0.048
64 grey levels			
$\mathbf{f_6}$ **(sum average)**	66.97 ± 1.59	67.67 ± 1.33	0.024
$\mathbf{f_{15}}$ **(cluster shade)**	-2846 ± 2541	-3750 ± 1545	0.044
8 grey levels (5 min post contrast)			
$\mathbf{f_6}$ **(sum average)**	9.23 ± 0.20	9.31 ± 0.17	0.040
16 grey levels			
$\mathbf{f_6}$ **(sum average)**	17.47 ± 0.39	17.63 ± 0.34	0.038
32 grey levels			
$\mathbf{f_6}$ **(sum average)**	33.94 ± 0.79	34.27 ± 0.67	0.041

Table 5.6: Summary of significant differences in texture parameters between node positive and node negative patients. The number of grey levels employed is detailed for each texture parameter.

5.1.4.4 Tumour grade derived from pre-treatment biopsy

Table 5.7 shows the mean/standard deviation or median/range and p-values for all 16 texture parameters for 16 grey levels at the 2 minute post contrast time point. Table 5.8 summarises the significant differences in texture found between patients biopsy grade. Significant differences were shown for parameters $f_4, f_6, f_7, f_8, f_{15}$ and f_{16}.

Texture parameters	Mean value ± Standard Deviation		P value
	Bi Gr 1 or 2	Bi Gr 3	
16 grey levels (2min post contrast)			
f_1 (angular 2nd moment)	0.010±0.001	0.010±0.001	0.282
f_2 (contrast)	8.78±1.93	8.28±2.04	0.239
f_3 (correlation)	0.80±0.05	0.81±0.49	0.243
f_4 (variance)	16.19±1.13	16.74±1.21	0.031
f_5 (inv diff moment)	0.41±0.03	0.42±0.04	0.088
f_6 (sum average)	17.80±0.24	17.57±0.39	0.001
f_7 (sum variance)	73.92±2.81	75.44±3.02	0.016
f_8 (sum entropy)	Median:4.94 Min:4.81 Max:4.95	Median:4.94 Min:4.91 Max:4.95	0.020mw
f_9 (entropy)	7.14±0.17	7.12±0.16	0.603
f_{10} (difference variance)	4.12±0.85	3.96±0.85	0.354
f_{11} (diff entropy)	2.72±0.15	2.68±0.18	0.211
f_{12} (info measure corr 1)	-0.22±0.05	-0.22±0.04	0.625
f_{13} (info measure corr 2)	0.89±0.03	0.89±0.04	0.391
f_{14} (maximal corr coeff)	0.82±0.05	0.82±0.05	0.584
f_{15} (cluster shade)	-64.58±17.72	-51.74±30.97	0.023
f_{16} (cluster prominence)	$1.04x10^4$±630.37	$1.07x10^4$±646.06	0.020

Table 5.7: Comparison of Biopsy grade of patients. Mean/SD or median/range and p-values for all texture parameters using 16 grey levels at the 2 minute post-contrast time point are shown. P-values determined using t-test or Mann Whitney test (labelled mw) as appropriate.

Time points

From table 5.8 the results clearly show most significant differences at 1-3 minute post contrast time points for the six textural parameters $f_4, f_6, f_7, f_8, f_{15}$ and f_{16}, demonstrating consistent differences between groups.

Grey levels

From Table 5.8 it appears that the number of grey levels used had minimal effect as similar p-values were obtained across all grey levels (8, 16, 32 and 64).

Texture Parameter	Grey Levels	P value
(1 min post contrast)		
$\mathbf{f_4}$ **(variance)**	All	<0.028
$\mathbf{f_6}$ **(sum average)**	All	0.001
$\mathbf{f_7}$ **(sum variance)**	All	<0.016
$\mathbf{f_8}$ **(sum entropy)**	16,64	<0.020
$\mathbf{f_{15}}$ **(cluster shade)**	8,16,64	<0.037
$\mathbf{f_{16}}$ **(cluster prominence)**	All	<0.025
(2 min post contrast)		
$\mathbf{f_4}$ **(variance)**	All	<0.039
$\mathbf{f_6}$ **(sum average)**	All	0.001
$\mathbf{f_7}$ **(sum variance)**	All	<0.022
$\mathbf{f_8}$ **(sum entropy)**	16.32.64	<0.030
$\mathbf{f_{15}}$ **(cluster shade)**	All	<0.026
$\mathbf{f_{16}}$ **(cluster prominence)**	All	<0.029
(3 min post contrast)		
$\mathbf{f_4}$ **(variance)**	All	<0.044
$\mathbf{f_6}$ **(sum average)**	All	0.001
$\mathbf{f_7}$ **(sum variance)**	All	<0.024
$\mathbf{f_8}$ **(sum entropy)**	16,32,64	<0.024
$\mathbf{f_{15}}$ **(cluster shade)**	All	<0.023
$\mathbf{f_{16}}$ **(cluster prominence)**	All	<0.024
(4 min post contrast)		
$\mathbf{f_6}$ **(sum average)**	All	0.003
$\mathbf{f_7}$ **(sum variance)**	8,32,64	<0.047
$\mathbf{f_8}$ **(sum entropy)**	16,32,64	<0.044
$\mathbf{f_{15}}$ **(cluster shade)**	All	<0.012
$\mathbf{f_{16}}$ **(cluster prominence)**	8,32,64	<0.055
(5 min post contrast)		
$\mathbf{f_6}$ **(sum average)**	All	<0.004
$\mathbf{f_8}$ **(sum entropy)**	32	<0.046
$\mathbf{f_{15}}$ **(cluster shade)**	All	<0.012

Table 5.8: Summary of significant differences in texture parameters between grade 1/2 and grade 3 patients. The number of grey levels employed is detailed for each texture parameter.

5.1.4.5 Summary

The most significant differences in texture parameters were found at the 1-3 minute post contrast time points. Nine of the 16 texture parameters showed significant differences: f_2 f_{10} and f_{11} for NR/PR data, f_6 and f_{15} for nodal status; and f_4, f_6 ,f_7, f_8 , f_{15} and f_{16} for the TNBC and Biopsy grade datasets. The number of significant differences are summarised in figure 5.9.

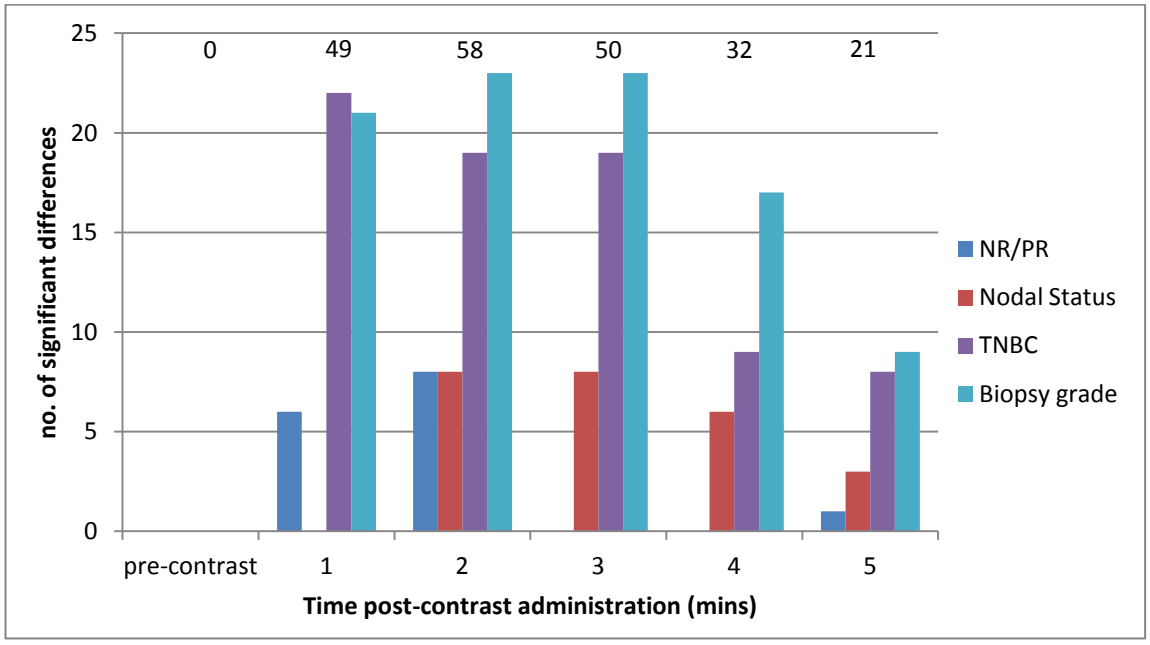

Figure 5.9: summary of significant differences for Nodal status, NR/PR, TNBC and biopsy grade data

Figure 5.10 shows example images from a representative slice of patients with (a) low f_2 (3.93) and f_{10} (1.97) values compared with (b) high f_2 (13.14) and f_{10} (5.70) values where increased heterogeneity is evident. Patient in image (a) categorised as follows; biopsy grade group: 3, TNBC: all others, Nodal status: -ve, response status: PR. Image (b) patient had biopsy grade group: 1 or 2, TNBC: TNBC, Nodal status: +ve, response status: NR.

Figure 5.11 shows representative slices with (a) high (18.22) and (b) low (16.67) f_6 values. Image (b) shows a necrotic tumour where the core of the lesion has not taken up contrast agent and therefore appears overall darker with low f_6 value in comparison to the image in (a). Patient in image (a) categorised as follows; biopsy grade group: 3, TNBC: all others, Nodal

status: +ve, response status: PR. Image (b) patient had biopsy grade group: 3, TNBC: TNBC, Nodal status: +ve, response status: NR.

Figure 5.10 demonstrates images with (a) high and (b) low f_8 (4.95, 4.91 respectively) and f_{16} (11962.79, 9228.78) values with the higher values appearing more uniform. Patient in image (a) categorised as follows; biopsy grade group: 3, TNBC: TNBC, Nodal status: -ve, response status: NR. Image (b) patient had biopsy grade group: 3, TNBC: all others, Nodal status: +ve, response status: information unavailable.

a) 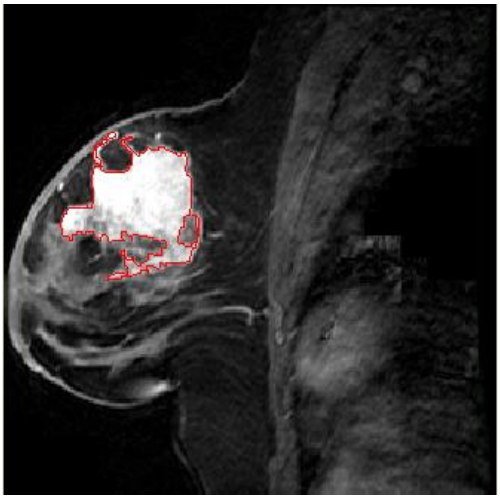 b) 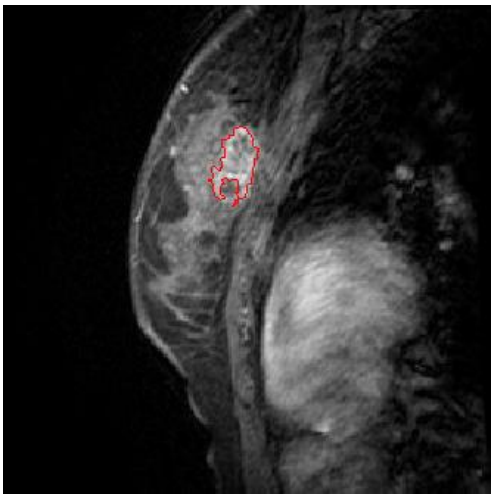

Figure 5.10: Images obtained at 2 minutes post contrast, in breast cancer patients prior to undergoing neoadjuvant chemotherapy. (a) Image from patient age 48, biopsy grade 3 (4 cycles EC, 4 cycles Docetaxel). Patient subsequently defined as partial responder with a >50% reduction in tumour size with low f_2 and f_{10} values for texture. (b) Image from patient age 39, biopsy grade 2 (4 cycles EC, 4 cycles Epirubicin and cyclophosphamide/paclitaxel). Patient subsequently defined as non responder with a 5% reduction in tumour size with high f_2 and f_{10} values

a) 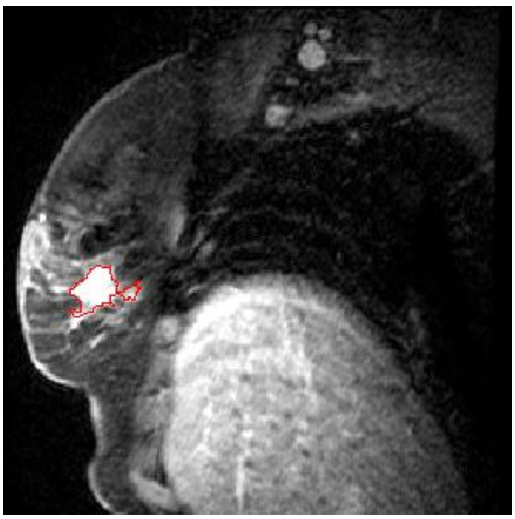 b) 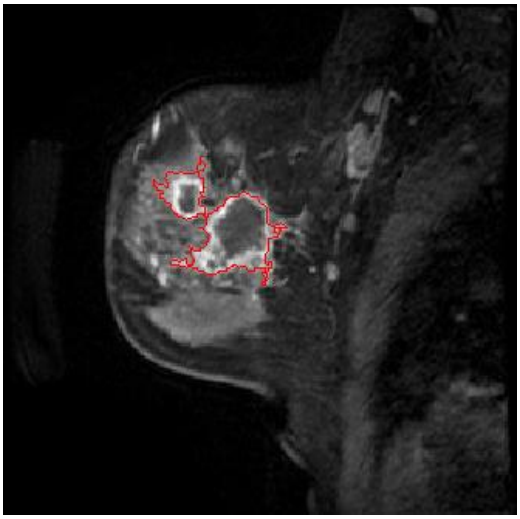

Figure 5.11: Images from breast cancer patients prior to undergoing neoadjuvant chemotherapy obtained at 2 minutes post contrast time point. (a) Image from a patient age 48, biopsy grade 3 (4 cycles EC, 4 cycles Docetaxel). Patient subsequently defined as not triple negative with a 94.3% reduction in tumour size with a high f_6 value for texture. (b) Image from a patient age 43, biopsy grade 3 (4 cycles EC, 4 cycles Docetaxel). Patient subsequently defined as ER- PR- HER2 –ve with a 33.9% increase in tumour size with a low f_6 value

a) 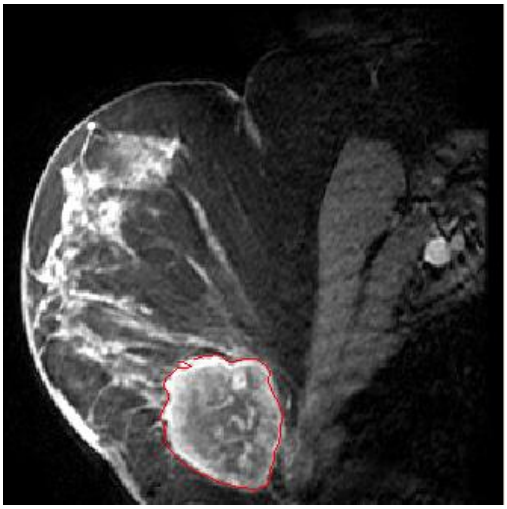 b) 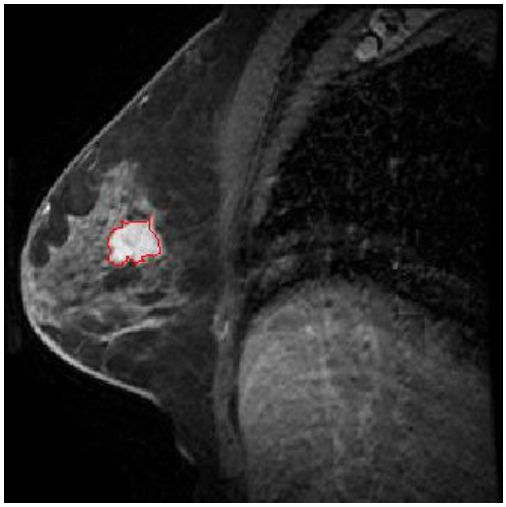

Figure 5.10: Images taken from patients with breast cancer prior to undergoing neoadjuvant chemotherapy taken at 2 minutes post contrast. (a) Sagittal image from a patient age 42, biopsy grade 3 (4 cycles EC, 3 cycles Docetaxel). Patient subsequently defined as ER- PR- HER2 – ve group with a 45.2% reduction in tumour size with high f_8 and f_{16} values for texture. (b) Sagittal image from a patient age 46, biopsy grade 3 (4 cycles Epirobicin and cyclophosphamide, 4 cycles Taxotere and Tamoxifen and then switched to Aromasin and radiotherapy). Patient subsequently defined as not triple negative with low f_8 and f_{16} values

5.1.5 Discussion

The results presented in this study demonstrated significant differences in textural features between partial responders and non responders to chemotherapy; the study showed that significant differences were found throughout all choice of grey levels when using histogram equalisation. It has also highlighted the importance of contrast enhanced MRI as no significant differences in texture were found in the pre contrast time point images, and more textural features showed significant differences around the 1-2 minute post contrast time points.

In Summary as per figure 5.9 the results show the highest number of significant differences in texture parameters were found at 1-2 minute post contrast. Figure 5.9 illustrates the fact that 75% of significant differences were found at 1 to 3 minutes post contrast time points.

Consistently significant differences were noted across all grey levels between PR and NR groups at the 2 minute post contrast time point for f_2 (contrast: a measure of local image variation [46]) and f_{10} (difference in variance: a measure of variation in the difference in grey levels between voxel pairs [46]). f_2 and f_{10} showed higher values for non responders suggesting that lesions with increased heterogeneity can be expected to have reduced chemotherapeutic response.

For TNBC data consistent significant differences across all grey levels were noted at 2 and 3 minute post contrast time points for texture parameters f_6 (sum average: measure of overall image brightness [46]), f_7 (sum variance: measure of how spread out the sum of the grey levels of voxel pairs is [46]), f_{15} and f_{16} (cluster shade/ cluster prominence: both gauge the perceptual concepts of uniformity and proximity [55]) and across 16, 32 and 64 grey levels for f_8 (sum entropy: measure of randomness of the sum of the grey of neighbouring pixels [46]). For f_6 the TNBC vs. all others data showed distinctly higher values for 'all others' suggesting patients with lower values for the texture parameter f_6 have poorer prognosis, f_7, f_8 , f_{15} and f_{16} had higher values for TNBC marker suggesting that patients with higher values in these

texture parameters having poor prognosis, and these findings seem to confirm Bhooshan's [46] observations that heterogeneous lesions are characterised by poorer response.

For Nodal status data consistent significant differences across all grey levels were noted at 2 and 3 minute post contrast time points for texture parameters f_6 and f_{15}. For f_6 higher values in data were noted in node +ve suggesting patients with poor prognosis having higher values for this texture parameter , f_{15} showed higher values for node –ve data suggesting patients with a lower value in f_{15} having a poor prognosis.

For biopsy grade data most significant differences were observed at 1-3 minute post contrast time points across all grey levels for parameters f_4(variance: measure of grey level distribution [46]), f_6 ,f_7, f_8, f_{15} and f_{16}.

To summarise node +ve, high grade, TNBC are associated with poorer prognosis and from this thesis results appear to be consistently more heterogeneous in appearance. Lesions with necrotic areas clearly appear more heterogeneous during contrast enhancement.

Limitations of this study include the fact that the data was not isotropic although the data was acquired using a 3D sequence and subsequently analysed in a multi slice fashion. Drawing ROIs on isotropic 3D images would be immensely time consuming whilst with multi slice 2D images a more true representation of the tumour is achieved than obtained with a single slice analysis. In order to gain isotropic 3D data the images would need to have been acquired using isotropic acquisition when patients were initially scanned, this in reality would be difficult to achieve with complete coverage without significantly degrading the temporal resolution.

Another limitation was that within this work a large number of statistical tests were performed. Although for the purpose of hypothesis generation the number of tests is less critical there is evidently a potential for type 1 errors to occur. However since the results appear to be relatively consistent across the number of grey levels and time points this indicates that the results were less likely due to chance.

Reducing grey levels improves counting statistics per co-occurrence matrix element and is understood to have some effect on discriminatory power. This wasn't found to be the case as it was noted that data was consistent across all grey levels. This needs further investigation as clearly having for example 2 grey levels would mean only a black and white image and would be difficult to distinguish one lesion from another. On an image with a higher number of grey levels the co-occurrence matrix would become sparse. The texture analysis results of an image analysed using 2 grey levels would be different to the one with a high number of grey levels. Further investigation could involve using a more varying number of grey levels as well as varying the distance between pixel pairs in the co-occurrence matrices.

Finally critics could argue that the study did not have a very large patient group. Although data from 100 patients was used during analysis there was not always a proportional split of data available. For example the group TNBC only contained 22 patients which was analysed against all other combinations of these markers having 49 patients. There was however a more proportional data representation with partial/non-responders data having 49 N/R and 40 P/R split. Nevertheless the results are encouraging enough to warrant further investigation in a larger patient cohort.

In conclusion this work has highlighted that textural differences between groups (based on biopsy grade or TNBC status) are apparent and appear to be most evident 1- 3 minutes post-contrast administration. Whilst the large number of statistical tests undertaken necessitates a degree of caution in interpreting the results, the fact that significant differences are consistently observed is encouraging.

5.2 Single slice vs. multi slice Texture analysis

5.2.1 Introduction

In section 5.1 a study was performed to systematically assess the efficacy of DCE-MRI based textural analysis in predicting response to chemotherapy in a cohort of breast cancer patients. Significant differences for texture with respect to nodal status and partial responders vs. non responders were found [85]. This section aims to compare texture analysis on the same data cohort but using a single slice and single ROI to verify if texture analysis works best on multi or single slice MR images. If proven that single slice works just as well this would save processing time by 4 fold (17 minutes per patient down to 4 minutes) as well as a significant reduction in time taken to define the ROI. Figures 5.11 and 5.12 show examples of the data in single slice and multi-slice forms.

5.2.2 Methods

100 patients were scanned on a 3.0T HDx scanner immediately prior to neo-adjuvant chemotherapy treatment. For all patients a 3D dynamic dataset was acquired using VIBRANT (FOV 20×20 cm, acquisition matrix 220×160, slice thickness 2 mm, 12 phases with average tdel=33.7 s, range 25.5-44.7 s) Malignant tissue ROIs were generated semi-automatically on all slices utilising early arterial phase data. Texture analysis was then performed on 2 minute post-contrast data, the reason being that 2 minute post-contrast data showed the best results for multi slice data therefore this time point was also used on single slice data. To prevent sparseness within subsequently calculated co-occurrence matrices the ROI data underwent grey level decimation via histogram equalisation. ROI data was reduced to 16 grey levels (reducing the number of grey levels improves SNR at the expense of discriminatory power). Tests were carried as as outlined in 5.1 but for response to chemotherapy and nodal status data only and were repeated on a single slice as opposed to multi slice in 5.1. The single slices were selected on the basis of largest ROI from each selection of slices in an attempt to try and cover the largest possible cross sectional area of the lesion.

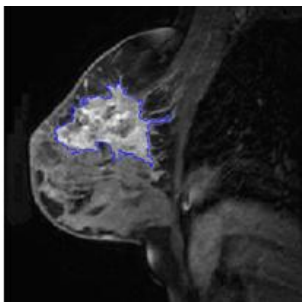

figure 5.11: single slice image of breast cancer patient undergoing neoadjuvant chemotherapy

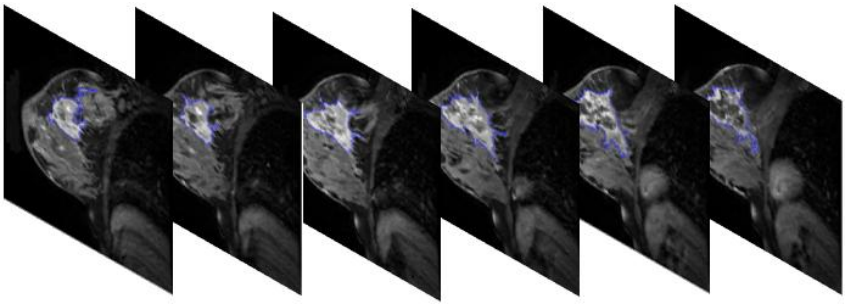

figure 5.12: multi slice images of breast cancer patient undergoing neoadjuvant chemotherapy

5.2.3 Results

Recalling from the previous result on multi slice data. Nodal status was determined in 91 patients (45 node –ve vs. 46 node +ve) and response data was available in 89 patients (40 partial responders vs. 49 non-responders). Response data refers to response to chemotherapy with respect to longest diameter of lesion where the decrease in cross sectional area was greater than 50%. Regarding nodal status significant differences in f_6 (sum average) and f_{15} (cluster shade) were noted at 2 minutes post-contrast administration for 16 grey levels. Differences were noted between partial responders and non-responders for f_2 (contrast) and f_{10} (difference variance). The same tests were repeated for single slice ROIs and no significant differences in texture were seen for nodal status or partial responders vs. non responders data (tables 5.9 and 5.10). A paired sample test for the single slice data against the multiple slice data was performed to establish whether values were in fact significantly different (table 5.11). The paired test revealed that all except parameter f_{16} showed p-values of <0.002 indicating texture data between multi and single was actually significantly different.

Multi slice: partial responders vs. non responders				**Single slice**: partial responders vs. non responders		
	PR (mean± sd)	NR (mean± sd)	*P value*	PR	NR	*P value*
f2 (contrast)	8.02±1.86	8.89±2.05	0.042	Median = 9.53 Range = 4.57 – 21.61	median = 9.56 Range = 2.19 – 23.12	0.908
f10 (difference (variance)	3.83±0.82	4.20±0.85	0.043	Median = 4.38 Range = 2.23 – 10.17	Median = 4.37 Range = 1.05 – 9.17	0.908

Table 5.9: PR vs. NR for multi slice (left) and single slice (right), parameters not listed showed no significant differences

Multi slice: Nodal status				**Single slice**: Nodal status		
	Nodel+ve (mean± sd)	Node -ve (mean± sd)	*P value*	Node +ve	Node –ve	*P value*
f6 (sum average)	17.73 ± 0.32	17.58 ± 0.37	0.043	Median =17.66 Range= 16.62 – 18.22	Median= 17.57 Range= 16.46-18.89	0.468
f15 (cluster shade)	(-)63.23 ± 19.37	(-)51.05 ±32.13	0.031	Median= (-)49.37 Range= (-)102.79 – 31.70	Median= (-)41.42 Range= (-)122.82- 69.11	0.704

Table 5.10: Nodal status (node +ve vs. node –ve) for multi slice (left) and single slice (right), parameters not listed showed no significant differences

Pair	*P value*
f1-f1	<0.001
f2-f2	<0.001
f3-f3	<0.001
f4-f4	<0.001
f5-f5	<0.001
f6-f6	0.001
f7-f7	0.002
f8-f8	<0.001
f9-f9	<0.001
f10-f10	<0.001
f11-f11	0.002
f12-f12	<0.001
f13-f13	<0.001
f14-f14	<0.001
f15-f15	<0.001
f16-f16	0.437

Table 5.11: Paired actual data from single slice with multiple slice texture parameters

5.2.5 Discussion

Single vs. multi slice results showed significant differences of <0.002 for all parameters except f_{16} in a paired sample comparison. Significant differences in f_6 and f_{15} for nodal status, and f_2 and f_{10} for response, are observed when run on multi slice MR images, but when tested with single slice data no significant differences were observed when only the largest ROI was analysed.

The study shows taking the largest cross sectional area does not necessarily highlight the most important region in terms of response discriminant. Despite the reduction in processing time clearly with single slice texture analysis we lose counting statistics and important tumour information is evidently missed. This appears to justify the use of multi slice data in textural analysis to maximise counting statistics. Texture analysis on small lesions must be treated with a degree of caution.

5.3 PCA & Logistic regression

5.3.1 Logistic regression (LR)

Logistic regression is an analytical technique which can be powerful when the outcome variable is dichotomous. With an increase in researchers having easy access to sophisticated statistical software LR has increased in popularity [86]. In this study logistic regression is used for the prediction of a dichotomous outcome for nodal status, PR/NR (with respect to lesion diameter), TNBC and biopsy grade data all of which were analysed for their textural features earlier in this chapter. Backward LR analysis was performed for 1 and 2 minute post contrast texture data only for 16 grey levels. This starts off with all 16 parameters and removes ones with p-values > 0.05 (least significant) and keeps performing LR until parameters in the end are the ones that can no longer be removed by LR, reporting the most significant parameters that would have an effect on outcome. LRA output consists of a single probability variable for each case (P_{LRA}). This is a continuous variable from 0 to 1 indicating the degree of certainty in classification. A LRA model is described by:

$$\mathrm{p_{LRA}} = \frac{1}{1+e^{-\mathrm{z}}} \quad \text{and } Z = \sum_{\mathrm{k}} \mathrm{a_k x_k} + \mathrm{C}$$

where each of the k variables are denoted by $\mathrm{x_k}$, their weighting factors by $\mathrm{a_k}$, and C is constant.

5.3.1.2 Response to Neoadjuvant Chemotherapy (% change in longest diameter)

Table 5.13 shows the classification table for the response data at 1 minute post contrast time point, it shows how once the z value was calculated SPSS statistics software predicted data split values and displays percentage correct values. For table 5.13:

$$z = 34.381f_5 + (-881.432)f_1 + (-6.027)$$

Table 5.14 highlights the classification table at 2 minutes post contrast time point

$$\text{where } z = -43.767f_3 + (-1.833)f_2 + (-986.745)f_1 + 60.033$$

1min Classification Table[a]

Observed			Predicted		
			PR_or_NR		
			Non-responder	Partial responder	Percentage Correct
Step 1	PR_or_NR	Non-responder	37	12	75.5
		Partial responder	23	17	42.5
	Overall Percentage				60.7

a. The cut value is .500

Table 5.13 Classification table for response to chemotherapy data at 1 minute post contrast time point

2min Classification Table[a]

Observed			Predicted		
			PR_or_NR		
			Non-responder	Partial responder	Percentage Correct
Step 1	PR_or_NR	Non-responder	32	17	65.3
		Partial responder	17	23	57.5
	Overall Percentage				61.8

a. The cut value is .500

Table 5.14 Classification table for response to chemotherapy data at 2 minutes post contrast time point

5.3.1.3 TNBC (ER–negative PR–negative HER2–negative) vs. all others

Table 5.15 shows the classification table for the TNBC data at the 1 minute post contrast time point

where $z = -0.046f_{15} + 174.736f_{12} + (-41.789)f_{11} + (-0.946)f_{7} + (-109.045)f_{5} + 4996.307f_{1} + 217.055$

Table 5.16 shows the classification table for the TNBC data at the 1 minute post contrast time point

where $z = -1.548f_{10} + (-0.602)f_{7} + 52.341$

1min Classification Table[a]

Observed			Predicted		
			ER_PR_HER2		Percentage
			E-P-H-	all others	Correct
Step 1	ER_PR_HER2	E-P-H-	12	10	54.5
		all others	6	43	87.8
	Overall Percentage				77.5

a. The cut value is .500

Table 5.15 Classification table for TNBC data at the 1 minute post contrast time point

2min Classification Table[a]

Observed			Predicted		
			ER_PR_HER2		Percentage
			E-P-H-	all others	Correct
Step 1	ER_PR_HER2	E-P-H-	9	13	40.9
		all others	5	44	89.8
	Overall Percentage				74.6

a. The cut value is .500

Table 5.16 Classification table for TNBC data at 2 minutes post contrast time point

5.3.1.4 Nodal status data (Node-negative vs. Node-positive)

Table 5.17 shows the classification table for the nodal status data at the 1 minute post contrast time point

$$\text{where } z = 61.337f_{14}+166.956f_{8}+4.190f_{6}+1.723f_{2}+(-962.808)$$

Table 5.18 shows the classification table for the nodal status data at the 2 minutes post contrast time point

$$\text{where } z = -0.015f_{16}+(-0.076)f_{15}+63.842f_{14}+10.973f_{10}+744.187f_{8}+(-2.793)f_{7}+5.121f_{6}+(-404.652)f_{5}+15.570f_{4}+13222.73f_{1}+(-3707.466)$$

1min Classification Table[a]

Observed			Predicted		
			Nodes		Percentage Correct
			Node -ve	Node +ve	
Step 1	Nodes	Node -ve	30	15	66.7
		Node +ve	16	30	65.2
	Overall Percentage				65.9

a. The cut value is .500

Table 5.17 Classification table for nodal status data at the 1 minute post contrast time point

2min Classification Table[a]

Observed			Predicted		
			Nodes		Percentage Correct
			Node -ve	Node +ve	
Step 1	Nodes	Node -ve	33	12	73.3
		Node +ve	9	37	80.4
	Overall Percentage				76.9

a. The cut value is .500

Table 5.18 Classification table for nodal status data at 2 minutes post contrast time point

5.3.1.5 Tumour grade derived from pre-treatment biopsy

Table 5.19 shows the classification table for the biopsy grade data at the 1 minute post contrast time point

where $z = -99.993f_{13}+(-220.730)f_{12}+44.187f_{11}+149.080f_{5}+2.730f_{4}+(-5181.843)f_{1}+(-134.559)$

Table 5.20 shows the classification table for the biopsy grade data at the 2 minutes post contrast time point

where $z = -2.199f_{6}+39.269$

1min Classification Table[a]

Observed			Predicted		
			Bi_Gr_all_3		Percentage Correct
			Grade 1 or 2	Grade 3	
Step 1	Bi_Gr_all_3	Grade 1 or 2	18	20	47.4
		Grade 3	10	45	81.8
	Overall Percentage				67.7

a. The cut value is .500

Table 5.19 Classification table for biopsy grade data at the 1 minute post contrast time point

2min Classification Table[a]

Observed			Predicted		
			Bi_Gr_all_3		Percentage Correct
			Grade 1 or 2	Grade 3	
Step 1	Bi_Gr_all_3	Grade 1 or 2	13	25	34.2
		Grade 3	13	42	76.4
	Overall Percentage				59.1

a. The cut value is .500

Table 5.20 Classification table for biopsy grade data at 2 minutes post contrast time point

5.3.1.6 Discussion

This section has shown that using LR outcome prediction is possible but further work is required. The analysis revealed that perfect separation of groups doesn't appear to be possible. A disappointing classification rate of around 60% was observed for response to chemotherapy and biopsy grade data. Classification for nodal status and TNBC data appeared more promising. Texture analysis in a clinical setting could only be useful as an aid to the radiologist's decision making process when all relevant MR data including pharmacokinetic modelling is utilised.

5.3.2 Principal component analysis (PCA)

As in section 5.1 when too many statistical tests are performed there exists the possibility that the results were simply by chance and therefore it would be beneficial to reduce the dimensionality of the data.

PCA is best explained by Jolliffe *"The central idea of principal component analysis (PCA) is to reduce the dimensionality of a data set consisting of a large number of interrelated variables, while retaining as much as possible of the variation present in the data set. This is achieved by transforming to a new set of variables, the principal components (PCs), which are uncorrelated, and which are ordered so that the first few retain most of the variation present in all of the original variables"* [87].

In order to calculate PCA the following steps are involved; obtaining the data, calculating the covariance matrix, calculating the eigenvectors (eigenvectors are perpendicular to each other and explain the variance in the data) and eigenvalues (eigenvectors have corresponding eigenvalues, which are ranked in order of size) of the covariance matrix. These steps need not be calculated manually as statistical analysis tools such as SPSS will automatically allow calculation of PCA on a given dataset.

For the purposes of this work there were in total 16 texture parameters calculated for each patient in the neoadjuvant dataset, each texture parameter was calculated at the 6 different time points (pre-contrast, 1 minute to 5 minute post-contrast) and at 4 different grey level choices (8, 16, 32, 64). Given all the variables it is evident there is a lot of data present as the calculation shows 16 (texture parameters) * 6 (time points) * 4 (grey levels) = 384, giving 384 individual bits of information per tumour. Clearly the large dimensionality of this data set could benefit from being reduced. There are various ways in which this could be achieved, for the purpose of this thesis the 6 times points were considered for each texture parameter and grey level, for example for the parameter f_2 the data at each time point (pre-contrast-5min) at 16 grey levels was used to apply PCA to. Tables 5.21, 5.22 and the scree plot in figure 5.13

highlight the preliminary results achieved. These results echo the findings for each texture parameter which all showed similar results after PCA was applied. From table 5.21 it is clear how the PCA has split the data into 6 components with component 1 holding 81% of the variance in data. Table 5.22 further highlights how component 1 for example has equal weighting for all variables (calculating the sum of all the variables and squaring gives an answer of 1, indicating PCA uses up each variable fully in its calculation methods). Figure 5.13 illustrates each components eigenvalue.

Component	Initial Eigenvalues		
	Total	% of Variance	Cumulative %
1	4.881	81.345	81.345
2	.618	10.303	91.649
3	.359	5.985	97.634
4	.090	1.504	99.138
5	.038	.635	99.774
6	.014	.226	100.000

Table 5.21: Total variance explained using PCA extraction method

	Component					
	1	2	3	4	5	6
f2_preContrast	.680	.724	.111	.034	-.020	-.002
f2_1min	.903	-.151	.384	-.028	.115	-.020
f2_2min	.961	-.190	.162	.011	-.092	.079
f2_3min	.978	-.161	-.034	-.011	-.102	-.081
f2_4min	.931	-.076	-.281	.210	.061	.007
f2_5min	.926	.060	-.305	-.210	.043	.018

Table 5.22: Component Matrix using PCA for 6 components extracted

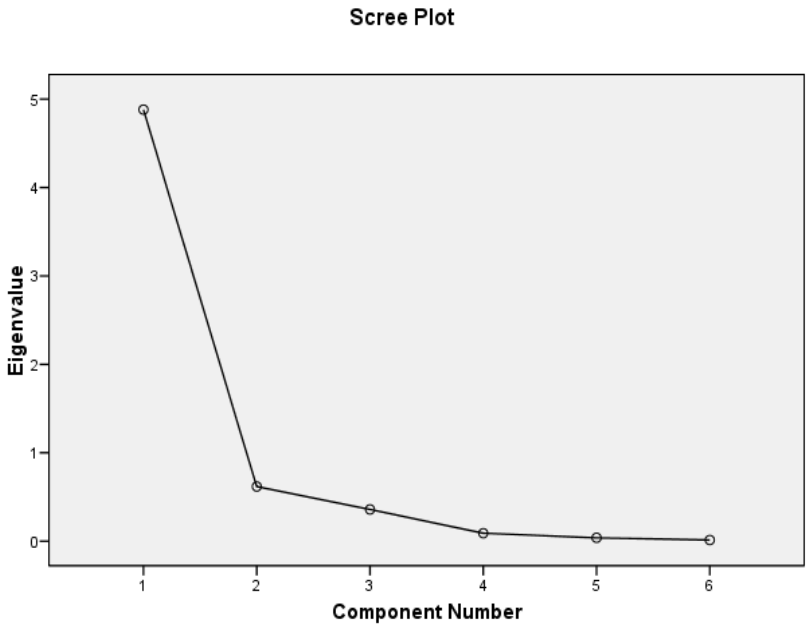

Figure 5.13: Scree plot showing eigenvalues for each of the 6 extracted components using PCA

This brief example demonstrated that PCA can be utilised in texture analysis. If sufficient information is present combining all f parameters at one time point and one grey level choice computationally time could be significantly reduced. Any future work would involve taking the components with the highest eigenvalues, in this case components 1 and 2 and performing analysis on these components as opposed to on the full set of 16 texture parameters. Reducing the large dimensionality of this dataset to 2 components would clearly reduce processing time significantly whilst retaining information from all 16 parameters as per the rules of PCA.

6 Wavelet Analysis

6.1 Introduction

Wavelets concentrate on looking at the different spatial frequencies within images as previously explained in the literature review chapter. Along with Gabor filters and Wigner transforms, wavelet transforms are one of the most commonly used time-frequency methods for calculating multiscale features in images. Wigner distributions suffer from interference between different components of a signal and Gabor filters are considered non-orthogonal in redundant features at different scales or channels, nevertheless Gabor filters have been used in texture segmentation. A Wavelet transform is a linear operation free from interference and is considered a good measure for texture analysis [88]. Many different functions exist that can be used as wavelets but the Haar function is especially suitable for image texture. A Haar-like feature looks at adjacent rectangular regions in a detection window at a specific location, it then sums up the pixel intensities in each region and the difference between these sums is calculated. This difference is then used to categorise sections of an image. A simple rectangular Haar-like feature can be defined as the difference of the sum of pixels of areas inside the rectangle, which can be at any position and scale within the original image [89]. This modified feature set is called *2-rectangle feature*, in addition there exist 3-rectangle and 4-rectangle features. The values indicate certain characteristics of a particular area of the image. Each feature type can indicate the existence (or absence) of certain characteristics in the image, such as edges or changes in texture. For example, a 2-rectangle feature can indicate where the border lies between a dark region and a light region [89].

The Haar wavelet is symmetric making it superior to other non-symmetric wavelets. Wavelet transform looks at directional variation and in a 2D image the analysis can be done in vertical, horizontal and diagonal directions.

6.2 One-dimensional Haar wavelet transform

The Haar wavelet is the simplest wavelet basis, here an example will be discussed to get a sense of how wavelets work [90]. Consider a one-dimensional image with a resolution of four pixels containing the following values

[9 7 3 5]

This can be represented in the Haar basis by computing a wavelet transform by first averaging the pixels together, pair wise giving the new lower resolution image with pixel values

[8 4]

The averaging process has clearly caused some information to be lost. In order to then recover the original four pixel values from the two averaged values, some details coefficients need to be sorted capturing the missing information. In the above example value 1 is chosen for the first detail coefficient, since the average computed is 1 less than 9 and 1 more than 7. The single number will allow the first two pixels of the original four-pixel image to be recovered. Similarly, the second detail coefficient is -1, since 4 + (-1) = 3 and 4 – (-1) = 5. Thus the original image is decomposed into a lower resolution (two-pixel) version and a pair of detail coefficients. Recursively repeating this process on the averages gives the full decomposition [90]

Resolution	Average	Detail coefficients
4	[9 7 3 5]	
2	[8 4]	[1 -1]
1	[6]	[2]

Finally the wavelet transform (wavelet decomposition) of the original four-pixel image can be defined to be the single coefficient representing the overall average of the original image, followed by the detailed coefficients in order of increasing resolution. Thus the wavelet

transform of the four-pixel original image for the one-dimensional Haar basis is:

[6 2 1 -1]

No information has been lost by this process of recursively averaging and differencing the coefficients (known as a filter bank). The original image and the transform both have 4 coefficients, and given the transform the image can be reconstructed to any resolution by recursively adding and subtracting the detail coefficients from the lower resolution versions.

6.3 Aims

The aims of this research include:

- Develop a robust software module in addition to the existing package for wavelet analysis of MRI data
- Apply developed software to cohort of 100 patients undergoing neoadjuvant chemotherapy of breast cancer, to help predict tumour response

6.4 Methods

The data acquisition and MRI protocols were exactly the same as mentioned in the texture analysis chapter which utilised the co-occurrence matrix approach. The same patient cohort was used and data was again split in the same way for analysis, the software module added to the existing software application adhered to software lifecycle as previously followed in the texture analysis chapter using co-occurrence method.

6.4.1 Patient Population

The data acquired from 100 patients, age range of 31-77 years, median age of 48 years, all undergoing neoadjuvant chemotherapy for treatment of locally advanced breast cancer at this Institute between April 2006 and September 2008 was retrospectively reviewed. This study was approved by the Local Ethics Committee and NHS Trust. Post treatment biopsy grade was known in 97 patients (4 not specified, 6 grade 1, 32 grade 2, 55 grade 3). Details of treatment regime were available in 95 patients, the majority of whom (57) had a combination of EC

(Epirubicin and Cyclophosphamide) and Docetaxel. MR data was acquired prior to treatment and information on tumour response was obtained on completion of all cycles of NAC. The number of days between initial baseline MR scan and chemotherapy starting ranged from 1-45 days with a median of 11.5 days.

After treatment the patients were categorized according to their response to chemotherapy: partial responders (PR) corresponding to a decrease in longest diameter of tumour of greater than 50% (40 patients) and non-responders (NR) corresponding to a decrease of less than 50% (49 patients). Data for remaining 11 patients was not available.

Data was also split based on factors that are known to influence response: TNBC (22 patients) vs. all other combinations of the three appropriate markers (49 patients) with 29 patients data unavailable; subdivided into nodal status by examining node negative (45 patients) vs. node positive (46 patients) with data in 9 patients not available; and tumour grade derived from pre-treatment biopsy, biopsy grade 1 or 2 (38 patients) vs. biopsy grade 3 (55 patients) and 7 patients data was not available.

6.4.2 MRI Protocol

MR acquisition protocol was as previously stated in section 5.1.2.2.

6.4.3 Statistical Analysis

Statistical analysis of the wavelet energy parameters was performed to establish whether the results were normally or non-normally distributed. The wavelet data was amalgamated and further combined with the patient data (PR or NR, Nodal status, TNBC and biopsy grade). Mann Whitney and *t*-tests were executed using SPSS on the combined data as appropriate.

6.4.4 Wavelet energy parameters

The wavelet coefficient image files were automatically generated using Matlab's in built wavelet toolbox so coding this functionality was not required for the purpose of this study. The saved coefficient files were generated using the neoadjuvant patient cohort as per in the

texture analysis study in chapter 5. Only the slices from each patient containing the largest ROI were processed using the wavelet analysis tool. A module in the software allowed the calculation of the wavelet energy levels by taking as input the generated coefficient image files and corresponding ROI file for each patient. Further details are described in the design specification section of this thesis (chapter 3) in which the process shows how the coefficient images were normalised prior to energy calculation. The energy parameters calculated for each ROI image were 12 in total for the Haar function at 4 levels, each level consisting of 3 directions. Energy levels are calculated as follows:

$$E_{subband,scale} = \frac{\sum_{x,y \in ROI} \left(d_{x,y}^{subband}\right)^2}{n}$$

Where n is the number of pixels in ROI, both at given scale and sub-band

In short the basic formula used in this study to calculate wavelet energy is the sum of each pixel squared divided by the total number of pixels. ROIs had to be reduced in size for successive scales in order to correspond to sub-band image dimensions. The output is a vector of features containing energies of wavelet coefficients calculated in sub-bands at successive scales. The software module generated for the purpose of this study outputs each patients energy levels in an excel spreadsheet where Directions 1,2 and 3 represent horizontal, vertical and diagonal directions respectively (fig 6.1) . Figure 6.3 illustrates example 2D wavelet output of a breast patient from the neoadjuvant data cohort obtained using the wavelet toolbox in Matlab using 4 Haar levels, figure 6.2 shows the original image.

	A	B
1		Wavelet Energy Results
2	energyWaveletHaar1Dir1	150.791874
3	energyWaveletHaar1Dir2	166.1194912
4	energyWaveletHaar1Dir3	17.63754465
5	energyWaveletHaar2Dir1	1017.01104
6	energyWaveletHaar2Dir2	1060.684529
7	energyWaveletHaar2Dir3	343.9940571
8	energyWaveletHaar3Dir1	6626.942639
9	energyWaveletHaar3Dir2	3441.183394
10	energyWaveletHaar3Dir3	1952.363587
11	energyWaveletHaar4Dir1	33975.98601
12	energyWaveletHaar4Dir2	18615.02495
13	energyWaveletHaar4Dir3	15668.31003
14	results for wavelet file	E04676_SL26.mat
15	generated by matlab@	02/03/2012 10:10
16		

Figure 6.1: example output from dicomreader software output of energy levels calculated from the wavelet coefficient images generated using Matlab's wavelet toolbox, where directions 1,2 and 3 represent horizontal, vertical and diagonal directions respectively. The results correspond to images in figures 6.2 and 6.3

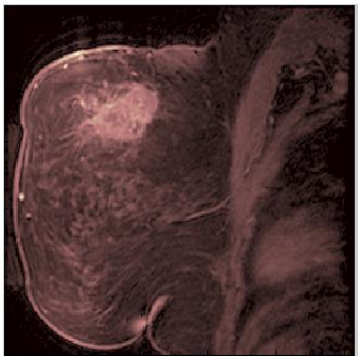

Figure 6.2: Original MR image of a breast patient undergoing neoadjuvant chemotherapy, patient is 58 year old female. Biopsy grade 3, TNBC, partial responder with respect to corresponding to a decrease in longest diameter of tumour of greater than 50%, nodal status data was unavailable. This image can be seen in figure 6.3 post 2D Haar wavelet analysis

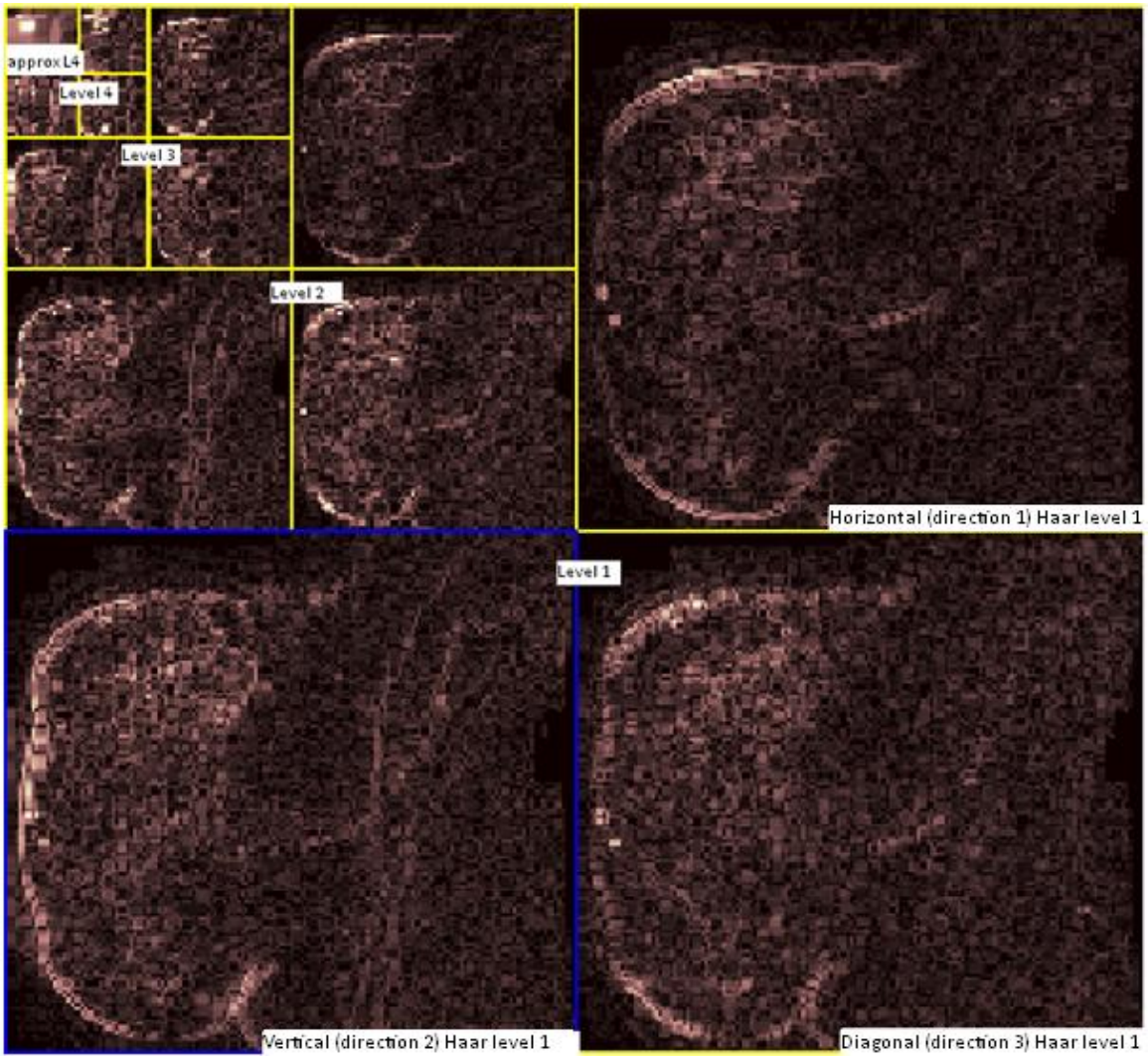

Figure 6.3: 2D wavelet coefficient output of a breast patient from the neoadjuvant data cohort obtained using the wavelet toolbox in Matlab using 4 Haar levels and three directions as labelled. The wavelet energy transform results can be seen in figure 6.1

6.5 Results

The wavelet transform energy values were calculated for the chosen slices, only the slice containing the largest ROI was analysed and wavelet coefficients saved, the ROI was then registered onto each generated image (images as per figure 6.3) i.e. 12 images per patient, because the images are scaled depending on the Haar level each ROI had to be scaled before being registered onto the image. Once this was established the energy was calculated and 12 wavelet parameters output per patient. Energy was calculated for the ROI only and each image was normalised between intensity values of 0 and 255 prior to wavelet analysis.

6.5.1 TNBC (Triple negative breast cancer) vs. non TNBC

Table 6.1 highlights the P values for the wavelet energy values for the three directions and four Haar levels that showed significant differences between TNBC and non TNBC. Table 6.2 shows all the results for this category at the 5 minute post contrast time point.

Wavelet Energy	Median; Range		P value
	TNBC	Non TNBC	
PC_1min			
Haar4 Direction 1	$4.19x10^4$; $2.20x10^3$ – $3.06x10^5$	$6.87x10^4$; $5.87x10^3$ – $1.05x10^6$	0.042 (Mann Whitney)
PC_2min			
Haar4 Direction 1	$4.85x10^4$; $3.01x10^3$ – $3.29x10^5$	$7.85x10^4$; $4.61x10^3$ – $1.01x10^6$	0.050 (Mann Whitney)
PC_3min			
Haar3 Direction 2	$1.03x10^4$; $2.82x10^3$ – $3.79x10^4$	$1.84x10^4$; $2.81x10^3$ - $1.67x10^5$	0.032 (Mann Whitney)
Haar4 Direction 1	$5.38x10^4$; $2.45x10^3$ - $3.48x10^5$	$8.00x10^4$; $3.38x10^3$ - $8.95x10^5$	0.043 (Mann Whitney)
Haar4 Direction 2	$4.57x10^4$; $8.18x10^3$ - $4.04x10^5$	$1.08x10^5$; 441.88 – $3.12x10^5$	0.047 (Mann Whitney)
PC_4min			
Haar3 Direction 2	$1.17x10^4$ (mean) $\pm 9.11x10^3$(sd)	$2.13x10^4$(mean) $\pm 2.04x10^4$(sd)	0.038
PC_5min			
Haar4 Direction 1	$6.48x10^4$ (mean) $\pm 7.51x10^4$(sd)	$1.29x10^5$(mean) $\pm 1.51x10^5$(sd)	0.027
Haar4 Direction 2	$3.79x10^4$; $7.48x10^3$ - $3.69x10^5$	$9.08x10^4$; 9.88 - $3.47x10^5$	0.045 (Mann Whitney)

Table 6.1: Summary for all time points including the mean/standard deviation or median/range and p-values for the wavelet transform energy parameters that showed significant differences between TNBC and non TNBC

Wavelet Energy	Mean ± standard deviation		P value
	TNBC	Non TNBC	
PC_5min			
Haar1 Direction 1	$2.74x10^2$ $\pm 2.75x10^2$	$2.75\ x10^2$ $\pm 1.17x10^2$	0.967
Haar1 Direction 2	$2.44x10^2$ $\pm 1.48x10^2$	$2.88x10^2$ $\pm 1.34x10^2$	0.231
Haar1 Direction 3	26.27±10.74	29.37±11.34	0.292
Haar2 Direction 1	$2.52x10^3$ $\pm 1.44\ x10^3$	$2.84x10^3$ $\pm 1.42x10^3$	0.397
Haar2 Direction 2	$1.99x10^3$ $\pm 1.10\ x10^3$	$2.51\ x10^3$ $\pm 1.15x10^3$	0.083
Haar2 Direction 3	$5.04\ x10^2$ $\pm 2.49\ x10^2$	$5.64x10^2$ $\pm 2.62x10^2$	0.379
Haar3 Direction 1	$1.57\ x10^4$ $\pm 1.27\ x10^4$	$1.84x10^4$ $\pm 1.23x10^4$	0.417
Haar3 Direction 2	$1.21x10^4$ $\pm 9.53\ x10^3$	$2.00x10^4$ $\pm 1.84x10^4$	0.063
Haar3 Direction 3	Median: $3.10x10^3$ Range: $1.16x10^3$ – $1.44x10^4$	Median: $3.96x10^3$ Range: $7.30x10^2$ – $3.10x10^4$	0.161 (Mann Whitney)
Haar4 Direction 1	$6.48x10^4$ $\pm 7.51x10^4$	$1.29x10^5$ $\pm 1.51x10^5$	0.027
Haar4 Direction 2	Median: $3.79x10^4$ Range: $7.48x10^3$ - $3.69x10^5$	Median: $9.08x10^4$ Range: 9.88 - $3.47x10^5$	0.045 (Mann Whitney)
Haar4 Direction 3	Median: $1.18x10^4$ Range: 3.95 $x10^3$ – $8.33x10^4$	Median: $1.89x10^4$ Range: $6.05\ x10^2$ - $1.53x10^5$	0.168 (Mann Whitney)

Table 6.2: Results at 5 minute post contrast time point showing the mean/standard deviation or median/range and p-values for the wavelet transform energy parameters markers. P-values highlighted showed significant differences between TNBC and non TNBC

Time points

The Haar level 4 direction 1 (horizontal) noted significant differences at 1,2,3 and 5 minutes post contrast time points. Haar level 4 direction 2 (vertical) and Haar level 3 direction 2 also showed 2 significant differences each. No significant differences were reported at pre-contrast phase. It is unclear why energy levels calculated in the diagonal direction revealed no

significant differences. It is worth noting that when looking at MR images in the diagonal direction the pixel to pixel distances are further apart than when looking in horizontal or vertical directions. Also all significant differences were found at levels 3 or 4 only.

6.5.2 PR or NR (% change in longest diameter)

Table 6.3 highlights the P values for the wavelet energy values for the three directions and four Haar levels that showed significant differences in wavelet energy based on PR or NR (partial responders or non-responders with respect to longest diameter of lesion). Table 6.4 shows all the results for this category at the 5 minute post contrast time point.

Wavelet Energy	Mean value ± Standard Deviation		P value
	NR	PR	
No contrast			
Haar1 Direction 2	$1.43x10^2$±1.12 $x10^2$	9.82±65.23	0.020
PC_1min			
Haar1 Direction 2	3.87 $x10^2$ ±2.10 $x10^2$	287.52±139.18	0.009
Haar1 Direction 3	34.93±15.30	28.72±12.42	0.042
Haar2 Direction 2	$3.17x10^3$±1.68 $x10^3$	$2.55x10^3$±1.03x 10^3	0.036
Haar2 Direction 3	7.18 $x10^2$ ±3.30 $x10^2$	5.70 $x10^2$ ±2.99 $x10^2$	0.031
PC_2min			
Haar1 Direction 2	3.70 $x10^2$ ±1.95 $x10^2$	2.63 $x10^2$ ±1.17$x10^2$	0.002
Haar1 Direction 3	34.32±14.59	27.86±11.00	0.023
Haar2 Direction 2	3.13x10^3±1.51 $x10^3$	2.37x10^3±874.86	0.004
Haar2 Direction 3	7.02 $x10^2$ ±3.11 $x10^2$	5.56 $x10^2$ ±3.02$x10^2$	0.029
Haar3 Direction 3	Median: $4.11x10^3$ Range: 689.68 – $5.36x10^4$	Median: $3.36x10^3$ Range: 769.24 – $8.87x10^3$	0.025 (Mann Whitney)
PC_3min			
Haar1 Direction 2	3.45 $x10^2$ ±1.94 $x10^2$	2.51 $x10^2$ ±1.09$x10^2$	0.008
Haar2 Direction 2	$2.95x10^3$±1.35 $x10^3$	$2.29x10^3$ ±8.82$x10^2$	0.007
Haar3 Direction 3	Median: $3.95x10^3$ Range: $1.12x10^3$ – $5.78x10^4$	Median: $3.06x10^3$ Range: 725.43 – $1.03x10^4$	0.021 (Mann Whitney)

PC_4min			
Haar1 Direction 2	3.10 x10^2 ±1.42 x10^2	2.27 x10^2 ±1.10x10^2	0.003
Haar2 Direction 2	2.64x10^3 ±1.23x10^3	2.06x10^3±925.26	0.013
Haar3 Direction 2	Median: 1.57x10^4 Range: 4.11x10^3 – 1.33x10^5	Median: 1.07x10^4 Range: 1.02x10^3– 5.44x10^4	0.024 (Mann Whitney)
Haar3 Direction 3	Median: 3.78x10^3 Range: 859.17 – 3.78x10^4	Median: 2.50x10^3 Range: 158.81 – 1.19x10^4	0.011 (Mann Whitney)
PC_5min			
Haar1 Direction 2	3.05 x10^2 ±1.41 x10^2	2.33 x10^2 ±1.12x10^2	0.014
Haar2 Direction 2	2.66x10^3 ±1.26x10^3	2.10x10^3±993.07	0.029
Haar3 Direction 2	2.10x10^4 ±1.83x10^4	1.25x10^4±8.26x 10^3	0.006
Haar3 Direction 3	Median: 4.00x10^3 Range: 1.12x10^3– 3.10x10^4	Median: 2.68x10^3 Range: 8.21 x10^2 – 1.47x10^4	0.012 (Mann Whitney)

Table 6.3: The P values for the wavelet energy values for the three directions and four Haar levels that showed significant differences in wavelet energy based on PR or NR (partial responders or non-responders with respect to longest diameter of lesion)

Wavelet Energy	Mean ± standard deviation		P value
	NR	PR	
PC_5min			
Haar1 Direction 1	$3.01x10^2$ $\pm1.53x10^2$	$2.69\ x10^2$ $\pm1.19x10^2$	0.297
Haar1 Direction 2	$3.05\ x10^2$ $\pm1.41\ x10^2$	$2.33\ x10^2$ $\pm1.12x10^2$	0.014
Haar1 Direction 3	30.31±13.36	26.68±11.29	0.191
Haar2 Direction 1	$3.15x10^3$ $\pm1.73\ x10^3$	$2.53x10^3$ $\pm1.45x10^3$	0.085
Haar2 Direction 2	$2.66x10^3$ $\pm1.26x10^3$	$2.10x10^3$±993.07	0.029
Haar2 Direction 3	$6.16\ x10^2$ $\pm3.35\ x10^2$	$5.10\ x10^2$ $\pm2.50x10^2$	0.116
Haar3 Direction 1	$1.93\ x10^4$ $\pm1.37\ x10^4$	$1.67x10^4$ $\pm1.21x10^4$	0.380
Haar3 Direction 2	$2.10x10^4$ $\pm1.83x10^4$	$1.25x10^4$±8.26x 10^3	0.006
Haar3 Direction 3	Median: $4.00x10^3$ Range: $1.12x10^3$– $3.10x10^4$	Median: $2.68x10^3$ Range: $8.21\ x10^2$ – $1.47x10^4$	0.012 (Mann Whitney)
Haar4 Direction 1	Median: $7.76x10^4$ Range: $3.22x10^3$– $7.77x10^5$	Median: $5.64x10^4$ Range: $2.74\ x10^3$ – $3.48x10^5$	0.204 (Mann Whitney)
Haar4 Direction 2	$1.03\ x10^5$ $\pm1.83\ x10^4$	$1.25x10^4$ $\pm8.26x10^3$	0.305
Haar4 Direction 3	Median: $1.71x10^4$ Range: $3.95x10^3$– $2.12x10^5$	Median: $1.72x10^4$ Range: $9.96x10^2$ – $8.33x10^4$	0.643 (Mann Whitney)

Table 6.4: Results at 5 minute post contrast time point showing the mean/standard deviation or median/range and p-values for the wavelet transform energy parameters markers. P-values highlighted showed significant differences between PR or NR (partial responders or non-responders with respect to longest diameter of lesion)

Time points

This group showed significant differences in wavelet energy values at all time points. With the exception of no contrast time point all other 1 minute to 5 minute post contrast time points showed at least 3 energy wavelet parameters as having significant differences. The parameter

for Haar level 1 in the vertical direction was the only one that showed consistency in significant differences across all pre and post contrast time points. In total this group highlighted 21 significant differences across all of the time points.

6.5.3 Nodal status; Node-negative vs. Node-positive

Table 6.5 highlights the P values for the wavelet energy values for the three directions and four Haar levels that showed significant differences in wavelet energy based on nodal status. Table 6.6 shows all the results for this category at the 5 minute post contrast time point.

Wavelet Energy	**Median; Range**		**P value**
	Node -ve	**Node +ve**	
No contrast			
Haar3 Direction 2	$3.40x10^3$; 57.20 – $3.72x10^4$	$7.14x10^3$; 635.39– $3.16x10^4$	0.023 (Mann Whitney)
PC_5min			
Haar3 Direction 2	$1.08x10^4$; $2.44x10^3$– $1.17x10^5$	$1.84x10^4$; $1.95x10^3$– $4.60x10^4$	0.030 (Mann Whitney)

Table 6.5: The P values for the wavelet energy values for the three directions and four Haar levels that showed significant differences in wavelet energy based on Nodal status

Wavelet Energy	Mean ± standard deviation		P value
	Node -ve	Node +ve	
PC_5min			
Haar1 Direction 1	$3.01x10^2$ $\pm1.63x10^2$	$2.88\ x10^2$ $\pm1.12x10^2$	0.648
Haar1 Direction 2	$2.71x10^2$ $\pm1.30x10^2$	$2.95x10^2$ $\pm1.34x10^2$	0.400
Haar1 Direction 3	29.39±14.04	30.09±10.96	0.795
Haar2 Direction 1	$2.99x10^3$ $\pm1.83\ x10^3$	$2.93x10^3$ $\pm1.39x10^3$	0.842
Haar2 Direction 2	$2.36x10^3$ $\pm1.24\ x10^3$	$2.66x10^3$ $\pm1.12x10^3$	0.246
Haar2 Direction 3	$5.57\ x10^2$ $\pm3.42\ x10^2$	$6.15x10^2$ $\pm2.60x10^2$	0.372
Haar3 Direction 1	$1.99\ x10^4$ $\pm1.49\ x10^4$	$1.67x10^4$ $\pm1.09x10^4$	0.266
Haar3 Direction 2	Median:$1.08x\ 10^4$ Range:$2.44x\ 10^3$– $1.17x10^5$	Median:$1.84x10^4$ Range:$1.95x10^3$–$4.60x10^4$	0.030 (Mann Whitney)
Haar3 Direction 3	Median:$3.17\ x10^3$ Range:$1.18x\ 10^3$ -$3.10\ x10^4$	Median:$4.17\ x10^3$ Range:$7.30x10^2$ - $1.48\ x10^4$	0.164 (Mann Whitney)
Haar4 Direction 1	Median:$6.49x\ 10^4$ Range:$6.85\ x10^3$-$5.96\ x10^5$	Median:$6.63x10^4$ Range:$2.74\ x10^3$-$7.77\ x10^5$	0.788 (Mann Whitney)
Haar4 Direction 2	$8.20\ x10^4$ $\pm8.51\ x10^4$	$1.06x10^5$ $\pm8.56x10^4$	0.211
Haar4 Direction 3	Median:$1.66\ x10^4$ Range:$6.05\ x10^2$- $1.53\ x10^5$	Median:$1.85x10^4$ Range:$9.96x10^2$-$2.12\ x10^5$	0.366 (Mann Whitney)

Table 6.6: Results at 5 minute post contrast time point showing the mean/standard deviation or median/range and p-values for the wavelet transform energy parameters markers. P-values highlighted showed significant differences between Node -ve and Node +ve

Time points

There were only 2 significant differences noted for the nodal status group, both were for the parameter at Haar level 3 in the vertical direction, one was at the no contrast time point and the second at the 5 minute post contrast (wash out) time point suggesting that there are no wavelet energy differences during the initial contrast enhancement.

6.5.4 Biopsy grade

Table 6.7 highlights the P values for the wavelet energy values for the three directions and four Haar levels that showed significant differences in wavelet energy based on biopsy grade. Table 6.8 shows all the results for this category at the 5 minute post contrast time point.

Time points

This group showed significant differences in wavelet energy values at all times points. At all pre and post contrast time points this group showed 1-2 energy parameters with significant differences with the exception of 5 minute post contrast time point showing significant differences in 4 of the parameters. The parameter for Haar level 3 in the vertical direction was the only one that showed consistency in significant differences across all post contrast time points. In total this group highlighted 12 significant differences across all of the time points.

Wavelet Energy	Median; Range		P value
	Bi Grade 1or2	Bi Grade 3	
No contrast			
Haar3 Direction 1	$7.27x10^3$; 647.79 - $2.84 x10^4$	$4.37x10^3$; 199.04 - $2.60 x10^4$	0.038 (Mann Whitney)
PC_1min			
Haar2 Direction 2	$3.26x10^3$(mean) ±1.50 $x10^3$(sd)	$2.63x10^3$(mean) ±1.40 $x10^3$(sd)	0.038
Haar3 Direction 2	$1.80x10^4$; $3.25 x10^3$ - $1.18 x10^5$	$1.30x10^4$; $3.18 x10^3$ - $5.28 x10^4$	0.049 (Mann Whitney)
PC_2min			
Haar2 Direction 2	$3.16x10^3$(mean) ±1.30 $x10^3$(sd)	$2.51x10^3$(mean) ±1.29 $x10^3$(sd)	0.019
Haar3 Direction 2	$2.46x10^4$(mean)±1.59 $x10^4$(sd)	$1.59 x10^4$(mean) ±1.10 $x10^4$(sd)	0.045
PC_3min			
Haar2 Direction 2	$2.96x10^3$(mean) ±1.23 $x10^3$(sd)	$2.40 x10^3$(mean) ±1.15 $x10^3$(sd)	0.025
Haar3 Direction 2	$1.77x10^4$; $3.31 x10^3$ - $1.67 x10^5$	$1.22x10^4$; $2.81 x10^3$ - $4.45 x10^4$	0.016 (Mann Whitney)
PC_4min			
Haar3 Direction 2	$2.25x10^4$(mean)±2.21 $x10^4$(sd)	$1.32 x10^4$(mean) ±9.60 $x10^3$(sd)	0.019
PC_5min			
Haar3 Direction 1	$2.23x10^4$(mean)±1.38 $x10^4$(sd)	1.61 $x10^4$(mean)±1.20 $x10^4$(sd)	0.028
Haar3 Direction 2	$1.52x10^4$; $1.95 x10^3$ - $1.17 x10^5$	$9.57x10^3$; $2.36 x10^3$ - $4.62 x10^4$	0.007 (Mann Whitney)
Haar3 Direction 3	$3.96x10^3$; $1.23 x10^3$ - $3.10 x10^4$	$3.05x10^3$; 730.50 - $1.47 x10^4$	0.034 (Mann Whitney)
Haar4 Direction 1	$8.87x10^4$; $5.74 x10^3$ - $5.97 x10^5$	$5.45x10^4$; $3.79 x10^3$ - $7.77 x10^5$	0.037 (Mann Whitney)

Table 6.7: The P values for the wavelet energy values for the three directions and four Haar levels that showed significant differences in wavelet energy based on biopsy grade

Wavelet Energy	Mean ± standard deviation		P value
	Bi Grade 1or2	Bi Grade 3	
PC_5min			
Haar1 Direction 1	$3.13x10^2$ $\pm 1.67x10^2$	$2.71\ x10^2$ $\pm 1.20x10^2$	0.167
Haar1 Direction 2	$2.81\ x10^2$ $\pm 1.23\ x10^2$	$2.62\ x10^2$ $\pm 1.35x10^2$	0.500
Haar1 Direction 3	31.05±14.81	27.42±10.93	0.191
Haar2 Direction 1	$3.33x10^3$ $\pm 1.88\ x10^3$	$2.64x10^3$ $\pm 1.41x10^3$	0.051
Haar2 Direction 2	$2.64x10^3$ $\pm 1.26x10^3$	$2.22x10^3$ $\pm 1.10x10^3$	0.101
Haar2 Direction 3	$6.27\ x10^2$ $\pm 3.61\ x10^2$	$5.26\ x10^2$ $\pm 2.47x10^2$	0.121
Haar3 Direction 1	$2.23x10^4$±1.38 $x10^4$	$1.61\ x10^4$±1.20 $x10^4$	0.028
Haar3 Direction 2	Median:1.52x 10^4 Range:1.95 $x10^3$ - $1.17\ x10^5$	Median:$9.57x10^3$ Range:$2.36\ x10^3$ - $4.62\ x10^4$	0.007 (Mann Whitney)
Haar3 Direction 3	Median:3.96x 10^3; Range:1.23 $x10^3$ - $3.10\ x10^4$	Median:$3.05x10^3$ Range:730.50 - $1.47\ x10^4$	0.034 (Mann Whitney)
Haar4 Direction 1	Median:8.87x 10^4 Range:5.74 $x10^3$ - $5.97\ x10^5$	Median:$5.45x10^4$ Range:$3.79\ x10^3$ - $7.77\ x10^5$	0.037 (Mann Whitney)
Haar4 Direction 2	Median:7.25x $x10^4$ Range:9.88 – $3.47\ x10^5$	Median:4.47x $x10^4$ Range:$7.48\ x10^3$ – $3.69\ x10^5$	0.728 (Mann Whitney)
Haar4 Direction 3	Median:2.07x $x10^4$ Range:6.05 $x10^2$ – $1.53x10^5$	Median:1.44x $x10^4$ Range:$3.58\ x10^3$ – $2.12x10^5$	0.163 (Mann Whitney)

Table 6.8: Results at 5 minute post contrast time point showing the mean/standard deviation or median/range and p-values for the wavelet transform energy parameters markers. P-values highlighted showed significant differences for biopsy grade

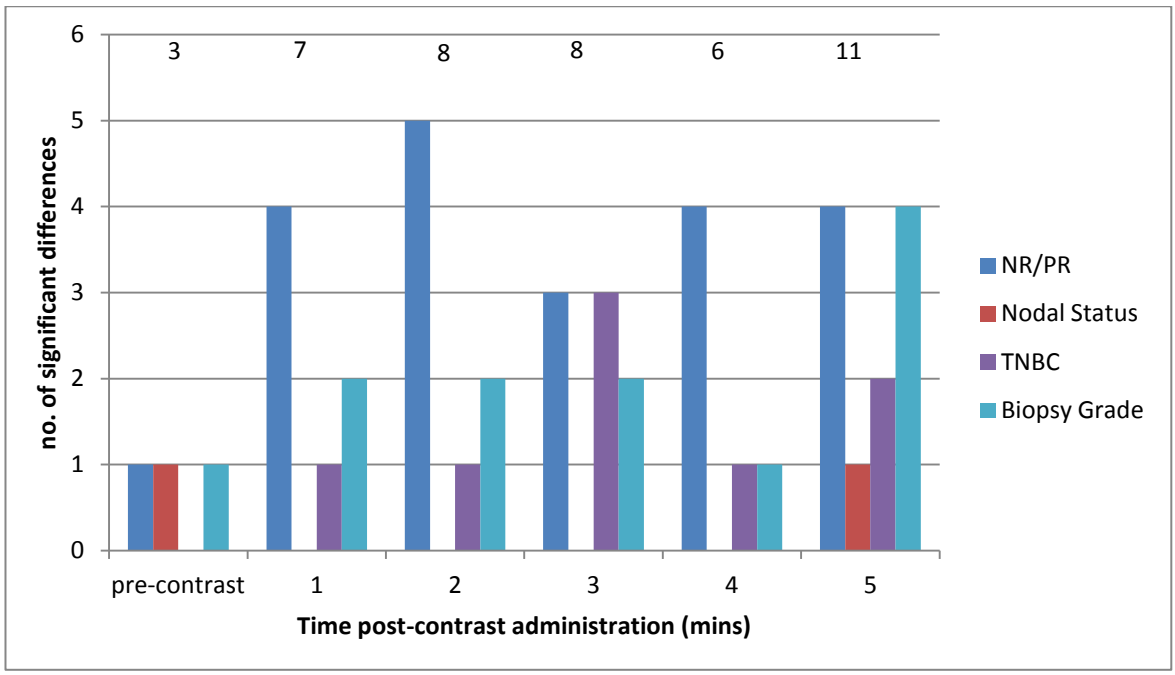

Figure 6.4: Summary of significant differences for all data groups for wavelet energy values

6.6 Discussion

The results presented in this chapter demonstrated significant differences in wavelet analysis energy parameters between partial responders and non responders of chemotherapy. Unlike texture analysis using Haralicks co-occurrence method in which the importance of contrast enhanced MRI was seen as only 2 significant differences in texture were found in the pre contrast time point images, wavelet analysis suggests that differentiating between groups can be successfully found in the pre-contrast stage. There were certain groups that clearly only showed significant differences post contrast such as TNBC vs. non TNBC. On the other hand nodal status only showed significant differences in the pre-contrast and washout phases. Groups such as PR vs. NR (% change in longest diameter) highlighted larger number of significant differences in post contrast time points than in pre-contrast. These results are summarised in figure 6.4.

Of the 43 significant differences highlighted in figure 6.4 for all the different groupings, wavelet analysis clearly shows the 5 minute post contrast time point performing better than

the others, pre-contrast time points showed the least number of significant differences and 1-4 minute post contrast time points were more consistent. It can be seen from figure 6.4 that for all the time points (pre-contrast, 1, 2, 3, 4 and 5 minutes post contrast) the significant differences were 6.98%, 16.28%, 18.6%, 18.6%, 13.95% and 25.58% respectively.

With respect to the different Haar levels (1, 2, 3 and 4) there the split in significant differences was 18.6%, 22.3%, 41.9% and 16.3% respectively, indicating that Haar level 3 revealed the most and Haar 4 the least significant differences. With respect to direction of wavelets analysed 16.3% of the differences were found in the horizontal direction, 62.8% vertical and 20.9% in the diagonal directions.

6.7 Conclusions

This work has highlighted that wavelet analysis energy levels can show differences between groups (based on TNBC, PR or NR with respect to % change in longest diameter, nodal status and biopsy grade) and are seen throughout all time points (pre and post contrast administration) with the highest number of total significant differences noted at 5 minutes post contrast. The vertical directions contain over 62% of the results, this directional bias is unexpected and somewhat surprising and would require further investigation in a larger data cohort, in addition it may be worth investigating into the fact that all the images acquired for this thesis have phase encoding in the vertical direction.

7 Texture Mapping

7.1 Introduction

Texture analysis was used to assess MR images in chapter 5 in which as with most previous studies, it was performed using generated areas investigating known ROI's. In addition to helping to score lesions using BI-RADS (section 2.3), MRI is also used as a screening tool. As with mammography any one patient can contain huge volumes of data, this is overcome by CAD systems to allow automated analysis. The idea behind the study in this chapter is to highlight areas of interest (possible lesions) using an additional function of the in house generated software tool, these highlighted areas can then be marked and used as an aid by radiologists for further investigation. This study aims to texture map DCE MR images of breast patients utilising the co-occurrence method but on a pixel by pixel basis in order to determine threshold values for normal, benign and malignant tissue and ultimately creating a functionality within the developed software to highlight hotspots outlining areas of interest (possible lesions). Benign and normal data was taken from screening data and malignant data from known malignancies.

7.2 Aims

The software developed for texture analysis will be extended; a texture mapping facility will be added which will analyse any given image pixel by pixel and perform texture analysis on each individual pixel, the result will be one new map per texture parameter (16 texture parameters as outlined in chapter 5). From the resulting maps individual pixel values will be analysed and processed in an attempt to try and threshold values for benign and malignant lesions as well as normal breast tissue. Once this is achieved these threshold values will aid in developing the software further to achieve a hot spot (lesion) detection functionality which will allow a user of the software to take any of the 16 texture mapped output image files and the software will automatically highlight hotspots (areas of interest) that may contain a lesion.

7.3 Methods

Data acquired was a series of high resolution 3D T1 weighted images of breast patients [TR range 4-4.8ms, TE range 1.5-1.9ms/Fr, 20x20cm or 22x22cm FOV, 256x256 matrix, 4-5.4mm slice thickness]. The study analysed images from 2 minute post contrast time points including 20 normal breast patients, 21 with known benign (taken from MR screening data) and 17 with known malignant (taken from MR breast images of known malignancies) lesions.

7.3.1 Segmentation

Segmentation was semi-automated within the software the user to highlight the area from nipple to chest wall prior to performing texture mapping. The user selects start and end points of where the image is to be segmented, the idea being this removes the chest wall area as well as noise present in front of the nipple area thus reducing the processing time of the mapping function. In fact by doing this for any given single breast image processing time was reduced from 15 to 4 minutes.

7.3.2 Pixel by pixel mapping

The software was an extension of the previously generated application where the author successfully used texture analysis using the co-occurrence matrices method to predict chemotherapy response in breast patients [85] as seen in chapter 5. Texture mapping was performed on the slice with the largest cross section of disease once the images had been segmented. The software used was an extension of the previously created application therefore all the underlying mathematical formulas and co-occurrence matrices method including histogram equalisation techniques and grey level variations used are the same as per the texture analysis covered in chapter 5. The biggest different in this study was the fact that the texture analysis was performed on a pixel by pixel basis on the whole image as opposed to a pre drawn ROI. The texture mapped output of that given pixel is placed in a new image (16 in total, one for each texture parameter) until every pixel is analysed and a map is generated for each texture parameter. Texture analysis was performed on a pixel by pixel basis specifying a

matrix size surrounding each pixel, from this a co-occurrence matrix is calculated for each pixel in the original image (figures 7.1 and 7.2), the result is that an image map is output for each of the 16 texture parameters. Larger matrix sizes will result in more blurred images for each texture parameter whereas smaller matrix sizes will have lower counting stats and if noise is present then the image becomes less accurate (figure 7.2). In this chapter a 5x5 matrix surrounding each pixel was. Figure 7.3 highlights an example of a benign case which has been analysed using the texture mapping feature, the figure shows each of the 16 maps produced given an MR image as input.

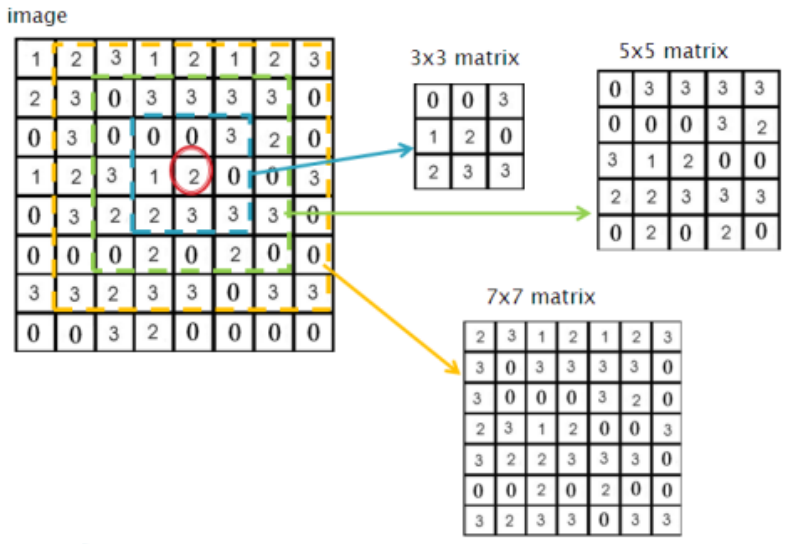

Figure 7.1: illustration shows how the in house software treats the surrounding pixels based on the specified matrix size, from this the co-occurrence matrix is calculated

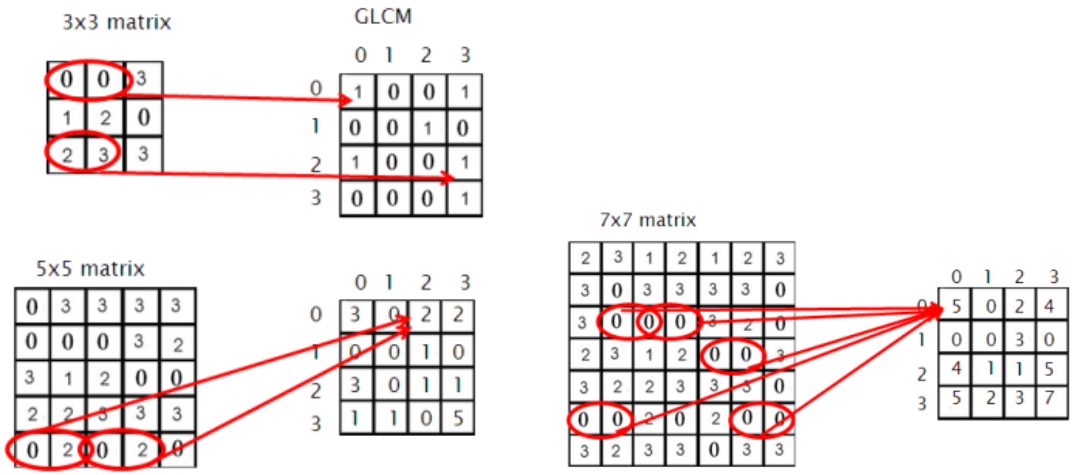

Figure 7.2: calculation for different matrix sizes (3, 5 and 7) clearly produce different corresponding co-occurrence matrices

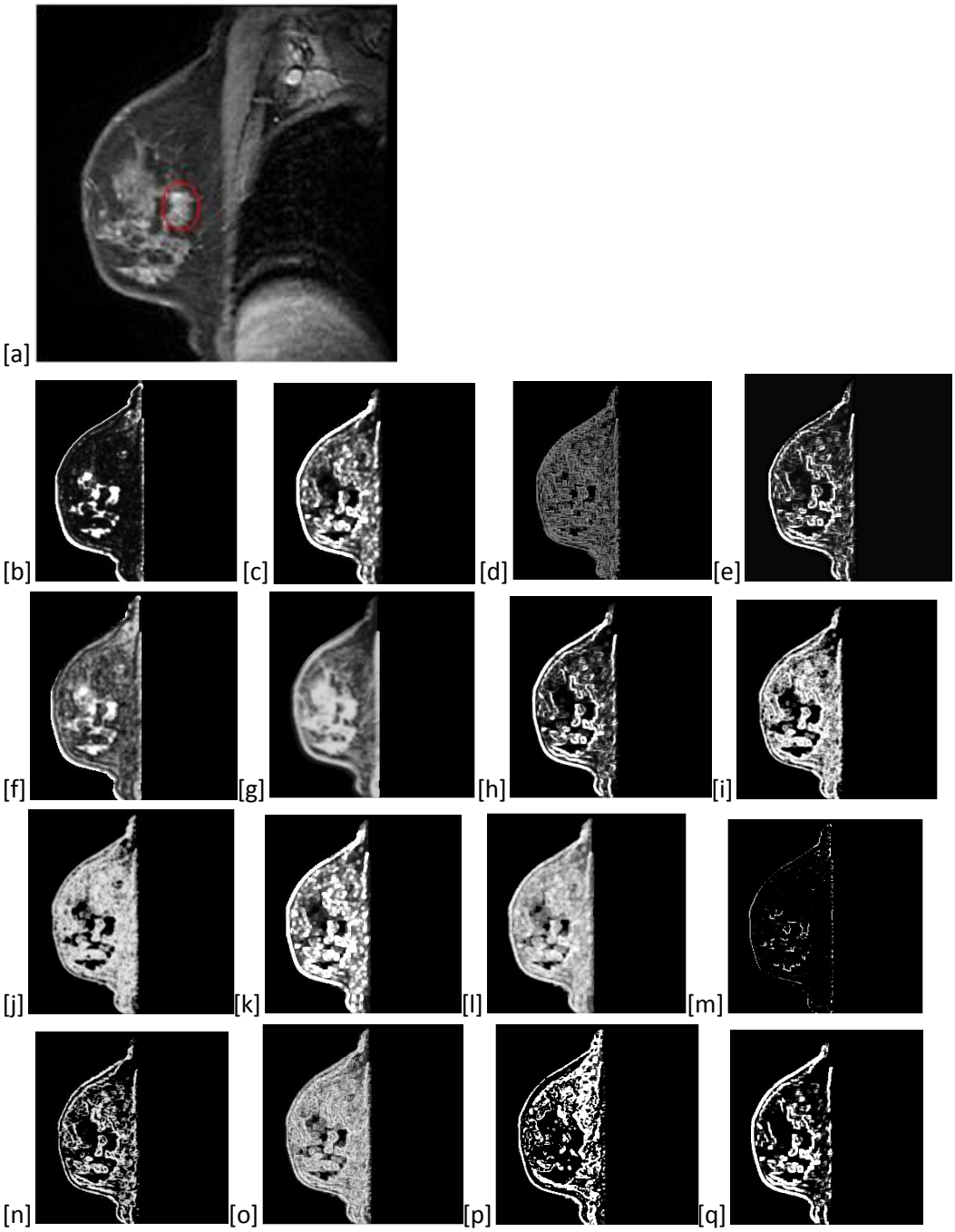

Figure 7.3: original MR image [a] acquired at 2 minute post contrast using a high resolution 3D T_1 weighted sequence. Patient is a 51 year old female with a benign lesion (highlighted after visual inspection and reference to radiological report). Radiologist report stated the lesion as having poorly defined margin with surrounding normal parenchyma, biopsy result revealed mild duct ectusia in the right breast. Maps were generated post segmentation of original MR image using the in house software's texture mapping feature, the maps [b-q] are of texture parameters f_1 to f_{16} respectively using a 5x5 matrix size

A module has been developed to search for hotspots in the texture mapped image whereby the software feature searches the image pixel by pixel for a specified range of pixel values and window size in order to highlight potential lesions.

7.3.3 FROC Analysis

The Free Response Operating Characteristic (FROC) curve is based on a regional analysis. The FROC paradigm is mainly used in the assessment of medical imaging systems, particularly in the evaluation and comparison of CAD algorithms [91, 92].

FROC analysis works in a similar way to ROC analysis, except that the false positive rate on the x-axis is replaced by the number of false positives per image. FROC analysis utilises location information, so that if a disease is highlighted in the appropriate location it is rewarded else it is penalised. The FROC analysis is more relevant to the clinical practice of radiology, where it is not only important to identify disease, but also to offer further guidance regarding other characteristics (such as location) of the disease.

Before FROC data can be analyzed, a definition of a detected region is needed. Although there are different opinions in the literature [92-94], in our work we use an ad hoc approach which classes the lesion as a detected true positive if the software highlights any part of the lesion. Whether this highlights only a fraction of the lesion or goes beyond the lesion it is still classified as a true positive. In later optimized versions of the software this could be adapted but this study is primarily proof of principle that lesion detection is in fact possible through texture mapping.

7.4 Results

7.4.1 Segmentation

Images were successfully segmented post processing, Figure 7.4 shows example of a malignant case pre and post segmentation

[a] 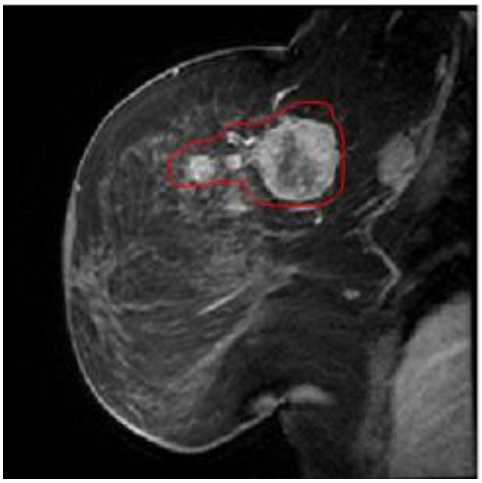 [b] 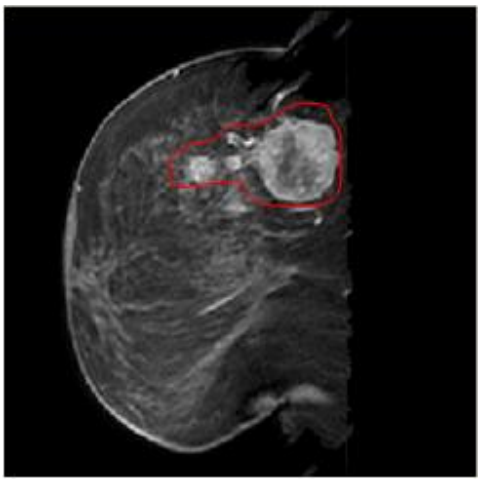

Figure 7.4: MR image of breast with known malignancy (highlighted area) [a] original image and [b] segmented image after elimination of areas posterior to and including the chest wall. Noise areas inferior to the nipple have also been removed to improve processing time

7.4.2 Texture Map

Table 7.1 shows the data from the benign and malignant patients after lesion detection (hotspot) feature was executed for the texture parameter f_1 using a matrix size of 5. The software revealed high overall sensitivity values (59-88%) varying depending on the input variables used for f_1. The average number of false positives per patient also varied depending on input variable from 0.4–5. The filtering technique involved viewing the histogram of each image and taking the lowest or middle range of values and use these as the input variables for identifying pixels as areas of interest. In addition changing matrix sizes allowed for average pixel value search regions to be varied.

Table 7.2 shows the data from the benign and malignant patients after lesion detection (hotspot) feature was executed for the texture parameter f_9 using a matrix size of 5. The software revealed high overall sensitivity values (74-94%) varying depending on the input variables used for f_9. The average number of false positives per patient also varied depending on input variable from 2–5.

	Lesion identified (ignoring edges/noise) Yes = 1/no = 0					No. Of additional areas (non lesion, not including edge outline/noise) joint areas classed as one lesion				
	***S1**	***S2**	***S3**	***S4**	***S5**	***S1**	***S2**	***S3**	***S4**	***S5**
B2	1	1	1	1	0	2	3	3	1	1
B4	1	1	1	0	0	4	2	1	0	0
B5	0	0	0	0	0	5	2	2	1	1
B6	1	1	0	0	0	6	3	4	2	1
B7	1	1	1	1	1	3	3	3	1	1
B8	0	0	0	0	0	2	0	0	0	0
B9	1	1	1	0	0	3	0	0	0	0
B10	1	1	1	1	1	3	1	2	2	1
B11	1	1	1	1	1	3	1	1	0	0
B13	1	1	0	0	0	2	1	1	0	0
B15	1	1	1	1	1	1	0	0	0	0
B16	1	1	1	1	1	7	5	3	3	0
B19	0	0	0	0	0	3	3	2	1	0
B20	1	1	1	1	1	2	2	3	1	0
B21	1	1	1	1	1	3	2	2	1	1
B23	1	1	1	1	0	8	4	2	1	0
B24	1	1	0	0	0	6	2	2	1	1
M1	1	1	1	1	1	4	1	0	0	0
M2	1	1	1	1	1	4	2	1	0	0
M3	0	0	0	0	0	8	5	1	0	0
M4	1	1	1	1	0	6	3	2	1	1
M5	1	1	1	1	0	7	7	2	2	0
M6	1	1	1	1	1	6	2	1	0	0
M7	1	1	1	1	1	9	8	3	2	2
M8	1	1	1	1	1	9	5	3	2	2
M9	1	1	1	1	1	7	4	1	0	0
M10	1	1	1	1	1	12	5	1	1	0
M11	1	1	1	1	1	4	2	0	0	0
M12	1	1	1	1	0	4	4	3	2	1
M13	1	1	1	1	1	8	4	1	1	1
M14	1	1	1	1	1	8	3	0	0	0
M15	1	1	1	1	1	3	0	0	0	0
M16	1	1	1	1	1	6	5	1	0	0
M17	1	1	1	1	1	3	1	0	0	0
Sensiti -vity	88.2	88.2	79.4	73.5	58.8					
Avg						5.0	2.8	1.5	0.8	0.4

*Table 7.1: Texture parameter f1 for benign (B) and malignant (M) cases, where *s1 = matrix size: 3, BIN size: 10, histogram value range: lowest (0.8-0.9), *s2 = matrix size: 5, BIN size: 10, histogram value range: lowest (0.8-0.9), *S3= matrix size: 7, BIN size: 10, histogram value range: lowest (0.8-0.9), *s4 = matrix size: 9, BIN size: 10, histogram value range: lowest (0.8-0.9), *s5 = matrix size: 11, BIN size: 10, histogram value range: lowest (0.8-0.9)*

case id	Lesion identified (ignoring edges/noise) Yes = 1/no = 0					No. Of additional areas (non lesion, not including edge outline/noise) joint areas classed as one lesion				
	***S1**	***S2**	***S3**	***S4**	***S5**	***S1**	***S2**	***S3**	***S4**	***S5**
B2	1	1	1	1	1	2	2	2	1	1
B4	1	1	1	0	0	5	4	3	2	0
B5	1	0	0	0	0	6	3	3	3	3
B6	1	1	1	0	0	8	7	4	4	4
B7	1	1	1	1	1	9	5	4	2	2
B8	1	0	0	0	0	2	2	1	0	0
B9	1	1	1	0	0	5	4	3	2	2
B10	1	1	1	1	1	4	2	1	1	1
B11	1	1	1	1	1	5	6	2	1	1
B13	1	1	0	0	0	5	3	1	1	1
B15	1	1	1	1	1	2	2	2	2	2
B16	1	1	1	1	1	8	6	3	3	2
B19	0	0	0	0	0	4	4	2	2	1
B20	1	1	1	1	1	2	2	2	1	0
B21	1	1	1	1	1	4	3	2	2	2
B23	1	1	1	1	1	9	5	3	3	1
B24	1	1	1	0	0	7	7	5	5	4
M1	1	1	1	1	1	6	3	3	3	3
M2	1	1	1	1	1	2	2	3	3	2
M3	0	0	0	0	0	6	4	3	1	1
M4	1	1	1	1	1	7	3	2	2	2
M5	1	1	1	1	1	5	3	4	2	2
M6	1	1	1	1	1	7	4	3	2	1
M7	1	1	1	1	1	5	5	4	2	1
M8	1	1	1	1	1	9	8	7	7	6
M9	1	1	1	1	1	7	5	2	2	2
M10	1	1	1	1	1	6	4	3	2	2
M11	1	1	1	1	1	2	1	0	0	0
M12	1	1	1	1	1	5	7	6	6	6
M13	1	1	1	1	1	5	4	2	1	1
M14	1	1	1	1	1	6	7	7	7	4
M15	1	1	1	1	1	5	5	4	4	4
M16	1	1	1	1	1	5	3	3	3	1
M17	1	1	1	1	1	5	4	4	4	4
Sensiti -vity	94.1	88.2	85.3	73.5	73.5					
Avg						5.3	4.1	3.0	2.5	2.0

*Table 7.2: Texture parameter f9 for benign (B) and malignant (M) cases, where*s1 = matrix size: 9, BIN size: 10, histogram value range: lowest (0.416-0.832), *s2 = matrix size: 9, BIN size: 8, histogram value range: lowest (0.52-1.04), *S3= matrix size: 9, BIN size: 4, histogram value range: lowest/second lowest (1.04-2.08), *s4 = matrix size: 9, BIN size: 13, histogram value range: middle (1.91-2.24)*

Table 7.3 shows the data from the benign and malignant patients after lesion detection (hotspot) feature was executed for the texture parameter f_{13} using a matrix size of 5. The software revealed high overall sensitivity values (62-94%) varying depending on the input variables used for $f_{13.}$ The average number of false positives per patient also varied depending on input variable from 2–6.3.

Benign cases

Figures 7.5-7.8 show the software output highlighting lesions of interest in a patient identified with a benign lesion. Figure 7.5 shows the original image with lesion area highlighted using the radiology report and visual inspection. Figure 7.6-7.8 show the image maps for texture parameters $f_{1,}$ f_9 and f_{13} respectively. In the cases such for f_9 and f_{13} the edges highlighted were ignored and not counted as part of false positive areas of interest as this is a flaw of the segmentation feature that would need optimising in the future that is allowing the edges to be highlighted as areas of interest.

case id	Lesion identified (ignoring edges/noise) Yes = 1/no = 0					No. Of additional areas (non lesion, not including edge outline/noise) joint areas classed as one lesion				
	***S1**	***S2**	***S3**	***S4**	***S5**	***S1**	***S2**	***S3**	***S4**	***S5**
B2	1	1	1	0	0	2	3	3	2	0
B4	1	1	0	0	0	7	4	3	1	0
B5	0	0	0	0	0	5	3	3	4	3
B6	1	1	1	0	0	10	5	3	3	2
B7	1	1	1	1	1	9	4	2	2	2
B8	0	0	0	0	0	4	0	0	0	0
B9	1	1	1	0	0	6	3	3	3	3
B10	1	1	1	1	1	6	1	1	2	1
B11	1	1	1	1	1	4	4	1	1	1
B13	1	1	0	0	0	3	3	1	1	1
B15	1	1	1	1	1	3	2	2	2	2
B16	1	1	1	1	1	8	3	3	2	0
B19	1	0	0	0	0	7	2	2	0	0
B20	1	1	1	1	1	3	2	2	1	1
B21	1	1	1	1	1	4	3	3	3	3
B23	1	1	1	0	0	6	3	1	0	0
B24	1	1	0	0	0	9	9	6	5	6
M1	1	1	1	1	1	5	5	3	3	5
M2	1	1	1	1	1	5	4	4	3	3
M3	1	0	0	0	0	5	4	1	1	1
M4	1	1	1	1	0	6	5	3	3	2
M5	1	1	1	1	1	6	4	2	0	0
M6	1	1	1	1	1	4	4	2	2	2
M7	1	1	1	1	1	10	4	2	1	2
M8	1	1	1	1	1	6	8	6	6	5
M9	1	1	1	1	1	11	6	2	2	2
M10	1	1	1	1	1	10	4	2	2	2
M11	1	1	1	1	1	4	1	1	0	0
M12	1	1	1	1	0	6	7	7	7	5
M13	1	1	1	1	1	11	6	3	3	3
M14	1	1	1	1	1	9	8	7	5	5
M15	1	1	1	1	1	6	4	3	3	3
M16	1	1	1	1	1	7	4	2	2	1
M17	1	1	1	1	1	7	5	5	5	5
Sensiti -vity	94.1	88.2	79.4	67.6	61.8					
Avg						6.3	4.03	2.8	2.4	2.1

*Table 7.3: Texture parameter f13 for benign (B) and malignant (M) cases, were *s1 = matrix size: 3, BIN size: 10, histogram value range: lowest (0.0999-0.2), *s2 = matrix size: 5, BIN size: 10, histogram value range: lowest (0.0999-0.2), *S3= matrix size: 7, BIN size: 10, histogram value range: lowest (0.0999-0.2), *s4 = matrix size: 9, BIN size: 10, histogram value range: lowest (0.0999-0.2), *s5 = matrix size: 11, BIN size: 10, histogram value range: lowest (0.0999-0.2)*

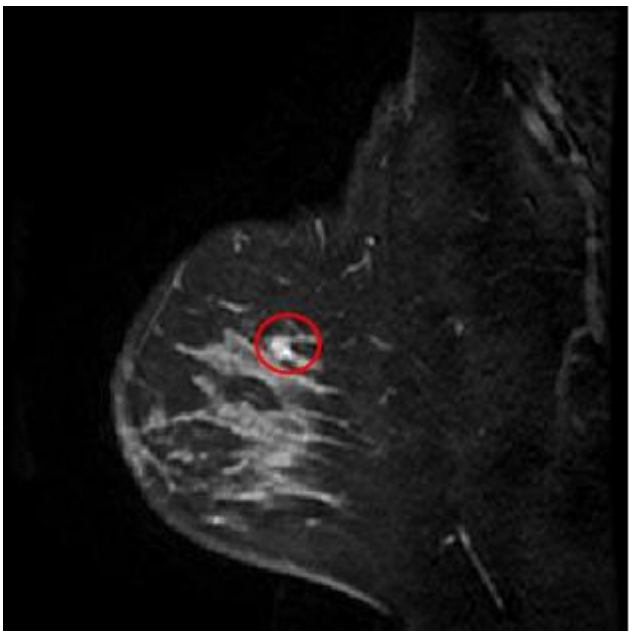

Figure 7.5: Original MR image with lesion area highlighted after visual inspection and reference to radiology report. Image acquired at 2 minutes post contrast using a high resolution 3D T_1 weighted sequence. Patient is a 40 years old female with a benign lesion (fibrodenoma and corresponding fibrocystic disease) in the left breast

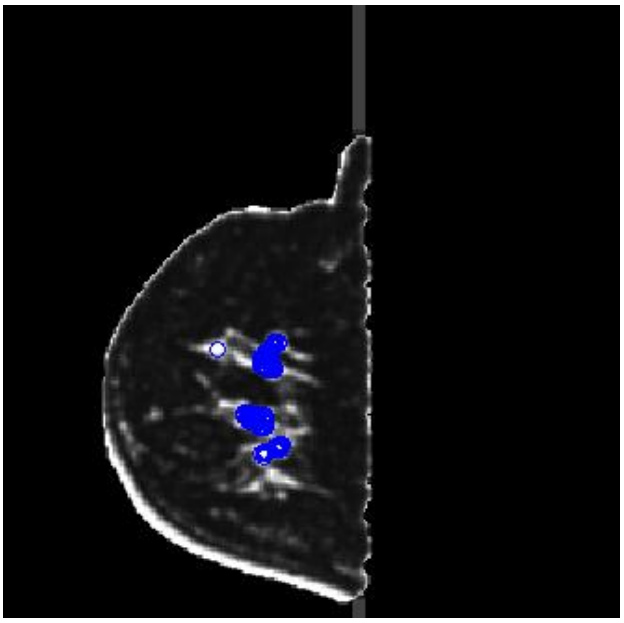

Figure 7.6: f_1 (angular second moment) map after lesion detection using hotspot analysis. In this case the lesion is highlighted automatically (blue areas) alongside additional areas of interest

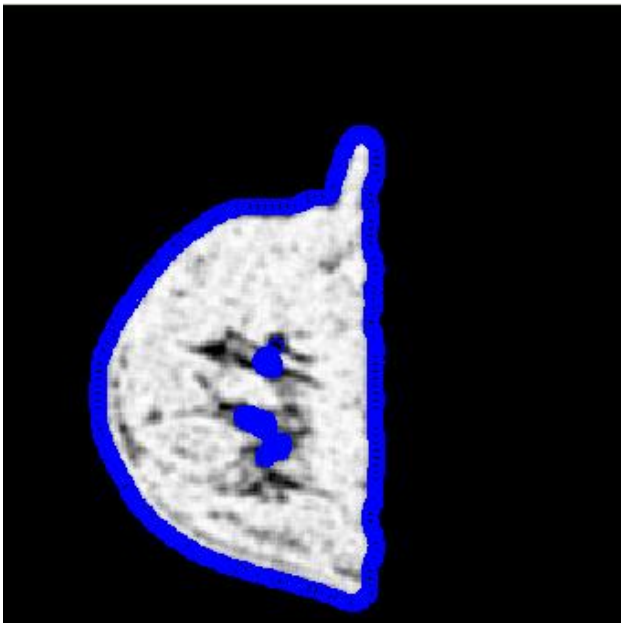

Figure 7.7: f_9 (entropy) map after lesion detection using hotspot analysis. In this case the lesion is highlighted automatically (blue areas) alongside additional areas of interest

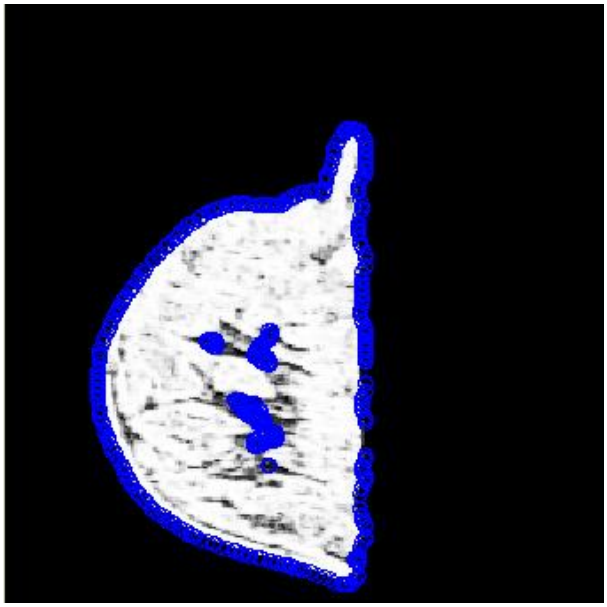

Figure 7.8: f_{13} (information measure of correlation 2) map after lesion detection using hotspot analysis. In this case the lesion is highlighted automatically (blue areas) alongside additional areas of interest

Malignant cases

Figures 7.9-7.12 show the software output highlighting lesions of interest in a patient identified with a malignant lesion. Figure 7.9 shows the original image with lesion area highlighted using the radiology report and visual inspection. Figures 7.10-7.12 show the image maps for texture parameters $f_{1,}$ f_9 and f_{13} respectively. As before in the cases for f_9 and f_{13} the edges highlighted were ignored and not counted as part of false positive areas of interest.

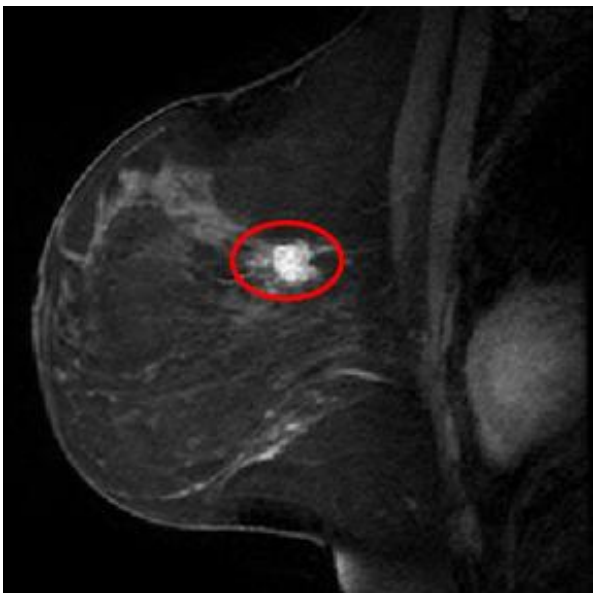

Figure 7.9: Original MR image with lesion area highlighted after visual inspection and reference to radiology report. Image acquired at 2 minutes post contrast using a high resolution 3D T_1 weighted sequence. Patient is a 46 years old female with a malignant lesion in the left breast

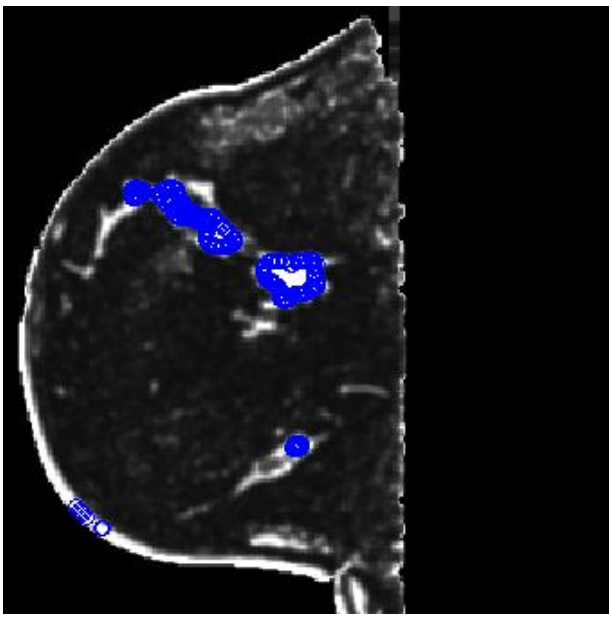

Figure 7.10: f_1 (angular second moment) map after lesion detection using hotspot analysis. In this case the lesion is highlighted automatically (blue areas) alongside additional areas of interest

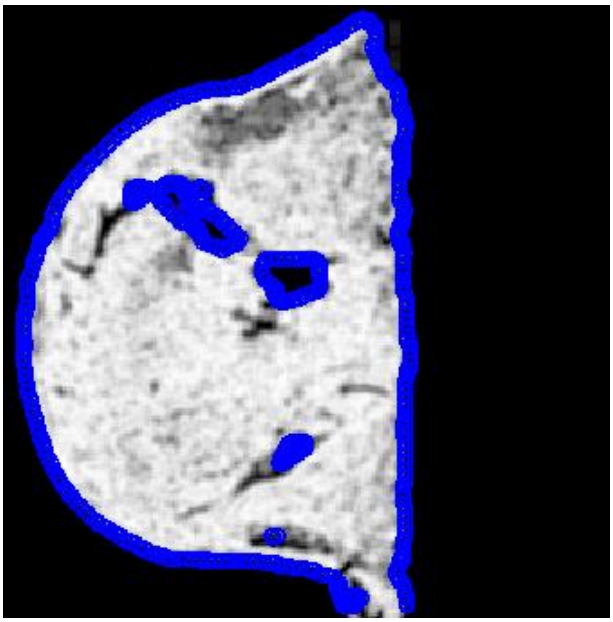

Figure 7.11: f_9 (entropy) map after lesion detection using hotspot analysis. In this case the lesion is highlighted automatically (blue areas) alongside additional areas of interest

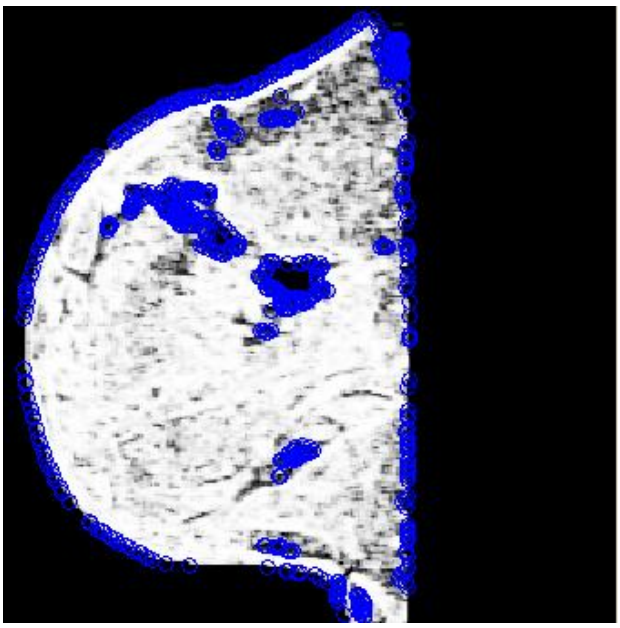

Figure 7.12: f_{13} (information measure of correlation 2) map after lesion detection using hotspot analysis. In this case the lesion is highlighted automatically (blue areas) alongside additional areas of interest

Normal cases

Figures 7.13-7.16 show the software output highlighting areas of interest in a normal patient. Figure 7.13 shows the original image. Figures 7.14-7.16 show the image maps for texture parameters f_1, f_9 and f_{13} respectively. As before in the cases for f_9 and f_{13} the edges highlighted were ignored and not counted as part of false positive areas of interest. As these are normal cases any lesion of interest is a false positive.

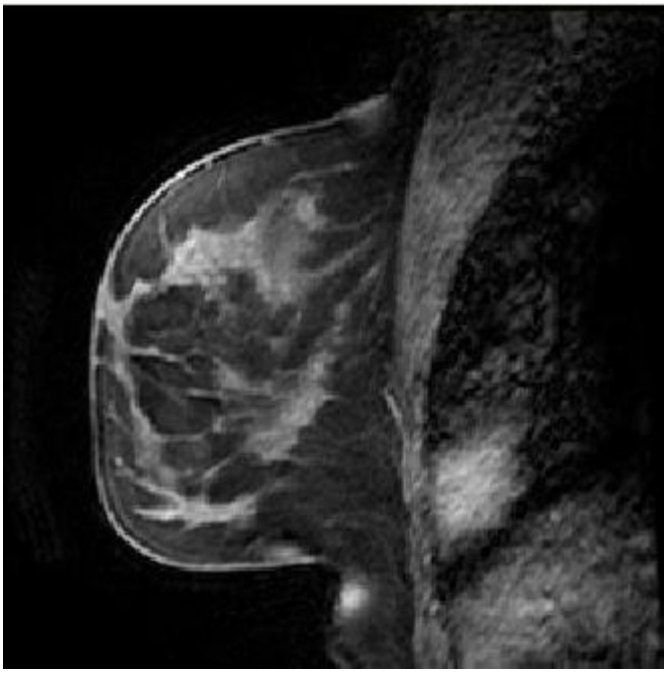

Figure 7.13: Original MR image of a normal patient. Image acquired at 2 minutes post contrast using a high resolution 3D T_1 weighted sequence. Patient is a 39 years old female

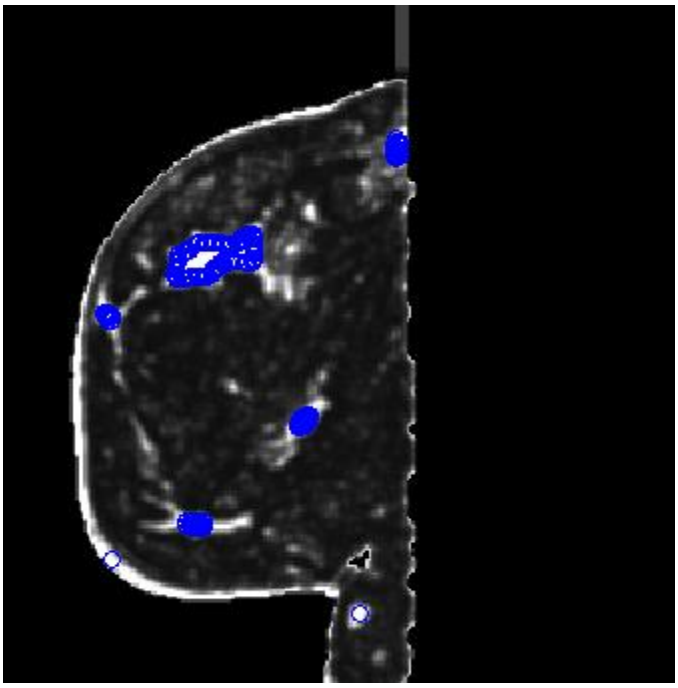

Figure 7.14: f_1 (angular second moment) map after lesion detection using hotspot analysis. In this case the lesions of interest are highlighted automatically (blue areas)

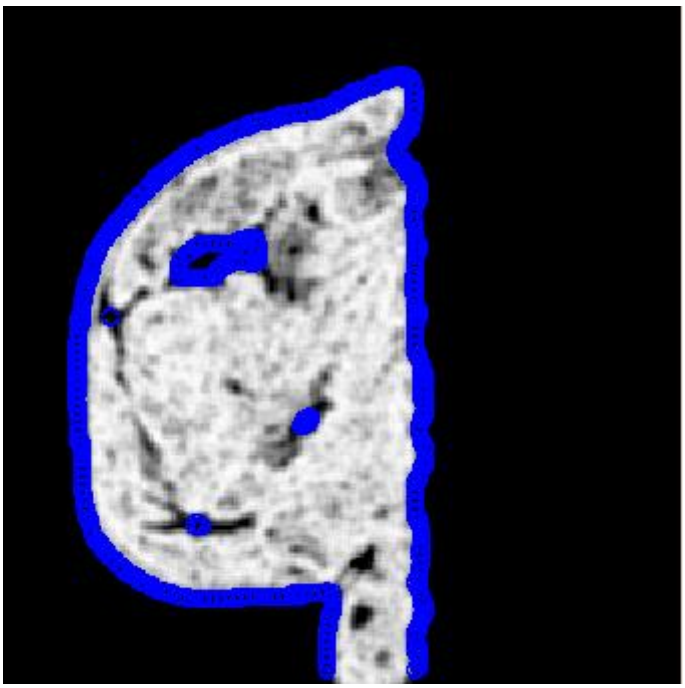

Figure 7.15: f_9 (entropy) map after lesion detection using hotspot analysis. In this case the lesions of interest are highlighted automatically (blue areas)

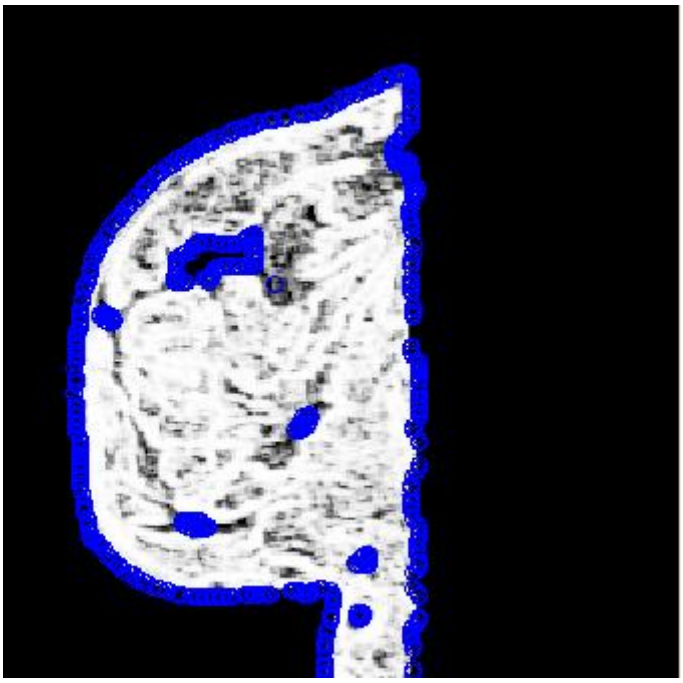

Figure 7.16: f_{13} (information measure of correlation 2) map after lesion detection using hotspot analysis. In this case the lesions of interest are highlighted automatically (blue areas)

7.4.3 FROC analysis

The FROC analysis in figure 7.17 shows the data from tables 7.1-7.3 for the three texture parameters f_1, f_9 and f_{13} and displays the sensitivity against the false positives per patient, highlighting that higher sensitivity is achievable at the expense of a higher number of false positive lesions. Figure 7.3[a] shows an example of a patient with a benign lesion, figures 7.18 and 7.19 show its corresponding texture mapped outputs for the texture parameter f_1 with zero false positives (fig 7.18) and high number of false positives (fig 7.19), in both examples the true positive is also highlighted. Figure 7.17 shows the data as having around 60-95% sensitivity when benign and malignant data is combined.

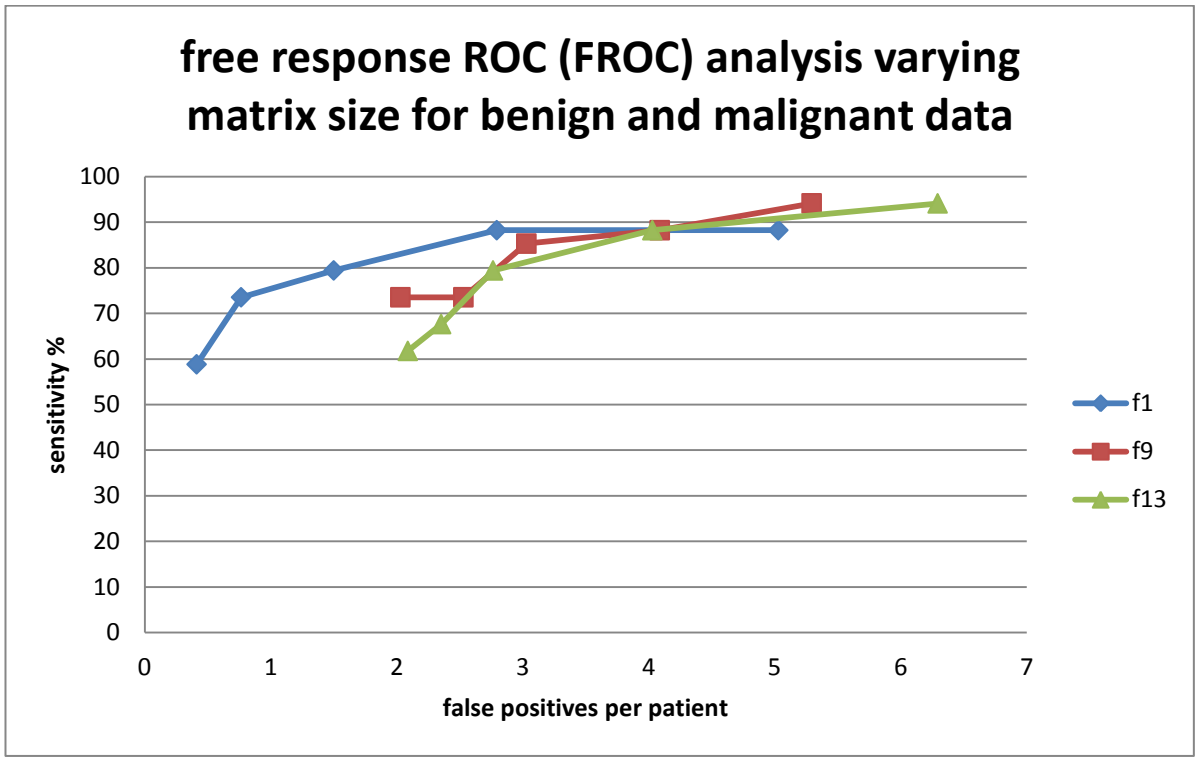

Figure 7.17: FROC analysis for benign and malignant data for texture parameter f_1, f_9 and f_{13}. The analysis shows that sensitivity gradually increases with false positives per patient

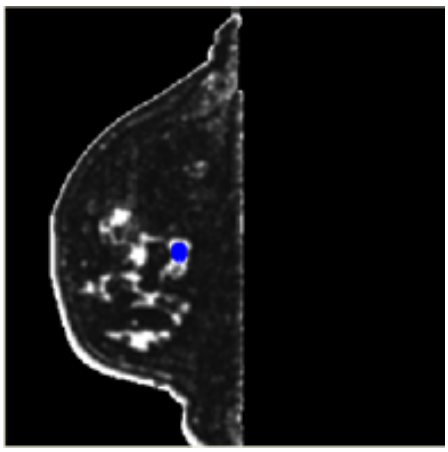

Figure 7.18: output showing patient in image in figure 7.3[a] after texture mapping performed and lesion detection function used to highlight suspicion regions. This example showed no false positives and highlighted the lesion (blue)

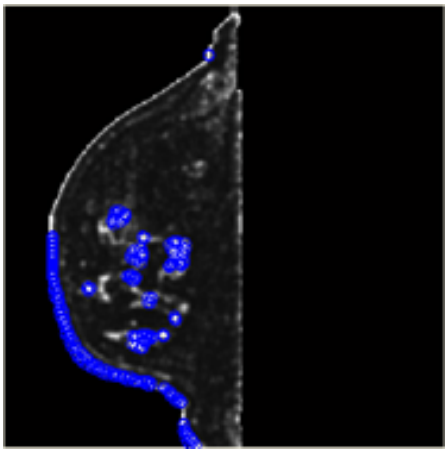

Figure 7.19: output showing patient in image in figure 7.3[a] after texture mapping performed and lesion detection function used to highlight suspicion regions. This example showed 7 false positives and highlighted the lesion as well. In this example edge of breast highlighted also in blue was not included in the count for false positive areas of interest

7.5 Discussion

This study has generated and analysed texture maps for normal, benign and malignant cases and has established that lesion detection is possible. This has potential as a screening tool although the hotspot lesion detection feature needs further optimisation in order to decrease the number of false positives and increase true positives. The segmentation feature of the software is relatively unsophisticated and would need further work in order to segment breast

tissue more accurately to eliminate noise and reduce false positives arising from the skin surface. Although an erosion feature was programmed into the software this was not used for this study as it seemed to incorrectly remove breast tissue in some cases instead of just eliminating breast edges. Optimisation of the erosion feature could be explored which was programmed as a function but not used in the analysis due to its in ability to distinguish breast from noise accurately.

The FROC analysis has provided useful insight into the data highlighting that overall sensitivity of a true positive lesion is good with sensitivity of benign and malignant combined of 60-95% (figure 7.17). Higher sensitivity is achieved at the expense of an increase in the number of false positives per patient. Only three of the 16 texture parameters were analysed due to the large amount of time required to analyse each parameter and measure its false positive rate and sensitivity. The texture maps have already been generated therefore this is something that can be reserved for a further study. This further work could indicate (especially if data is used in combination) that not all 16 texture parameters are needed - the goals may be achieved by using a single or a select few parameters as was done in this study using 3 parameters. Of the 3 parameters analysed f_1 appears to have the greatest area under the curve and therefore offers the most promise of any individual parameter.

Future work in order to optimise the analysis process would include looking at the other 13 texture parameters and running the same input variables. This study chose to look at texture parameter maps for f_1, f_9 and f_{13} as initial testing of these parameters using mock input variables worked well but looking at other parameters could possibly yield better results. Although the three parameters assessed used a thresholding method involving simple histogram based technique which took a set range from each texture map histogram, other means of thresholding need to be explored. One possible technique could be looking at each texture map on a pixel level at the known lesion area for all texture maps and attempt to look for patterns amongst pixel values of lesions and attempt to generate threshold values unique

to each texture parameter. Adjusting the variables further could be explored for example varying the matrix sizes used to include matrix sizes not explored in current tests. At the moment only 17 benign and 17 malignant cases were tested, once additional and more optimum input variables are established for the lesion detection feature a larger data cohort would yield a more accurate FROC analysis. Further testing is also needed to reduce the number of false positives especially in normal breast data.

From a software user perspective instead of showing lesion area on the texture mapped image, the whole process could be hidden and the user (radiologist) would simply run analysis and suspicion regions would be highlighted on the original MR image.

8 Shape Analysis

8.1 Introduction

Unlike in texture analysis where the most commonly used statistical technique due to its ability to study the 2nd order statistics of pixels at different spacings and angles is the Haralick model [95], the optimal shape features are not evident and there exists various ways of calculating mathematically the geometry of a given shape or lesion, from traditional means like circularity to features such as moment analysis. Bhooshan et al [46] used shape (geometric) analysis along with other computerised methods such as texture and kinetic features on DCE-MRI breast lesions in an attempt to make use of them as prognostic markers. The circularity feature proved to be an effective way of classifying Invasive Ductal Carcinoma (IDC) versus Ductal Carcinoma In Situ (DCIS) lesion. The study also recognised that DCIS can appear to be a mass-like enhancement; thus in their analysis both morphological and kinetic features were used for classification purposes. In this study an attempt is made to use shape parameters to assess tumour surface irregularity, and as a predictor of response to chemotherapy using a select few of the available shape descriptors.

8.2 Methods

100 patients were scanned on a 3.0T HDx scanner immediately prior to neo-adjuvant chemotherapy treatment. For all patients a 3D dynamic dataset was acquired using VIBRANT (FOV 20×20 cm, acquisition matrix 220×160, slice thickness 2 mm, 12 phases with average tdel=33.7 s, range 25.5-44.7 s) Malignant tissue ROIs were generated semi-automatically on all slices utilising early arterial phase data. Shape analysis was then performed on pre-contrast and 1, 2, 3, 4 and 5 minutes post-contrast data for the shape descriptors that involved pixel intensity in their calculations. For the other descriptors of shape that involved looking at the shape of the ROI only (normalised radial lengths, convexity and circularity), one given time point was taken (namely 2 minute post contrast) as the results for these shape descriptors do not take into account any pixel intensity values from the image therefore output would be the

same regardless of time point. The shape descriptors were output using an in house developed software application and included calculations involving radial length, convexity, circularity, moments, eigenvalue and eccentricity.

Radial length is the distance between a given point on the tumour surface and the tumour centroid, see figure 8.1. Once radial length was obtained the normalised radial lengths and mean normalised radial length were also calculated to remove size dependency. In addition the standard deviation of the normalised radial length was calculated which shows how much variation or "dispersion" there is from the average. A standard deviation value of 0 would suggest a circle. Skewness of normalised radial length was also measured as illustrated by figure 8.2 where a negative skew occurs when the bulk of the values lie to the right of the mean, a positive skew occurs when the bulk of the values lie to the left of the mean and a zero value indicates that the values are relatively evenly distributed on both sides of the mean. The final calculation involving radial length was kurtosis of normalised radial length, kurtosis measures whether the data is peaked or flat relative to a normal distribution as illustrated in figure 8.3.

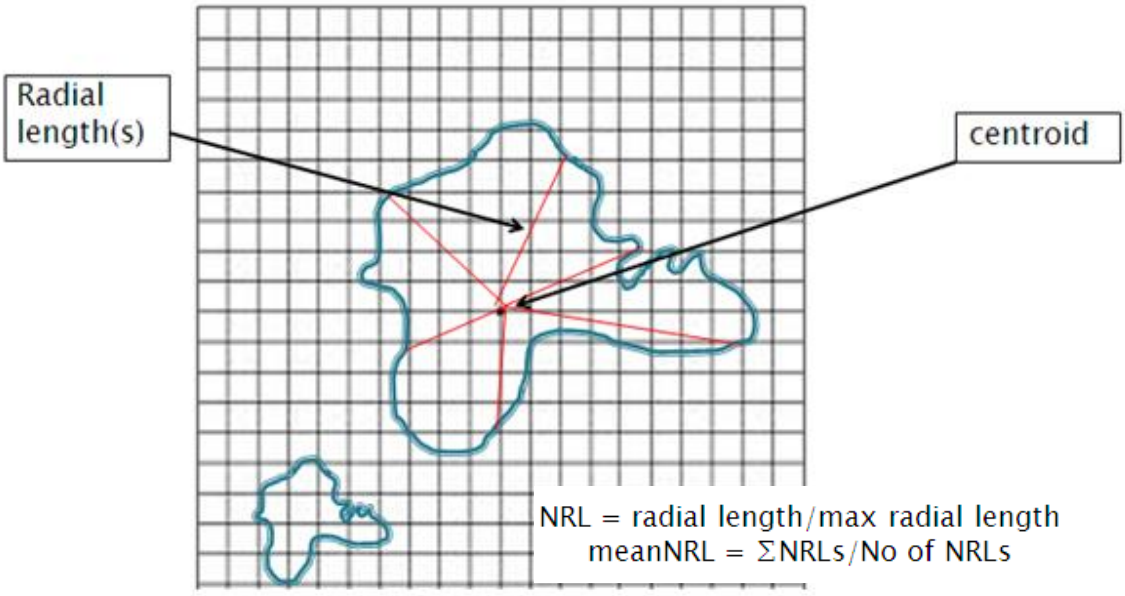

Figure 8.1: illustrates how on a given shape or lesion the radial lengths and centroid are determined and from these the NRL and meanNRL are calculated. The shrunk version of the shape in the bottom left of the figure shows that because the data is normalised size makes no difference as the NRL will be the same so long as the shape is not changed

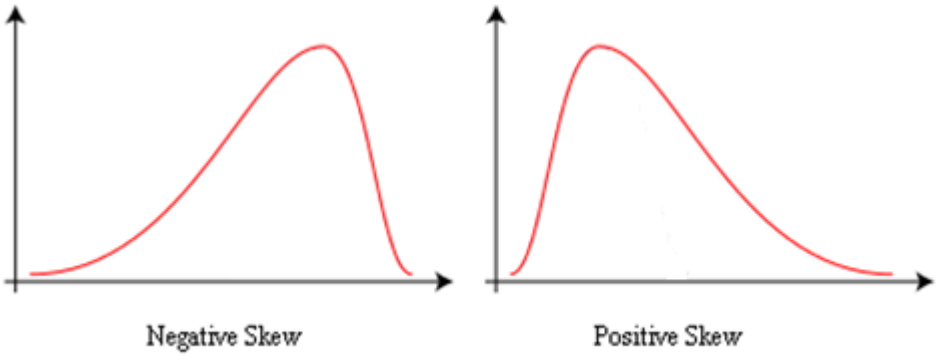

figure 8.2 [96]: illustrates how the bulk of the values in a negative skew (left) lie to the right of the mean, in a positive skew (right) bulk of the values lie to the left of the mean

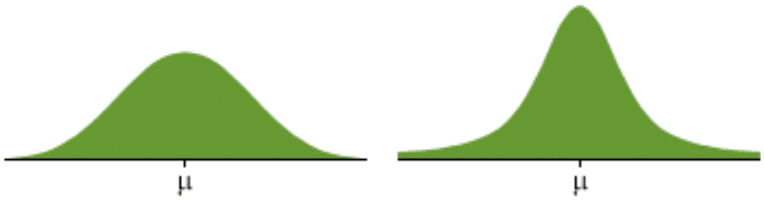

Figure 8.3 [97]: The graphs show low vs. high kurtosis. Kurtosis is a parameter that describes the shape of a random variables probability density function (PDF). Consider the two PDFs in the illustration above, these graphs illustrate the notion of kurtosis. The PDF of the right has higher kurtosis than the PDF on the left. It is more peaked in the centre and it has fatter tails

Convexity measures the number or size of concavities in a shape. Tumours can be spiculated suggesting invasion into the surrounding tissue with benign tumours tending to be less spiculated and having well-circumscribed margins (fig 8.4). Thus a measure of convexity could be useful. First the convex hull of the shape is calculated by taking the smallest convex polygon that can contain the region (see figure 8.5 for illustration). Convexity is then calculated as shape area/convex hull area expressed as a percentage. Since a circle or ellipse has no concavities they will have 100% convexity.

a) 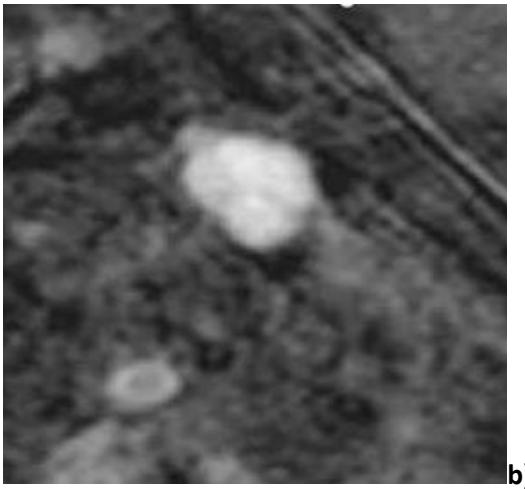 **b)** 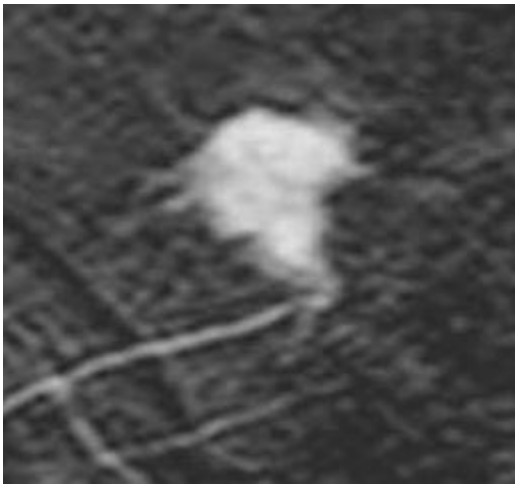

Figure 8.4 [98]: MRI of breast fibroadenoma with well-circumscribed margins (a) and MRI of invasive breast carcinoma with spiculated margins (b)

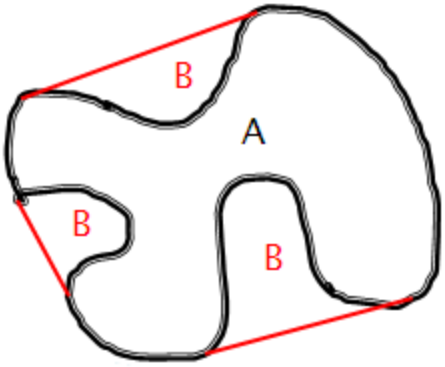

*Figure 8.5: illustrates how convexity is measured by first calculating the convex hull of the shape. The convex hull is the smallest polygon that can contain the region on the image, this is region A + regions B. The convexity of the image can be calculated using the formula A/(A+B)*100*

Circularity sometimes referred to as compactness is a measure of how closely packed a shape is or not. The formula is perimeter²/area with the most compact shape being a circle (4π), all other shapes have compactness values larger then 4π.

Image moments are a measure of a shapes statistical properties, where the first few terms give general shape and later terms fill in finer details (see figure 8.6). Moments are unique in that they are translate, rotate and scale invariant. The shape can be perfectly reconstructed if enough moments have been calculated. For the purpose of this study calculations included μ_{00}, μ_{01}, μ_{10}, μ_{02}, μ_{11}, μ_{20}, μ_{30}, μ_{03}, μ_{21} and μ_{12}. The following formulas illustrate how 1d moments are calculated

$$Mean,\ \ \mu = \frac{\sum_{x=0}^{N-1} xf(x)}{\sum_{x=0}^{N-1} f(x)} \qquad Variance,\ \ \sigma^2 = \frac{\sum_{x=0}^{N-1} (x-\mu)^2 f(x)}{\sum_{x=0}^{N-1} f(x)} \qquad skew = \frac{\sum_{x=0}^{N-1} (x-\mu)^3 f(x)}{\sum_{x=0}^{N-1} f(x)}$$

The above formulas show some familiar 1D moment calculations where f(x) represents pixel intensity value for the x^{th} pixel. As the moments increase the various calculations can be obtained by increasing the power of the variation around the mean i.e. 2^{nd} moment is variance

and 3rd moment is skew and so on. The nth moment about the mean is known as the nth central moment illustrated here

$$\mu_n = \frac{\sum_{x=0}^{N-1}(x-\mu)^n f(x)}{\sum_{x=0}^{N-1} f(x)}$$

In a similar way the following formula illustrates how the various moments are calculated for 2D.

$$\mu_{pq} = \sum_{x=0}^{M-1}\sum_{y=0}^{N-1}\left(x-\bar{x}\right)^p\left(y-\bar{y}\right)^q f(x,y)$$

Central moments for 2D objects where $\bar{x}$ and $\bar{y}$ (above) are the coordinates of the centre of mass given by the following formula

$$\bar{x} = \frac{\mu_{10}}{\mu_{00}} \quad \bar{y} = \frac{\mu_{01}}{\mu_{00}}$$

With μ_{00} the area of the object, the eigen vectors of this matrix correspond to the major and minor axes of the image intensity. By finding the eigenvalues of the covariance matrix we can find the eccentricity of the shape.

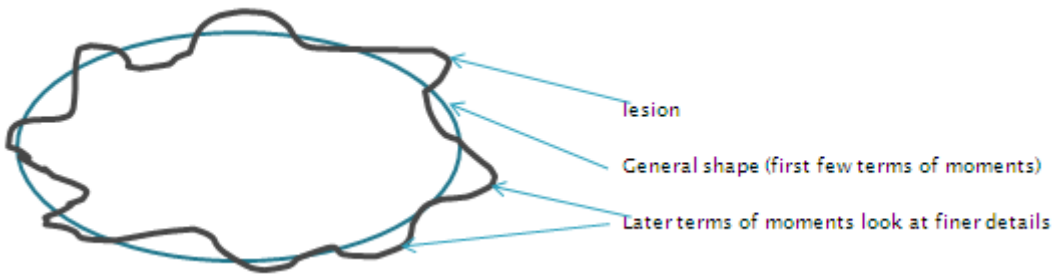

Figure 8.6: illustrates image moments and how the first few terms based on statistical properties give the general shape of the image and later terms look at finer details

Eigenvalue

The eigenvectors of a square matrix are the non-zero vectors which once multiplied by the matrix, remain either proportional to the original vector (change only in magnitude, not in direction) or become zero. Each eigenvectors corresponding eigenvalue is the factor by which the eigenvector changes when multiplied by the matrix [99]. Figure 8.7 illustrates an eigenvector.

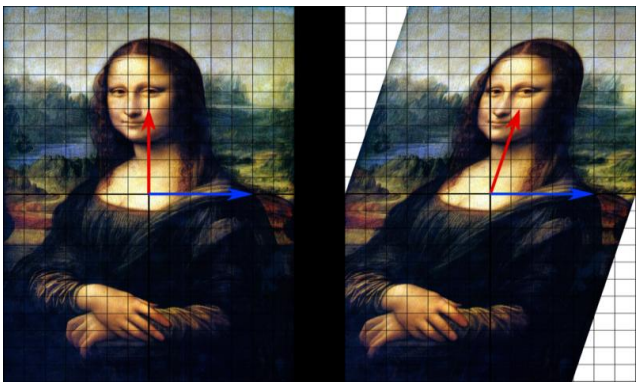

Figure 8.7 [99]: In this shear mapping the red arrow changes direction but the blue arrow does not. Therefore the blue arrow is an eigenvector, with eigenvalue 1 as its length is unchanged

Eccentricity is a measure of ratio of the longest cord of the shape to the longest cord perpendicular to it. The value is between 0 and 1, an ellipse whose eccentricity is 0 is actually a circle, while an ellipse whose eccentricity is 1 is a line segment (fig 8.8). The application created for this study takes into account pixel intensity and not just shape of lesion therefore eccentricity values differ depending on time point and grey levels used. Hence the largest cord is not necessarily the largest physical distance (fig 8.8). The formula for eccentricity is

$$\sqrt{1-\frac{\lambda_2}{\lambda_1}}$$

Where λ_2 is the distance from the centre to the focus of the ellipse and λ_1 is the distance from the centre to a vertex.

Calculations involving radial lengths (including mean, standard deviation, skewness and kurtosis), circularity and convexity were only performed at a single time point as these are descriptors of shape that do not take into account image pixel intensity values and hence the output would be the same regardless of which time point is taken for the calculation. All the other calculations i.e. calculations involving moments, eigenvalues and eccentricity take into account the underlying pixel intensity values and were therefore performed for all time points. All calculations were implemented on the slice with the largest distinct ROI area.

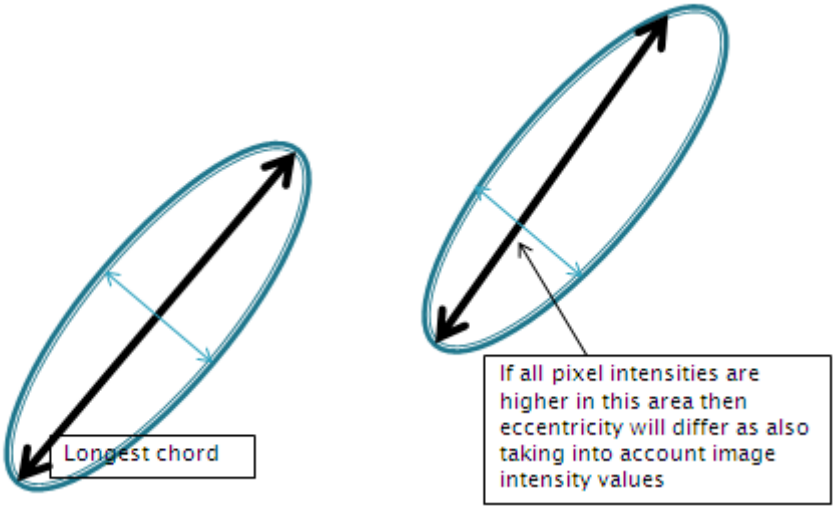

Figure 8.8: eccentricity is the ratio of the longest chord of the shape to the longest chord perpendicular to it. The value is between 0 and 1, an ellipse whose eccentricity is 0 is actually a circle, while and ellipse whose eccentricity is 1 is a line segment. If image pixel intensity is also taken into account rather than just the shape of lesion then values will differ depending on time point in acquisition and grey levels used when analysing image

8.3 MRI Protocol

MR acquisition protocol was as previously stated in section 5.1.2.2

8.4 Results

After treatment the patients were categorized according to their response to chemotherapy: partial responders (PR) corresponding to a decrease in longest diameter of tumour of greater than 50% (40 patients) and non-responders (NR) corresponding to a decrease of less than 50% (49 patients). Data for remaining 11 patients was not available.

Data was also split based on factors that are known to influence response: TNBC (22 patients) vs. all other combinations of the three appropriate markers (49 patients) with 29 patients data unavailable; subdivided into nodal status by examining node negative (45 patients) vs. node positive (46 patients) with data in 9 patients not available; and tumour grade derived from pre-treatment biopsy, biopsy grade 1 or 2 (38 patients) vs. biopsy grade 3 (55 patients) and 7 patients data was not available.

The data contained a mixture of normally distributed and non-normally distributed data and appropriate tests were performed, where data was found to be normally distributed t-tests were performed and for non-normally distributed data Mann-Whitney tests were performed using SPSS. As stated earlier in this chapter (section 8.2) the shape descriptors containing calculations of Normalised Radial Length (NRL), convexity and circularity do not take into account pixel intensity of the ROI values and therefore the results were the same across all pre and post-contrast time points for these 6 shape parameters. Hence if results show significant difference for kurtosisNRL shape parameter at 2 minute post contrast time point then this would be consistent across all time points. The box plots show the distribution of the nodal status data against circularity parameter (fig 8.9) and TNBC data against the kurtosisNRL shape descriptor (fig 8.10). The box plot for nodal status data shows that circularity mean values vary significantly for node +ve and node -ve but there is still a considerable amount of data overlap (p-value = 0.001). With the TNBC data the kurtosisNRL mean values are not that much different (p-value = 0.026) having considerable data overlap between TNBC and non-TNBC data.

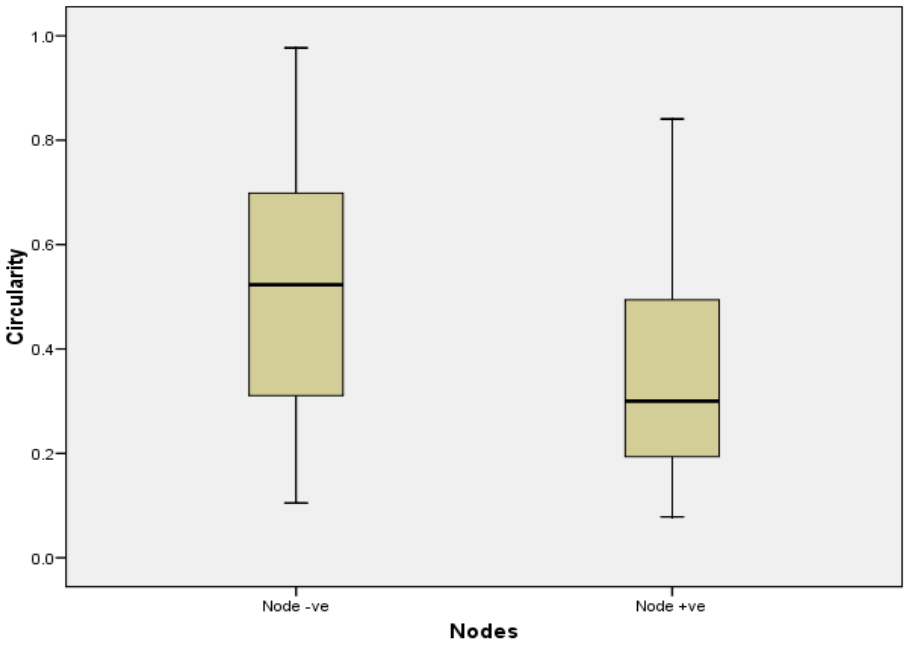

Figure 8.9: box and whisker plot showing distribution of nodal status data for the circularity shape descriptor

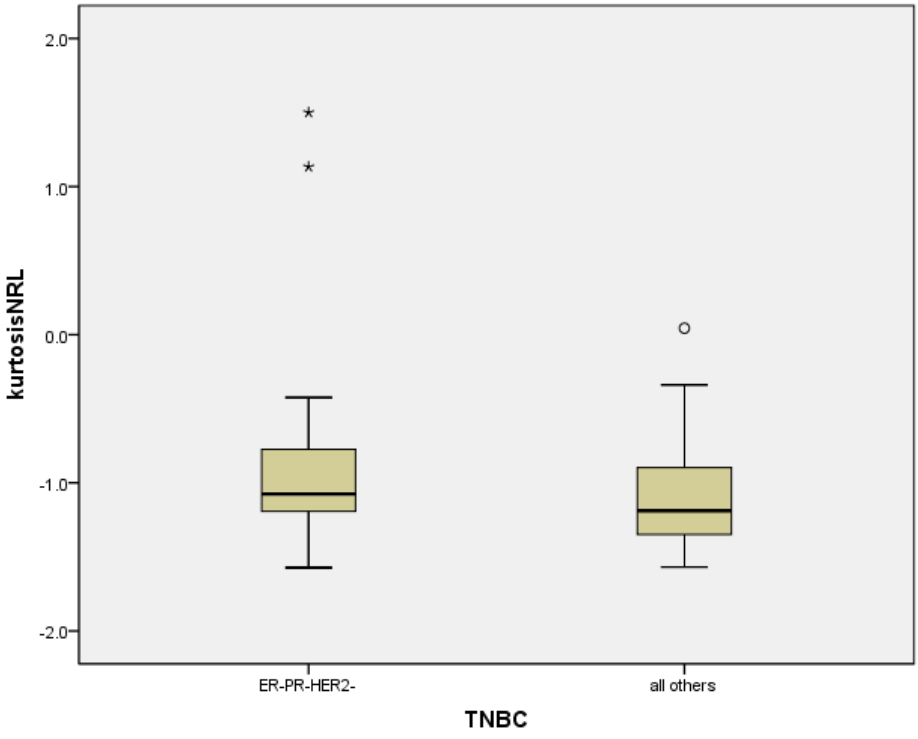

Figure 8.10: box and whisker plot showing distribution of TNBC data for the kurtosisNRL shape descriptor

8.4.1 Response to Neoadjuvant Chemotherapy (% change in longest diameter)

Table 8.1 shows the mean/standard deviation or median/range and p-values for all shape parameters for the results obtained at the 2 minute post contrast time point. There were no significant differences to report between groups.

Time points

No significant differences were seen on the pre-contrast or any of the post contrast phases.

Shape parameter	Mean value ± Standard Deviation		*P value*
	NR	**PR**	
2min post contrast			
Mean NRL	0.77±0.13	0.74±0.15	0.473
Stdev NRL	0.14±0.07	0.15±0.08	0.662
Skewness NRL	-0.03±0.33	-0.02±0.31	0.918
Kurtosis NRL	-1.07±0.50	-1.10±0.30	0.764
Convexity	77.07±13.14	76.95±14.48	0.966
Circularity	0.44±0.24	0.43±0.21	0.942
μ00	$1.11x10^{6}$±$8.13x10^{5}$	$1.34x10^{6}$±$1.02x10^{6}$	0.242
μ01	$0.5x10^{-9}$±$6.5x10^{-9}$	$-0.0x10^{-9}$±$1.11x10^{8}$	0.758
μ10	Median:$0.0x10^{-9}$ Min:$-3.2x10^{-8}$ Max:$8.5x10^{-8}$	Median: $1.5x10^{-9}$ Min: $-2.1x10^{-8}$ Max:$3.4x10^{-8}$	0.106 mw
μ02	Median:$6.53x10^{7}$ Min:$4.89x10^{5}$ Max:$1.29x10^{9}$	Median: $7.74x10^{7}$ Min: $7.80x10^{5}$ Max:$1.98x10^{9}$	0.723 mw
μ11	Median:$-3.13x10^{6}$ Min:$-4.41x10^{8}$ Max:$1.59x10^{8}$	Median: $-3.30x10^{6}$ Min: $-4.74x10^{8}$ Max:$9.45x10^{8}$	0.792 mw
μ20	Median:$6.16x10^{7}$ Min:$2.80x10^{5}$ Max:$1.80x10^{9}$	Median: $6.50x10^{7}$ Min: $1.73x10^{6}$ Max:$1.15x10^{9}$	0.463 mw
μ30	Median:$-9.49x10^{4}$ Min:-8.5710^{9} Max:$3.17x10^{9}$	Median: $-2.79x10^{6}$ Min: $-2.08x10^{10}$ Max:$1.39x10^{10}$	0.433 mw
μ03	Median:$-1.35x10^{6}$ Min:$-2.57x10^{9}$ Max:$1.68x10^{10}$	Median: $2.97x10^{6}$ Min: $-1.26x10^{10}$ Max:$3.08x10^{9}$	0.760 mw
μ21	Median:$2.44x10^{6}$ Min:$-6.68x10^{9}$ Max:$1.34x10^{10}$	Median: $6.23x10^{6}$ Min: $-2.48x10^{10}$ Max:$6.26x10^{9}$	0.463 mw
μ12	Median:$2.99x10^{6}$ Min:$-3.41x10^{6}$ Max:$4.58x10^{10}$	Median: $9.13x10^{6}$ Min: $-2.73x10^{10}$ Max:$4.41x10^{9}$	0.980 mw
Eigen value 1	Median:47.90 Min:3.34 Max:407.65	Median: 49.34 Min: 4.95 Max:283.00	0.882 mw
Eigen value 2	Median:104.69 Min:5.98 Max:737.15	Median: 117.14 Min: 23.82 Max:$1.38x10^{3}$	0.650 mw
Eccentricity	0.70±0.14	0.71±0.19	0.757

Table 8.1: Comparison of shape parameters between PR and NR patients. Mean/SD or median/range and p-values for all shape parameters at the 2 minute post-contrast time point are shown. P-values determined using t-test or Mann Whitney test (labelled mw) as appropriate

8.4.2 TNBC (ER–negative PR–negative HER2–negative) vs. all others

Table 8.2 shows the mean/standard deviation or median/range and p-values for all the shape parameters with highlighted areas demonstrating significant differences between groups for the results obtained at the 2 minute post contrast time point. Table 8.3 summarises the significant differences in shape between TNBC and non-TNBC patients across all time points. In this instance the shape descriptor kutosisNRL was the only parameter that showed a significant difference with a p-value of 0.026.

Time points

Significant differences were observed for the parameter kurtosisNRL. Since this parameter does take into account pixel intensity the result would be the same across all time points (Table 8.3).

Shape parameter	Mean value ± Standard Deviation		*P value*
	TNBC	**All others**	
2min post contrast			
Mean NRL	0.77±0.15	0.76±0.15	0.804
Stdev NRL	0.13±0.08	0.14±0.08	0.576
Skewness NRL	-0.03±0.36	$0.94x10^{-3}$±0.35	0.731
Kurtosis NRL	-0.81 ± 0.74	-1.11 ± 0.35	0.026
Convexity	74.42±14.71	76.56±13.92	0.559
Circularity	0.38±0.21	0.44±0.24	0.341
μ00	$1.30x10^{6}$±$9.50x10^{5}$	$1.21x10^{6}$±$8.63x10^{5}$	0.692
μ01	$1.21x10^{-9}$±$1.02x10^{-8}$	$0.24x10^{-9}$±$8.34x10^{-9}$	0.673
μ10	Median:$0.9x10^{-9}$ Min:$-3.2x10^{-8}$ Max:$3.4x10^{-8}$	Median:$0.9 x10^{-9}$ Min:$-5.3 x10^{-8}$ Max:$2.2 x10^{-8}$	0.931 mw
μ02	Median:$1.14x10^{8}$ Min:$7.80x10^{5}$ Max:$1.98x10^{9}$	Median:$7.65 x10^{7}$ Min:$4.89 x10^{5}$ Max:$1.29 x10^{9}$	0.542 mw
μ11	Median:$-2.29x10^{6}$ Min:$-4.74x10^{8}$ Max:$9.45x10^{8}$	Median:$-3.63 x10^{6}$ Min:$-4.41 x10^{8}$ Max:$3.95 x10^{8}$	0.263 mw
μ20	Median:$1.22x10^{8}$ Min:$1.73x10^{6}$ Max:$1.15x10^{9}$	Median:$6.36 x10^{7}$ Min:$2.80 x10^{5}$ Max:$1.80 x10^{9}$	0.263 mw
μ30	Median:$-3.00x10^{7}$ Min:$-2.08x10^{10}$ Max:$7.08x10^{9}$	Median:$-1.48 x10^{6}$ Min:$-2.12 x10^{10}$ Max:$5.51 x10^{9}$	0.419 mw
μ03	Median:$-2.73 x10^{6}$ Min:$-1.26 x10^{10}$ Max:$2.76 x10^{10}$	Median:$-1.35 x10^{6}$ Min:$-3.81 x10^{9}$ Max:$7.51 x10^{9}$	0.619 mw
μ21	Median:$-3.66 x10^{6}$ Min:$-2.48 x10^{10}$ Max:$5.02 x10^{9}$	Median:$2.44 x10^{6}$ Min:$-6.68 x10^{9}$ Max:$6.26 x10^{9}$	0.682 mw
μ12	Median:$1.13 x10^{6}$ Min:$-2.73 x10^{10}$ Max:$1.08 x10^{10}$	Median:$8.08 x10^{6}$ Min:$-3.41 x10^{9}$ Max:$1.58 x10^{10}$	0.441 mw
Eigen value 1	Median:74.98 Min:4.95 Max:378.18	Median:46.10 Min:3.34 Max:371.72	0.192 mw
Eigen value 2	Median:147.78 Min:23.82 Max:1.38	Median:97.67 Min:5.98 Max:737.15	0.139 mw
Eccentricity	0.73±0.18	0.70±0.16	0.481

Table 8.2: Comparison of significant differences in shape parameters between TNBC and non-TNBC patients. Mean/SD or median/range and p-values for all shape parameters at the 2 minute post-contrast time point are shown

shape parameters	Mean value ± Standard Deviation		P value
	TNBC	All others	
All phases			
Kurtosis NRL	-0.81 ± 0.74	-1.11 ± 0.35	0.026

Table 8.3: Summary of significant differences in shape parameters between TNBC and non-TNBC patients

8.4.3 Nodal status data (Node-negative vs. Node-positive)

Table 8.4 shows the mean/standard deviation or median/range and p-values for all shape parameters with highlighted areas demonstrating significant differences between groups for the results obtained at the 2 minute post contrast time point. Significant differences were noted for the shape parameters convexity and circularity with p-values of 0.003 and 0.001 respectively. Table 8.5 summarises the significant differences in shape between nodal status patients across all time points.

Time points

Significant differences were seen on the pre-contrast and 5 minute post-contrast time point for one of the moments shape calculations μ_{03}, which showed a p-value of 0.046 and 0.043 respectively highlighting a significant difference in this shape descriptor between nodal status data (Table 8.5). In addition significant differences were observed for the parameters convexity and circularity but with this parameter being of those that do not take into account pixel intensity the result would be the same across all time points.

Shape parameter	Mean value ± Standard Deviation		*P value*
	Node -ve	**Node +ve**	
2min post contrast			
Mean NRL	0.76±0.14	0.75±0.15	0.722
Stdev NRL	0.14±0.07	0.14±0.08	0.893
Skewness NRL	-0.6±0.32	0.01±0.30	0.320
Kurtosis NRL	-1.11±0.35	-1.05±0.48	0.502
Convexity	80.78 ± 12.76	72.21 ± 14.10	0.003
Circularity	0.51 ± 0.22	0.36 ± 0.21	0.001
μ00	Median:7.46 x10^{5} Min:8.26 x10^{4} Max:4.21 x10^{6}	Median:9.49 x10^{5} Min:2.30 x10^{5} Max:3.33 x10^{6}	0.400 mw
μ01	-1.2 x10^{-9}±9.3x10^{-9}	1.9x10^{-9}±8.0 x10^{-9}	0.085
μ10	Median:1.3 x10^{-9} Min:-3.2 x10^{-8} Max:8.5 x10^{-8}	Median:0.8 x10^{-9} Min:-2.1 x10^{-8} Max:2.2 x10^{-8}	0.880 mw
μ02	Median:4.91 x10^{7} Min:4.89 x10^{5} Max:1.98 x10^{9}	Median:8.78 x10^{7} Min:5.87 x10^{6} Max:1.29 x10^{9}	0.158 mw
μ11	Median:-1.67 x10^{6} Min:-4.74 x10^{8} Max:9.45 x10^{8}	Median:-4.63 x10^{6} Min:-4.41 x10^{8} Max:3.95 x10^{8}	0.068 mw
μ20	Median:5.21 x10^{7} Min:2.80 x10^{5} Max:1.75 x10^{9}	Median:7.76 x10^{7} Min:4.03 x10^{6} Max:1.39 x10^{10}	0.541 mw
μ30	Median:-2.28 x10^{6} Min:-2.08 x10^{10} Max:7.08 x10^{9}	Median:3.15 x10^{6} Min:-8.57 x10^{9} Max:1.39 x10^{10}	0.222 mw
μ03	Median:-5.94 x10^{6} Min:-1.26 x10^{10} Max:3.08 x10^{9}	Median:7.32 x10^{6} Min:-2.42 x10^{9} Max:1.68 x10^{10}	0.313 mw
μ21	Median:5.97 x10^{6} Min:-2.48 x10^{10} Max:1.34 x10^{10}	Median:-1.02 x10^{6} Min:-6.68 x10^{9} Max:6.26 x10^{9}	0.158 mw
μ12	Median:4.37 x10^{6} Min:-2.73 x10^{10} Max:6.60 x10^{9}	Median:1.16 x10^{7} Min:-3.41 x10^{9} Max:1.58 x10^{10}	0.246 mw
Eigen value 1	Median:47.90 Min:3.36 Max:283.00	Median:48.73 Min:13.81 Max:407.65	0.437 mw
Eigen value 2	Median:92.28 Min:5.98 Max:1.38	Median:122.55 Min:29.32 Max:737.15	0.136 mw
Eccentricity	0.68±0.17	0.73±0.15	0.142

Table 8.4: Comparison of significant differences in shape parameters between Nodal status patients data. Mean/SD or median/range and p-values for all shape parameters at the 2 minute post-contrast time point are shown

shape parameters	Mean value ± Standard Deviation		P value
	Node -ve	Node +ve	
All phases			
Convexity	80.78 ± 12.76	72.21 ± 14.10	0.003
Circularity	0.51 ± 0.22	0.36 ± 0.21	0.001
Pre contrast			
Mu03	$-3.21 \times 10^{8} \pm 1.62 \times 10^{9}$	$3.65 \times 10^{8} \pm 1.61 \times 10^{9}$	0.046
5 min post contrast			
Mu03	$-4.90 \times 10^{8} \pm 2.21 \times 10^{9}$	$7.41 \times 10^{8} \pm 3.25 \times 10^{9}$	0.043

Table 8.5: Summary of significant differences in shape parameters between nodal status patients data

8.4.4 Tumour grade derived from pre-treatment biopsy

Table 8.6 shows the mean/standard deviation or median/range and p-values for all shape parameters for the results obtained at the 2 minute post contrast time point. There were no significant differences to report between biopsy grade groups.

Time points

No significant differences were seen on the pre-contrast or any of the post contrast phases.

Shape parameter	Mean value ± Standard Deviation		*P value*
	Biopsy grade 1 or 2	**Biopsy grade 3**	
2min post contrast			
Mean NRL	0.74±0.14	0.78±0.15	0.272
Stdev NRL	0.15±0.07	0.13±0.08	0.315
Skewness NRL	-0.03±0.29	-0.05±0.34	0.757
Kurtosis NRL	-1.05±0.52	-0.95±0.64	0.435
Convexity	75.51±15.64	76.92±12.81	0.636
Circularity	0.44±0.24	0.42±0.21	0.601
μ00	$1.08 \times 10^{6} \pm 8.06 \times 10^{5}$	$1.36 \times 10^{6} \pm 1.05 \times 10^{6}$	0.167
μ01	$1.0 \times 10^{-9} \pm 8.9 \times 10^{-9}$	$-1.2 \times 10^{-9} \pm 7.8 \times 10^{-9}$	0.194
μ10	Median:1.1×10^{-9} Min:-2.0×10^{-8} Max:2.2×10^{-8}	Median:0.6×10^{-9} Min:-1.01×10^{-7} Max:8.5×10^{-7}	0.827 mw
μ02	Median:5.21×10^{7} Min:4.89×10^{5} Max:1.29×10^{9}	Median:7.83×10^{7} Min:7.80×10^{5} Max:1.98×10^{9}	0.189 mw
μ11	Median:-1.13×10^{7} Min:-4.41×10^{8} Max:3.95×10^{8}	Median:-3.75×10^{6} Min:-3.19×10^{8} Max:9.45×10^{8}	0.344 mw
μ20	Median:4.20×10^{7} Min:2.80×10^{5} Max:1.80×10^{9}	Median:8.24×10^{7} Min:1.73×10^{6} Max:2.32×10^{9}	0.080 mw
μ30	Median:-2.82×10^{6} Min:-8.57×10^{9} Max:1.39×10^{10}	Median:-1.63×10^{6} Min:-2.12×10^{10} Max:7.08×10^{9}	0.696 mw
μ03	Median:-2.80×10^{6} Min:-2.42×10^{9} Max:1.68×10^{10}	Median:5.29×10^{6} Min:-1.26×10^{10} Max:2.76×10^{10}	0.755 mw
μ21	Median:4.83×10^{6} Min:-6.68×10^{9} Max:6.26×10^{9}	Median:1.74×10^{6} Min:-2.48×10^{10} Max:1.34×10^{10}	0.645 mw
μ12	Median:1.19×10^{7} Min:-3.41×10^{9} Max:1.58×10^{10}	Median:1.05×10^{6} Min:-2.73×10^{10} Max:1.08×10^{10}	0.101 mw
Eigen value 1	Median:38.53 Min:3.36 Max:407.65	Median:51.57 Min:4.95 Max:378.18	0.059 mw
Eigen value 2	Median:89.89 Min:5.98 Max:737.15	Median:123.51 Min:23.81 Max:1.38×10^{3}	0.114 mw
Eccentricity	0.71±0.15	0.70±0.17	0.806

Table 8.6: Comparison of significant differences in shape parameters between tumour grade patients data. Mean/SD or median/range and p-values for all shape parameters at the 2 minute post-contrast time point are shown

8.4.5 Summary

Significant differences were seen in descriptors of convexity (p=0.003) and circularity (p=0.001) for the nodal status data. For the triple negative data significant differences were seen in kurtosis of normalised radial length (p=0.026). Some significant differences were found in the calculations for moments but these were not consistent across time points. No significant differences in shape descriptors were seen for response to neoadjuvant chemotherapy and biopsy grade data groups. Figures 8.11 and 8.12 illustrate some of the shape descriptors on MR images of the breast from the neoadjuvant chemotherapy data used for shape analysis. Figure 8.11 has low circularity and convexity values and high eccentricity value due to the lesions elongated shape. Figure 8.12 has high circularity and convexity values and low eccentricity value due to the lesion being rounder in nature.

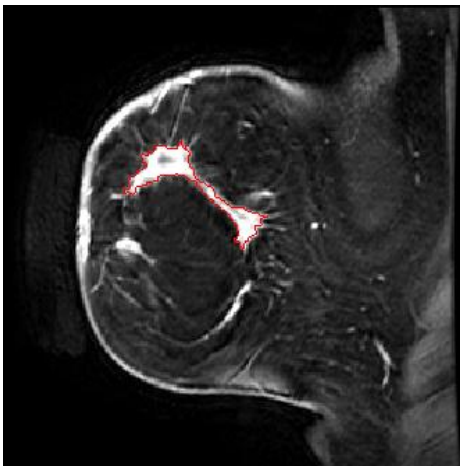

Figure 8.11: lesion with eccentricity value of 0.96, circularity 0.15, convexity 34.8, skewness NRL 0.27, and kurtosis NRL -0.91, ROI size 819 pixels

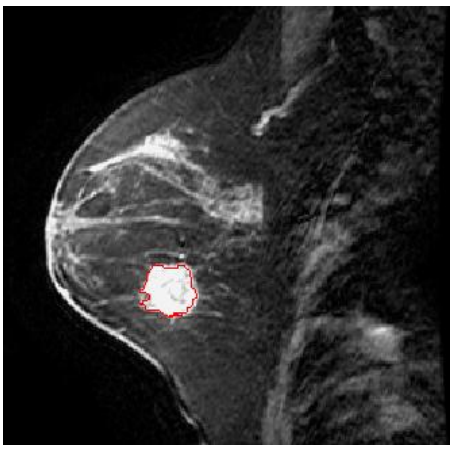

Figure 8.12: lesion with eccentricity value of 0.34, circularity 0.70, convexity 91.2, skewness NRL -0.19, and kurtosis NRL -1.37, ROI size 681 pixels

8.5 Discussion

This work has highlighted that although shape is a known factor used to distinguish benign and malignant lesions it does not seem that useful in predicting response. Some differences between groups were seen in shape descriptors, but unlike our earlier study using texture analysis in the same data cohort [85] gave a much higher and more consistent range of significant differences. Shape descriptors when combined with other morphological analysis techniques such as texture analysis may provide a small amount of additional information. When used on its own from the results seen in this study it appears to have relatively little use as a prognostic indicator for chemotherapy response prediction in breast cancer.

The limitations of this study included the fact that only a single cross section using the largest ROI for each patient was analysed, giving only a 2D representation of the tumour. When compared to previous texture analysis work [85] where multi slice 2D ROIs were used to try and give a more accurate representation of the tumour. Chapter 5 proved that multi slice texture analysis due to its higher counting stats was a good prognostic indicator in chemotherapy response prediction in breast cancer, yet when the same was applied to only a single slice using the largest cross sectional ROI the results were disappointing. Using a similar approach of multi slice analysis for the purpose of shape analysis could be a possible future

area of exploration, in practice this would probably be more complex in terms of coding such a feature. Aggregate measure of 2D shape may not be very representative of overall shape of a lesion. The alternative is to use 3D shape analysis which requires isotropic data and different mathematical models (e.g. sphericity). Another limitation is that the ROIs were semi-automatic (allowing manual editing), a hand drawn ROI with human error could undoubtedly have a large impact on shape and ultimately affect descriptors of shape when shape analysis is performed. As stated earlier in the chapter only a hand full of shape descriptors were explored in this study, many more exist, in particular the author would encourage any future work to look at margin sharpness of lesion. Levman [100] proposed a new technique and combined it with an existing method [101, 102] . Levman's [100] edge sharpness measurement is computed using voxels close to the edge of the lesion but still remaining within the lesion, it also accounts for voxels immediately neighbouring the lesion that are outside the lesion. The study utilised this method for the diagnosis of breast cancer. After comparison Levman found quantifying sharpness or variability of tumours margin performed best at the earlier time point. In conclusion this new mathematical method for measuring margins of lesion from breast MRI presented higher sensitivity (77%) and specificity 65%) than pre-existing mathematical sharpness measurements [101, 102] and could be useful in helping discriminate between malignant and benign lesions. It would be worth exploring this new method to test its usefulness as a prognostic indicator in chemotherapy response prediction in breast cancer, along with any other shape descriptors not used in this thesis.

9 Conclusions

This thesis has reviewed and outlined the importance of morphology in MR images in identifying and categorising lesions including the utility of the BI-RADS lexicon. It then went on to look at previous research in attempting to quantify MR images in both medical and non-medical fields, and found previous studies in the brain and breast had provided meaningful results when using various calculations of texture and shape analysis methods.

The author programmed a robust software package using the full software lifecycle to enable texture and shape analysis of MR images of the breast. Texture analysis reliably demonstrated its ability to differentiate between varying grades of foam in an agar embedded phantom despite them appearing visually indistinguishable on an MR image. High repeatability was demonstrated for these phantoms, with 12 of the 16 texture parameters being more repeatable with the larger ROI than the smaller ROI, this shows that the co-occurrence method of texture analysis relies heavily upon having high counting statistics This indicates that in clinical images distinguishing smaller lesions using texture analysis may be problematic. In a clinical setting repeatability will probably be worse due to lower SNR from clinical images.

Texture analysis using the Haralick co-occurrence and wavelet transform methods proved successful as prognostic indicators in chemotherapy response prediction in breast cancer using a neoadjuvant dataset. The most textural differences were noted between groups (based on biopsy grade or TNBC status) and appeared most evident 1- 3 minutes post-contrast administration. Furthermore no difference in texture was noted when a single slice was analysed as opposed to multi slice, further justifying the need for multi slice analysis in order to maximise counting statistics. Wavelet analysis energy levels can show differences between groups (based on TNBC, PR or NR with respect to % change in longest diameter, nodal status and biopsy grade) and are seen throughout all time points (pre and post contrast administration) with the highest number of total significant differences noted at 5 minutes post contrast.

The texture analysis technique using co-occurrence methods were then applied on a pixel by pixel basis to ultimately generate texture maps, this feature in the software allows the detection of suspicious lesions in MRI screening data with potential utility as an objective first reader. The study generated and analysed texture maps for normal, benign and malignant cases and established that lesion detection was possible. This has potential as a screening tool although the hotspot lesion detection feature needs further optimisation in order to decrease the number of false positives and increase the number of true positives.

Shape analysis using traditional shape descriptors such as circularity and convexity as well as moments calculations were less successful in predicting treatment response. Significant differences were seen in descriptors of convexity and circularity for the nodal status data. For the triple negative data significant differences were seen in kurtosis of normalised radial length. Some significant differences were found in the calculations for moments but these were not consistent across time points. No significant differences in shape descriptors were seen for response to neoadjuvant chemotherapy and biopsy grade data groups. It should be noted that whilst only a select few shape descriptors were explored, many more exist and recent literature has shown success in measure of margin sharpness of lesion. This could be a future area of exploration.

10 Future Work

From a software perspective the author would like to highlight that although the package created is robust and mathematically correct in its calculations of various texture and shape parameters, the software itself as with any new application does lack functionality from a usability aspect. None of the known errors affect the ability to generate high quality results, the problems that exist are merely from a usability aspect where some features are hard coded when they should be user selectable via the GUI screen. There also exist some functions which could in the future be combined as one single function from the users point of view. If this software package was ever to be released on a commercial scale or made available to other researchers these would need to be addressed, as this is an unlikely scenario for the purpose of this thesis they are documented in the user manual. Had there not been time limitations the author would have liked to integrate the software application with an environment such as .NET, this would not have only allowed the creation of a more sleek GUI, in addition it would give the software the ability to be hosted online available for the research community to use. The current software is written using MATLAB which due to its matrices based features proved one of the most efficient environments for DICOM image manipulation, the drawback of using MATLAB is that the GUI modules are not as good as the likes of .NET and cannot be hosted online. This can be overcome by integrating the current code with .NET coding environment. The author would also like to highlight that generating a well documented software adhering to the software life cycle was not a requirement of the thesis but the author being from a computer science background felt this was the only way to ensure the final products robustness and to ensure high quality results and accuracy compared to previous similar studies. In addition a well documented piece of software allows for ease of understanding particularly in support of any future development.

Texture analysis reliably demonstrated its ability to differentiate between varying grades of foam in an agar embedded phantom despite them appearing visually indistinguishable on an

MR image. This study proved that texture analysis demonstrates good repeatability in MR. This experiment could be repeated using a phantom that closely maps that of breast tissue.

Reducing grey levels improves counting statistics per co-occurrence matrix element and is understood to have some effect on discriminatory power. This wasn't found to be the case in chapter 5.1 as it was noted that data was consistent across all grey levels when assessing chemotherapeutic response using texture analysis. This needs further investigation as clearly having for example 2 grey levels would mean only a black and white image and would be difficult to distinguish one lesion from another. On an image with a higher number of grey levels the co-occurrence matrix would become sparse. The texture analysis results of an image analysed using 2 grey levels would be different to the one with a high number of grey levels. Further investigation could involve using a more varying number of grey levels as well as varying the distance between pixel pairs in the co-occurrence matrices. Whilst the large number of statistical tests undertaken necessitates a degree of caution in interpreting the results, the fact that significant differences are consistently observed is encouraging. Using a larger data cohort could further prove the ability of texture analysis as a chemotherapy response predictor.

The underlying texture analysis code using the Haralick method could be applied utilising a 3D co-occurrence matrix method as this would be in line with current studies that show evidence that a 3D co-occurrence matrix yields better results than a 2D version. In order to utilise such a method isotropic data would be required.

PCA was briefly introduced in chapter 5.3 in an attempt to reduce the dimensionality of the large data set. Further analysis combining all f parameters at one time point and one grey level choice could significantly reduce computation time if sufficient information is found to be present.

Chapter 6 looked at wavelet analysis as a method of texture analysis, the work highlighted that wavelet analysis energy levels can show differences between groups (based on TNBC, PR or NR with respect to % change in longest diameter, nodal status and biopsy grade). The vertical directions using the Haar wavelet contained over 62% of the results, this directional bias was somewhat surprising and would require further investigation in a larger data cohort.

Chapter 7 looked at lesion detection using texture mapping. This study generated and analysed texture maps for normal, benign and malignant cases and established that lesion detection was possible. This has potential as a screening tool although the hotspot lesion detection feature needs further optimisation in order to decrease the number of false positives and increase true positives. The segmentation feature of the software is relatively unsophisticated and would need further work in order to segment breast tissue more accurately to eliminate noise and reduce false positives arising from the skin surface. Although an erosion feature was programmed into the software this was not used for this study as it seemed to incorrectly remove breast tissue in some cases instead of just eliminating breast edges. Only three of the 16 texture parameters were analysed due to the large amount of time required to analyse each parameter and measure its false positive rate and sensitivity. The texture maps have already been generated therefore this is something that can be reserved for a further study. This further work could indicate (especially if data is used in combination) that not all 16 texture parameters are needed - the goals may be achieved by using a single or a select few parameters as was done in this study using 3 parameters. This study chose to look at texture parameter maps for f_1, f_9 and f_{13} as initial testing of these parameters using mock input variables worked well but looking at other parameters could possibly yield better results. In addition other means of thresholding need to be explored. At the moment only 17 benign and 17 malignant cases were tested, once additional and more optimum input variables are established for the lesion detection feature a larger data cohort would yield a more accurate FROC analysis. Further testing is also needed to reduce the number of false positives especially in normal breast data.

For the shape analysis work using a similar approach of multi slice analysis as was used in the texture analysis work in chapter 5 could be a possible future area of exploration, in practice this would probably be more complex in terms of coding such a feature. Aggregate measure of 2D shape may not be very representative of overall shape of a lesion. The alternative is to use 3D shape analysis which requires isotropic data and different mathematical models (e.g. sphericity). In addition it must be noted that only a hand full of shape descriptors were explored in this study, many more exist, in particular the author would encourage any future work to look at margin sharpness of lesion.

11 Appendices

11.1 User Manual

The software is available to use for the purpose of research with prior consent and arrangement from either the author or Dr Peter Gibbs on site at the MRI Centre, Hull Royal Infirmary, University of Hull. This is the user manual for the DicomReader software created for the purpose of this research PhD. Although a compiled version of the software will run on any PC or MAC without the need to install MATLAB developer tools some features are restricted and can only be used if a full version of MATLAB is installed. These are MATLAB only built in features such as the wavelet toolbox and imtool function used to read pixel values. Also some processing may require hard coding which again can only be done if a user has MATLAB developer tool installed with the imaging toolbox. This is however, even in its compiled form, fully functional software. Due to the fact its main purpose was a particular research study and not for commercial distribution or sales users may experience limited functionality. Saying this the full software lifecycle has been adhered to including testing especially in order to maintain the integrity of any applied formulas and algorithms of texture and shape. There are also various options that have been left in which were initially only coded for testing purposes such as the load chessboard function, these may be removed in later versions of the software.

11.1.1 Perform Texture Analysis on a single Image

Step 1:

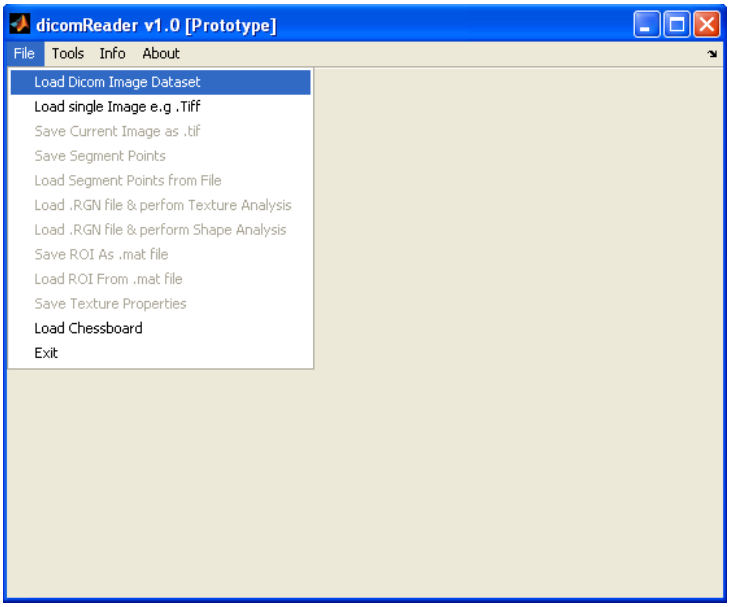

From the file menu select 'Load Dicom Image Dataset' if wanting to look at a whole series of images or select 'load single Image' if loading any other image format.

Step 2:

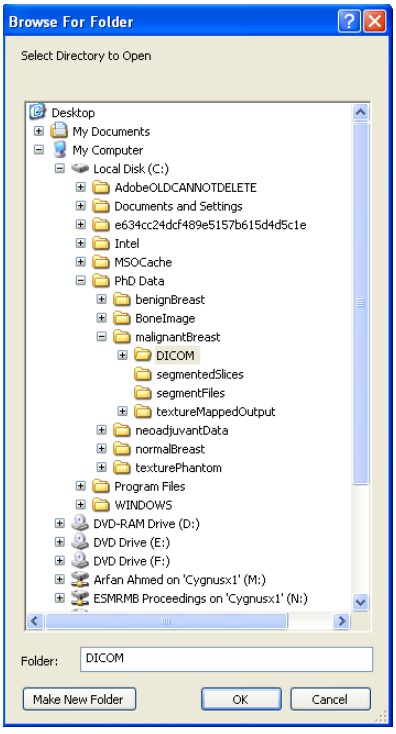

Select the directory where dicom image series are stored on your computer.

step 3:

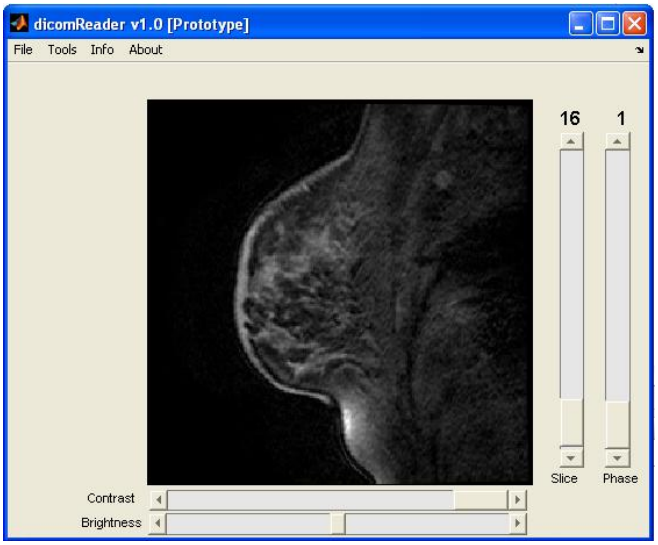

The above screen will now be displayed and the user can adjust slice and phase numbers using the vertical sliders and adjust brightness and contrast using the horizontal sliders. Note phase sliders will not work when loading single images in non dicom formats

Step 4:

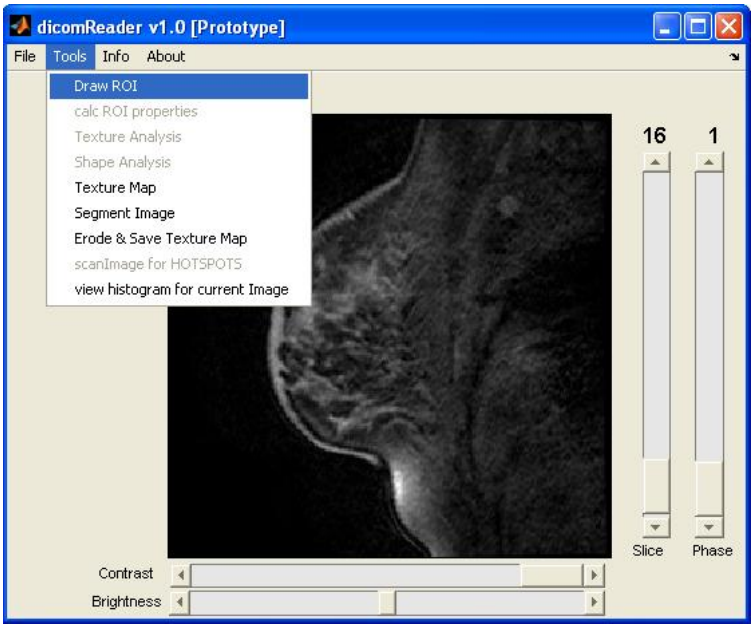

You can either load an existing saved ROI file by going to the File menu and selecting ‘load ROI from mat file’ or you can draw an ROI on the current image from the tools menu and selecting ‘Draw ROI’ sub menu

Step 5:

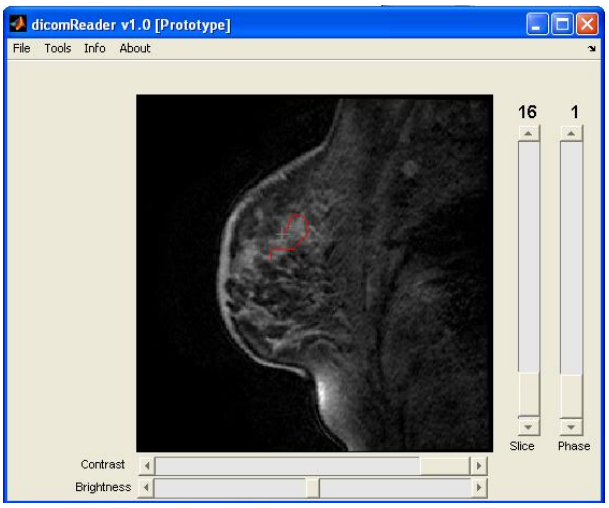

At this point a cursor will appear that will allow the user to freehand draw a region similar to the pencil tool found in most paint programs. Click on a point where the user wants to start drawing the region and once you have finished click on the screen for a second time at the end point. Note when drawing a ROI using this tool the software will display the ROIs data as shown on the screen in step 6.

Step 6:

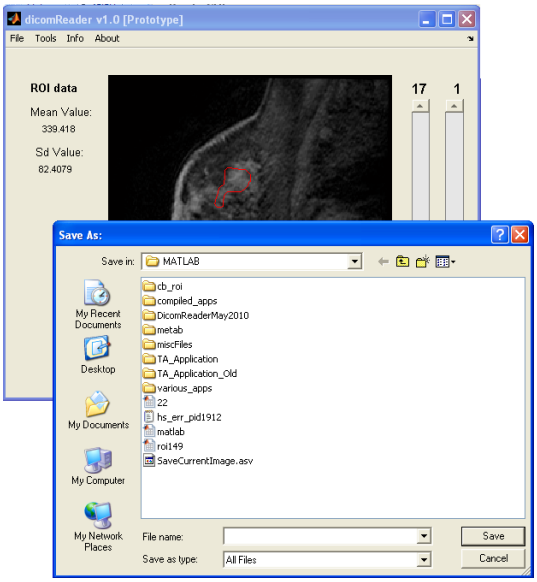

If the user wants to save the ROI that they have just drawn this can be done by going to the file menu and selecting ‘save ROI as .mat file’ and giving it the name they wish and saving it in any location on the computer.

Step 7:

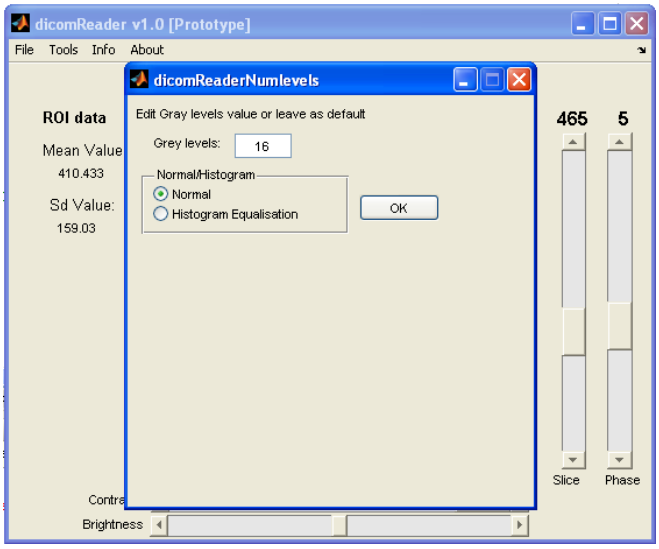

The user now needs to go to tools menu and select 'calc ROI properties' sub menu and the screen above will be displayed. Here the user can select the number of grey levels normally either 8, 16, 32 or 64. The user can choose to have the ROI histogram equalised or not by using the radio buttons and then click 'OK' button to continue.

Step 8:

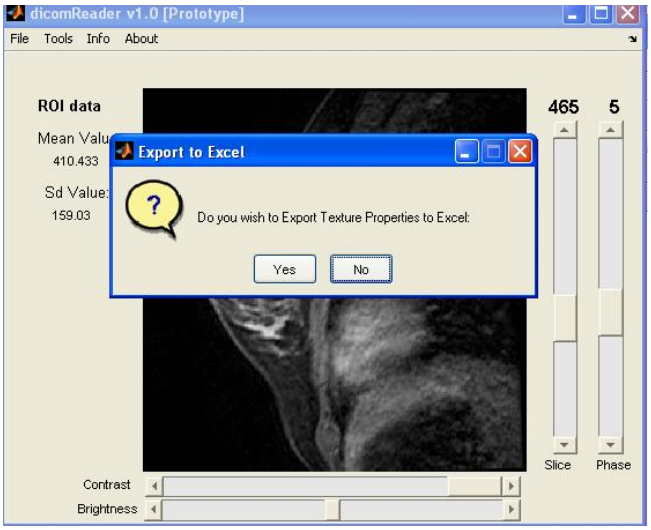

Once back on the main screen the user now needs to click again on the tools menu and select the 'Texture Analysis' sub menu and a popup menu will appear for the user to confirm if they wish to export the results to an excel spreadsheet. If the user does click 'Yes' an excel file will be saved in the same directory and with the same name as the original image location. The file

will look similar to the spreadsheet screenshot shown below and this concludes texture analysis on a single slice. Note: at the point of writing the user manual the file location to be saved was hard coded in saveAsExcel.m file. Users of the software will temporarily need to hardcode this if they wish to change the location, later versions of the software will add additional features to allow user to specify where file is to be saved.

	A	B	C	D	E	F
1		0° [0 1]	45° [-1 1]	90° [-1 0]	135° [-1 -1]	Average
2	f1_angularSecondMoment	0.017424558	0.016837794	0.018600675	0.014056356	0.016729846
3	f2 contrast	3.801612903	4.255462185	2.896381579	6.085808581	4.259816312
4	f3 correlation	0.74975388	0.718882165	0.805086948	0.598018736	0.717935432
5	f4 variance	5.786584287	5.617151331	6.22393579	4.653824788	5.570374049
6	f5 inverse diff moment	0.458506144	0.421899729	0.466607377	0.376344629	0.43083947
7	f6 sum Average	15.42741935	15.42857143	15.44572368	15.47524752	15.4442405
8	f7 sum Variance	26.97699011	26.73901561	27.79310671	24.74113649	26.56256223
9	f8 sum Entropy	4.349508878	4.336759762	4.384310538	4.27507333	4.336413127
10	f9 entropy	6.208820604	6.244829002	6.052297805	6.454300375	6.240061946
11	f10 difference Variance	1.556449011	1.608688652	1.03728521	2.281377643	1.620950129
12	f11 difference Entropy	2.214309383	2.230846291	1.998057958	2.506366841	2.237395118
13	f12 info Measure Of Correlation 1	-0.216163175	-0.207628172	-0.260373004	-0.147137382	-0.207825433
14	f13 infoMeasure Of Correlation 2	0.884477698	0.878969616	0.916388893	0.79889954	0.869683937
15	f14 maximal correlation coefficient	0.767543335	0.748009362	0.838174943	0.657074934	0.752700643
16	f15 cluster Shade	52.70948504	47.28876694	55.4529026	51.72707976	51.79455858
17	f16 cluster Prominence	1932.633513	1910.53316	2110.725483	1618.084791	1892.994237
18						
19	Mean of ROI	236.096124				
20	Standard Deviation of ROI	50.39770465				
21	Slice No	1				
22	Phase No	5				
23	Number of Gray Levels	16				
24						
25	Normal/Histogram:	NON-Histogram				
26	Image Id:	C:\PhD Data\neoadjuvantData\PC_2min\E05255				
27	generated by matlab@	17/11/2011 10:49				

11.1.2 Perform Texture Analysis on all slices with corresponding ROIs

For this function the user has a series of images saved in Dicom format and wishes to perform texture analysis using ROIs saved in binary file format. The feature will match up the ROIs to the corresponding slices and perform texture analysis on multiple slices.

Step 1:

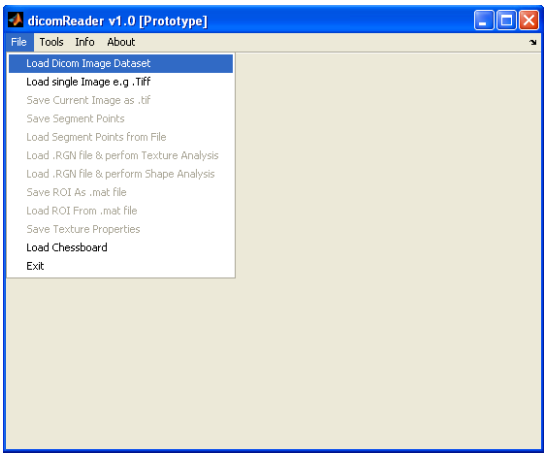

From the file menu select ‘Load Dicom Image Dataset’

Step 2: same as step 2 in ‘Perform Texture Analysis on a single Image’ section of user manual

Step 3: same as step 3 in ‘Perform Texture Analysis on a single Image’ section of user manual

Step 4:

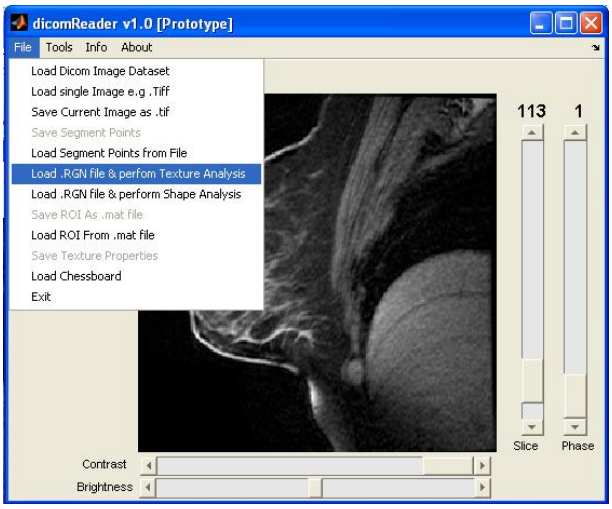

Go to file menu and select/click on the ‘Load .RGN file and perform Texture Analysis’ sub menu

Step 5:

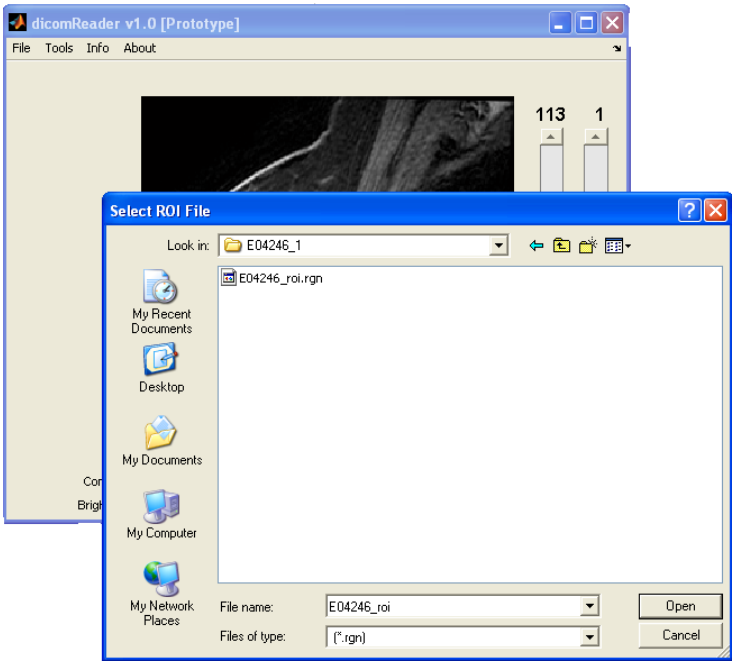

Select the ROI file with file extension .rgn corresponding to the series of images by double clicking he correct file

Step 6:

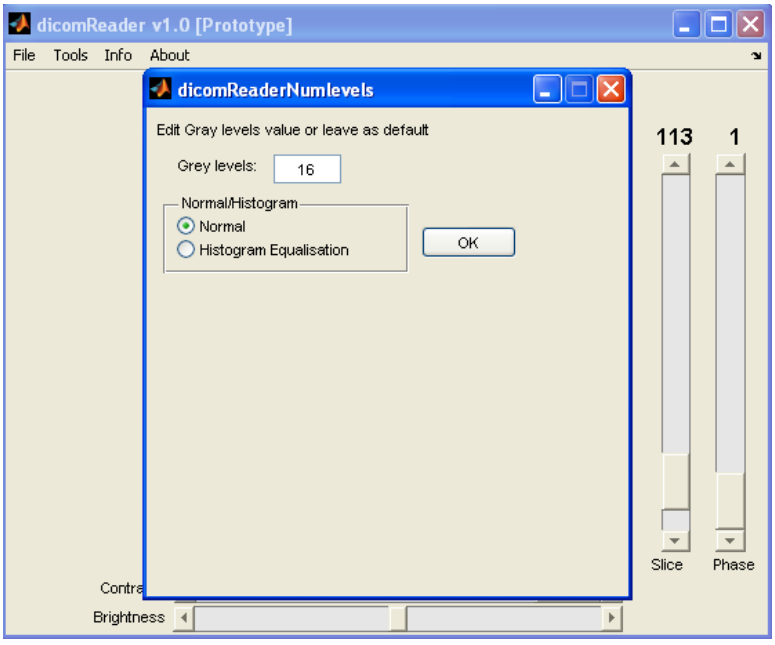

The user will be prompted by another screen where you can select number of grey levels and if the ROI should be histogram equalised or not prior to processing. Click ‘OK’

Step 7:

```
|================================================|
|################################################
|================= 99% completed =================|

            Estimated remaining time: 0:00
            Elapsed time:             0:03
```

A status bar similar to the one above will appear in the MATLAB command window

Step 8:

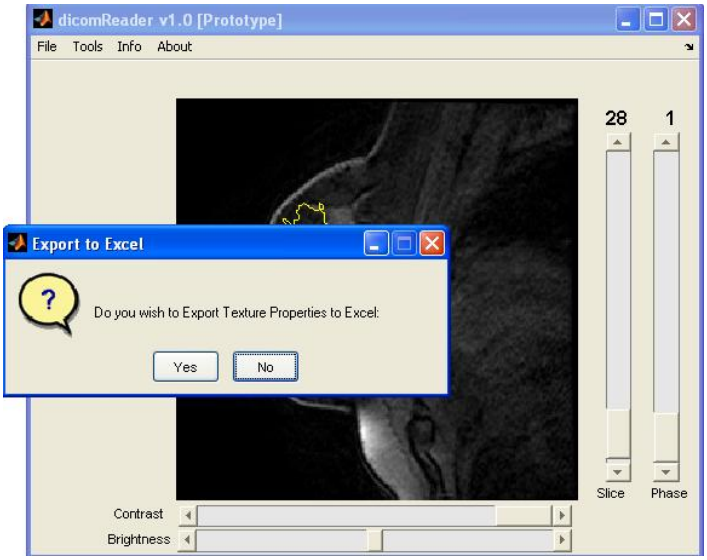

A popup menu will appear for the user to confirm if they wish to export the results to an excel spreadsheet. If the user does click 'Yes' an excel file will be saved in the same directory and with the same name as the original image location. The file will look similar to the spreadsheet screenshot shown below and this concludes texture analysis on a multiple slice using ROI file. User will also be able to scroll through the slices and see the loaded ROIs on each slice change, the correct slice will be automatically drawn onto each slice (if the .rgn file contained a ROI for the corresponding slice number). These ROIs and individual images can be saved using the 'save ROI as .mat file' under file menu and 'save image as tiff' sub menu.

correctOUTPUT2.xls

	A	B	C	D	E	F
1		0° [0 1]	45° [-1 1]	90° [-1 0]	135° [-1 -1]	Average
2	f1_angularSecondMoment	0.042410713	0.033087	0.038609638	0.032495554	0.036650652
3	f2 contrast	1.048607814	2.099202	1.299681931	1.809605792	1.564274404
4	f3 correlation	0.918651449	0.801613	0.88164103	0.792395493	0.848575294
5	f4 variance	3.812313604	3.141659	3.690639725	3.465118801	3.527432832
6	f5 inverse diff moment	0.677471213	0.581777	0.645956262	0.586934633	0.623034806
7	f6 sum Average	17.98303475	18.1114	17.99516361	18.03173973	18.03033328
8	f7 sum Variance	16.33172168	14.78538	16.09901369	15.67095657	15.72176716
9	f8 sum Entropy	4.035734707	3.968948	4.026152242	4.006898028	4.009433274
10	f9 entropy	5.073539546	5.472204	5.221095503	5.452477889	5.304829347
11	f10 difference Variance	0.543044763	1.032221	0.652116679	0.840963329	0.767086412
12	f11 difference Entropy	1.494454311	1.874514	1.613270847	1.78929891	1.692884498
13	f12 info Measure Of Correlation 1	-0.3603441	-0.22107	-0.311339533	-0.234562131	-0.281829144
14	f13 infoMeasure Of Correlation 2	0.93545985	0.819832	0.91369736	0.874406799	0.885848944
15	f15 cluster Shade	-21.18436378	-17.933	-20.97242063	-21.77883625	-20.46714906
16	f16 cluster Prominence	756.5553138	618.3808	738.5437406	712.2000248	706.4199634
17						
18	Mean of ROI	778.7692308				
19	Standard Deviation of ROI	299.4017111				
20	Slice No	72				
21	Phase No	1				
22						
23	generated by matlab@	22/12/2009 14:19				

Note: at the point of writing the user manual the file location to be saved was hard coded in saveAsExcel.m file, users of the software will temporarily need to hardcode this if they wish to change the location, later versions of the software will add additional features to allow user to specify where file is to be saved.

11.1.3 ROI draw, save and load

See steps 4-6 in the 'Perform Texture Analysis on a single Image' section of the user manual

11.1.4 Perform shape analysis

Very similar to texture analysis, as per sections 'Perform Texture Analysis on a single Image ´and 'Perform Texture Analysis on all slices with corresponding ROIs' in the user manual. The user can load an ROI or draw an ROI using the draw ROI function or load .rgn file containing all the ROIs on the corresponding series of images using the 'load .rgn and perform shape analysis' under the file menu. The software will automatically take the largest ROI and perform shape analysis on that region and the output will be saved in the root directory (normally C:) on computer. For a single ROI the user can simply select 'shape analysis under the tools menu.

The major difference for shape analysis is that the user does not input any additional parameters as with texture analysis.

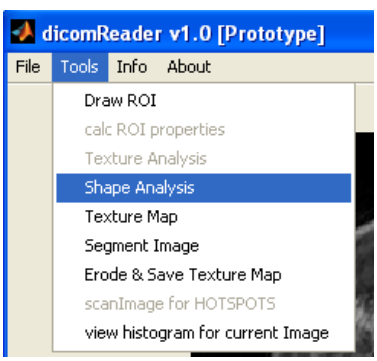

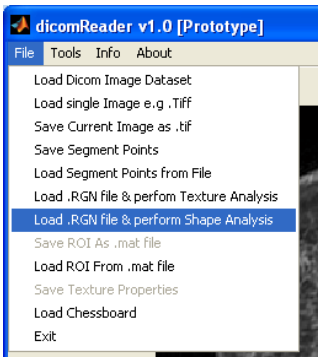

11.1.5 Perform texture mapping and hotspot search (scan image)

Step 1:

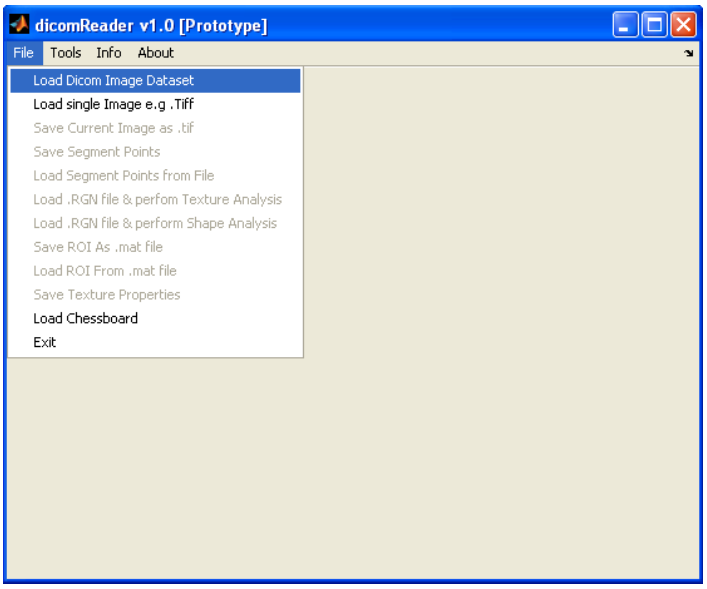

When faced with the main screen load an image either by loading a series of images via the 'load Dicom Image dataset' sub menu under file menu or by selecting 'load single image' sub menu.

Step 2:

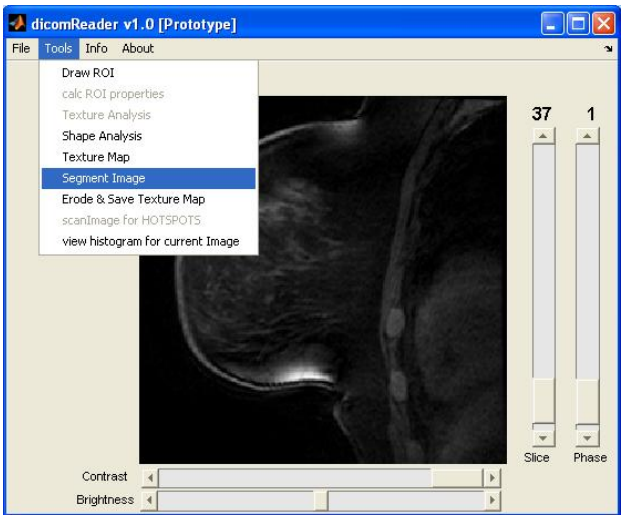

When desired image is on screen first a user can choose to segment the image, this is optional but segmenting the image will mean much faster processing time. Under the tools menu select segment image sub menu

Step 3:

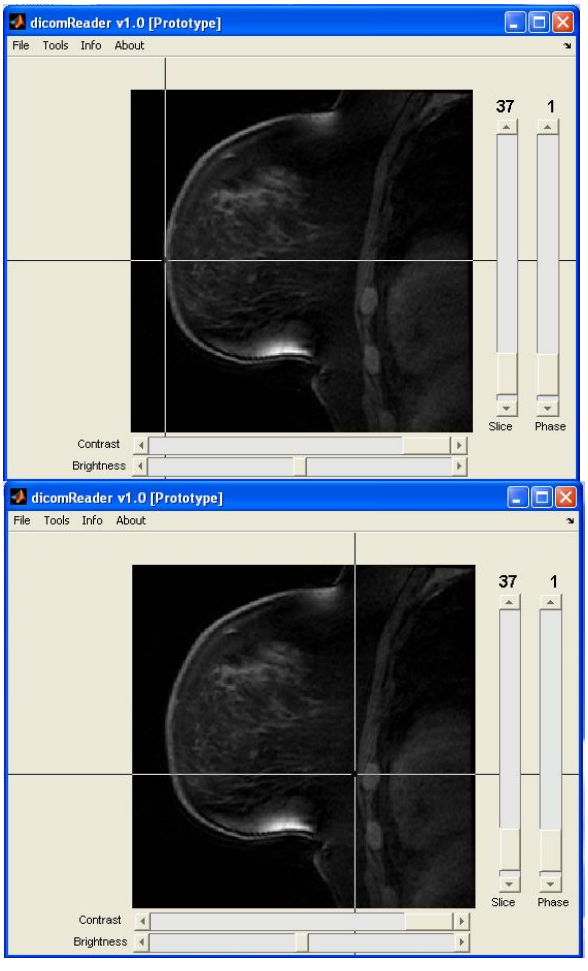

With the cursor select the start point by clicking the mouse (example nipple) and end point by clicking the mouse (example chest wall begins) and the image will be segmented ie anything before nipple will disappear (usually noise) and anything after the chest wall starts will also disappear as per screenshot below

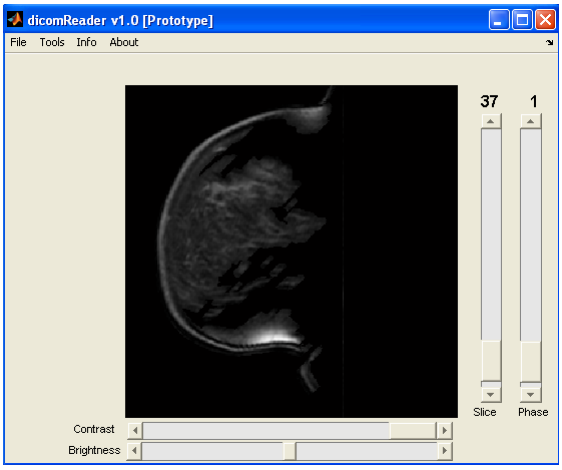

Step 4:

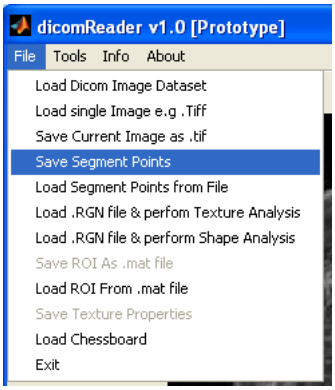

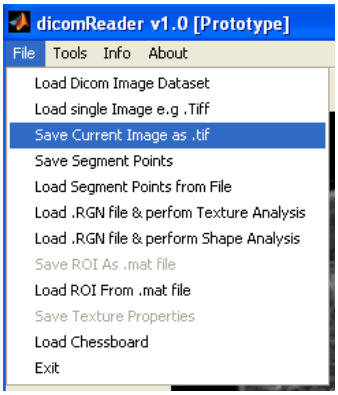

This is another optional step if the user wishes to save the segment point coordinates they can at this point by selecting the file menu and clicking on the sub menu ‘save segment points’ then save them anywhere on their computer. In addition the segmented version of the image can also be saved as a .tiff file by again going to the file menu and clicking on ‘save current image as .tiff’. Similarly if an image is already loaded and the user wished to apply previously saved segment coordinates to that image they can do so by going to file menu and selecting ‘load segment points from file’ sub menu.

Step 5:

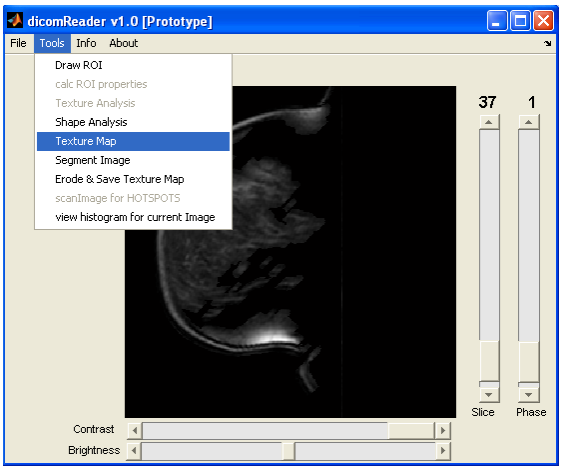

The user is now ready to texture map by clicking on the tools menu and selecting the 'texture map' sub menu

Step 6:

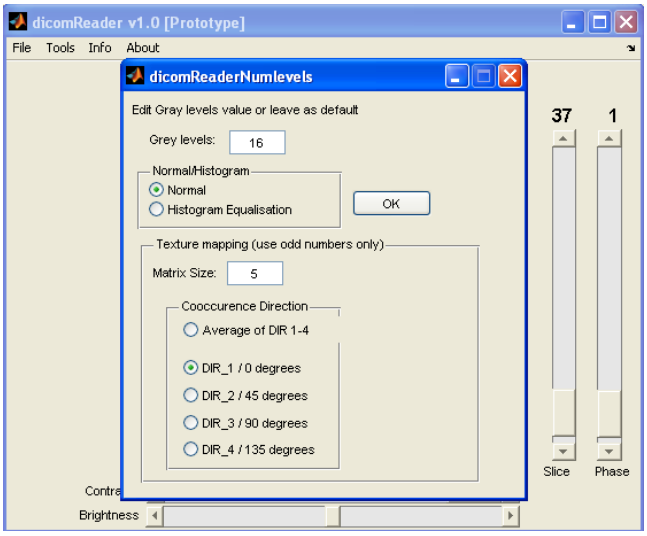

A pop up window will appear which will allow the user to input number of grey levels and histogram equalisation option. The matrix size of the texture mapping pixels can also be selecting or left to the default size of 5 and also in which direction the user wishes the calculation of the co-occurrence matrix to take place. By default the system uses the average of all directions which is also available as an option in the texture mapping function. Once the user is happy with their selection click the 'OK' button and processing will begin with a progress bar displayed in the MATLAB command window similar to the one in the screen shot

below. Processing depends on the size of the image and how much segmentation was done and can take anything from 2 minutes to 45 minutes. Once complete a message will be displayed in the MATLAB command window informing the user where the file has been saved as per screenshot below. The files will be saved as .tiff files and will consist of 16 new images one per texture parameter.

```
|==================================================|
|###
|================= 7% completed =================|

            Estimated remaining time: 0:46
            Elapsed time:             0:03
%%%%%%%%%%%%%%%%%%%%%%%%%%%%%%%%%%%%%%%%%%%%%%%%%%%%%%%%%%%%%%%%%%%%%%%%%%%%%%%%%%%%%%%%%%%%%%%%%%%%
Texture Mapping Complete.....

savefile =

C:\PhD Data\malignantBreast\DICOM\M10\NONHISTEQ16S37M5DIRAVGf16.tif

where S = Slice number and M = Matrix Size/Dimension used and DIR = cooccurence DIRECTION
%%%%%%%%%%%%%%%%%%%%%%%%%%%%%%%%%%%%%%%%%%%%%%%%%%%%%%%%%%%%%%%%%%%%%%%%%%%%%%%%%%%%%%%%%%%%%%%%%%%%
```

Step 7:

This is another optional step not part of the software but part of MATLAB in which the user can analyse the texture mapped images by opening them up using MATLABs imtool feature, this will only work with a full version of MATLAB developer tool with imaging toolbox. The user can first adjust the contrast if the image is not clear by clicking on the imtool tools menu and selecting ‘adjust contrast’ sub menu.

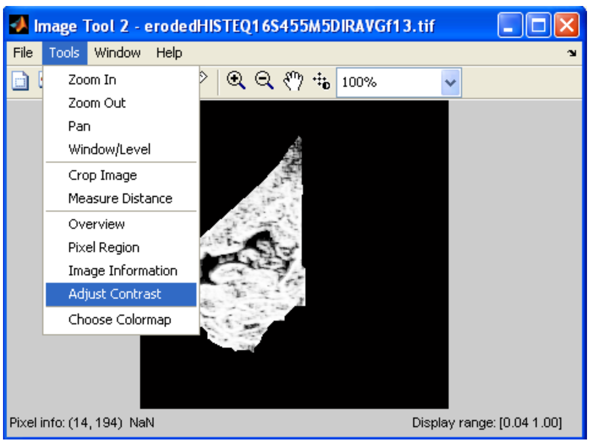

Step 8:

Again an optional step not part of the software but part of MATLAB. The user can select the pixel tool from the imtool tools menu and can then use the tool to look at individual pixel values overlaid on the actual image.

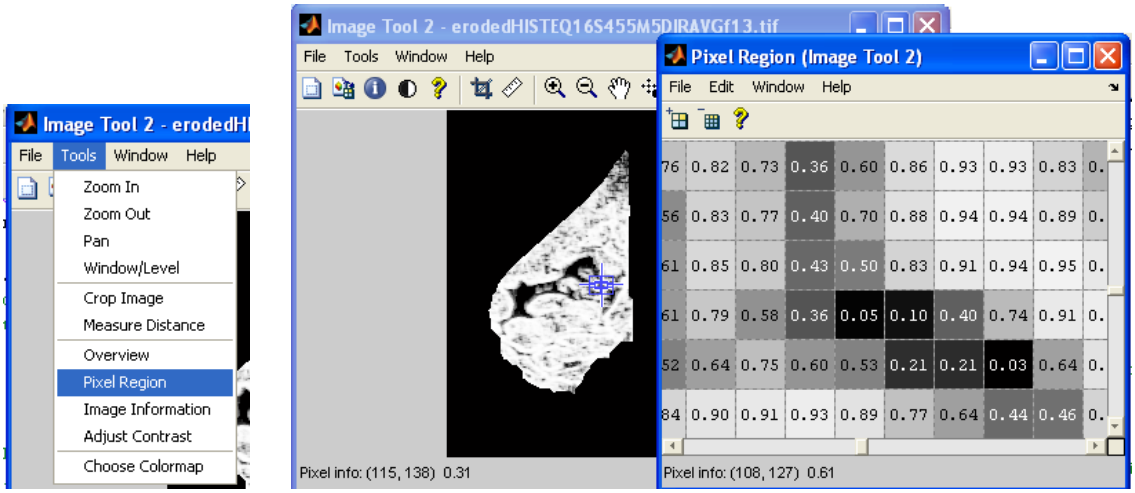

Step 9:

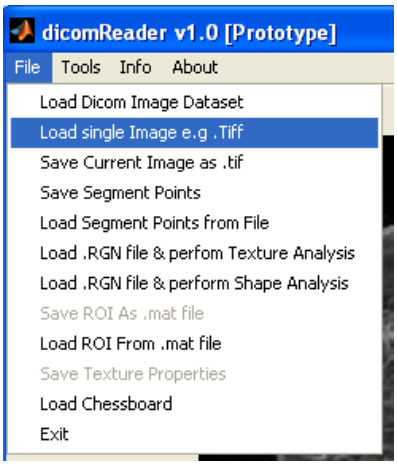

In the dicomreader software the user can select the texture mapped images and open an image using the ‘load single image’ sub menu ready to use the hotspot feature

Step 10:

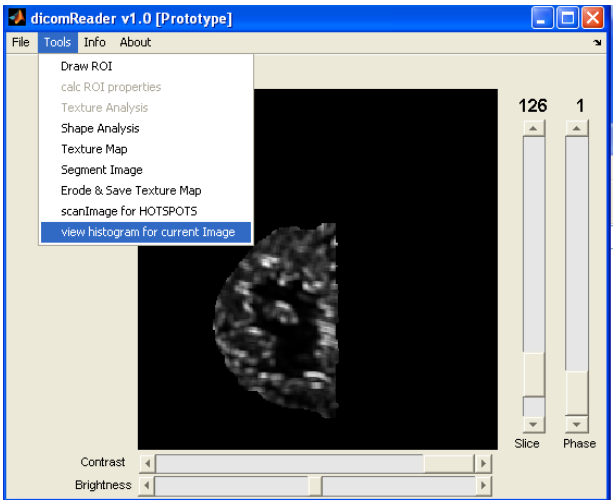

Under tools menu select view histogram for current image.

Step 11:

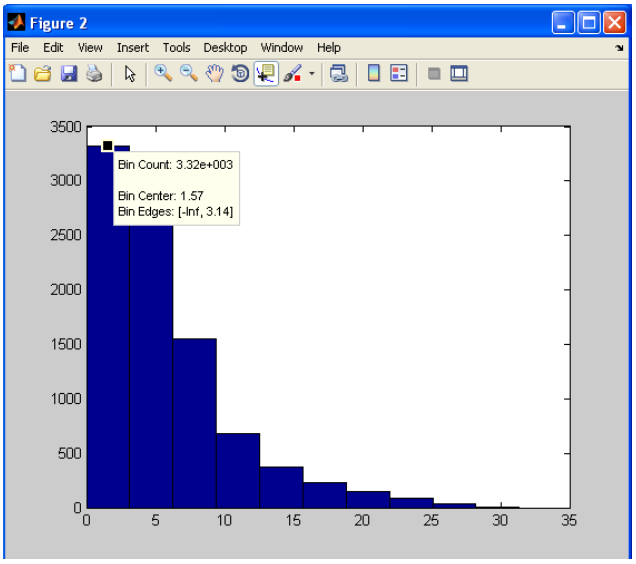

Once the histogram appears (this is a Matlab feature, so may only work with full MATLAB version and imaging tool box) on the tools menu select 'data cursor' and place the cursor on any of the histogram bars to get the bin edge values (these will be used for min and max values later). Note the bin size is hardcoded for each f (texture) parameter as the optimum differs for each one. This is done by altering the code in the viewHistogram.m file (again this is only something a developer can do with full MATLAB version, but later versions of this software will allow the user to set this).

Step 12:

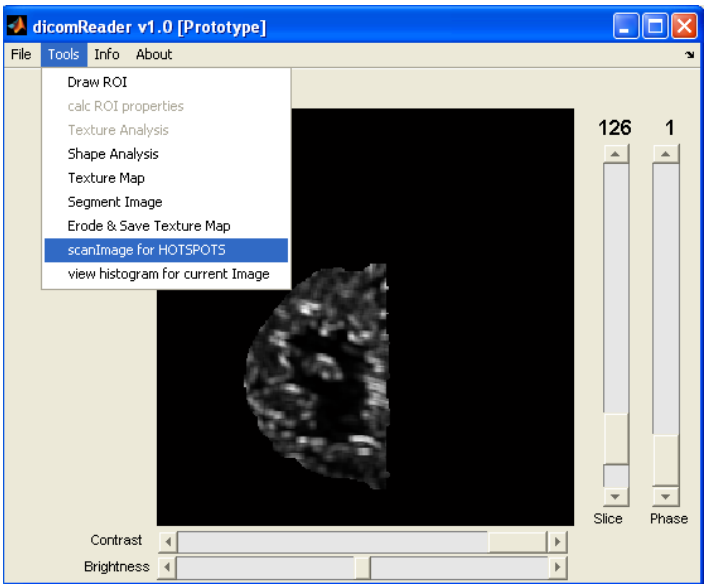

The user can click the 'scan image for HOTSPOTS' function under the tools toolbar in the dicomreader software window.

Step 13:

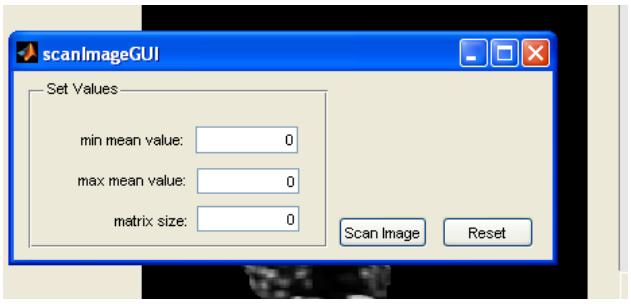

A new pop up window will appear. The user can enter the bin values from step 11 as the min and max and enter a matrix size (again this is something tweaked for each f parameter). The user can click scan image once appropriate values have been entered. Table 11.1 shows example values that could be used for each f parameter (these are just samples and are not the correct tweaked versions) table 11.1 is optimised for the eroded texture maps whereas table 11.2 is more appropriate for the raw texture mapped output images (these are recommended due to higher accuracy but in some cases edges will have to be ignored)

	Matrix size	Set Bin Size (in code)	Value range to use from histogram
F1	7	10	Lowest
F2	9	200	highest
F3	-	-	-
F4	9	200	highest
F5	3	150	highest
F6	3	200	highest
F7	5	200	highest
F8	3	300	highest
F9	9	10	Lowest
F10	5	300	highest
F11	3	300	highest
F12	-	-	-
F13	5	10	Lowest
F14	5	150	highest
F15	-	-	-
F16	7	1500	highest

Table 11.1: Optimal parameter settings for eroded texture maps

	Matrix size	Set Bin Size (in code)	Value range to use from histogram	Additional notes
F1	7	10	Lowest	Mostly 0.8 – 0.9
F2	9	200	highest	
F3	-	-	-	
F4	9	45	highest	
F5	9	5	lowest	
F6	7	50	Take the bin range from the highest value (x axis) in histogram	
F7	3	1250	highest	Use bin values mid to max
F8	3	13	lowest	Ignore edges
F9	9	10	Lowest	Ignore edges
F10	5	300	highest	Ignore edges and use bin values mid to max
F11	7	10	lowest	
F12	-	-	-	
F13	5	10	Lowest	Ignore edges
F14	3	10	highest	Ignore edges and use bin values mid to max
F15	-	-	-	
F16	7	1500	highest	Ignore edges and use bin values mid to max

Table 11.2: Optimal parameter settings for raw texture map.

Step 14:

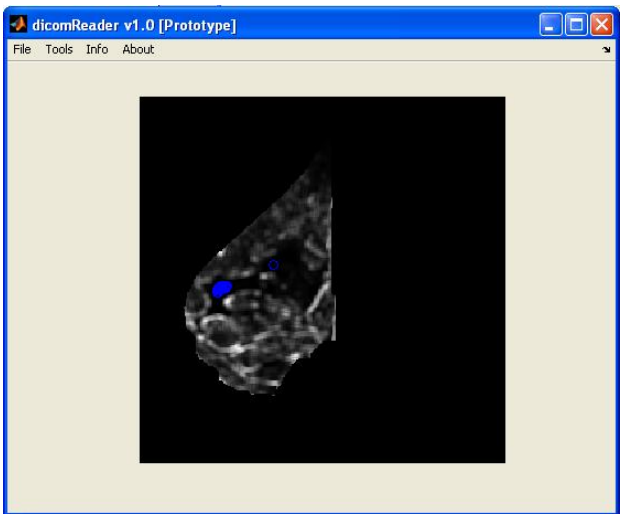

Suspected lesions or hotspots depending on the min/max and matrix size will be highlighted on the current image as above

Step 15:

An additional feature also exists to calculate and output into a spreadsheet min, max and mean pixel values for the current texture mapped image but this has not been added as a function in the GUI but can be run by a developer using a full version of MATLAB

This concludes texture mapping, other features not mentioned do exist but they are fairly self explanatory. For example, selecting the info menu user can view the dicom header information of the current dicom image on screen.

11.1.6 Perform wavelet analysis

Within DicomReader software the user can perform wavelet analysis based on the seven types of wavelet transforms available, but this can only be done with a full developer version of Matlab as the software uses Matlabs Wavelet Toolbox. The coefficient files for the seven wavelet types can be viewed and saved but the software only produced wavelet energy values for Haar wavelet transforms as this was the only one needed for the purpose of this research.

Step 1:

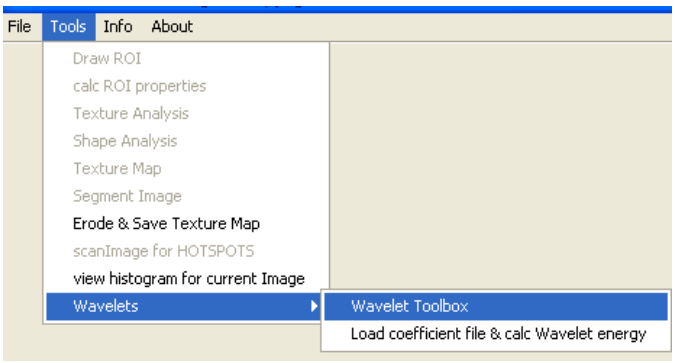

Select the Wavelet Toolbox feature from the Tools>Wavelets menu bar, the Wavelet toolbox shown in step 2 is loaded

Step 2:

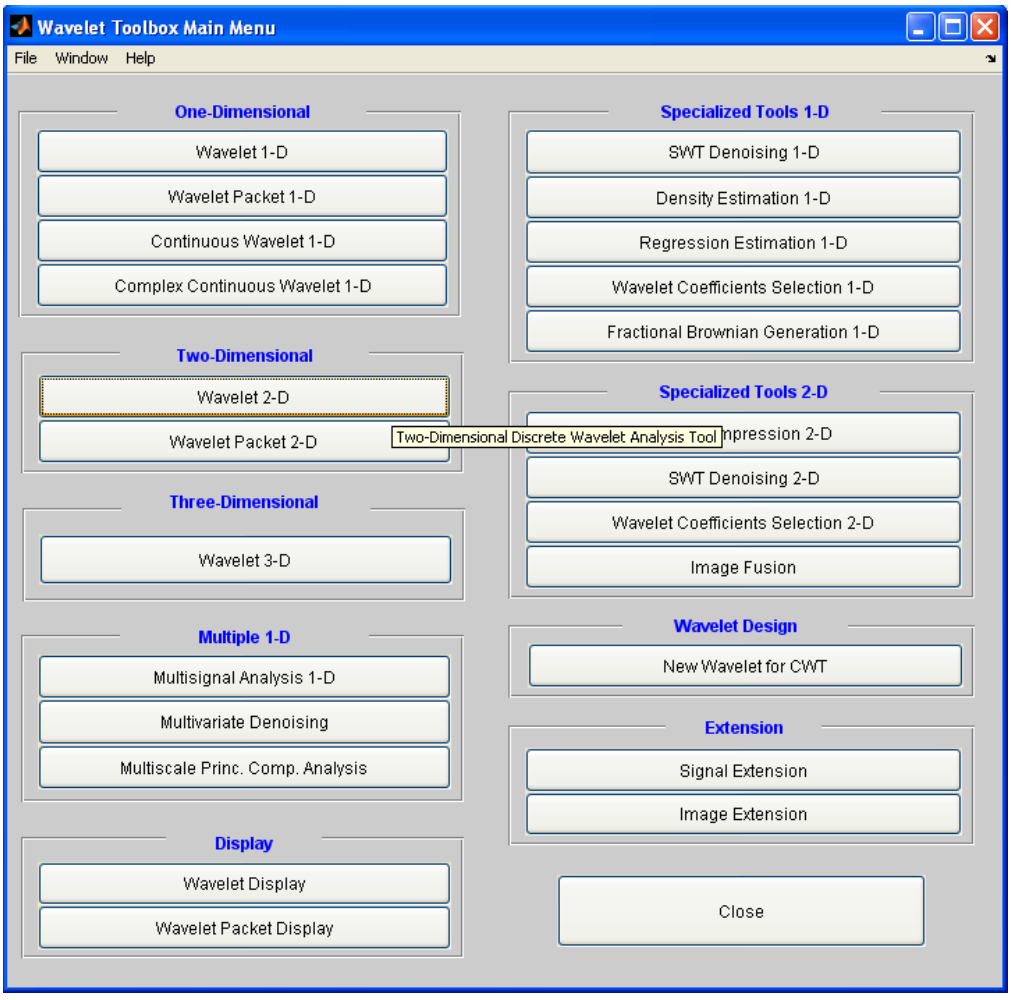

In order to load an image into the Matlab workspace in the command window type in the following code which will load an Image (I) and a normalised version of the image (I2), this code is also available in the normaliseImage.m file but its easier to type straight in to the

command window as this part of the software doesn't allow user to load an Image into the workspace that can be seen by the wavelet toolbox in a GUI type fashion.

```
I = dicomread('C:\PhD Data\neoadjuvantData\PC_1min\E09578\IM13');
%change this to point to image user wishes to analyse
maxI = max(I(:));
I2 = double(I)./double(maxI).*255;
```

Now returning to the Wavelet Toolbox interface as shown above go to the 'Two-Dimensional' heading and click on the 'Wavelet 2-D' button

Step 3:

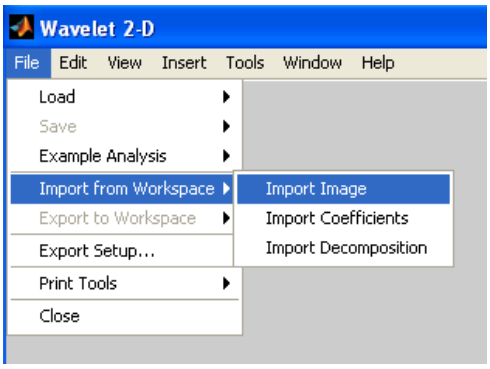

Under the file menu go to Import from workspace>Import Image.

Step 4:

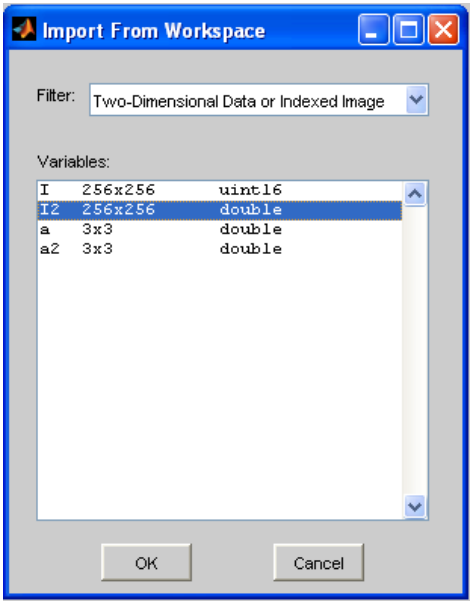

In the pop up window that appears select image I2 from the workspace that you loaded earlier in step 2 and click the ok button

Step 5:

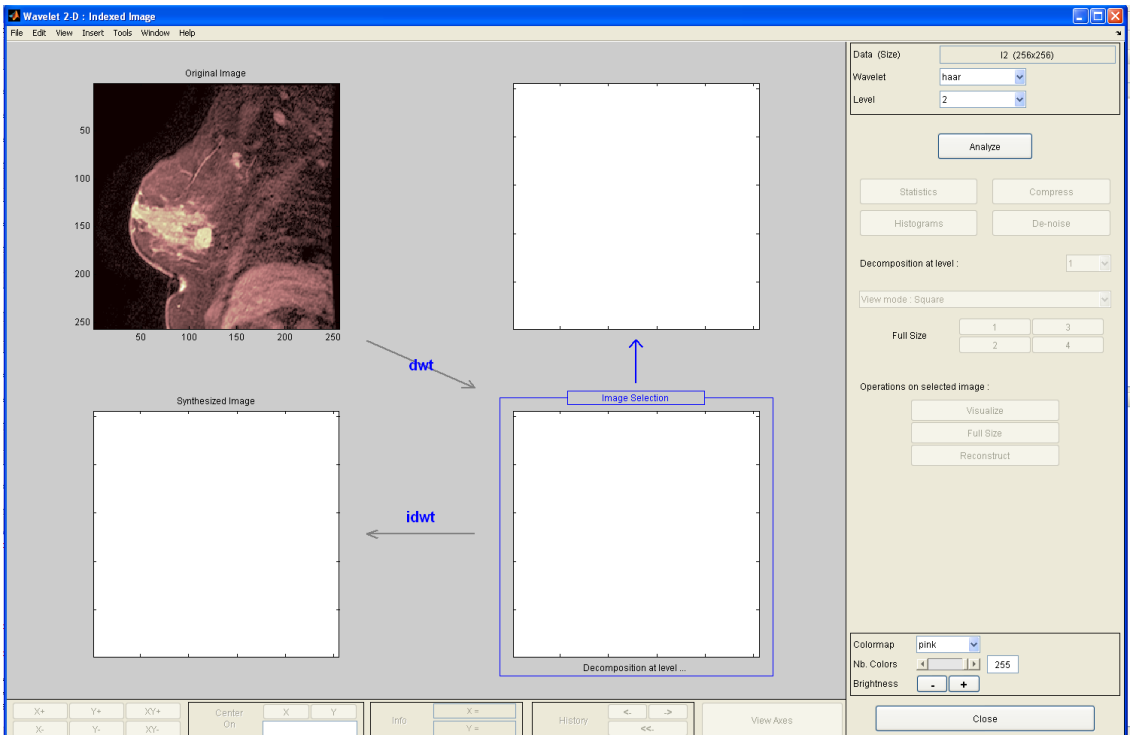

The image will now appear in the wavelet toolbox window. In the top right hand corner select in the drop down menus wavelet type ‘Haar’ and Level ‘4’ and click ‘Analyse’, the screen will display the wavelet images.

Step 6:

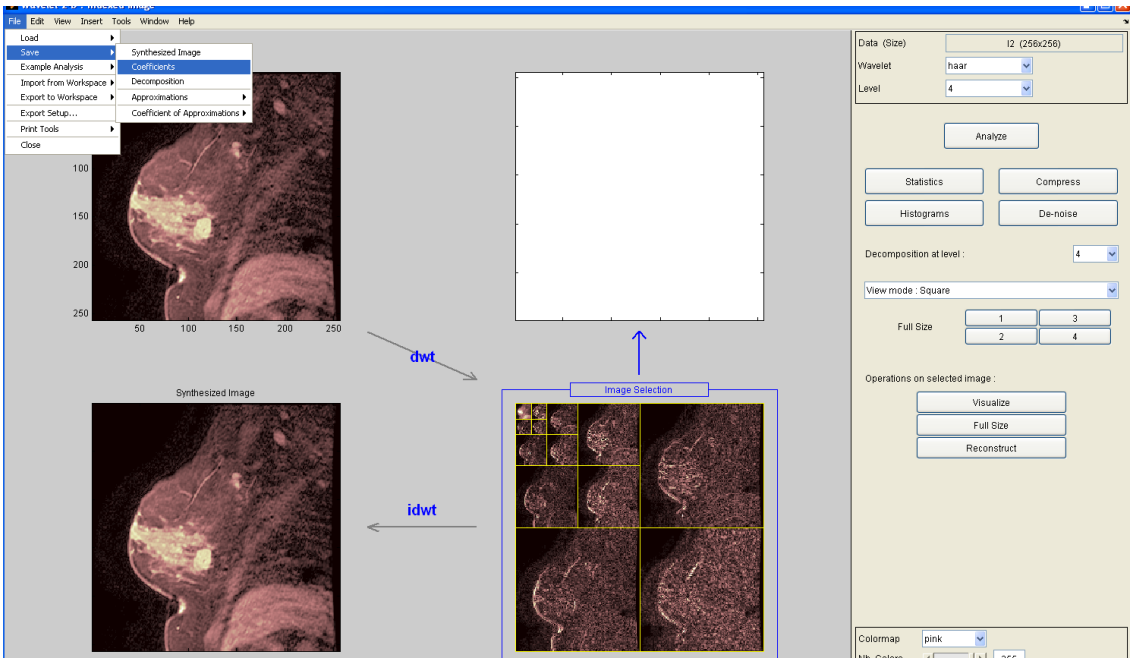

From the file menu select save>coefficients and when prompted save the file in an appropriate directory with a relevant name and click save.

This marks the end of the Matlabs wavelet toolbox use, exit the toolbox and go back to the DicomReader interface.

Step 7:

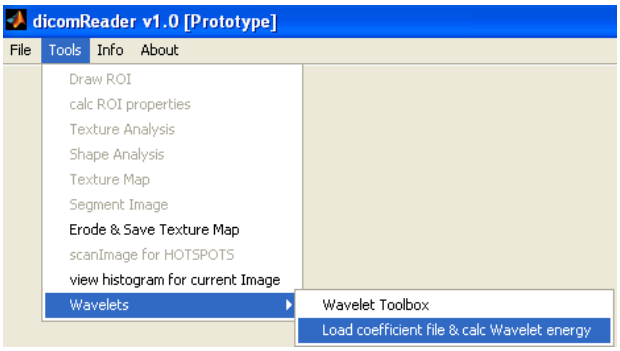

From the DicomReader go to Tools>Wavelets>Load coefficient file & calc Wavelet energy, user will be prompted to select the coefficient file which was created in step 6 and select the corresponding ROI file. Once correct files are selected click 'Open' and the processing will begin, the command window will display a 'successful' message when processing is complete and an excel spreadsheet will be output containing the energy values for the wavelet coefficient file. The command window will tell the user where this file has been saved.

Step 8:

	A	B
1		Wavelet Energy Results
2	energyWaveletHaar1Dir1	514.02221
3	energyWaveletHaar1Dir2	277.6825136
4	energyWaveletHaar1Dir3	26.61320496
5	energyWaveletHaar2Dir1	3451.948153
6	energyWaveletHaar2Dir2	3283.801534
7	energyWaveletHaar2Dir3	575.5715535
8	energyWaveletHaar3Dir1	57519.12953
9	energyWaveletHaar3Dir2	25373.88238
10	energyWaveletHaar3Dir3	1665.048188
11	energyWaveletHaar4Dir1	328897.0355
12	energyWaveletHaar4Dir2	9316.670665
13	energyWaveletHaar4Dir3	14446.51298
14	results for wavelet file	E04476_SL62.mat
15	generated by matlab@	02/03/2012 10:08

Excel spreadsheet can be viewed and display the energy values.

11.2 Conference presentations

1. Gibbs P, Ahmed A. *Texture Analysis of DCE-MRI of the Breast as a Predictor of Response*. In *19th ISMRM Annual meeting*. 2011. Montreal: ISMRM (e-poster)
2. Ahmed A, Gibbs P, Pickles MD and Turnbull LW. *Texture Analysis and Texture Mapping Software for High Field Strength MRI Breast Data.* Clinical Biosciences Institute Research Day, Hull, UK. (July 2010) (Poster)
3. Ahmed A, Gibbs P, Pickles MD and Turnbull LW. *Texture Analysis for chemotherapy response prediction in Breast Cancer.* Yorkshire Cancer Research (YCR) Annual Scientific Meeting, Harrogate, UK. (June 2011) (Poster)
4. Ahmed A, Gibbs P, Pickles MD and Turnbull LW. *Software for Lesion Detection of DCE MR Images of the Breast using Texture Mapping.* Yorkshire Cancer Research (YCR) Annual Scientific Meeting, Harrogate, UK. (June 2012) (Poster)
5. Ahmed A, Gibbs P, Pickles MD and Turnbull LW. *Texture Analysis for chemotherapy response prediction in Breast Cancer.* In 20th British chapter ISMRM Postgraduate symposium, Cambridge, UK. (June 2011) (Talk)
6. Ahmed A, Gibbs P, Pickles MD and Turnbull LW. *Texture Analysis Software for chemotherapy response prediction in Breast Cancer.* North of England Oncology Association, 3rd North of England Breast Cancer Symposium, University of Hull, UK. (May 2011) (Poster)
7. Ahmed A, Gibbs P, Pickles MD and Turnbull LW. *Texture Analysis of DCE Breast Imaging: Single slice vs. multi slice*. In 20*th ISMRM Annual meeting*. 2012. Melbourne, Australia: ISMRM (e-poster)
8. Ahmed A, Gibbs P, Pickles MD and Turnbull LW. *Software for Lesion Detection of DCE MR Images of the Breast using Texture Mapping.* In 21st British chapter ISMRM Postgraduate symposium, Bristol, UK. (March 2012) (Poster)
9. Ahmed A, Gibbs P, Pickles MD and Turnbull LW. *Software for lesion detection in MR images of the breast using texture mapping.* In International Journal of Computer Assisted Radiology and Surgery (CARS) Vol 7, page s253, Pisa, Italy. (June 2012) (Talk)
10. Ahmed A, Gibbs P, Pickles MD and Turnbull LW. *Texture analysis software for chemotherapy response prediction in breast cancer.* In International Journal of Computer Assisted Radiology and Surgery (CARS) Vol 7, page s254, Pisa, Italy. (June 2012) (Talk)
11. Ahmed A, Gibbs P, Pickles MD and Turnbull LW. *Software for chemotherapy response prediction in DCE breast images using shape descriptors.* In International Journal of Computer Assisted Radiology and Surgery (CARS) Vol 7, page s486, Pisa, Italy. (June 2012) (Poster)

11.3 Publications

Accepted

1. *Texture Analysis in assessment and prediction of chemotherapy response in Breast Cancer*, JMRI, accepted pending minor revisions, Sept 2012. Abstract:

Purpose

This paper systematically assesses the efficacy of DCE-MRI based textural analysis in predicting response to chemotherapy in a cohort of breast cancer patients.

Materials and Methods

100 patients were scanned on a 3.0T HDx scanner immediately prior to neo-adjuvant chemotherapy treatment. A software application to utilise texture features based on cooccurence matrices was developed. Texture analysis was performed on pre-contrast and 1-5 minutes post-contrast data.

Patients were categorised according to their chemotherapeutic response: partial responders corresponding to a decrease in tumour diameter over 50% (40) and non-responders corresponding to a decrease of less than 50% (4). Data was also split based on factors that influence response: TNBC (22) vs. non TNBC (49); node negative (45) vs. node positive (46); and biopsy grade 1 or 2 (38) vs. biopsy grade 3 (55).

Results

Parameters f_2 (contrast), f_4 (variance), f_{10} (difference in variance), f_6 (sum average), f_7 (sum variance), f_8 (sum entropy), f_{15}(cluster shade) and f_{16} (cluster prominence) showed significant differences between responders and partial responders of chemotherapy. Differences were mainly seen at 1-3 minutes post-contrast administration. No significant differences were found pre-contrast administration. Node +ve, high grade, TNBC are associated with poorer prognosis and appear to be more heterogeneous in appearance according to texture analysis.

12 Bibliography

1. Hájek M, D.M., Materka A, Lerski R *Texture analysis for magnetic resonance imaging*. 2006: med4. 225.
2. Donald W. McRobbie, E.A.M., Martin J. Graves, Martin R. Prince, *MRI from Picture to Proton*. Vol. 2. 2007: Cambridge University Press. 406.
3. IMAIOS. *Online medical training for healthcare professionals*. e-Courses: e-MRI [cited 2011 11/11]; Available from: http://www.imaios.com/en/e-Courses/e-MRI
4. ReviseMRI. *Study materials for physicists and other clinical scientists learning the basics of magnetic resonance imaging (MRI)* [cited 2009 01/12]; Available from: http://www.revisemri.com
5. Liney G. *What is MRI*. [cited 2009 11/12]; Available from: http://www.hull.ac.uk/mri/whatisMRI.html
6. Gibbs P. Lectures on MRI 2010, University of Hull, 2010
7. Umkcradres. *Magnetized nuclear spin systems* [cited 2010 11/05]; Available from: http://www.umkcradres.org/education/neuro/Spec/RADPAGE/Magnetized%20nuclear%20spin%20systems.htm

13 References

1. Bloch, F., W.W. Hansen, and M. Packard, *Nuclear Induction.* Physical Review, 1946. **69**(3-4): p. 127-127.
2. Purcell, E.M., H.C. Torrey, and R.V. Pound, *Resonance Absorption by Nuclear Magnetic Moments in a Solid.* Physical Review, 1946. **69**(1-2): p. 37-38.
3. Donald W. McRobbie, E.A.M., Martin J. Graves, Martin R. Prince, *MRI from Picture to Proton*. Vol. 2. 2007: Cambridge University Press. 406.
4. ReviseMRI. *Study MRI Physics*. image slice selection [cited 2011 11/11]; Available from: http://www.revisemri.com/images/sliceselection.gif.
5. IMAIOS. *Online medical training for healthcare professionals*. e-Anatomy: human anatomy, medical imaging and illustrations [cited 2011 11/11]; Available from: http://www.imaios.com/Media/Images/e-anatomy/Anatomical-terms-of-location-position-motion/planes-coronal-transverse-sagittal-anatomy-en.
6. Elmore Jg, A.K.L.C.D.F.S.W., *Screening for breast cancer.* JAMA: The Journal of the American Medical Association, 2005. **293**(10): p. 1245-1256.
7. Nyström, L., et al., *Long-term effects of mammography screening: updated overview of the Swedish randomised trials.* The Lancet, 2002. **359**(9310): p. 909-919.
8. Alexander, F.E., et al., *The Edinburgh Randomized Trial of Breast-Cancer Screening - Results after 10 Years of Follow-Up.* British Journal of Cancer, 1994. **70**(3): p. 542-548.
9. Wikipedia. *Mammography*. [cited 2010 12/12]; Available from: http://en.wikipedia.org/wiki/Mammography.
10. breastpathology.info. *Breast pathology on the web*. malignant microcalcification [cited 2010 12/12]; Available from: http://www.breastpathology.info/calcs_malig.html.
11. Freer, T.W. and M.J. Ulissey, *Screening Mammography with Computer-aided Detection: Prospective Study of 12,860 Patients in a Community Breast Center1.* Radiology, 2001. **220**(3): p. 781-786.
12. Gur, D., et al., *Changes in Breast Cancer Detection and Mammography Recall Rates After the Introduction of a Computer-Aided Detection System.* Journal of the National Cancer Institute, 2004. **96**(3): p. 185-190.
13. Ryan, S.E. *Salem Radiology Consultants*. Digital mammography [cited 2010 12/12]; Available from: http://www.salemradiology.com/mammography.htm.
14. Stavros, A.T., et al., *Solid breast nodules: use of sonography to distinguish between benign and malignant lesions.* Radiology, 1995. **196**(1): p. 123-134.
15. Irwig, L., N. Houssami, and C. van Vliet, *New technologies in screening for breast cancer: a systematic review of their accuracy.* Br J Cancer, 2004. **90**(11): p. 2118-2122.
16. Kuhl, C.K., et al., *Breast MR Imaging Screening in 192 Women Proved or Suspected to Be Carriers of a Breast Cancer Susceptibility Gene: Preliminary Results1.* Radiology, 2000. **215**(1): p. 267-279.
17. Kriege, M., et al., *Efficacy of MRI and Mammography for Breast-Cancer Screening in Women with a Familial or Genetic Predisposition.* New England Journal of Medicine, 2004. **351**(5): p. 427-437.
18. Lord, S.J., et al., *A systematic review of the effectiveness of magnetic resonance imaging (MRI) as an addition to mammography and ultrasound in screening young women at high risk of breast cancer.* European Journal of Cancer, 2007. **43**(13): p. 1905-1917.
19. Kuhl, C.K., *MRI of breast tumors.* European Radiology, 2000. **10**(1): p. 46-58.
20. Nunes, L.W., et al., *Diagnostic performance characteristics of architectural features revealed by high spatial-resolution MR imaging of the breast.* American Journal of Roentgenology, 1997. **169**(2): p. 409-15.
21. Wang, S.-C. *Magnetic Resonance Mammography: Treatment & Medication*

2012 [cited 2012 07/07]; Available from: http://dc238.4shared.com/doc/HBfJ5oAM/preview.html.
22. Boetes, C., et al., *Mr Characterization of Suspicious Breast-Lesions with a Gadolinium-Enhanced Turboflash Subtraction Technique.* Radiology, 1994. **193**(3): p. 777-781.
23. ACR *Breast imaging reporting and data system atlas* 2003.
24. Obenauer, S., K.P. Hermann, and E. Grabbe, *Applications and literature review of the BI-RADS classification.* European Radiology, 2005. **15**(5): p. 1027-1036.
25. Lazarus, E., et al., *BI-RADS Lexicon for US and Mammography: Interobserver Variability and Positive Predictive Value1.* Radiology, 2006. **239**(2): p. 385-391.
26. Raza, S., et al., *US of Breast Masses Categorized as BI-RADS 3, 4, and 5: Pictorial Review of Factors Influencing Clinical Management1.* Radiographics, 2010. **30**(5): p. 1199-1213.
27. Erguvan-Dogan, B., et al., *BI-RADS-MRI: a primer.* AJR. American journal of roentgenology, 2006. **187**(2): p. W152-60.
28. Elmore, J.G.W., C. K. Lee, C. H. Howard, D. H. , *Variability in Radiologists' Interpretation of Mammograms.* NEW ENGLAND JOURNAL OF MEDICINE, 1994. **331**(22): p. 1493.
29. Baker, J.A., P.J. Kornguth, and C.E. Floyd, *Breast imaging reporting and data system standardized mammography lexicon: observer variability in lesion description.* American Journal of Roentgenology, 1996. **166**(4): p. 773-8.
30. Berg, W.A., et al., *Breast Imaging Reporting and Data System.* American Journal of Roentgenology, 2000. **174**(6): p. 1769-1777.
31. Stoutjesdijk, M.J., et al., *Variability in the Description of Morphologic and Contrast Enhancement Characteristics of Breast Lesions onMagnetic Resonance Imaging.* Investigative Radiology, 2005. **40**(6): p. 355-362.
32. Kuhl, C.K., et al., *Dynamic Breast MR Imaging: Are Signal Intensity Time Course Data Useful for Differential Diagnosis of Enhancing Lesions?1.* Radiology, 1999. **211**(1): p. 101-110.
33. Subramanian, K.R., J.P. Brockway, and W.B. Carruthers, *Interactive detection and visualization of breast lesions from dynamic contrast enhanced MRI volumes.* Computerized Medical Imaging and Graphics, 2004. **28**(8): p. 435-444.
34. Pediconi, F., et al., *Color-coded automated signal intensity-curve for detection and characterization of breast lesions: Preliminary evaluation of a new software for MR-based breast imaging.* International Congress Series, 2005. **1281**(0): p. 1081-1086.
35. Ernesto Coto, S.G., Stefan Bruckner, Meister Eduard Gröller, Armin Kanitsar, Omaira Rodriguez *MammoExplorer: An Advanced CAD Application for Breast DCE-MRI*. 2005.
36. mediray. *CADstream* Breast [cited 2011 06/05]; Available from: http://www.mediray.gr/brochure.pdf
37. Lehman, C.D., et al., *A New Automated Software System to Evaluate Breast MR Examinations: Improved Specificity Without Decreased Sensitivity.* American Journal of Roentgenology, 2006. **187**(1): p. 51-56.
38. Padhani, A.R., *Dynamic contrast-enhanced MRI in clinical oncology: Current status and future directions.* Journal of Magnetic Resonance Imaging, 2002. **16**(4): p. 407-422.
39. Cron, G.O., F. Kelcz, and G.E. Santyr, *Improvement in breast lesion characterization with dynamic contrast-enhanced MRI using pharmacokinetic modeling and bookend T1 measurements.* Magnetic Resonance in Medicine, 2004. **51**(5): p. 1066-1070.
40. RxKinetics. *Pharmacokinetic Concepts* Pharmacokinetic modeling [cited 2011 05/03]; Available from: http://www.rxkinetics.com/pktutorial/1_5.html.
41. Di Giovanni, P., et al., *The accuracy of pharmacokinetic parameter measurement in DCE-MRI of the breast at 3 T.* Physics in Medicine and Biology, 2010. **55**(1): p. 121-132.
42. Freeborough, P.A. and N.C. Fox, *MR image texture analysis applied to the diagnosis and tracking of Alzheimer's disease.* Medical Imaging, IEEE Transactions on, 1998. **17**(3): p. 475-478.

43. Kovalev, V.A., et al., *Three-dimensional texture analysis of MRI brain datasets.* Medical Imaging, IEEE Transactions on, 2001. **20**(5): p. 424-433.
44. Mahmoud-Ghoneim, D., et al., *Three dimensional texture analysis in MRI: a preliminary evaluation in gliomas.* Magnetic Resonance Imaging, 2003. **21**(9): p. 983-987.
45. Agner, S., et al., *Textural Kinetics: A Novel Dynamic Contrast-Enhanced (DCE)-MRI Feature for Breast Lesion Classification.* Journal of Digital Imaging, 2011. **24**(3): p. 446-463.
46. Bhooshan, N., et al., *Cancerous Breast Lesions on Dynamic Contrast-enhanced MR Images: Computerized Characterization for Image-based Prognostic Markers.* Radiology, 2010. **254**(3): p. 680-690.
47. Chen, W., et al., *Volumetric texture analysis of breast lesions on contrast-enhanced magnetic resonance images.* Magnetic Resonance in Medicine, 2007. **58**(3): p. 562-571.
48. Gibbs, P. and L.W. Turnbull, *Textural analysis of contrast-enhanced MR images of the breast.* Magnetic Resonance in Medicine, 2003. **50**(1): p. 92-98.
49. James, D., B.D. Clymer, and P. Schmalbrock, *Texture detection of simulated microcalcification susceptibility effects in magnetic resonance imaging of breasts.* Journal of Magnetic Resonance Imaging, 2001. **13**(6): p. 876-881.
50. Sinha, S., et al., *Multifeature analysis of Gd-enhanced MR images of breast lesions.* Journal of Magnetic Resonance Imaging, 1997. **7**(6): p. 1016-1026.
51. Castellano, G., et al., *Texture analysis of medical images.* Clinical Radiology, 2004. **59**(12): p. 1061-1069.
52. Andrzej Materka, M.S. *Texture Analysis Methods – A Review*. 1998.
53. Haralick, R.M., K. Shanmugam, and I.H. Dinstein, *Textural Features for Image Classification.* Systems, Man and Cybernetics, IEEE Transactions on, 1973. **SMC-3**(6): p. 610-621.
54. Mathworks. *graycomatrix*. Create gray-level co-occurrence matrix from image [cited 2010 01/06]; Available from: http://www.mathworks.com/access/helpdesk/help/toolbox/images/graycomatrix.html.
55. Conners, R.W., M.M. Trivedi, and C.A. Harlow, *Segmentation of a high-resolution urban scene using texture operators.* Computer Vision, Graphics, and Image Processing, 1984. **25**(3): p. 273-310.
56. Kassner, A. and R.E. Thornhill, *Texture Analysis: A Review of Neurologic MR Imaging Applications.* American Journal of Neuroradiology, 2010. **31**(5): p. 809-816.
57. Zhang, D. and G. Lu, *Review of shape representation and description techniques.* Pattern Recognition, 2004. **37**(1): p. 1-19.
58. Wikipedia. *Gabor filter*. [cited 2011 05/05]; Available from: http://en.wikipedia.org/wiki/Gabor_filter.
59. Kunz, H., et al., *Feature extraction and supervised classification of MR images to support proton radiation therapy of eye tumors.* Computer Methods and Programs in Biomedicine, 2004. **73**(3): p. 195-202.
60. Yuan, X., et al., *Multi-scale feature identification using evolution strategies.* Image and Vision Computing, 2005. **23**(6): p. 555-563.
61. Lerski, R.A., et al., *VIII. MR image texture analysis—An approach to tissue characterization.* Magnetic Resonance Imaging, 1993. **11**(6): p. 873-887.
62. Kjær, L., et al., *Texture Analysis in Quantitative MR Imaging.* Acta Radiologica, 1995. **36**(2): p. 127-135.
63. Lerski, R.A. and L.R. Schad, *The use of reticulated foam in texture test objects for magnetic resonance imaging.* Magnetic Resonance Imaging, 1998. **16**(9): p. 1139-1144.
64. Lerski, R.A., et al., *Multicentre magnetic resonance texture analysis trial using reticulated foam test objects.* Magnetic Resonance Imaging, 1999. **17**(7): p. 1025-1031.

65. Waugh SA, L.R., Bidaut L, Thompson AM, *The influence of field strength and different clinical breast MRI protocols on the outcome of texture analysis using foam phantoms.* Med. Phys 2011. **38**(9): p. 5058-66.
66. Jirák, D., et al., *Texture analysis of human liver.* Journal of Magnetic Resonance Imaging, 2002. **15**(1): p. 68-74.
67. Szczypinski, M.S., A Materka, A. Klepaczko. *MaZda - User Manual*. [cited 2012 12/02]; Available from: http://www.eletel.p.lodz.pl/programy/mazda/download/mazda_manual.pdf.
68. Mathias, J.M., P.S. Tofts, and N.A. Losseff, *Texture analysis of spinal cord pathology in multiple sclerosis.* Magnetic Resonance in Medicine, 1999. **42**(5): p. 929-935.
69. Mayerhoefer, M.E., et al., *Texture analysis for tissue discrimination on T1-weighted MR images of the knee joint in a multicenter study: Transferability of texture features and comparison of feature selection methods and classifiers.* Journal of Magnetic Resonance Imaging, 2005. **22**(5): p. 674-680.
70. Jianhua, Y., J. Chen, and C. Chow, *Breast Tumor Analysis in Dynamic Contrast Enhanced MRI Using Texture Features and Wavelet Transform.* Selected Topics in Signal Processing, IEEE Journal of, 2009. **3**(1): p. 94-100.
71. Yang, W., et al., *Shape symmetry analysis of breast tumors on ultrasound images.* Computers in Biology and Medicine, 2009. **39**(3): p. 231-238.
72. Zabrodsky, H., S. Peleg, and D. Avnir, *Symmetry as a continuous feature.* Pattern Analysis and Machine Intelligence, IEEE Transactions on, 1995. **17**(12): p. 1154-1166.
73. Yokoyama, T., et al., *Image analysis of irregularity of cluster shape in cytological diagnosis of breast tumors: Cluster analysis with 2D-fractal dimension.* Diagnostic Cytopathology, 2005. **33**(2): p. 71-77.
74. Mohamed Eisa, M.R., A. F. El-Gamal, *Preliminary Diagnostics of Mammograms using Moments and Texture Features.* ICGST International Journal on Graphics, Vision and Image Processing, GVIP, 2009. **9**(5): p. 21-27.
75. ImageJ. *Fiji is just ImageJ*. Fiji Image processing package [cited 2010 02/01]; Available from: http://fiji.sc/wiki/index.php/Fiji.
76. Mathworks. *Analysing and enhancing images*. Analysing the texture of an image [cited 2009-2011; Available from: http://www.mathworks.co.uk/help/toolbox/images/f11-27972.html.
77. Cabrera, J.E. *Texture Analyzer*. [cited 2011 03/02]; Available from: http://rsbweb.nih.gov/ij/plugins/texture.html.
78. ISO, *Accuracy (trueness and precision) of measurement method and results - Part 1: General principles and definitions;.* ISO: Gene`ve, Switzerland,, 1994. **5725**(1).
79. Bland, J.M. and D.G. Altman, *Statistics Notes: Measurement error and correlation coefficients.* BMJ, 1996. **313**(7048): p. 744.
80. Sørlie, T., et al., *Gene expression patterns of breast carcinomas distinguish tumor subclasses with clinical implications.* Proceedings of the National Academy of Sciences, 2001. **98**(19): p. 10869-10874.
81. Sørlie, T., et al., *Repeated observation of breast tumor subtypes in independent gene expression data sets.* Proceedings of the National Academy of Sciences, 2003. **100**(14): p. 8418-8423.
82. CIP. *Cancer Imaging Program*. clinical trials [cited 2012 01/05]; Available from: http://imaging.cancer.gov/clinicaltrials/imaging.
83. Manton, D.J., et al., *Neoadjuvant chemotherapy in breast cancer: early response prediction with quantitative MR imaging and spectroscopy.* Br J Cancer, 2006. **94**(3): p. 427-435.
84. Wikipedia. *histogram equalisation*. [cited 2011 05/05]; Available from: http://www.wikipedia.org.
85. Gibbs P, Ahmed A. *Texture Analysis of DCE-MRI of the Breast as a Predictor of Response*. in *19th ISMRM Annual meeting*. 2011. Montreal: ISMRM.

86. Peng, C.Y.J., K.L. Lee, and G.M. Ingersoll, *An introduction to logistic regression analysis and reporting.* Journal of Educational Research, 2002. **96**(1): p. 3-14.
87. I.T, J., *Principal Component Analysis*. second ed. 2002: Springer Series in Statistics.
88. Hájek M, D.M., Materka A, Lerski R *Texture analysis for magnetic resonance imaging*. 2006: med4. 225.
89. Wikipedia. *Haar-like features*. [cited 2012 05/05]; Available from: http://en.wikipedia.org/wiki/Haar-like_features.
90. Stollnitz, E.J., T.D. DeRose, and D.H. Salesin, *Wavelets for computer graphics: a primer. 2.* Computer Graphics and Applications, IEEE, 1995. **15**(4): p. 75-85.
91. Bornefalk, H., *Estimation and Comparison of CAD System Performance in Clinical Settings1.* Academic Radiology, 2005. **12**(6): p. 687-694.
92. Kallergi M, C.G., Gaviria J., *Evaluating the performance of detection algorithms in digital mammography.* Med. Phys, 1999. **26**(2): p. 267-75.
93. Edwards, D.C., et al., *Maximum likelihood fitting of FROC curves under an initial-detection-and-candidate-analysis model.* Medical Physics, 2002. **29**(12): p. 2861-2870.
94. Penedo, M., et al., *Free-Response Receiver Operating Characteristic Evaluation of Lossy JPEG2000 and Object-based Set Partitioning in Hierarchical Trees Compression of Digitized Mammograms1.* Radiology, 2005. **237**(2): p. 450-457.
95. Haralick, R.M., *Statistical and structural approaches to texture.* Proceedings of the IEEE, 1979. **67**(5): p. 786-804.
96. Wikipedia. *Skew*. [cited 2011 05/05]; Available from: http://www.wikipedia.org.
97. riskglosssary. *Glossary, Encyclopedia & Resource Locator*. Kurtosis [cited 2011; Available from: http://www.riskglossary.com/link/kurtosis.htm.
98. Steven, B. *MRI contrast enhancement Screening*. Spatial resolution of MRI breast images can help distinguish between benign and malignant breast tumors 2010 [cited 2012 031/07]; Available from: http://www.breast-cancer.ca/screening/mri-breast-contrast-enhancement.htm.
99. Wikipedia. *eigenvectors*. [cited 2011 05/05]; Available from: http://en.wikipedia.org/wiki/Eigenvalues_and_eigenvectors.
100. Levman JE, M.A., *A margin sharpness measurement for the diagnosis of breast cancer from magnetic resonance imaging examinations.* Academic Radiology, 2011. **18**(12): p. 1577-81.
101. Gilhuijs, K.G., M.L. Giger, and U. Bick, *Computerized analysis of breast lesions in three dimensions using dynamic magnetic-resonance imaging.* Medical Physics, 1998. **25**(9): p. 1647-1654.
102. Gilhuijs, K.G., M.L. Giger, and U. Bick, *Automated feature extraction and classification of breast lesions in magnetic resonance images.* Proc SPIE, 1998(3338): p. 294-300.